Mathematical modeling and numerical simulation of innovative electronic nanostructures

Clément Jourdana

Università degli Studi di Pavia

PHD THESIS

In joint supervision, in order to obtain a

DOCTORAT DE L'UNIVERSITÉ DE TOULOUSE

Délivré par : Université Toulouse III Paul Sabatier (UT3 Paul Sabatier)
Discipline ou spécialité : Mathématiques Appliquées

and a

DOTTORATO IN MATEMATICA E STATISTICA

Serie : XXIV Ciclo
Rilasciato da : Università degli Studi di Pavia

Presented and defended by

Clément JOURDANA

on November 25^{th}, 2011

Title :

Mathematical modeling and numerical simulation of innovative electronic nanostructures

---

Doctoral schools :
Mathématiques Informatique Télécommunications (MITT)
Dottorato di Ricerca in Matematica e Statistica

Research laboratories :
Institut de Mathématiques de Toulouse, UMR 5219
Dipartimento di Matematica "F. Casorati" and IMATI - CNR

PhD supervisors :
Paola PIETRA and Pierre DEGOND standing in for Naoufel BEN ABDALLAH

Jury members :

P. Degond	*Research director*	CNRS IMT Toulouse	*Supervisor*
L. Desvillettes	*Professor*	CMLA ENS Cachan	*Reviewer*
A. Jüngel	*Professor*	TU Wien	*Reviewer*
I. Perugia	*Associate professor*	DIMAT Pavia	*Member*
P. Pietra	*Research director*	IMATI-CNR Pavia	*Supervisor*
J.-M. Roquejoffre	*Professor*	IMT Toulouse	*Member*

Acknowledgments

Il m'est impossible de commencer autrement qu'en ayant une pensée pour Naoufel Ben Abdallah, mon directeur de thèse à Toulouse. Naoufel m'a d'abord accueilli et encadré durant mon stage de master 2. A la fin de celui-ci, il m'a généreusement proposé et mis en place ce projet de cotutelle. Comme beaucoup de ses sujets de recherche, il s'agit d'un problème mathématique engendré directement par des applications innovantes. Je n'oublierai pas les séances de travail avec lui, où il m'a transmis de précieux conseils, m'apprenant à éclaircir des problèmes complexes. Je le remercie pour la confiance et le soutien qu'il m'a accordé et je suis très triste qu'il ne puisse pas voir le résultat final présenté dans ce manuscrit. Je me souviendrai de Naoufel comme un talentueux chercheur, un directeur de thèse enthousiaste et une généreuse personne.

Je remercie vivement Paola Pietra, ma directrice de thèse à Pavia. Immédiatement, Paola a été passionnée à l'idée d'encadrer une thèse en cotutelle et ainsi vivifier la collaboration en cours avec Naoufel. Elle m'a alors chaleureusement accueilli en Italie et à partir de ce moment-là elle a toujours été incroyablement disponible et attentive à ma progression. Elle s'est intéressée à tous les domaines de ma thèse et non pas seulement aux problèmes numériques dont elle est experte. Enfin, son soutien pour la rédaction de ce manuscrit a été primordial. Je tiens à souligner sa gentillesse, sa patience, son ouverture d'esprit... et mon seul regret est de ne toujours pas parler en italien avec elle.

C'est un honneur pour moi que Pierre Degond ait très gentiment accepté de suppléer Naoufel comme directeur de ma thèse à Toulouse. Je le remercie de m'avoir alors fait part de nombreux conseils avisés et d'avoir toujours su répondre à mes sollicitations de manière constructive. C'est également lui qui m'a encouragé à rédiger ce manuscrit pour soutenir cette thèse à la période la plus pertinente.

J'adresse tous mes remerciements à Laurent Desvillettes et Ansgar Jüngel pour l'intérêt qu'ils ont porté à mon travail en ayant accepté d'en être rapporteurs.

Je tiens à remercier également Ilaria Perugia et Jean-Michel Roquejoffre d'avoir accepté de faire partie de mon jury de thèse.

Je remercie chaleureusement Elise Fouassier, qui m'a d'abord co-encadré durant mon stage de master 2 et qui a ensuite régulièrement gardé un oeil éclairé sur ma progression. En plus de sa précieuse aide scientifique, je retiens son soutien spontané et ses conseils toujours réfléchis.

Je voudrais aussi remercier fortement David Sanchez. Son intérêt pour le ferromagnétisme et ses suggestions foisonnantes et judicieuses ont apporté une réelle plus value au travail relatif à la spintronique.

Je remercie sincèrement Nicolas Vauchelet qui par sa patience et sa clarté m'a permis de progresser de manière optimale dans l'analyse du modèle diffusif. La mise en place du projet Galilée no 25992ND (partenariat Hubert Curien France-Italie, géré par l'Agence Egide) a contribué au fait qu'il ait effectué plusieurs séjours à Pavia et a ainsi facilité notre enrichissante collaboration.

Je remercie Sergio Rovida. Sans son aide, je serais toujours en train d'installer une librairie ou de compiler mon code sur les serveurs de calculs.

Cette thèse a été effectuée en cotutelle entre l'Université Paul Sabatier de Toulouse et l'Università degli Studi di Pavia. Je remercie tout d'abord l'Istituto di Matematica Applicata e Tecnologie Informatiche du CNR qui a financé mes trois années de thèse. Dans cet institut de Pavia ainsi qu'à l'Institut de Mathématiques de Toulouse, il règne une ambiance conviviale et détendue qui m'a permis de m'intégrer facilement et de travailler pendant trois ans dans des conditions idéales. Les discussions dans les couloirs ou près de la machine à café ont toujours été fructueuses. Je remercie également le personnel administratif de ces deux instituts qui m'a facilité les démarches bureaucratiques.

Je remercie Durkbin et Rafa, qui sont arrivés quasiment en même temps que moi à Pavia. Ensemble, nous avons découvert l'Italie du Nord, de la région des lacs aux Dolomites, en passant par l'Oltrepo Pavese et la Ligurie. Grâce à leur présence, j'ai en quelque sorte aussi visité l'Espagne et la Corée du Sud. Egalement, ils ont réussi à me supporter au quotidien et ils m'ont constamment soutenu et conseillé. Promis, je n'oublierai jamais les fameux r.d.v. p.d.v.

D'autres thésards, post-docs,... ont partagé mon bureau ou un moment de ma thèse. Merci donc à Luigi, Alice, Massimiliano, Matthias, Simone, Andrea, Blanca, Ariel, Mukesh, Carlo, Stanislas, Yogesh, Ritesh, Marion... et tout ceux que j'oublie. Cette multi-culture m'a enrichi et a ancré définitivement le respect de l'autre dans ma ligne de conduite.

Je remercie également les copains de longues dates que ce soit de l'INSA, de Lectoure ou du Haou. J'espère vraiment que nous nous verrons un peu plus souvent à présent.

Enfin, je remercie vivement toute ma famille et particulièrement mes parents. Ils m'ont toujours laissé une très grande autonomie dans mes choix et les ont ensuite pleinement approuvés. Sans leur entière confiance et leur soutien sans faille, mon parcours ne se serait pas aussi bien passé.

Contents

Introduction

0.1 Introduction - version française

Dans cette thèse de doctorat, nous nous intéressons à la modélisation mathématique et à la simulation numérique de dispositifs nanoélectroniques innovants, tels que des nanostructures semiconductrices fortement confinées ou des matériaux ferromagnétiques multi-couches avec injection de spin.

Depuis le milieu du $20^{\text{ème}}$ siècle, un effort constant dans la miniaturisation des dispositifs électroniques a été entrepris. Les circuits intégrés contiennent toujours plus de composants, de plus en plus petits. La loi de Moore conjecture même, qu'à coût constant, le nombre de transistors qui peut être placé dans un circuit intégré double tous les deux ans. Ainsi, en 2011, un processeur contient généralement plus d'un milliard de transistors, chacun ayant une taille caractéristique de l'ordre de 20 nm. Cette miniaturisation permet également de fabriquer des composants électroniques dont les temps de réponse et la consommation en énergie sont sans cesse diminués.

Un exemple qui permet d'illustrer cette miniaturisation est celui de l'entreprise Intel qui vient d'annoncer en mai 2011 qu'ils "commencent en exclusivité mondiale la fabrication à grand volume de puces contenant des transistors à trois dimensions". Le transistor à trois dimensions (3D) n'est pas une nouveauté. Il a été découvert en 2002, déjà par Intel. La différence est qu'aujourd'hui, cette technologie est prête pour une production en masse. Dès les premiers mois de l'année 2012, les transistors 3D vont apparaitre dans nos ordinateurs, téléphones portables et nombreuses autres applications électroniques. Ce transistor à trois dimensions, appelé "Tri-gate", a une taille de 22 nm. Mais surtout, à faible tension, sa performance est 37 % plus importante que celle du précédent transistor d'Intel, un composant planaire de 32 nm. Il consomme également, pour une performance identique, la moitié d'énergie.

A l'heure actuelle, nous dénommons nanotechnologies, les études qui manipulent des structures, des dispositifs ou des systèmes matériels à l'échelle atomique ou moléculaire. Les nanotechnologies développent des objets et des matériaux dont la taille caractéristique varie entre 1 et 100 nanomètres (au moins dans une des dimensions). A cette échelle, les effets quantiques tels que les interférences ou l'effet tunnel sont prépondérants. Il existe même des composants électroniques (diodes à effet tunnel résonant ou diodes lasers par exemple) dont le fonctionnement

est exclusivement basé sur ces phénomènes quantiques. Un autre effet quantique important est le confinement : lorsque des dispositifs ont une ou plusieurs dimensions extrêmement petites, les particules ne peuvent se déplacer que dans les autres directions. C'est le cas notamment des nouvelles structures comme les fils quantiques de silicium ou les nanotubes de carbone où la section transversale est tellement rétrécie que le transport des électrons est confiné dans la direction longitudinale unidimensionnelle. Ce sont ces dernières structures que nous désignons comme nanostructures très fortement confinées, et que nous étudions dans les deux premières parties de cette thèse.

Une autre technologie émergente, qui fait l'objet de recherches intensives dans les laboratoires de physique, est la spintronique ou électronique de spin. Elle utilise le spin des électrons (ainsi que le moment magnétique associé) au lieu de leur charge comme c'est le cas dans les composants électroniques usuels. Cette technologie laisse présager des progrès considérables dans la construction de mémoires magnétiques, de réseaux logiques programmables à grande vitesse ou encore d'oscillateurs à hautes fréquences pour les télécommunications. Dans ce domaine, nous nous intéressons plus particulièrement, dans la troisième partie de cette thèse, au renversement d'aimantation par un transfert de spin dans un matériau ferromagnétique.

Les phénomènes physiques générés dans ces nouveaux dispositifs électroniques sont extrêmement complexes et ne sont pas encore parfaitement compris. Par exemple, une légère variation dans la structure cristalline d'un nanodispositif a une influence très significative sur ses propriétés électriques. De même, pour une valeur seuil du courant polarisé en spin, l'aimantation dans un matériau ferromagnétique multi-couches peut être renversée. Par conséquent, de manière à prévoir les comportements, à atteindre les limites de performances et à créer de futures configurations, une importante batterie de tests expérimentaux est nécessaire. Cette approche est longue et coûteuse. C'est pourquoi, la modélisation et la simulation numérique peuvent jouer un rôle considérable dans l'étude et l'amélioration de tels dispositifs. Un avantage non négligeable de cette approche numérique est la possibilité de travailler sur des dispositifs virtuels. Elle permet de réaliser des tests "idéaux" en s'affranchissant des contraintes de fabrication. Cette flexibilité est importante pour comprendre parfaitement le fonctionnement des nanoélectroniques et de la spintronique. De plus, une approche numérique donne le moyen de faire des études paramètriques, en faisant varier la valeur d'une ou plusieurs caractéristiques physiques (longueur, dopage, potentiel appliqué, courant injecté...). Cela permet de clarifier les mécanismes entrant en jeu voire de prédire des comportements singuliers. Les simulations sont aussi utiles pour déterminer, pour les différents paramètres, un intervalle de valeurs adéquat de manière à procéder aux tests expérimentaux de façon optimale. L'approche mathématique et numérique se révèle donc être un outil complémentaire aux expériences physiques.

Pour atteindre cet objectif, de nouveaux modèles mathématiques ont été développés. Lorsque on étudie un nouveau dispositif, le premier réflexe est de déterminer les phénomènes physiques dominants qui doivent absolument être pris en compte par la modélisation. Cela permet de choisir le modèle le plus approprié. Jusqu'à des tailles de l'ordre du micromètre, une description classique du transport des particules chargées, qui détermine notamment complètement les

trajectoires, est acceptable. Cependant, pour des dimensions inférieures à 100 nm, c'est beaucoup plus pertinent d'utiliser un modèle quantique prenant en compte les effets quantiques. En réalité, les choses sont légèrement plus compliquées et le choix du modèle adéquat ne dépend pas seulement de la taille du dispositif. Par exemple, il n'est pas facile d'insérer les collisions entre les particules dans les modèles quantiques. L'ajout d'un terme correctif quantique dans les modèles classiques est une possibilité. Une autre approche intéressante est l'utilisation d'un modèle hybride quantique-classique. En effet, les effets quantiques sont très souvent localisés dans des régions bien spécifiques. Il est alors possible de découper le domaine de manière à utiliser un modèle classique dans certaines zones et un modèle quantique dans les autres. Les différentes régions sont alors couplées entre elles par des conditions d'interface. Finalement, il est également important de préciser qu'au sein de ces deux principales catégories (classique et quantique), il existe une hiérarchie dans les modèles avec différents degrés de précision. Un compromis entre la précision physique et le coût numérique doit donc être trouvé.

D'un point de vue mathématique, les problèmes provenant des nanotechnologies et rencontrés pour décrire les nouveaux dispositifs électroniques sont très souvent des problèmes multi-échelles. Différents phénomènes physiques entrent en jeu et se produisent à des échelles de temps ou d'espace différentes. C'est la raison pour laquelle il est nécessaire de concevoir de nouveaux modèles qui prennent en compte de manière optimale ces différentes échelles. Les problèmes multi-échelles sont nombreux et variés. D'une part, nous trouvons les problèmes qui contiennent des singularités (chocs, couches limites,...) dans un endroit ou un temps précis. Pour ceux-là, une solution possible consiste à utiliser une description microscopique près des singularités et une autre plus grossière dans le reste du domaine. Pour d'autres problèmes, les multi-échelles coexistent. Il est alors nécessaire d'insérer l'information provenant de l'échelle la plus petite dans celle émanant de la plus grande. En résumé, le véritable challenge est de développer un modèle et/ou une méthode numérique qui permette en même temps de décrire convenablement tous les phénomènes physiques et d'utiliser une discrétisation la moins raffinée possible (ce qui se traduit par un gain en temps de calcul et en utilisation de la mémoire).

De nombreuses approches existent pour traiter cette résolution multi-échelles. D'un point de vue mathématique, nous pouvons citer les techniques d'homogénéisation qui consistent à résoudre une équation macroscopique dans laquelle nous avons incorporé avec des quantités moyennées l'information de l'échelle plus petite (homogénéisation double échelle, décomposition en fonctions enveloppes...), les méthodes de décomposition de domaines qui couplent différentes équations dans différentes régions à travers des conditions d'interfaces (comme nous l'avons déjà expliqué pour les approches hybrides quantiques-classiques), les développements asymptotiques qui reposent sur l'établissement de la limite lorsque un petit paramètre tend vers zéro... D'un point de vue numérique, de nombreuses possibilités sont également envisageables. Par exemple, un maillage adaptatif permet de raffiner la discrétisation uniquement aux endroits et aux instants où cela est nécessaire, les méthodes d'éléments finis avec des fonctions de base spéciales incorporent l'information multi-échelles dans le choix de ces fonctions...

Cette thèse de doctorat, comme son titre l'indique, est consacrée à la modélisation mathématique et la simulation numérique de dispositifs électroniques innovants. Cette thématique fait pleinement intervenir les difficultés et les solutions citées ci-dessus. D'une part, nous nous intéressons à la dérivation de nouveaux modèles (quantiques ou classiques), essentiellement basés sur l'étude des différentes échelles apparaissant dans les phénomènes physiques qui régissent ces nanostructures. D'autre part, nous proposons des simulations numériques rapides et précises de ces dispositifs qui pourraient être utilisées en complément des expérimentations physiques. A long terme, ce travail devrait permettre d'améliorer le comportement des futurs composants électroniques et éventuellement de prédire de nouvelles architectures encore plus performantes. Ce rapport de thèse est organisé de la manière suivante. Le chapitre 1 est consacré à un rappel des principales notions physiques utilisées dans ce travail. Ensuite, nous distinguons trois parties différentes :

- Dans la première partie, nous présentons la dérivation et les simulations numériques d'un modèle avec masse effective pour décrire le transport quantique des électrons dans des nanostructures très fortement confinées (Chapitres 2 et 3).
- La deuxième partie est consacrée à l'étude du transport non ballistique dans ces mêmes nanostructures très fortement confinées. Nous analysons un modèle de transport diffusif (Chapitre 4) et puis nous présentons une approche hybride quantique-classique (Chapitre 5).
- Dans la dernière partie, nous étudions un sujet brûlant de la spintronique. Nous modélisons et simulons le renversement d'aimantation dans un matériau ferromagnétique multi-couches sous l'effet d'un courant de spin (Chapitre 6).

Dans la suite de l'introduction, nous détaillons le contenu de chaque chapitre. La plupart sont écrits sous forme d'articles et peuvent être lus de manière indépendante.

0.2 Introduzione - versione italiana

In questa tesi di dottorato siamo interessati alla modellazione matematica e alla simulazione numerica di dispositivi nanoelettronici innovativi, come nanostrutture a semiconduttore fortemente confinate o materiali ferromagnetici multistrato a iniezione di spin.

A partire dalla metà del 20-simo secolo si è intrapreso uno sforzo costante nella miniaturizzazione dei dispositivi elettronici. I circuiti elettronici contengono un numero di componenti in continuo aumento. La celebrata legge di Moore congettura che, a costo costante, il numero di transistori che può essere posta su un circuito integrato raddoppia approssimativamente ogni due anni. Ne consegue che nel 2011 un processore contiene più di un miliardo di transistori, ciascuno con una taglia caratteristica dell'ordine di 20 nm. Questa miniaturizzazione permette

inoltre di fabbricare componenti elettroniche i cui tempi di risposta e i cui consumi energetici sono in costante diminuizione.

Un esempio che permette di illustrare i traguardi dell'industria elettronica è rappresentato dall'annuncio del Maggio 2011 dell'impresa Intel sull'inizio in esclusiva mondiale della "produzione su larga scala di chips contenenti transistori tri–dimensionali". Il transistore tri–dimensionale non è una novità in sè, in quanto è stato scoperto nel 2002 dalla stessa Intel. La grande differenza è che ora (2011) questa tecnologia è matura per una produzione di massa, con la conseguenza che transistori tri–dimensionali appariranno nei nostri computer, telefoni cellulari e molte altre applicazioni elettroniche a partire dai primi mesi del 2012. Questo transistore tri-dimensionale, denominato "Tri-gate", ha una dimensione caratteristica di 22 nm e fornisce, a basso voltaggio, fino al 37 % di aumento di prestazioni rispetto ai precedenti transistori Intel planari di 32 nm. Inoltre, a parità di prestazioni, consuma metà dell'energia di un transistore planare di 32 nm.

Attualmente si chiamano nanotecnologie gli studi che manipolano le strutture, i dispositivi o i sistemi materiali ad una scala atomica o molecolare. Le nanotecnologie sviluppano oggetti o materiali la cui dimensione caratteristica varia tra 1 e 100 nanometri (almeno in una delle direzioni). A questa scala, gli effetti quantistici, come le interferenze o l'effetto tunnel, sono preponderanti. Esistono addirittura componenti elettroniche (ad esempio i diodi ad effetto tunnel risonante o i diodi laser) il cui funzionamento è basato su questi fenomeni quantistici. Un altro fenomeno quantistico di grande rilevanza è il confinamento : quando i dispositivi hanno una o più dimensioni estremamente piccole, il trasporto delle particelle non può che avvenire nelle altre direzioni. Questo è ad esempio il caso di strutture innovative come i nanofili di silicio o i nanotubi di carbonio, la cui la sezione trasversale è così minuscola che il trasporto degli elettroni è confinato nella direzione longitudinale monodimensionale. Sono queste ultime strutture che definiamo come "nanostrutture fortemente confinate" e che sono oggetto di studio nelle due prime parti di questa tesi.

Un'altra tecnologia emergente, oggetto di ricerche intensive nei laboratori di fisica, è la cosiddetta "spintronica". In luogo della carica elettronica utilizzata nei più comuni dispositivi elettronici, la spintronica sfrutta lo spin degli elettroni e il momento magnetico associato. Questa tecnologia lascia presagire dei progressi significativi nella costruzione di memorie magnetiche, di circuiti logici programmabili ad alta velocità, o ancora di oscillatori ad alta frequenza per le telecomunicazioni. In questo ambito, ci interessiamo in particolare, nella terza parte di questa tesi, all'inversione di magnetizzazione in un materiale ferromagnetico mediante trasferimento di spin.

I fenomeni fisici generati da questi nuovi dispositivi elettronici sono estremamente complessi e non ancora completamente compresi. Per esempio, una piccola variazione nella struttura cristallina di un nanodispositivo ha una grande influenza nelle sue proprietà elettriche. Allo stesso modo, la magnetizzazione di un materiale ferromagnetico multistrato può essere invertita per una valore di soglia della corrente di spin. Di conseguenza, per riuscire a prevederne i comportamenti,

a stabilirne i limiti di prestazioni, o a progettare nuove configurazioni, è necessario utilizzare un grande numero di esperimenti. Questo tipo di approccio è lungo ed estremamente costoso. Pertanto la modellazione e la simulazione numerica possono avere un ruolo considerevole nel migliorare questi dispositivi. Un vantaggio non trascurabile di un approccio numerico è la possibilità di lavorare su dispositivi virtuali, permettendo di realizzare test "ideali" che non sono limitati da vincoli di fabbricazione. Questa flessibilità è importante per progredire nella comprensione della nanoelettronica e della spintronica. Uno studio parametrico, che consiste nel far variare una o più caratteristiche del dispositivo studiato (lunghezza, profilo di drogaggio, voltaggio applicato, corrente iniettata $\cdots$), può permettere di comprenderne il funzionamento o addirittura di predirne alcuni comportamenti singolari. Le simulazioni sono anche utili per determinare, per i diversi parametri, un intervallo di valori adeguato in modo da poter focalizzare i test sperimentali in modo ottimale. L'approccio matematico e numerico si rivela dunque come uno strumento complementare agli esperimenti fisici.

Per raggiungere questo scopo si sono sviluppati modelli matematici. Di fronte allo studio di un nuovo dispositivo, la prima riflessione riguarda i fenomeni fisici dominanti che devono essere presi in considerazione dal modello. Questo permette di scegliere il modello matematico più appropriato. Fino a dimensioni dell'ordine del micron, per il trasporto di particelle cariche è accettabile una descrizione classica, che ne determina completamente le traiettorie. Invece, per lunghezze caratteristiche inferiori a 100 nanometri, è molto più pertinente l'utilizzo di un modello in grado di descrivere i fenomeni quantistici. In realtà, le cose sono un po' più complicate e la scelta del modello non dipende unicamente dalla taglia del dispositivo. Per esempio, non è facile tener conto delle collisioni tra particelle nei modelli quantistici. Una possibilità è quella di aggiungere un termine correttivo di tipo quantistico nei modelli classici. Un altro approccio interessante è l'utilizzo di un modello ibrido classico–quantistico. Spesso i fenomeni quantistici avvengono in regioni localizzate, cosicchè il dominio può essere decomposto in diverse zone, in modo da utilizzare un modello classico in alcune regioni e un modello quantistico nelle altre. Le diverse regioni devono poi essere accoppiate mediante opportune condizioni di interfaccia. Infine, è importante ricordare che all'interno di queste due vaste categorie di modelli (classici e quantistici) esistono gerarchie di modelli con diversi gradi di precisione. Si tratta ogni volta di cercare un compromesso ragionevole tra l'accuratezza fisica e il costo numerico.

Dal punto di vista matematico, i problemi provenienti dalle nanotecnologie e utilizzati per descrivere dispositivi elettronici innovativi sono molto spesso problemi a scale multiple. Diversi fenomeni fisici entrano in gioco e si manifestano a diverse scale temporali e/o spaziali. Per questo è necessario concepire nuovi modelli che permettano di tener conto in maniera ottimale delle diverse scale. I problemi multi–scala sono numerosi e di vario tipo. Da un lato si trovano problemi che contengono singolarità (shocks, strati limite, $\cdots$) in regioni o intervalli temporali localizzati. In questi casi, una soluzione possibile consiste nell'utilizzare una descrizione più accurata (microscopica) nell'intorno della singolarità e una più grossolana nel resto del dominio. Per altri problemi, le scale multiple coesistono. È allora necessario incorporare le informazioni provenienti dalla scala più piccola nella descrizione del fenomeno ad una scala più grande. Rias-

sumendo, la vera sfida è di sviluppare un modello e/o un metodo numerico che permettano allo stesso tempo di descrivere in modo sufficientemente accurato i fenomeni fisici in gioco e di utilizzare un passo di discretizzazione il meno raffinato possibile (cosa che si traduce in un guadagno nei tempi di calcolo e nell'utilizzazione di memoria).

Numerosi sono gli approcci per affrontare problemi multiscala. Dal punto di vista matematico, possiamo ricordare le tecniche di omogeneizzazione (tra cui l'omogeneizzazione a doppia scala, o la decomposizione mediante funzioni inviluppo, $\cdots$) che consistono nel trovare equazioni macroscopiche nelle quali sono incorporate le quantità microscopiche, sotto forma di opportune medie; i metodi di decomposizione del dominio che si basano sull'accoppiamente di equazioni differenti nelle differenti regioni attraverso adeguate condizioni di interfaccia (come abbiamo già ricordato per gli approcci ibridi classici–quantistici); gli sviluppi asintotici, che permettono di passare al limite quando un (piccolo) parametro tende a zero; $\cdots$ Anche dal punto di vista numerico sono numerose le possibilità per affrontare problemi multiscala. Per esempio, l'utilizzo di metodi adattivi permette di raffinare il passo di discretizzazione unicamente nelle zone e agli istanti temporali dove è necessario; metodi agli elementi finiti con funzioni di base costruite *ad hoc* possono incorporare le informazioni multi–scala nella forma stesse di queste funzioni; $\cdots$

Come già indicato dal titolo, questa tesi di dottorato è dedicata alla modellazione matematica e alla simulazione numerica di dispositivi elettronici innovativi. Questa tematica fa emergere molte delle difficoltà e dei rimedi legati alle scale multiple citati in precedenza. Da un lato, ci interessiamo alla derivazione di nuovi modelli (quantistici o classici), basati essenzialmente sullo studio delle diverse scale che appaiono nei fenomeni fisici che reggono le nanostrutture considerate. Dall'altro, proponiamo simulazioni numeriche efficienti ed accurate che possono essere utilizzate a complemento di esperimenti fisici. A lungo termine, questo lavoro dovrebbe permettere di descrivere il comportamento di future componenti elettroniche ed eventualmente di predire nuove architetture ancor più performanti. Questa tesi è organizzata come segue. Nel Capitolo 1 si presentano le principali nozioni di fisica utilizzato in questo lavoro. In seguito si distinguono tre diverse parti:

- Nella prima parte presentiamo la derivazione e la simulazione numerica di un modello a massa efficace per descrivere il trasporto quantistico in nanostrutture fortemente confinate (Capitoli 2 e 3).
- La seconda parte è dedicata al trasporto non balistico sempre in nanostrutture fortemente confinate. Si analizza un modello di trasporto diffusivo (Capitolo 4) e, in seguito, si presenta un approccio ibrido classico–quantistico (Capitolo 5).
- Nell'ultima parte si studia un problema di grande interesse in spintronica. Modelliamo e simuliamo l'inversione di magnetizzazione in un materiale ferromagnetico multi–strato sotto l'effetto di una corrente di spin (Capitolo 6).

Nel seguito dell'introduzione dettagliamo il contenuto dei vari capitoli. Sono per lo più scritti sotto forma di articoli e possono essere letti in maniera indipendente.

0.3 Introduction - english version

In this PhD thesis, we are interested in the mathematical modeling and the numerical simulation of innovative electronic nanodevices such as ultra-scaled confined semiconductor based nanostructures or ferromagnetic multilayers with spin injection.

Since the middle of the 20^{th} century, an important effort in electronics concerns the device miniaturization. An integrated circuit contains a number of components constantly increasing. In fact, the Moore's law conjectures that the number of transistors that can be placed inexpensively on an integrated circuit doubles approximately every two years. It results that in 2011, the number of transistors in a processor is superior to one billion and the transistor feature size is of the order of 22 nm. The continue miniaturization allows also to produce electronic components with decreasing operating time, as well as with lower energy consumption.

As example, we mention that the company Intel announces in May 2011 that they "will begin high-volume manufacturing of chips featuring the world's first three-dimensional transistor". The three dimensional transistor is not a novelty, it was discovered by Intel itself in 2002. The change is that in 2011 this technology is ready for a mass production and thus 3D transistor will appear in computers, mobile phones and many other electronic applications in early 2012. This 22 nm three dimensional transistor, called Tri-Gate, provides up to 37 percent performance increase at low voltage versus Intel's 32 nm planar transistors. Moreover, it consumes less than half the power when at the same performance as 32 nm planar transistors.

Nowadays, we denote by nanotechnologies the studies which manipulate matter or device at an atomic and molecular scale. Nanotechnology deals with structures sized between 1 to 100 nanometers in at least one dimension, and involves developing materials or devices possessing at least one dimension within that size. Quantum mechanical effects such that interferences or tunneling are very important at this scale. Even, some components, e.g. resonant tunneling diodes or quantum well lasers, inherently employ quantum phenomena in their operation. Another important quantum effect is the confinement. Some structures have one or more extremely small dimensions and electrons propagate only along the other directions. In new three dimensional structures such that nanowires or nanotubes, the dimension of the transversal cross section is so thin that the transport is confined in the one dimensional longitudinal direction. These structures are referred as ultra-scaled confined nanostructures, and they are studied in the two first parts of this thesis.

Another emerging technology, which is the subject of an extensive research in physics, is the spintronics. Spintronics exploits the spin of electrons and its associated magnetic moment, instead of its electronic charge (as it is the case in numerous electronic components). In particular, it promises a great impact in constructing magnetic access memories, fast programmable logic, high-density recording or high-frequency oscillators for telecommunications. In this field, we are interested in particular, in the third part of this thesis, in the magnetization switching of a ferromagnetic material driven by a spin transfer.

Physical phenomena generated in these innovative electronic devices are extremely complex and still not well understood. For example, a minor variation in the crystal structure of a nanodevice may have a significant influence in its electric properties. Also, for a threshold value of the spin current, the magnetization in a ferromagnetic multilayer material can be switched. Thus, in order to predict their behavior, to access their performance limits and to design new configurations, an important experimental test battery is necessary. Of course, this approach is long and expensive. That is why the modeling and the numerical simulation can play an important role to improve the performance of such devices. One advantage of the numerical approach is that it works with virtual device. We can proceed to "ideal" tests, without taking in account the process constraints. This flexibility is important for the understanding advancements in nanoelectronics and spintronics. A parametric study, which consists of varying one or more characteristics of the device (length, doping profile, applied voltage, injected current...), can allow to understand the mechanisms and even to predict some singular behaviors. The numerical simulations are also useful to determine an adequate interval of values for the different parameters in order to perform the experimental tests in an optimal way. They acts as a complementary tool to the physical experiments.

To reach this goal, mathematical models have been developed. For a given device, the first step is to determine the dominant physical phenomena to be taken into account. It allows to choose an appropriate mathematical model. Up to lengths in order of the micrometer, a classical description of the charged particles, which completely determines trajectories, is acceptable. On the contrary, for characteristic lengths inferior to 100 nanometers, it is much more relevant to use a quantum approach that describes the quantum effects. In reality, things are more complicate and the adequate model is not chosen only in function of the device length. For instance, quantum models generally do not consider collisions between particles. A possibility is to add some corrective quantum terms in the classical models. Another interesting approach is to use a hybrid quantum-classical model. Often the quantum effects take action in localized regions, so that the domain can be decomposed into regions where either a classical or a quantum model is used. These regions are finally coupled using interface conditions. Finally, it is also important to mention that in each of these two wide categories (of classical and quantum models), hierarchies of models with different degrees of accuracy exist. A reasonable balance between physical accuracy and affordable computational costs must be considered.

From a mathematical point of view, problems coming from nanotechnologies and used to describe innovative electronic devices are almost always multiscaled problems. For the different involved phenomena, there are various time and space scales. That is the reason why it is necessary to conceive new models, that take into account in an optimal way the different scales. The multiscaled problems are various. On the one hand, there are problems that contain singularities (shocks, boundary layers...) in a precise place. For these problems, a solution might be to use a small scale description around the singularities and a larger scale one in the rest of the domain. On the other hand, in some problems, the multi-scales coexist in the entire domain. Thus, it is necessary to incorporate the small scale information into the larger scale description.

To summarize, the challenge is to find a model and/or a numerical method that allow at the same time to avoid the use of an ultra refined mesh (resulting in a decreasing of the time and memory costs) and to describe the involved phenomena with a significant accuracy.

Numerous approaches exist for a multiscaled resolution. From a mathematical point of view, we can mention the homogenization techniques (including double scaled homogenization, envelope function decomposition...) that consist of finding a macroscopic equation in which averaged microscopic quantities are inserted, the domain decomposition methods which couple different equations used in different regions through interface conditions (as we already mentioned for the hybrid quantum-classical approach), the asymptotic expansions which perform the limit when a small parameter tends to zero... From a numerical point of view, the possibilities are also multiples. For example, the adaptive mesh methods allow to refine the discretization when and where it is essential, the finite element methods with special basis functions incorporate the multiscaled information inside the choice of the basis functions...

This PhD thesis, as suggested by the title, is devoted to the mathematical modeling and the numerical simulation of innovative electronic devices. It brings into play many of the difficulties and of the remedies mentioned above. On the one hand, we are interested in the derivation of new models (quantum or classical), essentially based on the study of the various scales that appear in the phenomena involved in these nanostructures. On the other hand, we propose some accurate and efficient numerical simulations that should be used in complementarity of the physical experiments. In the long term, this work should be useful to improve the behavior of future electronic devices, and eventually to predict new performant architectures. This PhD thesis is organized as follows. In Chapter 1, the physical background of the present work is briefly presented in order to introduced the main notions used in this thesis. Then, three main parts are distinguished :

- In the first part, we present the derivation and the simulation of an effective mass model, describing the quantum motion of electrons in an ultra-scaled confined nanostructure (Chapters 2 and 3).
- The second part is devoted to non–ballistic transport in ultra–scaled confined nanostructure. First, we analyze a diffusive transport model (Chapter 4) and afterwards, we study a hybrid classical-quantum approach (Chapter 5).
- In the last part, we study a challenging problem in spintronics. We model and simulate the magnetization switching of a ferromagnetic material driven by a spin-current (Chapter 6).

In the rest of this introduction, we detail the content of each chapter. Most of them are written as articles and they can be read independently.

0.4 Content description

Part I and Part II : Modeling and simulation of ultra-scaled confined nanostructures

In the first two parts of this PhD thesis, we are interested in modeling the electron transport in ultra–scaled strongly confined nanostructures (like nanowires [25, 28] and nanotubes [42, 4]). They are becoming promising components in the future nanoelectronics. The extreme miniaturization reached by the electronic devices brings the necessity of using new models to describe the electron transport. To a reduced channel length it corresponds also a strong reduced lateral dimension. When the cross–section diameter is below 3 nm, the strong confinement affects the energy band structure and bulk material properties cannot be used in the simulations. The physical quantities needed for the simulations depend indeed on the device under consideration, for instance they depend on the number of atoms in the cross–section, on the growing orientation of a silicon wire, or on the way the carbon nanotube is rolled-up (see [32], e.g., and references therein). Atomistic *ab-initio* computations give an accurate description of the transport in these innovative devices (see [47], e.g.), but they are computationally too demanding, and cannot be used in a device design framework.

The aim of these two parts is to present new models (in a quantum mechanical framework, as well as in a classical one), that allow for computationally efficient simulations, for describing the transport in ultra–scaled confined devices. In Part *I*, a ballistic transport is considered. The model amounts to a set of one dimensional effective mass Schrödinger equations in the longitudinal direction, one for each energy band, coupled with a 3D Poisson equation for the self–consistent electrostatic potential. In Part *II*, we assume that the evolution of charged particles is mainly driven by collisions with phonons. The transport is described by a single one dimensional drift-diffusion equation, in which we incorporate the averaged quantities obtained in the derivation of the previous quantum effective mass model. The coupling with the 3D Poisson equation is analogous to Part *I*. Finally, in Part *II*, we also study a spatial coupling between the quantum model and the classical one. This hybrid strategy allows to use the quantum model in regions where quantum effects are strong and to couple it to the classical model in the rest of the device domain where collisions play an important role in the transport. Moreover, in order to assess the capability of the models to describe the transport in a strongly confined structure, both in Part *I* and in Part *II*, numerical experiments are performed for a very simplified one wall carbon nanotube. The effort in the modeling and in the numerical implementation (including high-performance computations) allows to obtain computationally efficient simulations.

The core part of these models lies in the derivation of a new effective mass approximation for nanowires/nanotubes. The effective mass approximation allows to replace the motion of an electron in a periodic potential by the motion of a "fictitious" particle in vacuum with a modified mass, called effective mass. It is a well known approximation in solid state physics (see [6, 59], e.g.) and it received recent attention in the mathematical literature. We recall

results for 3D periodic crystals obtained by means of Wigner function techniques [51], two-scale homogenization arguments [2, 1] or envelope function decompositions [7]. We also mention [55], where effective mass results are given for nonlinear Schrödinger equations related to Bose–Einstein condensates on optical lattices, and [27], where the effective mass approximation is performed for a Schrödinger equation singularly perturbed by a confinement potential and a strong magnetic field. This commonly used effective mass approximation is valid under the assumption of infinite periodic structure. For the strongly confined devices considered here, this assumption is not valid anymore in the transversal directions which include only few ions. Thus, our work consists in deriving a new effective mass approximation for such devices.

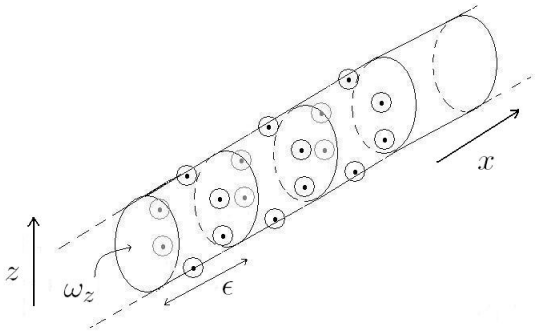

Figure 0.1: Schematic representation of an ultra-scaled confined nanostructure.

The nanostructure (see Fig.0.1) is represented by a three dimensional domain $\Omega = \omega_x \times \omega_z$, where ω_x denotes the one dimensional longitudinal section, and ω_z the two dimensional cross–section. Since the cross–section is composed only of few ions, its diameter is comparable to the typical spacing between lattice sites, that will be denoted by ϵ. The starting point of our work is to consider a Schrödinger equation on an infinite wire ($\omega_x = \mathbb{R}$). The lattice potential generated by the lattice structure fast oscillates at the microscopic scale ϵ, and the homogenization scaling (see Section 2.2) brings into play the variables $(\frac{x}{\epsilon}, \frac{z}{\epsilon})$ in the periodic potential. At the same time, the variable z in the cross–section can be considered as fast variable and it can be consequently rescaled as $z' = \frac{z}{\epsilon}$. Denoting by $\omega_{z'}$ the scaled cross–section, we consider the following scaled Schrödinger equation

$$\begin{aligned} &\imath\partial_t\psi^\epsilon = -\tfrac{1}{2}\partial_{xx}\psi^\epsilon - \tfrac{1}{2\epsilon^2}\Delta_{z'}\psi^\epsilon + \tfrac{1}{\epsilon^2}W_{\mathcal{L}}(\frac{x}{\epsilon}, z')\psi^\epsilon + V(x,z')\psi^\epsilon \quad (x,z') \in \mathbb{R}\times\omega_{z'}, \\ &\psi^\epsilon = 0 \text{ for } z' \in \partial\omega_{z'}. \end{aligned} \tag{0.4.1}$$

This equation describes electrons subject to a lattice potential $W_{\mathcal{L}}$ as well as to a slowly varying potential V. More precisely, in our applications, V will be the self–consistent potential, solution of a Poisson equation in the entire three dimensional structure. This external potential V is acting both on the macroscopic scale x and on the microscopic scale $\frac{z}{\epsilon}$ and it is assumed to be slowly varying in x. The particularity is that the lattice potential $W_{\mathcal{L}}$ can be considered periodic only in the longitudinal direction since the cross-section comprises only few ions.

Due to the dominant terms in (0.4.1), in Part I the asymptotic model will be derived averaging out not only the lattice potential, but also the lateral dimension, in order to incorporate the effects of the microscopic scale into the macroscopic description of the electron motion. In the spirit of homogenization techniques, we define a unit cell $\mathcal{U} = (-1/2, 1/2) \times \omega_{z'}$ associated with our ultra-scaled confined nanostructure. Moreover, this unit cell has the specificity to contain all the atoms of the cross-section. Then, as usual in quantum mechanics, we assign to our structure the following Bloch problem in the unit cell $\mathcal{U}$:

$$\begin{cases} -\frac{1}{2}\Delta_{y,z'}\chi_n + W_{\mathcal{L}}\chi_n = E_n\chi_n. \\ \chi_n(y,z') = 0 \quad \text{on } \partial\omega_{z'}, \quad \chi_n \text{ 1-periodic in } y. \\ \int_{\mathcal{U}} |\chi_n|^2 dy dz' = 1. \end{cases} \tag{0.4.2}$$

We use here the notation y to emphasize that we work in the rescaled transport variable such that the periodicity set is $(-1/2, 1/2)$. The eigenfunctions χ_n are called Bloch functions and the eigenvalues E_n correspond to the energy bands. We point out that the boundary conditions are representative of our confined problem. Indeed, we consider the periodicity only in the transport direction and we choose homogeneous Dirichlet conditions in other directions in order to impose confinement.

As we will detail in Chapter 2, following [7], the asymptotic process, which consists in using an envelope function decomposition to obtain the effective mass approximation, brings into play some relevant averaged quantities, based on the Bloch functions. In particular, a n^{th} band effective mass m_n^* will be given by

$$\frac{1}{m_n^*} = 1 - 2\sum_{n' \neq n} \frac{P_{nn'}P_{n'n}}{E_n - E_{n'}}, \tag{0.4.3}$$

where

$$P_{nn'} = \int_{\mathcal{U}} \partial_x \chi_{n'}(y,z')\chi_n(y,z')\, dy dz' \tag{0.4.4}$$

are the matrix elements of the gradient operator between Bloch functions. Also, an effective potential will be defined by

$$V_{nn}(x) = \int_{\omega_{z'}} V(x,z) g_{nn}(z')\, dz', \tag{0.4.5}$$

with

$$g_{nn}(z') = \int_{-1/2}^{1/2} |\chi_n(y,z')|^2\, dx. \tag{0.4.6}$$

We can say that g_{nn}'s are the quantities that contain information of the strongly confined cross-section. They allow to make the link between the one dimensional transport direction and the three dimensional nanostructure.

The work presented in this PhD thesis, consists on the one hand (in Part I) in performing the asymptotic process in order to present how these effective quantities, which retain the effects

of the crystal structure and of the confinement, are incorporated into the quantum electron transport modeled by a set of Schrödinger equations. On the other hand (in Part II), it consists in studying in which way these effective quantities can be inserted in other commonly used transport models and in particular in a new drift-diffusion equation. A hybrid classical-quantum approach incorporating these effective quantities is also presented. Moreover, in all cases, we are interested in self-consistent computations. It means that the slowly varying potential V is solution of a Poisson equation in the 3D device. The peculiarity comes in the definition of the macroscopic charge density which combines the confinement information of the cross-section with the one dimensional transport density. Generally speaking, it is given by

$$\rho(x,z) = \sum_{n\in\mathbb{N}} N_{1D}^n(x) g_{nn}(z'). \tag{0.4.7}$$

N_{1D}^n is the 1D density carried by the n-th band, given by the transport equations, defined differently according to the models under consideration, as we will describe in the next sections.

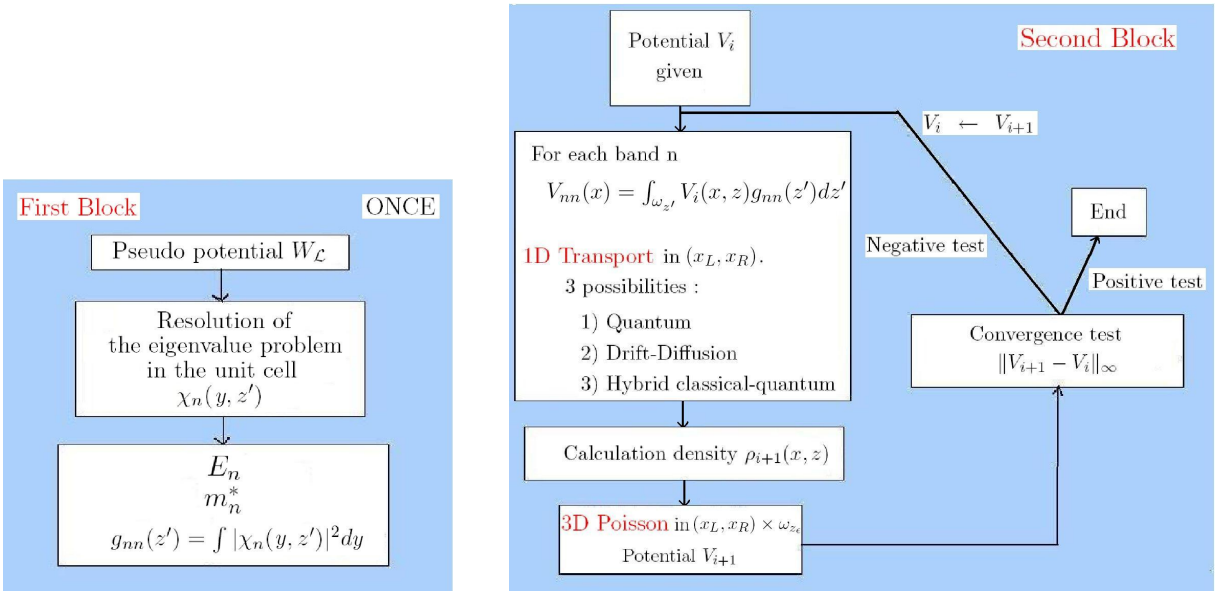

Figure 0.2: General organization of the effective mass models.

The iterative algorithm used in the simulations can be described at once (for the different transport models). It consists of two steps (see the schematic representation Fig.0.2). The first step requires the resolution of the generalized Bloch problem (0.4.2) in the unit cell $\mathcal{U}$, and it provides, for each band n, the energies E_n, the effective mass m_n^* and the functions g_{nn}. This computation is done only once for a given device. Then, the second step is the coupling between the one dimensional transport equations and the three dimensional Poisson equation, incorporating the physical parameters computed in the previous step. The computation of the self-consistent potential and the charge density is made by an iterative method of Gummel type [33, 24]. As we will described in the following, the one dimensional transport equations are given either by a set of effective mass Schrödinger equations (Chapters 2 and 3), or by a single

nanowire drift-diffusion equation (Chapter 4), or by a hybrid coupling of the two previous models made through a spatial decomposition (Chapter 5).

We notice that the derivation of the asymptotic model is done for a nanostructure of infinite longitudinal extension ($\omega_x = \mathbb{R}$). In the numerical parts, we implement this asymptotic model for a bounded domain ($\omega_x = (x_L, x_R)$), assuming that $|\omega_x| >> \epsilon$. This requires to add adequate boundary conditions, as we will explain in Chapter 3. The analysis of the drift-diffusion Poisson system in the Chapter 4 is also done for a bounded domain since we are interested in the existence of solutions in view of numerical simulations.

Chapter II : Derivation of the quantum effective mass model

In this chapter, we study the formal derivation of the quantum effective mass asymptotic model for an ultra-scaled confined nanostructure considered with an infinite extension in the longitudinal direction ($\omega_x = \mathbb{R}$). We remind that due to the strong confinement, the crystal lattice is considered periodic only in the one dimensional transport direction and an atomistic description of the entire cross–section is given. Therefore, the one dimensional device dependent Schrödinger equations (one for each energy band n) are found averaging out not only the lattice potential, but also the lateral dimension. The key tool to find this asymptotic model is the use of an envelope function decomposition. The approach follows the work of [7], where the effective mass approximation in the case of 3D periodic potentials is obtained using, as orthonormal basis for the decomposition, generalized Bloch functions in the form introduced by [40]. This choice has the advantage to completely separate the oscillating part of the wave function and the slowly varying part.

As we have just described, the starting point is the Schrödinger equation (0.4.1). Then, the small scale information, coming from the crystal lattice, is given by the Bloch problem (0.4.2) and it is necessary to incorporate them into the larger scale description. More precisely, we can prove that there exists a unique sequence $\{f_n(x)|n \in \mathbb{N}\}$, such that

$$\psi^\epsilon(x, z') = \sum_{n\in\mathbb{N}} f_n^\epsilon(x)\chi_n(\frac{x}{\epsilon}, z') \ . \tag{0.4.8}$$

The functions f_n are called the envelope functions of ψ^ϵ with respect to the basis $\{\chi_n|n \in \mathbb{N}\}$.

It allows to derive an asymptotic model. Assuming that all the eigenvalues E_n of the problem (0.4.2) are simple (non–degenerate case), we finally obtain that the effective dynamics is given by an infinite set of 1D Schrödinger equations that in the n^{th} band have the form

$$\imath\partial_t h_{em,n}(t, x) = -\frac{1}{2m_n^*}\partial_{xx} h_{em,n}(t, x) + V_{nn}(x)h_{em,n}(t, x). \tag{0.4.9}$$

In the degenerate case, the final set of equations is not decoupled anymore. Indeed, assuming that each eigenvalue E_n of the problem (0.4.2) has multiplicity $\alpha_n \geq 1$ and denoting by $\chi_{n,\alpha}$,

with $1 \leq \alpha \leq \alpha_n$, the α_n eigenvectors associated with E_n, the degenerate effective mass dynamics is described by a set of $\alpha_n \times \alpha_n$ system, where the generic n-α^{th} equation has the form

$$\imath\partial_t h_{em,n,\alpha}(t,x) = -\frac{1}{2m^*_{n,\alpha}}\partial_{xx} h_{em,n,\alpha}(t,x) + \sum_{\alpha'=1}^{\alpha_n} V_{(n,\alpha\ n,\alpha')}(x) h_{em,n,\alpha'}(t,x). \tag{0.4.10}$$

The effective mass $m^*_{n,\alpha}$ is now defined by

$$\frac{1}{m^*_{n,\alpha}} = 1 - 2\sum_{n'\neq n}\sum_{\alpha'=1}^{\alpha_{n'}} \frac{P_{(n,\alpha\ n',\alpha')}P_{(n',\alpha'\ n,\alpha)}}{E_n - E_{n'}}, \tag{0.4.11}$$

and the quantities $P_{(n,\alpha\ n',\alpha')}$ and $V_{(n,\alpha\ n',\alpha')}$ are defined analogously to (0.4.4) and (0.4.5).

In order to obtain these asymptotic results, we first derive the exact dynamics of the envelope functions of the solution of the initial Schrödinger equation (0.4.1). Then, we formally pass to the limit in the term containing the slowly varying potential V and we obtain a $k \cdot p$ model. Using perturbation techniques, we diagonalize the $k \cdot p$ Hamiltonian and we construct an effective mass operator. Finally, the effective mass dynamics (0.4.9) or (0.4.10) is obtained filtering the fast oscillations in time and passing to the limit $\epsilon \to 0$.

We point out that in the non–degenerate case, each envelope function has a fast oscillating scale in time related to the corresponding eigenvalue of the Bloch problem, so that an adiabatic decoupling occurs, as it is common for fast oscillating systems (see [56], e.g.). Thus, an infinite set of decoupled equations is obtained. In the degenerate case, the final system is not decoupled anymore. To each multiple eigenvalue it corresponds a system of coupled Schrödinger equations with dimension equal to the multiplicity of the eigenvalue. The kinetic part of the limiting effective mass Hamiltonian is diagonal and the coupling occurs through the potential.

In fact, we remind that, in the case of nanowire/nanotube, the generalized Bloch waves, that are constructed taking into account the confinement, are "localized" in the transverse direction, so that the Brillouin zone is one dimensional and the associated wave vector k is a scalar. Consequently, the use of the asymptotic expansion for the perturbed eigenvalues is justified not only in the non–degenerate case, but also in the degenerate one (see [38, 52]), and we obtain a diagonal kinetic part in the limiting Hamiltonian (0.4.10).

Finally, in Chapter 2, we discuss the formal limit of the particle density when $\epsilon \to 0$ in view of self–consistent computations. In the non-degenerate case, we obtain that $\int_{\mathbb{R}} |\psi^\epsilon(t,x,z')|^2 dx$ converges formally to the averaged term

$$\int_{\mathbb{R}} \Big(\sum_{n\in\mathbb{N}} |h_{em,n}(t,x)|^2 g_{nn}(z') \Big) dx,$$

where, in the superposition of the densities, the multiplication by g_{nn}'s allows to take into account the effects of the cross-section confinement. In the same way, for the degenerate case, we find that $\int_{\mathbb{R}} |\psi^\epsilon(t,x,z')|^2 dx$ converges formally to the averaged term

$$\int_{\mathbb{R}} \Big(\sum_{n\in\mathbb{N}}\sum_{\alpha=1}^{\alpha_n}\sum_{\alpha'=1}^{\alpha_n} h_{em,n,\alpha}(t,x)\overline{h_{em,n,\alpha'}(t,x)} g_{(n,\alpha\ n,\alpha')}(z') \Big) dx,$$

A coupling among bands corresponding to the same eigenvalue is present. Nevertheless, the coupling disappears if we integrate in the variable z', because of the orthogonality of the $\chi_{n,\alpha}$'s. This definition of the 3D electron density is a peculiarity of the ultra-scaled confined nanostructures.

Chapter III : Numerical simulations for a simplified carbon nanotube

In this chapter, we present numerical simulations of the asymptotic model derived in the previous chapter. The simulations aim at testing the capability of the model to describe the electron transport in an ultra-scaled confined structure and they will be carried out in a very simplified case. It is a one–wall carbon nanotube with a cross-section made of 12 atoms disposed on a squared frame, surrounded by one atom layer of dielectric acting like an insulator (see Fig.0.3). The transport problem is solved for a gate-all-around FET (Field Effect Transistor) with channel length equal to 10 nm doped with a donor concentration equal to $N_D^- = 10^{21}$ m^{-3}, with Source and Drain regions 10 nm long, largely doped ($N_D^+ = 10^{26}$ m^{-3}). For carbon, the lattice spacing ϵ is equal to 3.57 Å. Therefore, the wire cross-section edge (equal to $6\epsilon \approx 2nm$) is tiny compared to the longitudinal length equals to 30 nm. Concerning the lattice potential $W_{\mathcal{L}}$, we choose a pseudo-potential used by [60] for ab-initio atomistic-based electronic density calculations for carbon nanotubes.

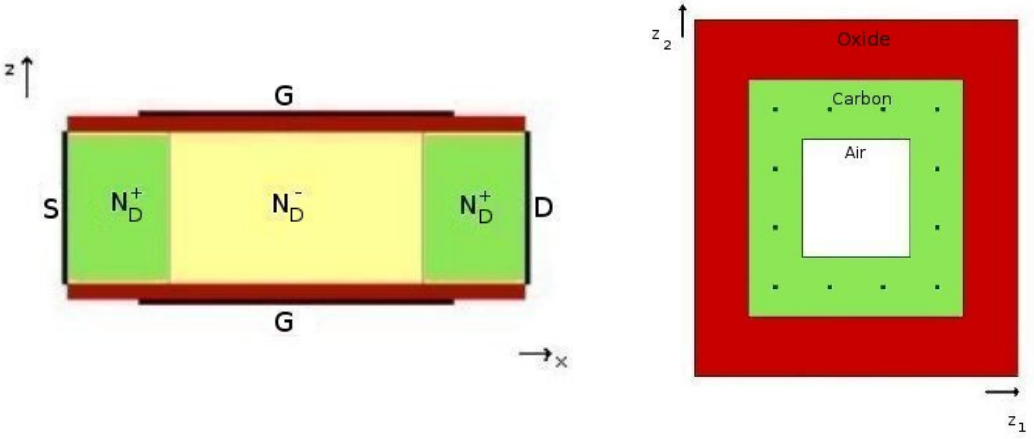

Figure 0.3: Longitudinal section (left) and transversal cross-section (right) of the simplified carbon nanotube with a squared transversal cross-section containing 12 atoms.

We consider here the non-degenerate case. The electron transport in the longitudinal direction is described by a sequence of 1D stationary Schrödinger equations of the form (0.4.9) on a bounded domain ($\omega_x = (x_L, x_R)$). The system is considered as an open quantum system : electrons are injected from the leads considered as reservoirs, they travel through the channel (active region) and they leave the device through another reservoir. So, for each n^{th} band and for each wave vector k, we consider the stationary Schrödinger equation

$$-\frac{1}{2m_n^*}\partial_{xx}\psi_n^k(x) + V_{nn}(x)\psi_n^k(x) = \mathcal{E}_n^k\psi_n^k(x), \qquad x \in \omega_x, \tag{0.4.12}$$

with $\mathcal{E}_n^k = \frac{k^2}{2m_n^*} + V_{nn}(x_L)$ if $k > 0$ and with $\mathcal{E}_n^k = \frac{k^2}{2m_n^*} + V_{nn}(x_R)$ if $k < 0$. Transparent Boundary Conditions (TBCs) [31, 39, 13, 3, 5, 29] are used to complete the system.

Then, we remind that the electrostatic behavior of the device is described by the self-consistent electrostatic potential solution of a Poisson equation in the 3D device :

$$-\Delta V_P(x,z) = N_D(x,z) - \rho(x,z), \qquad (x,z) \in \omega_x \times \omega_z. \tag{0.4.13}$$

N_D is the prescribed doping density. Boundary conditions are chosen in order to model the applied Drain-Source voltage V_{DS} at ohmic contacts and the gate voltage V_G that modulate the number of free electrons. When V_{DS} is null, we say that the system is at thermal equilibrium. The macroscopic charge density ρ is given by (0.4.7) and in an open system, electrons are considered in mixed states such that the 1D density carried by the n^{th} band is given by superimposing the densities of states injected from the reservoirs, that is

$$N_Q^n(x) = \int_{\mathbb{R}} \phi_n(k) |\psi_n^k(x)|^2 dk, \tag{0.4.14}$$

where $\phi_n(k)$ characterizes the electron injection from the reservoirs. In the subsequent simulation, the Boltzmann statistics is used. Finally, the current density is given by

$$J(x) = \sum_{n\in\mathbb{N}} \frac{1}{m_n^*} \int_{\mathbb{R}} \phi_n(k) \Im\Big(\overline{\psi_n^k(x)} \partial_x \psi_n^k(x)\Big) dk, \qquad x \in \omega_x. \tag{0.4.15}$$

We refer to [13, 11, 45, 46] for analytical results on the Schrödinger-Poisson system and to [16, 49] for numerical schemes in a subband decomposition framework.

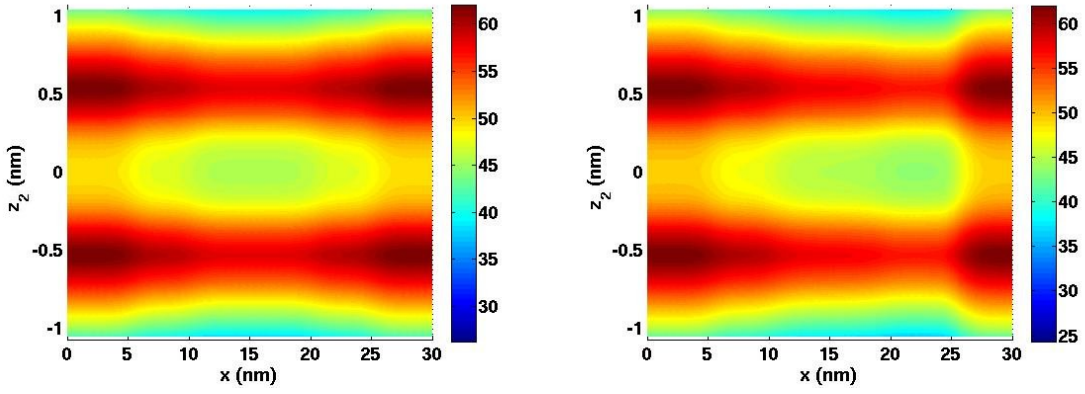

Figure 0.4: 2D slice (crossing 2 nuclei) of density in logarithmic scale at equilibrium (left) and for $V_{DS} = 0.2$ V (right), with $V_G = -0.1$ V. x-axis is the transport direction.

After a precise description of the algorithm (implemented to resolve the 1D Scrödinger - 3D Poisson system with a Gummel iterative method) and of the tricky numerical points (Fermi level determination, boundary conditions...), we present in Chapter 3 the obtained numerical results. In particular, the transport from Source to Drain is illustrated by Fig.0.4, that represents the

density, in logarithmic scale, in a 2D slice (crossing two ions) along the transport direction (x-axis in the picture) for a fixed gate voltage. Comparing the thermal equilibrium picture (left) with the one for $V_{DS} = 0.2$ V (right), we clearly observe the electron motion from the left to the right.

Also, in Fig.0.5, the output characteristics of our simplified device (again for a fixed gate voltage) are presented taking in account three bands. These curves are qualitatively in accordance with physical results. In particular, we observe a current saturation. So, we can say that, even in this over simplified problem, the model is able to capture the behavior of the current and thus to describe the electron transport in a strongly confined structure.

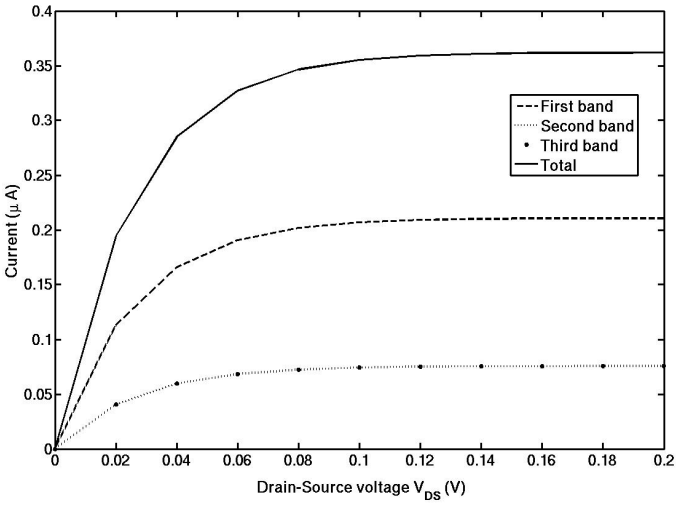

Figure 0.5: Current-voltage characteristics for $V_G = -0.1$ V.

Chapter IV : Analysis of a diffusive effective mass model for nanowires

In this chapter, we consider a non-ballistic transport where the evolution of charged particles is mainly driven by collisions with phonons. Indeed, as we have seen in the description of the previous chapter, we have in mind to study the transport for a FET. It contains an active zone between two largely doped regions, the Source and the Drain. In these doped regions, collisions play an important role and they are not included in our previous quantum model. A widely used model to describe such kind of transport is the drift-diffusion equation (see [37, 41, 43] e.g.). We also refer e.g. to [12] (and to the bibliography in [37]) for hierarchies of diffusive models for electron transport in semiconductors.

Consequently, we propose in this chapter to derive and analyze a self-consistent model describing the diffusive transport in an ultra-scaled confined structure, taking into account the interactions of charged particles with phonons. As previously, the longitudinal direction is assumed to be large compared to the wire section but the transport is now described by a drift-

diffusion equation. As before, the electrostatic potential solves a Poisson equation where the macroscopic charge density has the form (0.4.7). On the one hand, we study the derivation of this Nanowire Drift-Diffusion Poisson model by performing a diffusive limit from a sequence of Boltzmann equations, one for each band. It allows to see how the effective quantities computed from the Bloch problem (0.4.2) are incorporated in the classical transport equation. We assume here that the eigenvalues E_n of (0.4.2) are all simple. On the other hand, we present an existence result for this model in a bounded domain.

Let us start by introducing the Boltzmann equation in the diffusive scaling used to for ultra-scaled confined nanostructures. It governs the evolution of the distribution function $f_n(t,x,p)$ on the n^{th} band. The time variable t is nonnegative, the position variable is denoted by x and the momentum variable by p. The equation writes [50, 58]

$$\partial_t f_n^\eta + \frac{1}{\eta}\Big(v_n \partial_x f_n^\eta - \partial_x V_{nn} \partial_p f_n^\eta\Big) = \frac{1}{\eta^2}\mathcal{Q}_B(f^\eta)_n, \tag{0.4.16}$$

where η is the scaled mean free path, assumed to be small. In this equation, v_n is the velocity given by $v_n(p) = \frac{p}{m_n^*}$, m_n^* the n^{th} band effective mass (0.4.3) and $V_{nn}(t,x)$ the effective potential energy associated with the n^{th} band (0.4.5). The collision operator $\mathcal{Q}_B$, describing the scattering between electrons and phonons, is assumed in the linear BGK approximation for Boltzmann statistics. It reads

$$\mathcal{Q}_B(f)_n = \sum_{n'=1}^{+\infty} \int_{\mathbb{R}} \alpha_{n,n'}(p,p')\Big(\mathcal{M}_n(p) f_{n'}(p') - \mathcal{M}_{n'}(p') f_n(p)\Big) dp' \tag{0.4.17}$$

where the function $\mathcal{M}_n$ is the Maxwellian

$$\mathcal{M}_n(t,x,p) = \frac{1}{\sqrt{2\pi m_n^* \mathcal{Z}(t,x)}} e^{-\left(\frac{p^2}{2m_n^*} + E_n + V_{nn}(t,x)\right)} \tag{0.4.18}$$

normalized such that

$$\sum_{n=1}^{+\infty} \int_{\mathbb{R}} \mathcal{M}_n dp = 1. \tag{0.4.19}$$

The repartition function $\mathcal{Z}$ is thus given by

$$\mathcal{Z}(t,x) = \sum_{n=1}^{+\infty} e^{-\left(E_n + V_{nn}(t,x)\right)}. \tag{0.4.20}$$

The formal diffusive limit of the Boltzmann equation (0.4.16) as $\eta \to 0$ is obtained using a Hilbert expansion. We assume that f_n^η can be decomposed as

$$f_n^\eta = f_{0,n} + \eta f_{1,n} + \eta^2 f_{2,n} + ... \tag{0.4.21}$$

Inserting this decomposition in (0.4.16) and identifying terms with respect to powers of η, we obtain

$$\mathcal{Q}_B(f_0)_n = 0 \quad \Rightarrow \quad f_{0,n} = N_s(t,x)\mathcal{M}_n,$$

$$\mathcal{Q}_B(f_1)_n = v_n\partial_x f_{0,n} - \partial_x V_{nn}\partial_p f_{0,n} = v_n\mathcal{M}_n\Big(\partial_x N_s + N_s\partial_x V_s\Big) \quad \text{taking} \quad V_s(t,x) = -\ln \mathcal{Z}(t,x),$$
$$\mathcal{Q}_B(f_2)_n = \partial_t f_{0,n} + v_n\partial_x f_{1,n} - \partial_x V_{nn}\partial_p f_{1,n}.$$

Using the properties of the collision operator, we obtain, after some calculations, the following single drift-diffusion equation

$$\partial_t N_s - \partial_x\Big(D\big(\partial_x N_s + N_s\partial_x V_s\big)\Big) = 0, \tag{0.4.22}$$

where D is a diffusion coefficient. This drift-diffusion equation consists of a conservation equation in the transport direction of the particle density $N_s(t,x)$. We still have a coupling with a 3D Poisson equation since $V_s(t,x)$ is an effective potential depending on the slowly varying potential $V(t,x,z)$. The macroscopic charge density, entering in the second member of the Poisson equation, is given by (0.4.7) where the 1D density carried by the n-th band is now defined by

$$N_C^n(t,x) = \int_{\mathbb{R}} N_s(t,x)\mathcal{M}_n(p)dp = N_s(t,x)\frac{e^{-\left(E_n+V_{nn}(t,x)\right)}}{\mathcal{Z}(t,x)}. \tag{0.4.23}$$

This overall system, that we named Nanowire Drift-Diffusion Poisson (NDDP) problem, has a structure somehow similar to a system studied in [15, 57, 58, 48, 36], which was a diffusive model based on the subband decomposition method.

In Chapter 4, after describing this diffusive limit, we analyze the overall system for a bounded domain. The existence of the NDDP problem is proven by a convex minimization technique. The drift-diffusion equation determines the value of the surface density N_s in terms of the electrostatic potential V, while the Poisson equation allows to compute the potential V as a function of the surface density N_s. The overall problem (taking some boundary conditions such that we can use the elliptic regularity of the Poisson equation) is then solved by a fixed-point procedure for the unknown N_s.

An important quantity for this kind of system is the relative entropy W, here defined by

$$W = \sum_{n=1}^{+\infty}\int_{\omega_x}\Big(N_C^n\ln\Big(\frac{N_C^n}{\underline{N_C^n}}\Big) - N_C^n + \underline{N_C^n}\Big)dx + \frac{1}{2}\int_\Omega |\nabla(V-\underline{V})|^2 dxdz, \tag{0.4.24}$$

where $\underline{N_C^n}$ and $\underline{V}$ are two extensions of the boundary data, respectively on ω_x and on Ω. Therefore, the $L\log L$ bound on the density and the H^1 bound on the potential are the natural estimates for this model.

We notice that we cannot obtain for this model an a-priori L^2 estimate on the surface density N_s and we have to work in the natural framework $L\log L$ given by the entropy (see [57] e.g.). For this framework, usual techniques consist of regularizing the overall problem NDDP defining a linear operator $\mathcal{R}^\delta$ for a small parameter $\delta \in (0,1)$ such that $\mathcal{R}^\delta \to Id$ as $\delta \to 0$. We obtain a-priori estimates (mass, relative entropy, dissipation) and prove the existence of solutions for the regularized system with a fixed point argument. And finally, we use the uniform estimates to pass to the limit $\delta \to 0$ in the solution of the regularized system to obtain solutions of the unregularized system. We point out that these techniques do not give uniqueness of the solution.

To finish, in the case of thermodynamic equilibrium boundary data, we can prove the existence of a unique stationary solution. Moreover, the relative entropy allows to prove the convergence of a transient solution towards this stationary solution when the time grows to infinity.

Chapter V : Hybrid classical-quantum approach : modeling and simulations

In many semiconductor devices, quantum effects take place in a localized region whereas in the rest of the device domain transport can be considered as classical. Thus, it can be interesting to follow a spatial hybrid strategy [10, 26, 9] which consists of using a quantum model in regions where quantum effects are strong and to couple it with a classical model in the rest of the device domain. With respect to the pure quantum model of Chapter 2, this strategy results in an improvement of the model (allowing to take into account particle collisions in the highly doped regions) and in a decreasing of the computational cost (thanks to the reduction of the region where the complex and computationally demanding quantum model is used).

In this chapter, the drift-diffusion model, detailled in Chapter 4, is coupled with the quantum effective mass model developed in Chapters 2 and 3. We assume that the device domain in the transport direction x is divided into a quantum zone $\omega_Q = (x_1, x_2)$, with $x_L < x_1 < x_2 < x_R$ and a classical zone $\omega_C = (x_L, x_R) \backslash \omega_Q$ (see Fig.0.6).

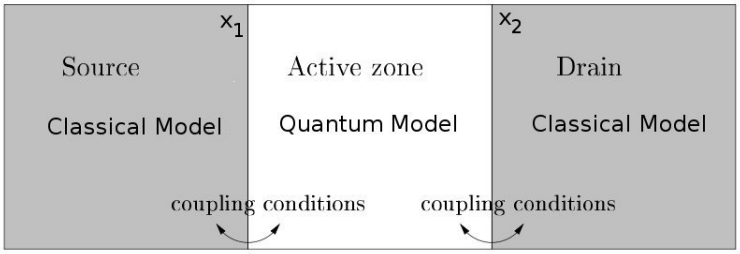

Figure 0.6: Schematic representation of hybrid model regions.

The main difficulty is given by the derivation of the interface conditions between these two models. Here, we follow the method described in [9]. The authors get an analytic expression for the connection conditions by writing the continuity of the current at interfaces. Without entering in details in this introduction (details based on the expression of the current in the quantum part), the two open sets (x_L, x_1) and (x_2, x_R) are connected through the conditions :

$$J(x_1) = J(x_2) =: J, \tag{0.4.25}$$

$$e^{\varphi(x_1)} - e^{\varphi(x_2)} = \Theta_{\mathcal{Q}} J. \tag{0.4.26}$$

J is the current, φ is the unknown quasi-fermi energy and $\Theta_{\mathcal{Q}}$ is a positive coefficient depending on the reflection-transmission coefficients (quantum part). In the special case where we use the Boltzmann statistics, $\Theta_{\mathcal{Q}}$ can be computed explicitly.

So, the algorithm for the hybrid approach is the following. At each Gummel iteration, for a given potential V, we solve the effective mass Schrödinger equations (0.4.12) for each band n and each wave vector k on ω_Q. We obtain the wave functions ψ_n^k and the transmission coefficients and we use them to compute the coefficient Θ_Q. Then, we solve the drift-diffusion equation (0.4.22) on ω_C with the interface conditions and we obtain the quasi-fermi energy φ. It allows to determine both the classical density N_C^n and the quantum density N_Q^n on each band n. The hybrid one dimensional density is then defined by

$$N_{1D}^n(x) = \begin{cases} N_Q^n(x) & \text{for } x \in \omega_Q, \\ N_C^n(x) & \text{for } x \in \omega_C. \end{cases}$$

Finally, as usual, the macroscopic three dimensional charge density is computed by (0.4.7) and we solve the 3D Poisson equation to obtain the new value of the potential V.

In order to guarantee conservation properties for the current, we use a mixed finite element scheme to solve the drift-diffusion equation. We refer to [19] and references therein, for a general presentation on mixed finite elements, to [21, 22, 23, 20], for mixed finite elements for the drift–diffusion equation in density formulation, and to [34, 35], for the quasi-fermi level formulation.

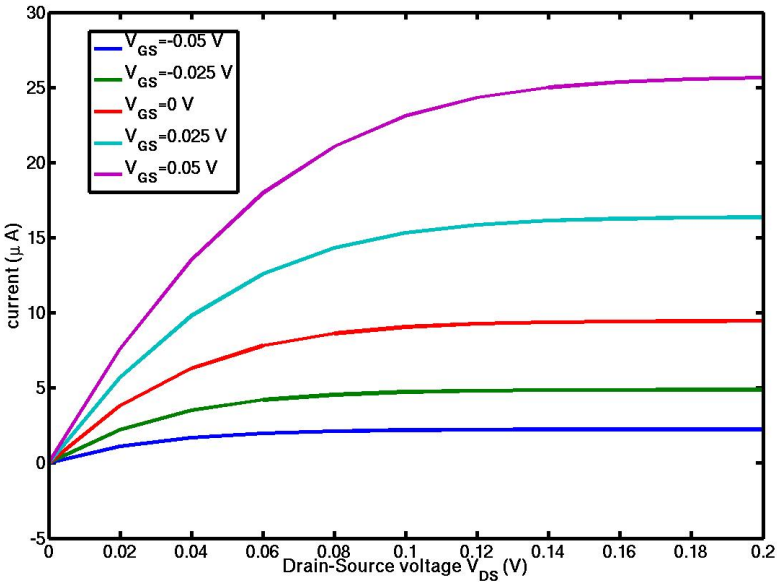

Figure 0.7: Current-Voltage characteristics for five gate voltages V_G.

After a precise description of this hybrid approach, we continue Chapter 5 by a presentation of the numerical results obtained for our ultra simplified carbon nanotube. For example, we present in Fig.0.7, the output characteristics for different gate voltages. As expected, we notice that the current in the transistor increases with the gate potential and that the saturation regime occurs for larger Drain-Source voltages. In this chapter, we also present different simulations

that allow us to discuss the advantages of our different models : fully quantum approach, drift-diffusion system and hybrid method.

Finally, the last part of Chapter 5 is dedicated to high-performance computations. In particular, we took an interest in parallelization, in order to decrease the overall computational cost. For example, the resolution of the linear system associated with the 3D Poisson equation represents an expensive part of the code and can be scalable. The performance is determined by analyzing speed-up curves which display the execution time in function of the number of processors used in the cluster.

Part III : On a model of magnetization switching driven by a spin-current

Chapter VI : Modeling and numerical simulations

In the last part of this PhD thesis, we are interested in a different innovative nanostructure : a ferromagnetic multilayer material. It is a spintronic device in the sense that it exploits the spin of electrons. The spin of electrons represents a two-state quantum system. It means that for a chosen direction of measurement, the spin can be determined to be parallel "spin-up" or antiparallel "spin-down" (see [62] for a review on spintronics and its applications). Recent mathematical works propose matrix transport models for spin systems. We mention for example [14, 30] where a hierarchy of diffusion models for spin transport is derived by applying a diffusion asymptotics to the Boltzmann equation, or [8] where a quantum drift-diffusion model is discussed for a spin-polarized bidimensional electron gas. More recently, in [44], a spin-coherent drift-diffusion model is derived and numerical tests are proposed for one-dimensional multilayer structures. Our work is slightly related to [44] in the sense that we consider the same kind of multilayer structures with "spin injection". Nevertheless, our main interest is to study the behavior of the magnetization, coupling the spin density with the local magnetization, rather than deriving the spin-polarized transport equation.

The idea of this chapter is to model and to simulate the magnetization switching induced by a spin polarized current (without applying any external magnetic field). The magnetization is reversed by an additional spin transfer torque. This concept was discovered by Slonczewski [54] and Berger [17] in 1996 and it is of great interest to construct magnetic memories.

The physical device proposed by [54, 17] is a magnetic multilayer mainly composed of two ferromagnetic layers (a thick ferromagnet F^- and a thin one F^+) separated by a nonmagnetic spacer layer (see Figure 0.8). Initially, the two magnetizations $\vec{M}^-(t=0)$ and $\vec{M}^+(t=0)$ respectively in F^- and F^+ are polarized in a different direction (θ is the angle between $\vec{M}^-(t=0)$ and $\vec{M}^+(t=0)$). In order to induce the switching of the magnetization in the thin layer, an electric current is injected in the device at the left end of the thick layer F^-, perpendicularly to the layers (along the x axis). The thick ferromagnetic layer F^- (around 100 nm) acts as a polarizer. Its magnetization does not move under the spin current influence, whereas the spin density is polarized in the direction of the magnetization when passing through the F^-

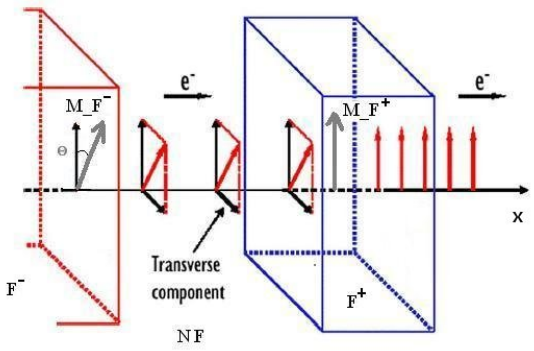

Figure 0.8: A multilayered ferromagnetic device proposed by Slonczewski.

layer. On the contrary, the second ferromagnetic layer F^+ is thin (around 1-5 nm) such that its magnetization can move driven by the spin current. The spin density, which is polarized along $\vec{M}^-$ crossing F^-, reaches F^+ with a transverse component with respect to $\vec{M}^+$. Then, a torque is established between this transverse component and the magnetization $\vec{M}^+$. When the spin transfer is enough intense (that is to say when the injected current is enough important), $\vec{M}^+$ can be completely switched.

The mathematical model we study here is a simplified version of that introduced by Zhang, Levy and Fert [61] (see also [53] for details). This model couples equations on the spin density and the local magnetization. The local magnetization satisfies a Landau-Lifshitz equation with an additional term in the effective field. The equation satisfied by the spin density is a diffusion equation with an additional torque term where the magnetization appears.

As noticed in [61, 53], there are various scales for the different phenomena involved in the magnetization reversal process. In order to study these multi-scales, we first write our one dimensional model in an adimensionalized form, using a small parameter ε which physically corresponds to the ratio between the thicknesses of the ferromagnetic layers (the thin one over the thick one). In the scaled form, we denote $\vec{m}^- : \mathbb{R}^+ \times (-1,0) \to \mathbb{R}^3$ and $\vec{M}^- : \mathbb{R}^+ \times (-1,0) \to \mathbb{R}^3$ respectively the spin density vector and the local magnetization in the thick ferromagnetic material F^-, and $\vec{m}^+ : \mathbb{R}^+ \times (0,1) \to \mathbb{R}^3$ and $\vec{M}^+ : \mathbb{R}^+ \times (0,1) \to \mathbb{R}^3$ respectively the spin density vector and the local magnetization in the thin ferromagnetic material F^+. Writing all the constants in terms of ε, we obtain the following dimensionless equations, written for $t \geq 0$,

$$\begin{cases} \varepsilon^2 \partial_t \vec{m}^- - \partial_x^2 \vec{m}^- + \dfrac{\vec{m}^- \times \vec{M}^-}{\varepsilon^2} + \vec{m}^- = 0, \quad x \in (-1,0), \\ \partial_t \vec{M}^- = -\vec{M}^- \times \left(c(\vec{M}^- \cdot \vec{u}^-)\vec{u}^- + \dfrac{\vec{m}^-}{\varepsilon} + \nu \partial_x^2 \vec{M}^- \right) + \alpha \vec{M}^- \times \partial_t \vec{M}^-. \end{cases} \tag{0.4.27}$$

$$\begin{cases} \varepsilon^2 \partial_t \vec{m}^+ - \dfrac{1}{\varepsilon^2} \partial_x^2 \vec{m}^+ + \dfrac{\vec{m}^+ \times \vec{M}^+}{\varepsilon^2} + \vec{m}^+ = 0, \quad x \in (0,1), \\ \partial_t \vec{M}^+ = -\vec{M}^+ \times \left(c(\vec{M}^+ \cdot \vec{u}^+)\vec{u}^+ + \dfrac{\vec{m}^+}{\varepsilon} + \dfrac{\nu}{\varepsilon^2} \partial_x^2 \vec{M}^+ \right) + \alpha \vec{M}^+ \times \partial_t \vec{M}^+. \end{cases} \tag{0.4.28}$$

These equations are completed with boundary and interface conditions (at $x = -1$, $x = 0$ and $x = 1$). We notice immediately that ε orders are different in the two ferromagnetic materials. We can guess for example that, in the thick ferromagnetic material F^-, $\vec{m}^- \times \vec{M}^- = 0$ when $\varepsilon \to 0$. So, the spin density is polarized in the direction of the magnetization. In Chapter 6, we study more precisely the different time and space scales that appear in the model. The first important point is the existence of a boundary layer of thickness ε at the right end of the thick layer. The second point is the existence of very fast temporal oscillations at scale t/ε^4 for the spin density. More precisely, there is a transverse component of the spin density in the thick layer that is purely oscillating, whereas the thick layer should act as a polarizer.

In order to construct an appropriate numerical scheme, also valid for small values of ε, it is important to take into account these various scales. The two main ideas that we develop in Chapter 6 are the following. First, for the space discretization, due to this boundary layer, it is preferable to use a non-uniform mesh, refined near the interface in the thick material. Then, since the behavior of the spin density is quite different in the directions parallel or transverse to the magnetization, we use a finite element method for the equation on $\vec{m}$, using special basis functions adapted to this phenomenon. These basis functions are exponential functions that decrease with a different order in the directions parallel and transverse to the magnetization. Second, it is important to treat the very fast time oscillations at scale t/ε^4. In the phenomenon we are interested (the magnetization reversal), they are not relevant and we avoid them. To that purpose, we "filter" these oscillations by using an implicit scheme for the time discretization of the equation on the spin density, using a time step much bigger than ε^4. Moreover, we use an averaged spin density (with respect to the fast time variable) to compute the magnetization.

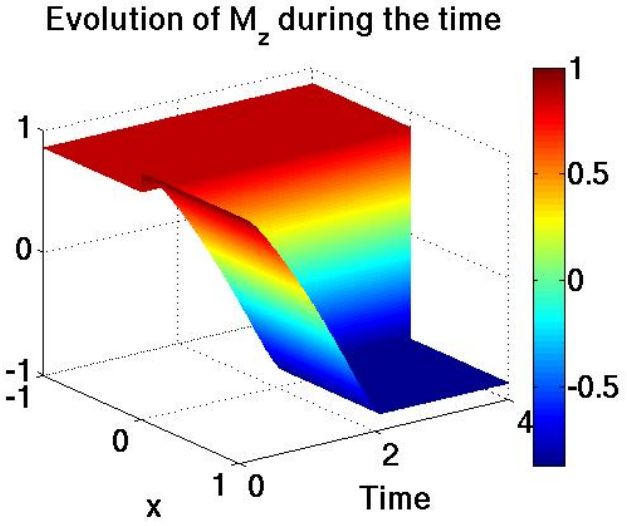

Figure 0.9: Evolution of the M_z component during the time.

This appropriate numerical scheme allows us to recover numerically various results of physical experiments. In particular, in Fig.0.9, we observe that the magnetization in the thick ferromagnet

F^- remains at equilibrium whereas it moves in F^+ under the spin current influence. After $t = 2$, the magnetization is completely switched. The different results presented in Chapter 6 (and in particular the impact of the injected current intensity on this switching phenomenon) allow us to conclude that our numerical simulations are in accordance with physical experiments.

Finally, in Chapter 6, we perform a formal asymptotic study of (0.4.27)–(0.4.28) as ε tends to 0 in order to recover a simplified asymptotic model (that will be much easier to handle numerically). To find such a model, we introduce the various scales appearing previously : the two time scales t and t/ε^4 and the two space scales x and x/ε. Again, we do not want to compute the oscillating part, so we omit this time scale. The first idea is then to use a basic WKB ansatz. We develop each quantity as a sum of powers of ε and we compute the first profiles. The obtained limit model shows the "right" properties with respect to physical experiments, up to convergence. In fact, a main restriction is that the derivation is based on an assumption which is not satisfied anymore when the magnetization is completely switched. In order to obtain a limit model with a bigger domain of validity, we look for a second model, using a "Chapman-Enskog" approach. Roughly, the idea is to keep a dependence on the parameter ε in the first profiles in order to track in a better way the change of behavior. After presenting formally these two limit models, we discuss in Chapter 6 their validity with simulations by making numerical comparisons with the full system.

Bibliography

[1] G. Allaire, A. Arnold, P. Degond, and T. Y. Hou. *Quantum transport.* Lecture Notes in Mathematics. Springer-Verlag, Berlin, 2008. Modelling, analysis and asymptotics, Lectures from the C.I.M.E. Summer School, held in Cetraro, 2006.

[2] G. Allaire and A. Piatnitski. Homogenization of the Schrödinger equation and effective mass theorems. *Comm. Math. Phys.*, 258(1):1–22, 2005.

[3] X. Antoine, A. Arnold, C. Besse, M. Ehrhardt, and A. Schädle. A review of transparent and artificial boundary conditions techniques for linear and nonlinear Schrödinger equations. *Commun. Comput. Phys.*, 4(4):729–796, 2008.

[4] J. Appenzeller, J. Knoch, R. Martel, V. Derycke, S.J. Wind, and P. Avouris. Carbon nanotube electronics. *IEEE Trans. Nanotechnol.*, 1(4):184 – 189, 2002.

[5] A. Arnold. Mathematical concepts of open quantum boundary conditions. *Trans. Theory Stat. Phys.*, 30(4-6):561–584, 2001.

[6] N.W. Ashcroft and N.D. Mermin. *Solid State Physics.* Saunders College Publishing, 1976.

[7] L. Barletti and N. Ben Abdallah. Quantum Transport in Crystals: Effective Mass Theorem and K·P Hamiltonians. *Comm. Math. Phys.*, 307:567–607, 2011.

[8] L. Barletti and F. Méhats. Quantum drift-diffusion modeling of spin transport in nanostructures. *J. Math. Phys.*, 51(5):053304, 20, 2010.

[9] M. Baro, N. Ben Abdallah, P. Degond, and A. El Ayyadi. A 1d coupled Schrödinger drift-diffusion model including collisions. *J. Comput. Phys.*, 203(1):129 – 153, 2005.

[10] N. Ben Abdallah. A hybrid kinetic-quantum model for stationary electron transport. *J. Statist. Phys.*, 90(3-4):627–662, 1998.

[11] N. Ben Abdallah. On a multidimensional Schrödinger-Poisson scattering model for semiconductors. *J. Math. Phys.*, 41(7):4241–4261, 2000.

[12] N. Ben Abdallah and P. Degond. On a hierarchy of macroscopic models for semiconductors. *J. Math. Phys.*, 37(7):3306–3333, 1996.

[13] N. Ben Abdallah, P. Degond, and P. A. Markowich. On a one-dimensional Schrödinger-Poisson scattering model. *Z. Angew. Math. Phys.*, 48(1):135–155, 1997.

[14] N. Ben Abdallah and R. El Hajj. On hierarchy of macroscopic models for semiconductor spintronics. Preprint, University of Toulouse 3.

[15] N. Ben Abdallah, F. Méhats, and N. Vauchelet. Diffusive transport of partially quantized particles: existence, uniqueness and long-time behaviour. *Proc. Edinb. Math. Soc. (2)*, 49(3):513–549, 2006.

[16] N. Ben Abdallah, M. Mouis, and C. Negulescu. An accelerated algorithm for 2D simulations of the quantum ballistic transport in nanoscale MOSFETs. *J. Comput. Phys.*, 225(1):74–99, 2007.

[17] L. Berger. Emission of spin waves by a magnetic multilayer traversed by a current. *Phys. Rev. B*, 54(13):9353–9358, 1996.

[18] H. Brezis. *Analyse fonctionnelle*. Collection Mathématiques Appliquées pour la Maîtrise. [Collection of Applied Mathematics for the Master's Degree]. Masson, Paris, 1983.

[19] F. Brezzi and M. Fortin. *Mixed and hybrid finite element methods*, volume 15 of *Springer Series in Computational Mathematics*. Springer-Verlag, New York, 1991.

[20] F. Brezzi, L. D. Marini, S. Micheletti, P. Pietra, R. Sacco, and S. Wang. Discretization of semiconductor device problems. I. In *Handbook of numerical analysis. Vol. XIII*, Handb. Numer. Anal., XIII, pages 317–441. North-Holland, Amsterdam, 2005.

[21] F. Brezzi, L. D. Marini, and P. Pietra. Méthodes d'éléments finis mixtes et schéma de Scharfetter-Gummel. *C. R. Acad. Sci. Paris Sér. I Math.*, 305(13):599–604, 1987.

[22] F. Brezzi, L. D. Marini, and P. Pietra. Numerical simulation of semiconductor devices. In *Proceedings of the Eighth International Conference on Computing Methods in Applied Sciences and Engineering (Versailles, 1987)*, volume 75, pages 493–514, 1989.

[23] F. Brezzi, L. D. Marini, and P. Pietra. Two-dimensional exponential fitting and applications to drift-diffusion models. *SIAM J. Numer. Anal.*, 26(6):1342–1355, 1989.

[24] Ph. Caussignac, B. Zimmermann, and R. Ferro. Finite element approximation of electrostatic potential in one-dimensional multilayer structures with quantized electronic charge. *Computing*, 45(3):251–264, 1990.

[25] Y. Cui, Z. Zhong, D. Wang, W. U. Wang, and C. M. Lieber. High performance silicon nanowire field effect transistors. *Nano Letters*, 3(2):149–152, 2003.

[26] P. Degond and A. El Ayyadi. A coupled Schrödinger drift-diffusion model for quantum semiconductor device simulations. *J. Comput. Phys.*, 181(1):222–259, 2002.

[27] F. Delebecque-Fendt and F. Méhats. An effective mass theorem for the bidimensional electron gas in a strong magnetic field. *Comm. Math. Phys.*, 292(3):829–870, 2009.

[28] X. Duan, C. Niu, V. Sahi, J. Chen, J. W. Parce, S. Empedocles, and J. L. Goldman. High-performance thin-film transistors using semiconductor nanowires and nanoribbons. *Nature*, 425:274–278, 2003.

[29] M. Ehrhardt and A. Arnold. Discrete transparent boundary conditions for the Schrödinger equation. *Riv. Mat. Univ. Parma (6)*, 4:57–108, 2001.

[30] R. El Hajj. Diffusion models for spin transport derived from the spinor boltzmann equation. *Comm. Math. Sci.* (to appear).

[31] W. R. Frensley. Boundary conditions for open quantum systems driven far from equilibrium. *Rev. Mod. Phys.*, 62(3):745–791, 1990.

[32] E. Gnani, A. Gnudi, S. Reggiani, M. Luisier, and G. Baccarani. Band effects on the transport characteristics of ultrascaled snw-fets. *IEEE Trans. Nanotechnol.*, 7(6):700 –709, 2008.

[33] H.K. Gummel. A self-consistent iterative scheme for one-dimensional steady state transistor calculations. *IEEE Trans. Electron Devices*, 11(10):455 – 465, 1964.

[34] F. Hecht and A. Marrocco. Mixed finite element simulation of heterojunction structures including a boundary layer model for the quasi-fermi levels. *COMPEL*, 13(4):757–770, 1994.

[35] F. Hecht, A. Marrocco, E. Caquot, and M. Filoche. Semiconductor device modelling for heterojunctions structures with mixed finite elements. *COMPEL*, 10(4):425–438, 1991.

[36] C. Heitzinger and Ringhofer C. A transport equation for confined structures derived from the Boltzmann equation. *Comm. Math. Sci.*, 9(3):829–857, 2011.

[37] A. Jüngel. *Transport equations for semiconductorsSemiconductor equations.* Lecture Notes in Physics No. 773. Springer, Berlin, 2009.

[38] T. Kato. *Perturbation theory for linear operators.* Springer-Verlag, Berlin, second edition, 1976.

[39] C. S. Lent and D. J. Kirkner. The quantum transmitting boundary method. *J. Appl. Phys.*, 67(10):6353–6359, 1990.

[40] J. M. Luttinger and W. Kohn. Motion of electrons and holes in perturbed periodic fields. *Phys. Rev.*, 97(4):869–883, 1955.

[41] P.A. Markowich, C.A. Ringhofer, and C. Schmeiser. *Semiconductor equations.* Springer-Verlag, Vienna, 1990.

[42] P.L. McEuen, M.S. Fuhrer, and H. Park. Single-walled carbon nanotube electronics. *IEEE Trans. Nanotechnol.*, 1(1):78 –85, 2002.

[43] M. S. Mock. *Analysis of mathematical models of semiconductor devices*, volume 3 of *Advances in Numerical Computation Series.* Boole Press, Dún Laoghaire, 1983.

[44] C. Negulescu and S. Possanner. Diffusion limit of a generalized matrix boltzmann equation for spin-polarized transport. Submitted.

[45] F. Nier. Schrödinger-Poisson systems in dimension $d \leq 3$: the whole-space case. *Proc. Roy. Soc. Edinburgh Sect. A*, 123(6):1179–1201, 1993.

[46] F. Nier. A variational formulation of Schrödinger-Poisson systems in dimension $d \leq 3$. *Comm. Partial Differential Equations*, 18(7-8):1125–1147, 1993.

[47] A. Pecchia, L. Salamandra, L. Latessa, B. Aradi, T. Frauenheim, and A. Di Carlo. Atomistic modeling of gate-all-around si-nanowire field-effect transistors. *IEEE Trans. Electron Devices*, 54(12):3159 –3167, 2007.

[48] P. Pietra and N. Vauchelet. Modeling and simulation of the diffusive transport in a nanoscale double-gate mosfet. *J. Comput. Electron.*, 7:52–65, 2008.

[49] E. Polizzi and N. Ben Abdallah. Subband decomposition approach for the simulation of quantum electron transport in nanostructures. *J. Comput. Phys.*, 202(1):150 – 180, 2005.

[50] F. Poupaud. Diffusion approximation of the linear semiconductor Boltzmann equation: analysis of boundary layers. *Asymptotic Anal.*, 4(4):293–317, 1991.

[51] F. Poupaud and C. Ringhofer. Semi-classical limits in a crystal with exterior potentials and effective mass theorems. *Comm. Partial Differential Equations*, 21(11-12):1897–1918, 1996.

[52] M. Reed and B. Simon. *Methods of modern mathematical physics, IV - Analysis of operators*. Academic Press [Harcourt Brace Jovanovich Publishers], New York, 1978.

[53] A. Shpiro, P. M. Levy, and S. Zhang. Self-consistent treatment of nonequilibrium spin torques in magnetic multilayers. *Phys. Rev. B*, 67(10):104430, 2003.

[54] J.C. Slonczewski. Current-driven excitation of magnetic multilayers. *Journal of Magnetism and Magnetic Materials*, 159:L1–L7, 1996.

[55] C. Sparber. Effective mass theorems for nonlinear Schrödinger equations. *SIAM J. Appl. Math.*, 66(3):820–842, 2006.

[56] S. Teufel. *Adiabatic perturbation theory in quantum dynamics*, volume 1821 of *Lecture Notes in Mathematics*. Springer-Verlag, Berlin, 2003.

[57] N. Vauchelet. Diffusive transport of partially quantized particles: $L \log L$ solutions. *Math. Models Methods Appl. Sci.*, 18(4):489–510, 2008.

[58] N. Vauchelet. Diffusive limit of a two dimensional kinetic system of partially quantized particles. *J. Stat. Phys.*, 139(5):882–914, 2010.

[59] T. Wenckebach. *Essential of Semiconductor Physics*. Wiley, Chichester, 1999.

[60] D. Zhang and E. Polizzi. Efficient modeling techniques for atomistic-based electronic density calculations. *J. Comput. Electron.*, 7:427–431, 2008.

[61] S. Zhang, P. M. Levy, and A. Fert. Mechanisms of spin-polarized current-driven magnetization switching. *Phys. Rev. Lett.*, 88(23):236601, 2002.

[62] I. Zutić, J. Fabian, and S. Das Sarma. Spintronics: Fundamentals and applications. *Rev. Mod. Phys.*, 76(2):323–410, Apr 2004.

Chapter 1

An introduction to the semiconductor physics

In this chapter, we introduce the main physical notions that will be used through this PhD thesis. We first present some basic aspects of quantum mechanics and solid-state physics. It allows us to define what a semiconductor is. Then, we say few words about the equations generally used to described the classical transport of charged particles in these semiconductors. Next, we make a brief description of electronic devices simulated in this PhD thesis. In particular, we present the Metal-Oxide-Semiconductor Field-Effect Transistors as well as new structures such as silicon nanowires and carbon nanotubes. Finally, we finish with a basic introduction to spintronics. For more details, we refer for example to [3, 29, 53, 55, 58, 57] for textbooks of solid-state and semiconductor physics, and to [35, 36, 41, 42] for mathematical textbooks of semiconductor equations.

1.1 Notions of quantum mechanics

Let us start to remind some important notions of quantum mechanics for describing the transport of particles in physical systems. In 1924, Louis de Broglie formulated the postulate of wave-particle duality claiming that all matter (matter being defined as anything which has a mass, in particular atoms, electrons and other particles), not just light, has a wave-like nature. For example, the interference patterns can be explained by the wave theory whereas the fact that we can find the matter at a specific position can be explained only by the particle theory. He related the wave vector k and the momentum p with the relation

$$p = \hbar k, \tag{1.1.1}$$

where $\hbar = \frac{h}{2\pi} \approx 1,054 \times 10^{-34}$ $J.s$ is the reduced Planck constant. The wavelength λ associated with the particle is given by

$$\lambda = \frac{2\pi}{k}. \tag{1.1.2}$$

Using the kinetic energy E given by the relation $E = \frac{p^2}{2m}$, where m is the mass of the particle, the de Broglie wavelength writes

$$\lambda = \frac{h}{\sqrt{2mE}}. \tag{1.1.3}$$

To have an idea of these lengths, for an electron at 0,1 eV, the wavelength is in order of 4 nm.

In quantum mechanics, we associate with a particle of mass m in a real potential energy $V(x)$ at the time t, a complex-valued function $\Psi(t,x)$, called wave function of the particle, which follows the Schrödinger equation

$$\imath\hbar\frac{\partial}{\partial t}\Psi(t,x) = H\Psi(t,x), \tag{1.1.4}$$

where H is the Hamiltonian given by

$$H = -\frac{\hbar^2}{2m}\Delta + V(x). \tag{1.1.5}$$

$\imath$ denotes the imaginary unit and $\hbar$ is the reduced Plank constant. The first term of the Hamiltonian represents the kinetic energy, whereas the second term corresponds to the potential energy. We denote by $\mathfrak{Re}(z)$ and $\mathfrak{Im}(z)$, respectively the real part and the imaginary part of a complex number z. Moreover, $\overline{z}$ is the conjugate of z. An important quantity associated with the wave function Ψ is the modulus square $|\Psi(t,x)|^2 = \Psi(t,x)\overline{\Psi(t,x)}$ which can be interpreted as the probability to find the particle in position x at time t. A simple computation allows to obtain

$$\begin{aligned}\partial_t|\Psi|^2 &= \partial_t\overline{\Psi}\Psi + \overline{\Psi}\partial_t\Psi = 2\mathfrak{Re}(\overline{\Psi}\partial_t\Psi) = -\frac{\hbar}{m}\mathfrak{Im}(\overline{\Psi}\Delta\Psi)\\ &= -\frac{\hbar}{m}\mathfrak{Im}\Big(\overline{\Psi}\mathrm{div}(\nabla\Psi)\Big) = -\frac{\hbar}{m}\mathrm{div}\Big(\mathfrak{Im}(\overline{\Psi}\nabla\Psi)\Big),\end{aligned}$$

since $\mathfrak{Im}(\nabla\Psi.\nabla\overline{\Psi}) = 0$. We deduce the conservation law

$$\partial_t n + \frac{1}{q}\mathrm{div}J = 0, \tag{1.1.6}$$

introducing the quantities

$$n = |\Psi|^2 \quad \text{and} \quad J = \frac{q\hbar}{m}\mathfrak{Im}(\overline{\Psi}\nabla\Psi). \tag{1.1.7}$$

n is interpreted as the electron density and J as the electron current density.

Next, when the Hamiltonian does not depend on time, we can find solutions of (1.1.4) in the form

$$\Psi(t,x) = e^{-\imath\frac{Et}{\hbar}}\psi(x), \tag{1.1.8}$$

where E is a real number, corresponding to an energy. Introducing this expression in (1.1.4) gives the so-called stationary Schrödinger equation

$$H\psi(x) = E\psi(x). \tag{1.1.9}$$

Consequently, ψ can be seen as an eigenfunction and E as an eigenvalue of the Hamiltonian H.

To finish this part, we want to illustrate two important quantum effects, the tunneling effect and the energy quantization, that are relevant for describing quantum transport in electronic devices. We study the stationary Schrödinger equation in a one dimensional case where the potential energy $V(x)$ is simplified to a step, a barrier or a well.

• **Step potential :** We take $V(x) = 0$ if $x < 0$ and $V(x) = V > 0$ if $x > 0$. The solution of (1.1.9) in the domain $x < 0$ can be written

$$\psi(x) = Ae^{\imath k_0 x} + Be^{-\imath k_0 x} \quad \text{with} \quad k_0 = \sqrt{\frac{2mE}{\hbar^2}}. \tag{1.1.10}$$

The first term corresponds to the ingoing wave with an amplitude A whereas the second term is the reflected wave of amplitude B. We define the reflection coefficient by

$$R = \frac{|B|^2}{|A|^2}. \tag{1.1.11}$$

Next, we solve (1.1.9) in the domain $x > 0$. We need to distinguish two cases :

- Case $E > V$: The solution has the form

$$\psi(x) = Ce^{\imath k_1 x} + De^{-\imath k_1 x} \quad \text{with} \quad k_1 = \sqrt{\frac{2m(E-V)}{\hbar^2}}. \tag{1.1.12}$$

The first term is the transmitted wave of amplitude C and the second term corresponds to a wave coming from $+\infty$ that we assume to be null ($D = 0$). In $x = 0$, we impose the continuity of the wave function and of its derivative. We obtain the relations

$$A + B = C \quad \text{and} \quad k_0(A - B) = k_1 C.$$

Thus, we can express B and C in function of A. We finally find that

$$R = \Big(\frac{1 - k_1/k_0}{1 + k_1/k_0}\Big)^2.$$

The reflection coefficient is not null, contrary to the results of classical mechanics. It is purely a quantum effect.

- Case $E < V$: The solution has the form

$$\psi(x) = Ce^{-k_2 x} + De^{k_2 x} \quad \text{with} \quad k_2 = \sqrt{\frac{2m(V-E)}{\hbar^2}}. \tag{1.1.13}$$

The first term corresponds to the vanishing wave. Moreover, since the wave function is bounded in $+\infty$, we assume that $D = 0$. The continuity equations in $x = 0$ gives

$$\imath(A + B) = C \quad \text{and} \quad \imath k_0(A - B) = -k_2 C.$$

Again, we express B and C in terms of A. In accordance to classical mechanics, we find $R = 1$. Nevertheless, $C \neq 0$ and thus the probability to find the particle in the domain $x > 0$ is not null in this quantum case. It fast decreases to zero when the wave enters in the step potential.

• **Barrier potential :** We take $V(x) = 0$ if $x < 0$ or $x > L$ and $V(x) = V > 0$ if $0 < x < L$. As previously, when $E < V$, we can show that the transmission coefficient in the domain $x > L$ is not null. This phenomenon, which consists of having a probability to find the particle after the barrier, is called tunneling effect and it is the basic operation mechanism for example in tunneling diodes.

• **Well potential :** We take $V(x) = +\infty$ if $x < 0$ or $x > L$ and $V(x) = 0$ if $0 < x < L$. In this case, the particle is trapped in the well potential and the wave function is null for $x < 0$ and $x > L$. In the domain $0 < x < L$, the solution of (1.1.9) has the form of (1.1.10). Imposing the continuity of the wave function in $x = 0$ and $x = L$, we find

$$A + B = 0 \quad \text{and then} \quad \sin(k_0 L) = 0.$$

It implies that the wave vector k_0 can only take discrete values

$$k_0 = \frac{n\pi}{L}, \quad n \in \mathbb{Z}, \tag{1.1.14}$$

and consequently it gives a quantification of the energy, that is the discrete values E_n are given by

$$E_n = \frac{\hbar^2 k_0^2}{2m} = n^2 \frac{\hbar^2 \pi^2}{2mL^2}. \tag{1.1.15}$$

Finally the normalization condition $\int_0^L |\psi_n(x)|^2 dx$, stating that the probability to find the particle in the well is equal to 1, allows to conclude that

$$\psi_n(x) = \frac{1}{\sqrt{2L}} \sin(k_0 x).$$

To summarize, the tunneling effect in the barrier potential or the quantization of energy states in a well potential are physical phenomena specific to quantum mechanics.

1.2 Notions of solid-state physics

We now review some facts about the crystal structure of solids in order to understand how to define a semiconductor.

1.2.1 Crystal structure

A crystal structure is a unique arrangement of atoms (or molecules,...) in a solid. It is composed of a pattern, a set of atoms arranged in a particular way, and a lattice exhibiting long-range order and symmetry. The infinite periodic array of atoms is a so-called Bravais lattice L defined by

$$L = \{l_1 \vec{a_1} + l_2 \vec{a_2} + l_3 \vec{a_3} \mid l_i \in \mathbb{Z}\} \subset \mathbb{R}^3, \tag{1.2.1}$$

where $\vec{a_i} \in \mathbb{R}^3$ are the basis vectors of L. They are called primitive vectors of the lattice. To all Bravais lattices L, we can associate a reciprocal lattice L^* given by

$$L^* = \{l_1\vec{a_1^*} + l_2\vec{a_2^*} + l_3\vec{a_3^*} \mid l_i \in \mathbb{Z}\} \subset \mathbb{R}^3, \tag{1.2.2}$$

where the primitive vectors $\vec{a_i^*} \in \mathbb{R}^3$ are the dual basis. They are determined such that

$$\vec{a_i} \cdot \vec{a_j^*} = 2\pi\delta_{ij}. \tag{1.2.3}$$

Next, we define the centred fundamental domain $\mathcal{C}$ of L (also called primitive cell), which is

$$\mathcal{C} = \Big\{x \in \mathbb{R}^3,\ x = \sum_{n=1}^{3} \alpha_n \vec{a_n} \mid \alpha_n \in \Big[-\frac{1}{2}, \frac{1}{2}\Big]\Big\}. \tag{1.2.4}$$

When translated by all vectors of the lattice L, it covers the entire space $\mathbb{R}^3$ without overlapping and without leaving gaps. In the same way, the centered fundamental domain $\mathcal{B}$ of L^*, called the first Brillouin zone, is defined by

$$\mathcal{B} = \Big\{k \in \mathbb{R}^3,\ k = \sum_{n=1}^{3} \alpha_n \vec{a_n^*} \mid \alpha_n \in \Big[-\frac{1}{2}, \frac{1}{2}\Big]\Big\}. \tag{1.2.5}$$

Thus, we clearly have

$$|\mathcal{C}|\ |\mathcal{B}| = (2\pi)^3, \tag{1.2.6}$$

where $|.|$ represents the volume measure. For example, $|\mathcal{C}| = a_1 \cdot (a_2 \times a_3) = \det(a_1, a_2, a_3)$.

Finally, let $x \in L$ and $k \in L^*$, we immediately find that $e^{\imath k \cdot x} = 1$, using (1.2.3). It underlines that the position vector x and the vector k have to be seen as conjugate variables. Consequently, k is called wave vector and it has the dimension of inverse length.

1.2.2 Electrons in a periodic potential

The periodic crystal structure, just described, generates a potential which is responsible for the electronic properties of the solid. This potential is described by ions (nuclei and core electrons) and valence electrons. Let the state of the many-particle system be described by the wave function $\psi(x)$, where $x = (x_1, ..., x_M) \in \mathbb{R}^{3M}$ is the vector of all possible positions $x_j \in \mathbb{R}^3$ of the M electrons. Then, the Hamiltonian of the quantum system consists of the kinetic energy part, the electron-ion interactions and the electron-electron interactions. It leads to

$$H = \sum_{j=1}^{M} \Big(-\frac{\hbar^2}{2m}\Delta_j + V_{ei}(x_j)\Big) + V_{ee}(x), \tag{1.2.7}$$

where Δ_j is the laplacian acting only on the variable x_j, V_{ei} is a periodic potential energy which describes the interactions of a single electron with the ions and V_{ee} is a potential energy which takes in account the electron-electron interactions. These potentials are superposition of Coulomb potentials.

Consequently, at large scale (millions of atoms), the computation of the eigenvalue problem (1.1.9) is a significant challenge. It is necessary to make approximations to simplify the problem. In particular, it is possible to replace the electron-electron interactions by an effective single-particle potential. This is done by the so called Hartree-Fock approximation which allows to reduce a 3M-dimensional problem to a 3-dimensional one. Without entering in details, we just recall here that the (modified) Hartree-Fock equation has the following form

$$-\frac{\hbar^2}{2m}\Delta\psi_j(x) + V_L(x)\psi_j(x) = E_j(x)\psi_j(x) \quad x \in \mathbb{R}^3,\ j = 1, .., M. \tag{1.2.8}$$

The effective potential energy V_L has the periodicity of the Bravais lattice (at least for perfect crystals)

$$V_L(x+y) = V_L(x) \quad \forall\ x \in \mathbb{R}^3,\ \forall\ y \in L. \tag{1.2.9}$$

For example, it can be a periodic square-well potential in the simple Kronig-Penney model which describe a one dimensional single-crystal lattice. For more physically relevant cases, we can consider a pseudo-potential which is an effective potential constructed to replace the atomic all-electron potential such that core electrons are "frozen" being considered together with the nuclei.

1.2.3 Bloch Theorem

Due to the periodicity of the effective potential V_L, we can imagine to reduce the whole-space stationary Schrödinger equation to an eigenvalue problem on the elementary cell of the lattice. It is possible with the Bloch Theorem [12]. It is an application in solid-state physics of the Floquet theorem for ordinary differential equations [30].

Theorem 1.2.1. *Let V_L be a periodic potential energy (i.e. (1.2.9) holds). Then, the whole-space eigenvalue problem*

$$H\psi(x) = -\frac{\hbar^2}{2m}\Delta\psi(x) + V_L(x)\psi(x) = E\psi(x) \quad x \in \mathbb{R}^3, \tag{1.2.10}$$

can be reduced to an eigenvalue problem on the primitive cell $\mathcal{C}$, such that for each element of the Brillouin zone $k \in \overline{\mathcal{B}}$,

$$H\psi_k(x) = E(k)\psi_k(x) \quad \textit{with} \quad \psi_k(x+y) = e^{\imath k\cdot y}\psi_k(x), \quad x \in \mathcal{C},\ y \in L. \tag{1.2.11}$$

For each $k \in \overline{\mathcal{B}}$, this eigenvalue problem admits a complete orthonormal set of eigenfunctions $\{\psi_{n,k} \mid n \in \mathbb{N}\}$ in $L^2(\mathcal{C})$, with the corresponding increasing sequence of real eigenvalues $E_1(k) \leq E_2(k) \leq ...$ (counted with their multiplicities) satisfying $E_n(k) \to +\infty$ when $n \to +\infty$. The spectrum of H is given by the union of the closed intervals $\{E_n(k), k \in \overline{\mathcal{B}}\}$ for $n \geq 1$.

This Bloch theorem introduces the concept of the energy band structure for semiconductors. Indeed, the function $k \mapsto E_n(k)$ is called dispersion relation and the set $\{E_n(k) \mid k \in \mathcal{B}\}$ is the

n^{th} energy band of the crystal. The ranges of all these energy bands do not fill the entire energy line $\mathbb{R}$, that is to say there may exist energies $\mathcal{E}$ for which there is no band $n \in \mathbb{N}$ and no wave vector k such that $E_n(k) = \mathcal{E}$. The connected sets of energies with this non-existence property are called energy gaps. As we will see later in the subsection 1.2.5, they allows to classify the solids in metals, insulators and semiconductors.

Moreover, the eigenfunction $\psi_{n,k}$ of (1.2.11), called Bloch waves, can be written as

$$\psi_{n,k}(x) = e^{\imath k \cdot x} \chi_{n,k}(x) \quad x \in \mathcal{C},\ k \in \mathcal{B}, \tag{1.2.12}$$

where $\chi_{n,k}$ are periodic functions with respect to L, called Bloch functions, satisfying

$$\chi_{n,k}(x+y) = \chi_{n,k}(x) \quad x \in \mathbb{R}^3,\ y \in L. \tag{1.2.13}$$

It means that $\psi_{n,k}$ can be seen as plane waves modulated by some periodic functions which describe the lattice. Inserting (1.2.12) in (1.2.11), we find that $\chi_{n,k}$ are eigenvectors of the fiber Hamiltonian

$$\Big(\frac{\hbar^2}{2m}|k|^2 - i\frac{\hbar^2}{m}k.\nabla - \frac{\hbar^2}{2m}\Delta + V_L(x)\Big)\chi_{n,k} = E_n(k)\chi_{n,k}. \tag{1.2.14}$$

We remark also that, when $k = 0$, the equation (1.2.14) simplifies to

$$\Big(-\frac{\hbar^2}{2m}\Delta + V_L(x)\Big)\chi_{n,0} = E_n(0)\chi_{n,0}. \tag{1.2.15}$$

$E_n(0)$ is the energy in the n^{th} band at $k = 0$ and $\chi_{n,0}$ is the associated real Bloch function. For fixed k (including $k = 0$), the $\chi_{n,k}$'s form a complete orthonormal basis of $L^2(\mathcal{C})$ [15].

1.2.4 Effective mass approximation

An important approximation in solid-states physics (and fundamental in the study of semiconductors) is the effective mass approximation. It consists of averaging the periodic potential generated by the periodic lattice structure, letting the number of ions going to infinity. This approximation relies on the hypothesis that the crystal lattice spacing is very small compared to the characteristic length scale.

A possible way to understand the effective mass approximation is the following. We consider an electron moving in a crystal structure. It is subject to an internal crystal force F_{int} and to an external force F_{ext}. The Newton's law gives

$$m\frac{dv}{dt} = F_{int} + F_{ext}. \tag{1.2.16}$$

We can consider this particle as a quasi particle moving in vacuum with an effective mass m^*. It obeys to

$$m^*\frac{dv}{dt} = F_{ext}. \tag{1.2.17}$$

This effective mass m^* contains all the effects of the lattice potential on the electron. We can define for a wave packet the mean velocity in the n^{th} band in function of the energy band

$$v_n(k) = \frac{1}{\hbar}\nabla_k E_n(k). \tag{1.2.18}$$

Differentiation with respect to t gives

$$\frac{dv_n(k)}{dt} = \frac{1}{\hbar}\frac{d^2E_n(k)}{dk^2}.\frac{dk}{dt}, \tag{1.2.19}$$

where $\frac{d^2E_n(k)}{dk^2}$ is the Hessian matrix. On the other hand, introducing the crystal momentum $p = m^*v_n$, we have

$$m^*\frac{dv_n}{dt} = \frac{dp}{dt} = \hbar\frac{dk}{dt}, \tag{1.2.20}$$

where the second equality is due to (1.1.1). Consequently, we obtain an expression of the effective mass tensor

$$(m^*)^{-1} = \frac{1}{\hbar^2}\frac{d^2E_n(k)}{dk^2}. \tag{1.2.21}$$

If we evaluate the Hessian of $E_n(k)$ near a local minimum (respectively a maximum) k_0 i.e. $\nabla E_n(k_0) = 0$, then the Hessian is a symmetric positive (respectively negative) definite matrix which can be diagonalized. We write a Taylor expansion of $E_n(k)$ and if we assume that the effective masses are equal in all directions (isotropic condition), we can write neglecting higher-order terms

$$E_n(k) = E_n(k_0) + \frac{\hbar^2|k|^2}{2m^*}. \tag{1.2.22}$$

It means that the energy of an electron near a band minimum of an isotropic material is equal to the energy of a free electron in a vacuum where the electron mass m is replaced by the effective mass m^*. This relation (1.2.22), called the parabolic band approximation, is valid for wave vectors k sufficiently close to a local minimum k_0. Nevertheless, in some cases, the higher-order terms cannot be negligible and a non parabolic band approximation is necessary (Kane model for example). But it is far from the scope of this chapter and we do not detail it.

It is also possible to derive an approximation of the energy band $E_n(k)$ starting from the Hamiltonian introduced in (1.2.14), using for example a perturbation theory. In this part, we only present a mathematically non rigorous computation. To simplify the exposition, we consider a one dimensional problem. We start from the equation (1.2.14) for the functions $\chi_{n,k}$ that we write in the form

$$(H_0 + H_1)\chi_{n,k} = E_n(k)\chi_{n,k}, \tag{1.2.23}$$

where

$$H_0 = -\frac{\hbar^2}{2m}\partial_{xx} + V_L(x) \quad \text{and} \quad H_1 = -\imath k\frac{\hbar^2}{m}\partial_x + k^2\frac{\hbar^2}{2m}. \tag{1.2.24}$$

Defining the quantum momentum operator $P = -\imath\hbar\partial_x$, it explains why this method is generally called the $k \cdot p$ method.

Next, we assume that the solutions of

$$H_0\chi_{n,0} = E_n(0)\chi_{n,0} \quad x \in \mathcal{C}, \tag{1.2.25}$$

with periodic boundary conditions, are known. $\mathcal{C}$ is the one dimensional elementary cell. Since the operator H_0 is real and self-adjoint, the eigenfunctions $\chi_{n,0}$ are real. We denote $< ., . >$ the scalar product in $L^2(\mathcal{C})$. We also define the quantities

$$P_{nn'} =< \partial_x \chi_{n',0}, \chi_{n,0} > \tag{1.2.26}$$

which are the matrix elements of the first order derivative operator between Bloch functions $\chi_{n,0}$. Here, we assume that all the eigenvalues $E_n(0)$ are simple (non degenerate case).

We differentiate (1.2.23) with respect to k. It gives

$$\frac{dH_1}{dk}\chi_{n,k} + (H_0 + H_1)\frac{d\chi_{n,k}}{dk} = \frac{dE_n}{dk}\chi_{n,k} + E_n\frac{d\chi_{n,k}}{dk}. \tag{1.2.27}$$

A second differentiation gives

$$\frac{d^2H_1}{dk^2}\chi_{n,k} + 2\frac{dH_1}{dk}\frac{d\chi_{n,k}}{dk} + (H_0 + H_1)\frac{d^2\chi_{n,k}}{dk^2} = \frac{d^2E_n}{dk^2}\chi_{n,k} + 2\frac{dE_n}{dk}\frac{d\chi_{n,k}}{dk} + E_n\frac{d^2\chi_{n,k}}{dk^2}. \tag{1.2.28}$$

• We write (1.2.27) for $k = 0$ and we project it on $\chi_{n,0}$. Using the orthonormality of $\chi_{n,0}$'s and the selfadjointness of $H_0 + H_1$ with (1.2.23), it leads to

$$\frac{dE_n(k)}{dk}\Big|_{k=0} =< \frac{dH_1(k)}{dk}\Big|_{k=0}\chi_{n,0}, \chi_{n,0} > .$$

Since $\frac{dH_1(k)}{dk} = \frac{k\hbar^2}{m} - \imath\frac{\hbar^2}{m}\partial_x$, we immediately find that

$$\frac{dE_n(k)}{dk}\Big|_{k=0} = 0. \tag{1.2.29}$$

• Next, we write (1.2.27) for $k = 0$ and we project it on $\chi_{n',0}$, with $n \neq n'$. We find that

$$< \frac{dH_1(k)}{dk}\Big|_{k=0}\chi_{n,0}, \chi_{n',0} > +E_{n'}(0) < \frac{d\chi_{n,k}}{dk}\Big|_{k=0}, \chi_{n',0} >= E_n(0) < \frac{d\chi_{n,k}}{dk}\Big|_{k=0}, \chi_{n',0} >,$$

that we simplify to

$$< \frac{d\chi_{n,k}}{dk}\Big|_{k=0}, \chi_{n',0} >= \frac{< \frac{dH_1(k)}{dk}|_{k=0}\chi_{n,0}, \chi_{n',0} >}{E_n(0) - E_{n'}(0)} = -\imath\frac{\hbar^2}{m}\frac{P_{n'n}}{E_n(0) - E_{n'}(0)}. \tag{1.2.30}$$

• Finally, we write (1.2.28) for $k = 0$ and we project it on $\chi_{n,0}$. Using the selfadjointness of $H_0 + H_1$ with (1.2.23) as well as (1.2.29), we obtain

$$\frac{d^2E_n(k)}{dk^2}\Big|_{k=0} =< \frac{d^2H_1(k)}{dk^2}\Big|_{k=0}\chi_{n,0}, \chi_{n,0} > +2 < \frac{dH_1(k)}{dk}\Big|_{k=0}\frac{d\chi_{n,k}}{dk}\Big|_{k=0}, \chi_{n,0} > .$$

Since $\frac{d^2H_1(k)}{dk^2} = \frac{\hbar^2}{m}Id$, we immediately find that the first term of the second member is equal to $\frac{\hbar^2}{m}$ by orthonormality of $\chi_{n,0}$'s. To treat the second term, we decompose $\frac{d\chi_{n,k}}{dk}\Big|_{k=0}$ in the basis $\{\chi_{n,0}|n \in \mathbb{N}\}$

$$\frac{d\chi_{n,k}}{dk}\Big|_{k=0} = \sum_{n'\in\mathbb{N}} < \frac{d\chi_{n,k}}{dk}\Big|_{k=0}, \chi_{n',0} > \chi_{n',0}. \tag{1.2.31}$$

Thus,

$$< \frac{dH_1(k)}{dk}\Big|_{k=0} \frac{d\chi_{n,k}}{dk}\Big|_{k=0}, \chi_{n,0} >= -\imath \frac{\hbar^2}{m} \sum_{n' \in \mathbb{N}} < \frac{d\chi_{n,k}}{dk}\Big|_{k=0}, \chi_{n',0} >< \partial_x \chi_{n',0}, \chi_{n,0} > .$$

First, we point out that $P_{nn} = 0$, since integrating by parts we have $P_{nn'} = -P_{n'n}$. Moreover, we use (1.2.30) and we finally obtain

$$< \frac{dH_1(k)}{dk}\Big|_{k=0} \frac{d\chi_{n,k}}{dk}\Big|_{k=0}, \chi_{n,0} >= (-\imath)^2 \frac{\hbar^4}{m^2} \sum_{n' \neq n} \frac{P_{nn'} P_{n'n}}{E_n(0) - E_{n'}(0)}.$$

Thus, we deduce the following expression

$$\frac{1}{\hbar^2} \frac{d^2 E_n(k)}{dk^2}\Big|_{k=0} = \frac{1}{m} - 2\frac{\hbar^2}{m^2} \sum_{n' \neq n} \frac{P_{nn'} P_{n'n}}{E_n(0) - E_{n'}(0)} := \frac{1}{m_n^*}. \tag{1.2.32}$$

Consequently, the n^{th} effective mass is given summing the contribution of the nearest bands n'. Obviously, this formulation (1.2.32) is not anymore defined in the degenerate case which has to be analyzed for example by the methods of degenerate perturbation theory.

The approach used in Chapter 2 to obtain the effective mass approximation for ultra-scaled confined nanostructures is instead based on the work by the physicists Kohn and Luttinger [40] (and followed in [5] for a mathematical study for 3D crystals) that makes use of an asymptotic expansion on the basis

$$u_{n,k}(x) = e^{\imath k \cdot x} \chi_{n,0}(x). \tag{1.2.33}$$

An advantage of this basis is that, since the wave vector k appears only in the plane wave and not in the periodic function $\chi_{n,0}$, a separation between the fast oscillating scale (associated with the periodic potential) and the slow motion carried by the plane wave is possible (see later Remark 2.3.2).

1.2.5 Band structure and Fermi level

As we have seen previously (see Bloch Theorem 1.2.1), the crystal lattice generates a periodic potential and a consequence is that the spectrum of the Hamiltonian will be constituted of bounded intervals (called bands) separated by energy gaps.

Electrons are fermions and follow the Pauli exclusion principle : two identical fermions must not occupy the same quantum state simultaneously. Moreover, electrons fill different bands with an increasing energy, starting by the lowest energy states. So, we define the valence band as the highest band where electrons are normally present at absolute zero temperature (without thermal agitation). It is located below the conduction band, separated from it by a gap. Moreover, the Fermi level E_F is the highest energy that an electron can occupy at absolute zero temperature. The Fermi level is sometimes defined in function of the chemical potential μ such that $E_F = -q\mu$ where q is the elementary charge.

When the temperature increases, the thermal agitation changes the electronic properties. So, the occupation probability of a state of energy E is given by the Fermi-Dirac distribution (see Fig.1.1)

$$f_{FD}(E - E_F) = \frac{1}{1 + e^{\beta(E-E_F)}}, \tag{1.2.34}$$

where $\beta = k_B T$, T being the temperature and k_B the Boltzmann constant. When, $E - E_F \gg k_B T$, the Fermi-Dirac statistics can be approximated by the Maxwell-Boltzmann distribution function

$$f_B(E - E_F) = e^{-\beta(E-E_F)}. \tag{1.2.35}$$

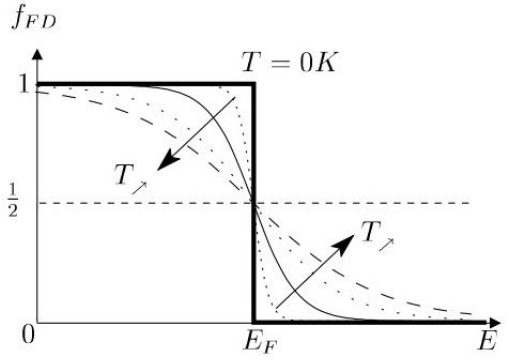

Figure 1.1: Fermi-Dirac distribution function for different temperatures T (from [50]).

So, the position of the Fermi level, in relation to the valence and the conduction band, determines the electrical conductivity of the crystal. We distinguish the metals, the insulators and the semiconductors, as we can see in Fig.1.2. In this figure, the blue regions represent parts of the spectrum filled by electrons. In metals, the Fermi level is inside the conduction band. With the thermal agitation, electrons can move to a neighboring free state. It creates an electrical conductivity. On the contrary, in insulators, the Fermi level is in the band gap. This gap is too large (superior to 3 ev) to be passed through. Electrons are blocked in the full valence band and the material resists to the flow of electric charges. In semiconductors, the Fermi level is also in the forbidden band but in this case the gap is smaller (up to about 3 eV). Due to the thermal agitation, electrons can be excited from the valence band to the conduction band, where a lot of states are free. Moreover, they leave behind electron holes i.e. unoccupied states in the valence bands. Both the conduction band electrons and the valence band holes contribute to the electrical conductivity. In fact, the holes themselves do not move but a neighboring electron can move to fill the hole, leaving a hole at the previous place. In this way, the holes behave as if they were actual positive charged particles.

1.2.6 Semiconductor doping

The property of semiconductors that makes them most useful for constructing electronic devices is that their conductivity may easily be modified by introducing impurities into their crystal

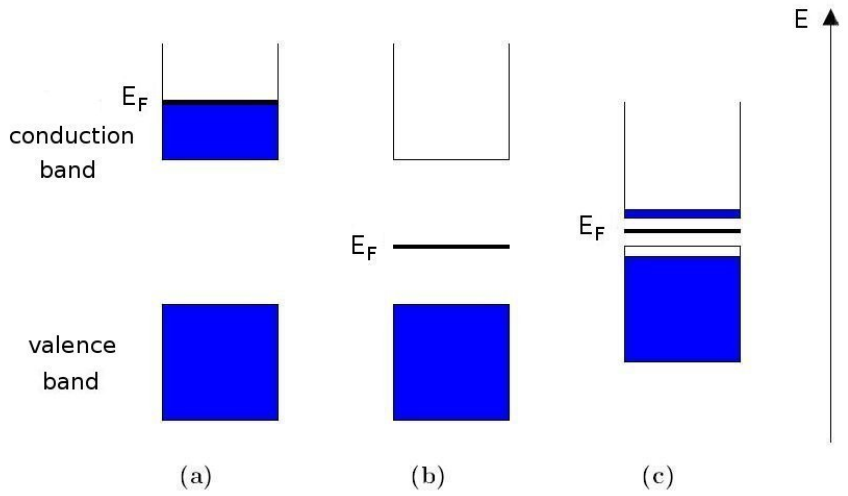

Figure 1.2: Band structure of a metal (a), an insulator (b) and a semiconductor (c)

lattice. The process of adding controlled impurities to a semiconductor is call doping. The amount of impurities (also called dopants) varies its level of conductivity. We named intrinsic semiconductor a pure semiconductor without any impurity. The concentration of electrons n and holes p is equivalent i.e. $n = p = n_i$ where n_i is defined as the intrinsic carrier concentration. Inversely, doped semiconductors are called extrinsic.

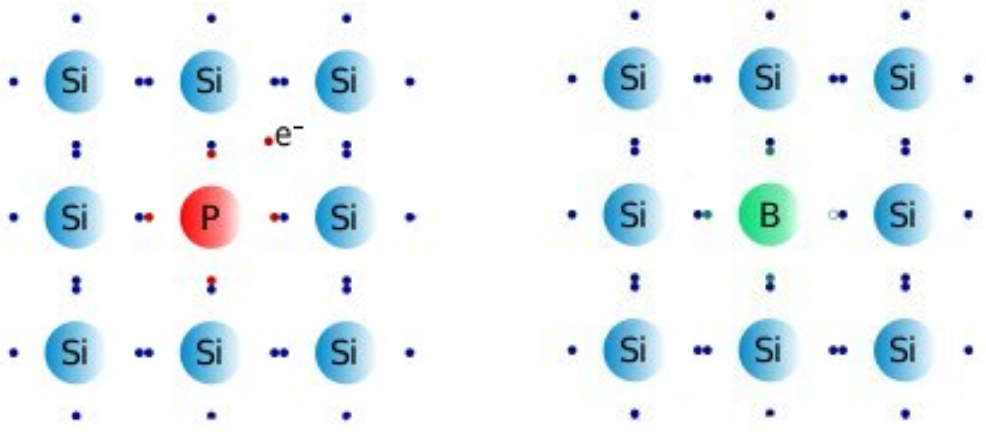

Figure 1.3: Illustration of the n-type doping (left) and the p-type doping (right), from $http://fr.wikipedia.org/wiki/Dopage\_(semi\text{-}conducteur)$.

The materials chosen as suitable dopants depend on the atomic properties of both the dopant and the material to be doped. We have two types of dopants, illustrated in Fig.1.3. The donors, incorporated into the crystal lattice, donate valence electrons to the material and create an

excess of negative charges. On the contrary, the acceptors produce a hole and create a positive charge carrier. Consequently, a semiconductor doped with a donor density N_D^+ superior to the acceptor density N_A^- is called n-type semiconductor. In the opposite case, we have a p-type semiconductor.

1.2.7 Charge density and electrostatic potential

Finally, we shall consider the charge density ρ which comes from the unbalance between donors N_D^+ and free electron density n and also between acceptors N_A^- and free hole density p. We write

$$\rho = q(N_D^+ - N_A^- - n + p), \tag{1.2.36}$$

where q is the elementary charge. To simplify, in this PhD thesis, we study only the transport of electrons and the charge density is restricted to

$$\rho = q(N_D - n). \tag{1.2.37}$$

Then, the electrostatic potential V_P induced by charges is solution of a Poisson equation

$$-\nabla\Big(\epsilon_r(x)\nabla V_P(x)\Big) = \frac{\rho(x)}{\epsilon_0}. \tag{1.2.38}$$

where ϵ_0 is the vacuum permittivity and ϵ_r is the relative permittivity of the semiconductor under consideration. It is important to remind that the quantity V_P being in the Poisson equation is a potential expressed in Volts. In the Schrödinger equations described previously, the quantity V corresponds to a potential energy expressed in Joules. For electrons, the two quantities are linked by the relation $V = -qV_P$.

To conclude this part, we consider the Schrödinger equation

$$\imath\hbar\frac{\partial}{\partial t}\Psi(t,x) = -\frac{\hbar^2}{2m}\Delta\Psi(t,x) + V_L(x)\Psi(t,x) + V(x)\Psi(t,x), \tag{1.2.39}$$

where $V_L(x)$ is a periodic potential generated by the lattice ions and $V(x)$ is a slowly varying potential, which can be for example the result of an external applied potential and a self-consistent potential solution of the Poisson equation (1.2.38). This Schrödinger-Poisson system is a well-described quantum model to describe the transport of electrons in semiconductors [9, 6, 46, 47].

1.3 A basic presentation of the semi-classical transport models

In the previous parts, we have introduced some quantum models which take into account quantum effects (like energy quantization, tunneling...). In semiconductor modeling, it exists another important category of models, the classical models. They are based on a classical description of

the electron ensemble, with completely determined trajectories and continuously varying quantities. Even if nowadays the dimensions of the semiconductor devices become smaller and smaller (and thus quantum transport phenomena play an important role), the classical models continue to occupy a large part in the semiconductor studies. A main reason is that the treatment of collision particles is well understood in these classical models. In our case, we have in mind to study electrical devices which contains an active zone between two largely doped regions acting as electron reservoirs. In these regions, phonon-electron collisions play an important role and it is necessary to take them into account in our simulations.

In this section, we start at the microscopic level where the model describes the individual motion of particles. Then, we arrive to a kinetic model, based on a statistical picture of the electron ensemble. At this level, we introduce the Boltzmann equation and in particular we discuss the different possible scalings. Finally, we present an example of microscopic model, the drift-diffusion model, which is derived from the Boltzmann equation by a diffusive limit, dealing with averaged quantities which depend only on the position and time variables.

1.3.1 From Newton's equations to Boltzmann equation

We consider a system of M particles of mass m evolving without collisions. At the fundamental level, we can describe this system according to Newton's laws. Each particle, labeled with an index i ($i = 1, ..., M$), is described by its position $x_i \in \mathbb{R}^3$ and its momentum $p_i = m\ v_i \in \mathbb{R}^3$ (where v_i is the velocity of the particle). It leads the following system :

$$\partial_t x_i = \frac{p_i}{m} \quad \text{and} \quad \partial_t p_i = F_i(x_1, ..., x_M), \tag{1.3.1}$$

where F_i is the force applied on the particle i by the other particles and by the external forces.

It is computationally very expensive to solve this system. Moreover, it is not easy to know the exact number of particles contained in the system. That is the reason why it is common to use a less precise description level that it is called kinetic level. At this scale, the system is described by a distribution function $f(x, p, t)$. The physical meaning of this distribution function is that $f(x, p, t)dxdp$ is the number of particles in the elementary volume $dxdp$ at time t. Then, all particles coming from the same point (x, p) in the phase-space domain follow the same trajectory

$$\partial_t X = \frac{P}{m} \quad \text{and} \quad \partial_t P = F(X, t).$$

We write that the density is conserved along this trajectory

$$\frac{d}{dt} f(X(t), P(t), t) = 0.$$

Consequently, we obtain the Vlasov equation

$$\partial_t f(x, p, t) + \frac{p}{m}.\nabla_x f(x, p, t) + F(x, t).\nabla_p f(x, p, t) = 0. \tag{1.3.2}$$

We note also that from the distribution function $f(x,p,t)$, we can derive macroscopic quantities, like the particle density

$$n(x,t) = \int_{\mathbb{R}^3} f(x,p,t)dp, \tag{1.3.3}$$

the current density

$$J(x,t) = \int_{\mathbb{R}^3} \frac{p}{m} f(x,p,t)dp, \tag{1.3.4}$$

and the energy density

$$\mathcal{E}(x,t) = \int_{\mathbb{R}^3} \frac{|p|^2}{2m} f(x,p,t)dp. \tag{1.3.5}$$

Macroscopic models, discussed in the next subsection, describe the evolution of these quantities. Formally, integrating the Vlasov equation (1.3.2) over $p \in \mathbb{R}^3$, we immediately find the conservation law

$$\partial_t n(x,t) + \mathrm{div}_x J(x,t) = 0, \tag{1.3.6}$$

since the third term is zero after an integration by parts.

The Vlasov equation does not take into account collisions between charged particles. A collision operator $Q(f)$ can be introduced in the right inside. Usually, this operator is nonlocal and nonlinear in f. It leads to the Vlasov equation with a collision operator which is called the Boltzmann equation [18, 56]

$$\partial_t f(x,p,t) + \frac{p}{m}.\nabla_x f(x,p,t) + F(x,t).\nabla_p f(x,p,t) = Q(f). \tag{1.3.7}$$

Finally, if the force $F(x,t)$ is considered conservative, we can write it as $F(x,t) = -\nabla_x V(x,t)$ where V is a potential energy. We obtain

$$\partial_t f + \{H, f\} = Q(f), \tag{1.3.8}$$

where $\{a,b\} = \nabla_x b \nabla_p a - \nabla_x a \nabla_p b$ denotes the Poisson bracket and $H = \frac{p^2}{2m} + V(x,t)$ is the Hamiltonian of the system.

1.3.2 Scalings of the Boltzmann equation

In order to identify the small parameters and to perform the asymptotic limits leading to the macroscopic models, we need to scale the Boltzmann equation. We define a characteristic length L and a characteristic time T. We also choose that the characteristic mass is m_e the mass of electrons. We deduce the other characteristic values : the momentum $\overline{p} = \frac{m_e L}{T}$ and the energy $\overline{V} = \frac{m_e L^2}{T^2}$. Finally, we define a second time scale τ which corresponds to the mean time between two collisions called mean collision time. The length associated with this time scale $\lambda = \sqrt{\frac{\hbar\tau}{m_e}}$ is called mean free path.

We now assume that the mean free path is much smaller than the device diameter. It means that the particle will undergo many collisions during its way through the device. So we introduce the small parameter

$$\eta = \frac{\lambda}{L} << 1. \tag{1.3.9}$$

At this point, it is possible to choose two scalings. First, we consider that the mean collision time is smaller than the characteristic time $\tau = \eta T$. It is called hydrodynamic scaling. We perform the following change of variables

$$x' = \frac{x}{L}, \quad t' = \frac{t}{T}, \quad m' = \frac{m}{m_e}, \quad V' = \frac{V}{\overline{V}}, \quad p' = \frac{p}{\overline{p}} \quad \text{and} \quad Q'(f) = \tau Q(f).$$

The distribution function is a probability and therefore, it is already dimensionless. We omit the primes and we obtain the following scaled Boltzmann equation

$$\partial_t f + \frac{p}{m}.\nabla_x f - \nabla V.\nabla_p f = \frac{Q(f)}{\eta}. \tag{1.3.10}$$

Secondly, we consider that the mean collision time is even smaller than that from the hydrodynamic scaling $\tau = \eta^2 T$. It is called diffusive scaling and we obtain the following scaled Boltzmann equation

$$\partial_t f + \frac{1}{\eta}\Big(\frac{p}{m}.\nabla_x f - \nabla V.\nabla_p f\Big) = \frac{Q(f)}{\eta^2}. \tag{1.3.11}$$

The choice of the scaling (hydrodynamic or diffusive) depends on the equilibrium states associated with the collision operators. For simplicity, in this introduction, we do not make explicit the structure of the collisions operators and we refer to [36, 42, 7] for instance. We only say that it is possible to derive (at least formally) two main categories of macroscopic models. Generally speaking, the derivation can be carried out by multiplying the Boltzmann equation by functions depending on the momentum and then by integrating over the momentum space. The obtained set of equations must be then complemented by suitable closure conditions. A quite general approach is given by the so called "entropy minimization principle" ([36, 39] and references therein). Starting from the hydrodynamic scaling, it is possible to derive hydrodynamic models of hyperbolic type ([13, 2] and references therein). Starting from the diffusive scaling, a diffusive limit allows to derive the macroscopic models [41, 42, 36, 35] such that SHE (Spherical Harmonic Expansion) [14, 21, 7], Energy-Transport [8, 10, 25, 19, 7] and Drift-Diffusion [33, 51]. In this PhD thesis, we only study a Drift-Diffusion model and thus we do not describe more precisely the other models.

1.3.3 Drift-Diffusion model

The drift-diffuison equation consists of a mass conservation equation for the electron density, supplemented with a constitutive equation for the current that describes the combined effects of diffusion and of drift under the action of the electric field. The drift-diffusion equation in scaled variable has the following form

$$\partial_t n + \mathrm{div} J = 0, \tag{1.3.12}$$

with

$$J = -\Big(\nabla_x n + n\nabla_x V\Big). \tag{1.3.13}$$

$n(x,t)$ is the particle density and $V(x,t)$ a potential energy. It is an appropriate model for devices not too small (length > 1 μm) when we do not need to take into account the thermal effects.

The rigorous derivation from the Boltzmann equation is done for instance in [51] in the linear case, [11] with a 1D Poisson coupling and [43] in the multi-dimensional case. Moreover, we can say that the drift-diffusion model is well understood analytically (existence analysis [44, 31]) and numerically (see i.e. [34, 52], [16] and references therein).

Using the Boltzmann statistics, the current (1.3.13) can be written in a slightly different form. It is common to introduce the Slotboom variable $u(x,t)$ such that $u = ne^V$. We obtain

$$J = -\Big(\nabla_x u \; e^{-V}\Big). \tag{1.3.14}$$

Finally, we can also define the Fermi level $E_F(x,t)$ such that $e^{E_F} = ne^V$ and we obtain

$$J = -\Big(\nabla_x E_F \; e^{E_F - V}\Big). \tag{1.3.15}$$

A comparison between the various dependent variables for the analysis and the simulation of the drift-diffusion equation is for instance addressed in [49, 42].

To finish this section, we mention another large category of models used to describe the transport of electrons in semiconductors : the quantum macroscopic models [1, 28, 27, 26, 24, 23, 22, 37, 38, 17, 20]. The derivation of these macroscopic models from the microscopic ones (Schrödinger equation or Wigner equation) in the quantum setting is based on a similar methodology to the one in the classical setting (entropy minimization). These models are not discussed in this PhD thesis. Nevertheless, in the future, it may be interesting to investigate in this direction. It can be interesting for example to derive a quantum drift-diffusion model for ultra-scaled confined nanostructures and to compare numerical simulations with those presented in this thesis.

1.4 Generalities about the simulated electronic devices

In this part, we describe the electrical devices that are used in the numerical simulations of this PhD thesis. On the one hand, we present the FETs (Fields-Effect Transistors) which are one of the components the most commercialized nowadays. On the other hand, we introduce two new structures, the silicon nanowires and the carbon nanotubes, which will be certainly essential in the future. Due to the extremely small dimensions, the transversal wire/tube sections contain only few atoms and we name them ultra-scaled confined nanostructures. A lot of expectations are made in the capability to use these structures to build new miniature electronic components (and for instance new transistors).

1.4.1 The Field-Effect Transistors

The Field-Effect Transistor FET relies on an electric field to control the shape of a channel of one type of charge carrier in a semiconductor material. To simplify, they are composed of a conductive region, called Channel, connected to two electron reservoirs, the Source (emitter) and the Drain (collector). Applying at the extremities a Drain-Source voltage V_{DS}, electrons (or holes) flow from the Source to the Drain and a current I_{DS} is established. It is proportional to the conductance g of the channel through

$$I_{DS} = gV_{DS}. \tag{1.4.1}$$

The conductance is given by $g = \frac{S}{L}\sigma$, where L is the channel length, S the channel section and $\sigma = q(n\mu_n + p\mu_p)$ the conductivity of the material (μ_n and μ_p are respectively the mobilities of the electrons and the holes).

There are different possibilities to modulate the conductance and thus the current. For example, in a Junction Field-Effect Transistor JFET, the section varies. In a Metal-Oxide-Semiconductor Field-Effect Transistor MOSFET, the electron density n or the hole density p varies, applying a gate voltage V_{GS} (see the illustration Fig.1.4). We note that the gate is insulated from the semiconductor by a dielectric layer (oxide for instance).

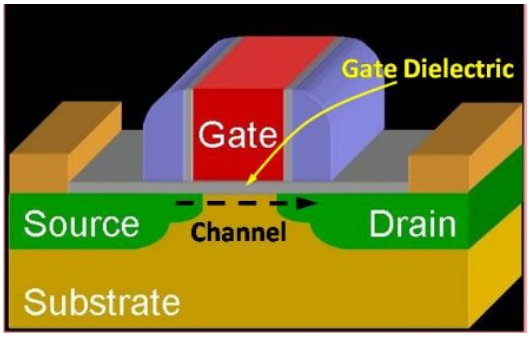

Figure 1.4: Cross section of a MOSFET
(from $http://www.isi.edu/\sim vernier/EE327/ee327\_2005.html$).

To understand how a FET controls the flow of electrons from the Source to the Drain by affecting the size and the shape of the channel created and influenced by the applied voltages, we choose to study a n-channel MOSFET. We obtain the current-voltage characteristics presented in Fig.1.5. A negative gate voltage V_{GS} narrows the channel and the flow of electron decreases. The transistor is blocked for a gate potential inferior to $V_{GS,off}$. It means that the channel is completely close and it acts like a switch. On the contrary, a positive V_{GS} increases the channel size and allows electrons to flow easily. We call inversion layer the region where electrons create the conductive channel.

Let us now suppose that V_{GS} is fixed. Then, the conductivity of the n-channel depends on the applied Drain-Source voltage V_{DS}. Four different cases have to be distinguished. First,

we have $V_{DS} << V_{sat}$ (linear part). For weak Drain-Source potentials, the conductivity of the channel remains almost constant, in such a way that the channel acts like a resistance. Therefore, the current I_{DS} is proportional to V_{DS}. Secondly, we have $V_{DS} < V_{sat}$ (sublinear part). The channel conductivity decreases at the Drain side, creating a significant asymmetrical change in the shape of the channel. It leads to a sublinear growth of the current with V_{DS}. Thirdly, we reach $V_{DS} = V_{sat}$. It is a voltage at which the width of the inversion layer at the Drain side is zero. At this point, called pinch-off point, the semiconductor is no more in inversion and the current reaches a saturation value. Finally, we have $V_{DS} > V_{sat}$ (saturation part). The pinch-off point begins to move towards the Source and leaves behind a region, which is no more in inversion. The effective channel length is thus reduced to the distance between the source and the pinch-off point. The current remains essentially constant to the saturation value.

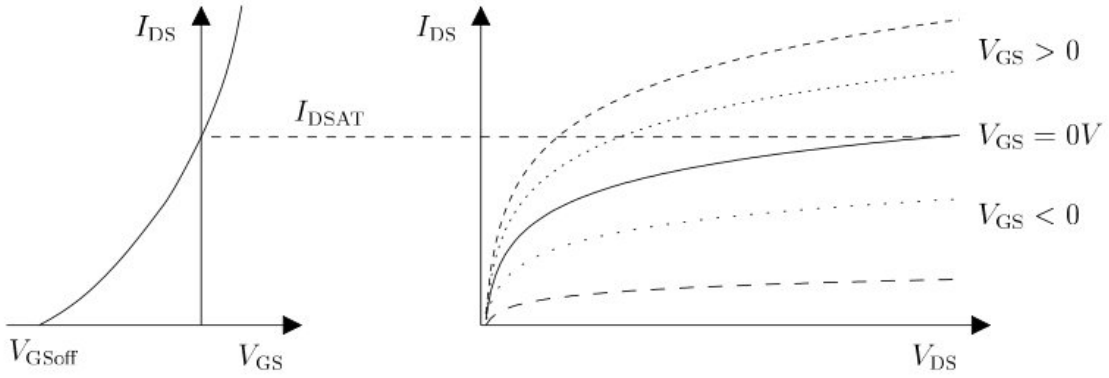

Figure 1.5: Current-voltage characteristics of a MOSFET (from [50]).

To finish this description of FETs, we precise that nowadays the continue miniaturization allows to produce FETs always more sophisticated and complex, with increasing electronic behavior. As we already mention in the introduction, Intel has developed a Tri-gate transistor which employs a single gate stacked on top of two vertical gates, allowing for essentially three times the surface area for electrons to travel. In Fig.1.6, we present other new architectures. In particular, there is a device with a Double-Gate (see i.e. [4, 54]) and another with a gate all-around (the gate material surrounds the channel region on all sides, see i.e. [48, 32]). These innovative FETs allow an increased gate control over the channel and perspectives of high-speed operation. When the channel length is reduced, the so-called short-channel effects become increasingly severe (drain-induced barrier lowering, surface scattering, impact ionization...). Moreover, high-energy electrons can enter into the oxide, where they can be trapped, giving rise to oxide charging that accumulates with time and affects the device performance. For short channel devices, the band structure becomes extremely sensitive. In particular, a non parabolicity and/or a strong band coupling are of importance. Of course, in view of physical accuracy, these atomistic effects have to be taken into account in the models used for numerical simulations.

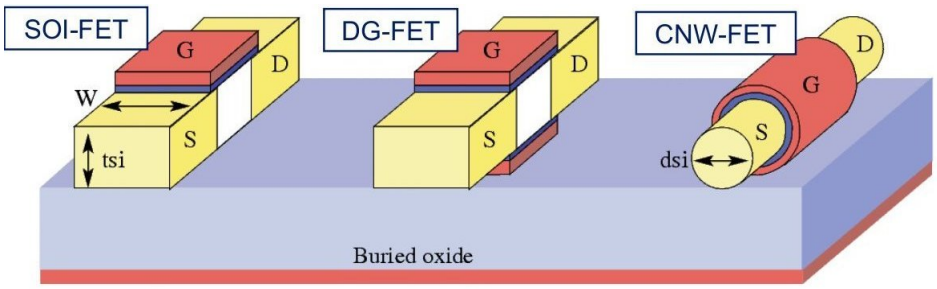

Figure 1.6: Examples of new FET architectures
(from Lecture "Numerical simulation of ballistic quantum transport in silicon nanowires accounting for full band effects" by G. Baccarani, E. Gnani, A. Gnudi, S. Reggiani and M. Rudan at *Multiscale Analysis for Quantum Systems and Applications*, Rome, October 2007).

1.4.2 Silicon nanowires

To complete this description of nanodevices, we say few words about silicon nanowires and carbon nanotubes. We consider these two structures as ultra-scaled confined nanostructures because of the extremely small dimensions of the transversal cross section. A nanowire can be defined as a structure that has a thickness constrained to tens of nanometers or less. At these scales, quantum mechanical effects are important, that why a nanowire is also called quantum wire.

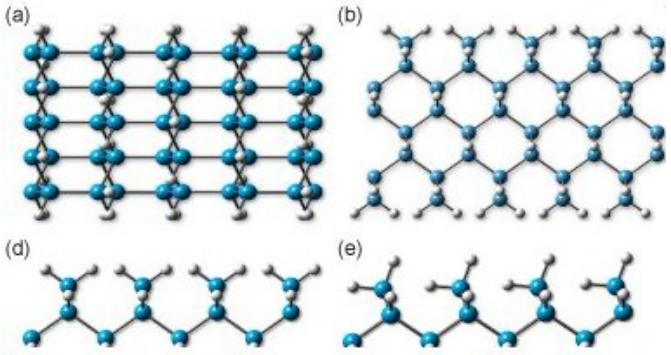

Figure 1.7: Illustration of different silicon nanowire structures
(from $https://www.llnl.gov/str/May07/Williamson.html$).

In Fig.1.7, we present some examples of silicon nanowires SiNWs. These structures, essentially because of their very small dimensions, exhibit unique or superior electronic, optical, mechanical, thermal and chemical properties. An example concerns the electrical properties of SiNWs. The confinement influences the resistivity. It causes an increase of the ionization energy. In particular for nanowires with diameters below 20 nm, the effect is significant and we need to take it into account.

SiNWs are actively investigated for technological applications to chemical, biological and environmental sensors, field-effect transistors, solar cells, lithium batteries, logic circuits... For example, concerning the solar cells, the key steps are the photon absorption and the charge collection. Silicon nanowire has a crystal structure which allows to improve these three steps and it is a promising candidate to convert photons to charges efficiently. It has been shown that a solar cell based on SiNWs can achieve efficient absorption of sunlight by using only one per cent of the active material required in a conventional solar cell. To finish, we mention that the SiNW Field-Effect Transistors are also investigated. These new materials are expected to create higher speed devices. But, at the moment, they still have a too high power consumption.

1.4.3 Carbon nanotubes

Carbon nanotubes CNTs are a layer of graphene made of carbon atoms with a cylindrical nanostructure (see Fig.1.8). Their name is derived from their size, since the diameter of a carbon nanotube is on the order of a few nanometers while they can be up to 10 cm in length. Like the nanowires, because of these dimensions, electrons propagate only along the longitudinal direction of the tube (we mention it as a one-dimensional transport). Moreover, the electron transport involves many quantum effects.

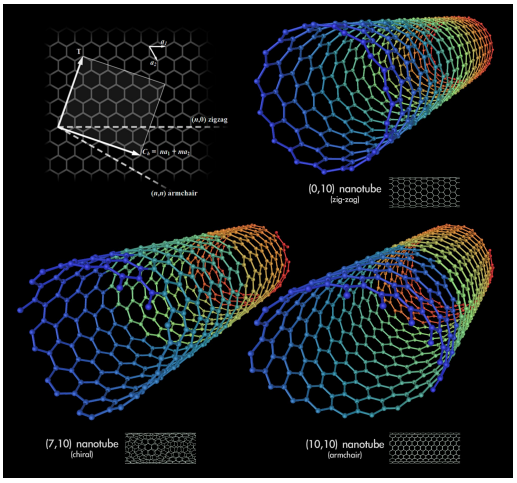

Figure 1.8: Illustration of different carbon nanotube structures
(from $http://ebdetu.fr/wordpress/2011/07/tag/nanotube\text{-}de\text{-}carbone/$).

These cylindrical carbon molecules have novel properties, making them potentially useful in many applications in nanotechnology, electronics, optics, and other fields of materials science. In particular, they exhibit extraordinary strength and unique electrical properties, and are efficient thermal conductors. We also mention that A. Geim and K. Novoselov obtained the 2010 Nobel prize in physics for “groundbreaking experiments regarding the two-dimensional material graphene”.

Here, we are only interested in electrical applications of carbon nanotubes. For example, a nanotube formed by joining two nanotubes of different diameters end to end can act as a diode, suggesting the possibility of constructing computer circuits entirely of nanotubes. However, nowadays, a major obstacle to the nanotubes is the lack of technology for a mass production. It is difficult to place them correctly and even if they can be precisely positioned, engineers are still not completely able to control the types (conducting, semiconducting...) of nanotubes that appear.

Semiconducting CNTs are also used to build carbon nanotube field-effect transistors CNTFETs. They are promising due to their superior electrical characteristics over usual MOSFETs. Long channel CNTFETs exhibit near-ballistic transport characteristics, resulting in ultra high speed devices. Recent works study the advantages of various forms of CNTFETs. And, it seems that tunneling CNTFETs offer better characteristics compared to other CNTFET structures, in particular for low power applications.

To conclude, we precise that the structure of a carbon nanotube strongly affects its electrical properties, because of the symmetry and the unique electronic structure of graphene. Moreover, curvature effects in small diameter carbon nanotubes can also strongly influence the electrical properties. It gives a large number of possible carbon nanotube devices and numerical simulations are certainly an interesting tool to complete the work of physicists.

1.5 A brief introduction to spintronics

To finish this introductive chapter, we make a short presentation of spintronics since the Part *III* of this PhD thesis is dedicated to a problem related to the spin of electrons. Spintronics is an emerging technology which exploits the spin of electrons and its associated magnetic moment, instead of its electronic charge (as it is the case in numerous electronic components). The underlying physics studies interactions between local moments and spin accumulation of conduction electrons. The spin of an electron represents a two-state quantum system. It means that for a chosen direction of measurement, the electron spin can be determined to be parallel (spin-up) or antiparallel (spin-down).

One of the first appearance of spintronics is "the discovery of the Giant MagnetoResistance" GMR independently by A. Fert and P. Grünberg (2007 Nobel prize in physics). It is a quantum mechanical magnetoresistance effect observed in thin structures composed alternatively of ferromagnetic and non magnetic layers. They observed a significant change in the electrical resistance depending on the fact that the magnetizations of adjacent ferromagnetic layers are in a parallel or an antiparallel alignment. For parallel alignment, the resistance is relatively low, instead for antiparallel alignment it is relatively high. The main application of the GRM is in the read heads of fast modern hard drives. A hard disk storing binary information can use the difference in resistance between parallel and antiparallel layer alignments as a method of storing 1 and 0. An extension of GRM is the tunneling magnetoresistance (TMR) where electrons travel to the

layers across a thin insulating tunnel barrier. To have an idea of performances, TMR allows to obtain disk drive densities exceeding 1 Terabyte per square inch.

Another important field of spintronics are the semiconductor-based spintronic devices. In particular, futures applications may include a spin-based transistor having advantages over MOSFET devices. The idea is that the Source gives a spin-polarized electron instead the Drain works as a spin detector. The gate voltage still controls the current but modifying the spin of electrons. Nevertheless, spin effects in semiconductors are still not well understood and one of the few application nowadays is a semiconductor laser using spin-polarized electrical injection.

In the Part *III* of this PhD thesis, we study a problem which is more related to the GMR effect than to the semiconductor spintronic devices. A recent discovery introduces the concept of switching the magnetization direction of a ferromagnetic in a multilayered structure driven by a current perpendicular to the layers. The central idea is of a spin torque transfer from a polarized current to the magnetization of the layer. This discovery was an important break through in spintronics and it is the subject of numerous researches with the intention of applications for magnetic memories, fast magnetic logic and also for microwave frequency devices in telecommunication. We will present a mathematical modelization and numerical simulations of this mechanism.

Bibliography

[1] M. G. Ancona and G. J. Iafrate. Quantum correction to the equation of state of an electron gas in a semiconductor. *Phys. Rev. B*, 39(13):9536–9540, 1989.

[2] A. M. Anile, N. Nikiforakis, V. Romano, and G. Russo. Discretization of semiconductor device problems. II. In *Handbook of numerical analysis. Vol. XIII*, Handb. Numer. Anal., XIII, pages 443–522. North-Holland, Amsterdam, 2005.

[3] N.W. Ashcroft and N.D. Mermin. *Solid State Physics*. Saunders College Publishing, 1976.

[4] G. Baccarani and S. Reggiani. A compact Double-Gate MOSFET model comprising quantum-mechanical and nonstatic effects. *IEEE Trans. Electron Devices*, 46(8):1656 –1666, 1999.

[5] L. Barletti and N. Ben Abdallah. Quantum Transport in Crystals: Effective Mass Theorem and K·P Hamiltonians. *Comm. Math. Phys.*, 307:567–607, 2011.

[6] N. Ben Abdallah. On a multidimensional Schrödinger-Poisson scattering model for semiconductors. *J. Math. Phys.*, 41(7):4241–4261, 2000.

[7] N. Ben Abdallah and P. Degond. On a hierarchy of macroscopic models for semiconductors. *J. Math. Phys.*, 37(7):3306–3333, 1996.

[8] N. Ben Abdallah, P. Degond, and S. Genieys. An energy-transport model for semiconductors derived from the Boltzmann equation. *J. Statist. Phys.*, 84(1-2):205–231, 1996.

[9] N. Ben Abdallah, P. Degond, and P. A. Markowich. On a one-dimensional Schrödinger-Poisson scattering model. *Z. Angew. Math. Phys.*, 48(1):135–155, 1997.

[10] N. Ben Abdallah, L. Desvillettes, and S. Génieys. On the convergence of the Boltzmann equation for semiconductors toward the energy transport model. *J. Statist. Phys.*, 98(3-4):835–870, 2000.

[11] N. Ben Abdallah and M. L. Tayeb. Diffusion approximation for the one dimensional Boltzmann-Poisson system. *Discrete Contin. Dyn. Syst. Ser. B*, 4(4):1129–1142, 2004.

[12] F. Bloch. Über die Quantenmechanik der Elektronen in Kristallgittern. *Zeitschrift für Physik A Hadrons and Nuclei*, 52:555–600, 1929.

[13] F. Bouchut, F. Golse, and M. Pulvirenti. *Kinetic equations and asymptotic theory*, volume 4 of *Series in Appl. Math. (Paris)*. Gauthier-Villars, 2000. Edited and with a foreword by B. Perthame and L. Desvillettes.

[14] J.-P. Bourgade. On spherical harmonics expansion type models for electron-phonon collisions. *Math. Methods Appl. Sci.*, 26(3):247–271, 2003.

[15] H. Brezis. *Analyse fonctionnelle.* Collection Mathématiques Appliquées pour la Maîtrise. [Collection of Applied Mathematics for the Master's Degree]. Masson, Paris, 1983.

[16] F. Brezzi, L. D. Marini, S. Micheletti, P. Pietra, R. Sacco, and S. Wang. Discretization of semiconductor device problems. I. In *Handbook of numerical analysis. Vol. XIII*, Handb. Numer. Anal., XIII, pages 317–441. North-Holland, Amsterdam, 2005.

[17] G. Cassano, C. de Falco, C. Giulianetti, and R. Sacco. Numerical simulation of tunneling effects in nanoscale semiconductor devices using quantum corrected drift-diffusion models. *Comput. Methods Appl. Mech. Engrg.*, 195(19-22):2193–2208, 2006.

[18] C. Cercignani. *The Boltzmann equation and its applications.* Springer-Verlag, Berlin, 1988.

[19] I. Choquet, P. Degond, and C. Schmeiser. Energy-transport models for charge carriers involving impact ionization in semiconductors. *Transport Theory Statist. Phys.*, 32(2):99–132, 2003.

[20] C. de Falco, E. Gatti, A. L. Lacaita, and R. Sacco. Quantum-corrected drift-diffusion models for transport in semiconductor devices. *J. Comput. Phys.*, 204(2):533–561, 2005.

[21] P. Degond. An infinite system of diffusion equations arising in transport theory: the coupled spherical harmonics expansion model. *Math. Models Methods Appl. Sci.*, 11(5):903–932, 2001.

[22] P. Degond, S. Gallego, and F. Méhats. An entropic quantum drift-diffusion model for electron transport in resonant tunneling diodes. *J. Comput. Phys.*, 221(1):226–249, 2007.

[23] P. Degond, S. Gallego, and F. Méhats. Isothermal quantum hydrodynamics: derivation, asymptotic analysis, and simulation. *Multiscale Model. Simul.*, 6(1):246–272, 2007.

[24] P. Degond, S. Gallego, and F. Méhats. On quantum hydrodynamic and quantum energy transport models. *Commun. Math. Sci.*, 5(4):887–908, 2007.

[25] P. Degond, C. D. Levermore, and C. Schmeiser. A note on the energy-transport limit of the semiconductor Boltzmann equation. In *Transport in transition regimes (Minneapolis, MN, 2000)*, volume 135 of *IMA Vol. Math. Appl.*, pages 137–153. Springer, New York, 2004.

[26] P. Degond, F. Méhats, and C. Ringhofer. Quantum energy-transport and drift-diffusion models. *J. Stat. Phys.*, 118(3-4):625–667, 2005.

[27] P. Degond, F. Méhats, and C. Ringhofer. Quantum hydrodynamic models derived from the entropy principle. In *Nonlinear partial differential equations and related analysis*, volume 371 of *Contemp. Math.*, pages 107–131. Amer. Math. Soc., 2005.

[28] P. Degond and C. Ringhofer. Quantum moment hydrodynamics and the entropy principle. *J. Statist. Phys.*, 112(3-4):587–628, 2003.

[29] D. K. Ferry and S. M. Goodnick. *Transport in nanostructures.* Cambridge Univ. Press, 1997.

[30] G. Floquet. Sur les équations différentielles linéaires à coefficients périodiques. *Ann. Sci. École Norm. Sup. (2)*, 12:47–88, 1883.

[31] H. Gajewski and K. Gröger. On the basic equations for carrier transport in semiconductors. *J. Math. Anal. Appl.*, 113(1):12–35, 1986.

[32] E. Gnani, S. Reggiani, A. Gnudi, P. Parruccini, R. Colle, M. Rudan, and G. Baccarani. Band-structure effects in ultrascaled silicon nanowires. *IEEE Trans. Electron Devices*, 54(9):2243 –2254, 2007.

[33] F. Golse and F. Poupaud. Limite fluide des équations de Boltzmann des semi-conducteurs pour une statistique de Fermi-Dirac. *Asymptotic Anal.*, 6(2):135–160, 1992.

[34] H.K. Gummel. A self-consistent iterative scheme for one-dimensional steady state transistor calculations. *IEEE Trans. Electron Devices*, 11(10):455 – 465, 1964.

[35] A. Jüngel. *Quasi-hydrodynamic semiconductor equations.* Progress in Nonlinear Differential Equations and their Applications, 41. Birkhäuser Verlag, Basel, 2001.

[36] A. Jüngel. *Transport equations for semiconductorsSemiconductor equations.* Lecture Notes in Physics No. 773. Springer, Berlin, 2009.

[37] A. Jüngel and D. Matthes. A derivation of the isothermal quantum hydrodynamic equations using entropy minimization. *Z. Angew. Math. Mech.*, 85(11):806–814, 2005.

[38] A. Jüngel, D. Matthes, and J. P. Milišić. Derivation of new quantum hydrodynamic equations using entropy minimization. *SIAM J. Appl. Math.*, 67(1):46–68, 2006.

[39] C. D. Levermore. Moment closure hierarchies for kinetic theories. *J. Statist. Phys.*, 83(5-6):1021–1065, 1996.

[40] J. M. Luttinger and W. Kohn. Motion of electrons and holes in perturbed periodic fields. *Phys. Rev.*, 97(4):869–883, 1955.

[41] P. A. Markowich. *The stationary semiconductor device equations.* Springer-Verlag, Vienna, 1986.

[42] P.A. Markowich, C.A. Ringhofer, and C. Schmeiser. *Semiconductor equations.* Springer-Verlag, Vienna, 1990.

[43] N. Masmoudi and M. L. Tayeb. Diffusion limit of a semiconductor Boltzmann-Poisson system. *SIAM J. Math. Anal.*, 38(6):1788–1807 (electronic), 2007.

[44] M. S. Mock. On equations describing steady-state carrier distributions in a semiconductor device. *Comm. Pure Appl. Math.*, 25:781–792, 1972.

[45] C. Negulescu. *Asymptotical models and numerical schemes for quantum systems.* PhD thesis, Université Paul Sabatier Toulouse 3, 2005.

[46] F. Nier. Schrödinger-Poisson systems in dimension $d \leq 3$: the whole-space case. *Proc. Roy. Soc. Edinburgh Sect. A*, 123(6):1179–1201, 1993.

[47] F. Nier. A variational formulation of Schrödinger-Poisson systems in dimension $d \leq 3$. *Comm. Partial Differential Equations*, 18(7-8):1125–1147, 1993.

[48] A. Pecchia, L. Salamandra, L. Latessa, B. Aradi, T. Frauenheim, and A. Di Carlo. Atomistic modeling of gate-all-around si-nanowire field-effect transistors. *IEEE Trans. Electron Devices*, 54(12):3159 –3167, 2007.

[49] S. J. Polak, C. Den Heijer, W. H. A. Schilders, and P. Markowich. Semiconductor device modelling from the numerical point of view. *Int. J. Numer. Meth. Engrg.*, 24(4):763–838, 1987.

[50] E. Polizzi. *Modélisation et simulations numériques du transport quantique ballistique dans les nanostructures semi-conductrices.* PhD thesis, Institut National des Sciences Appliquées de Toulouse, 2001.

[51] F. Poupaud. Diffusion approximation of the linear semiconductor Boltzmann equation: analysis of boundary layers. *Asymptotic Anal.*, 4(4):293–317, 1991.

[52] D.L. Scharfetter and H.K. Gummel. Large-signal analysis of a silicon Read diode oscillator. *IEEE Trans. Electron Devices*, 16(1):64 – 77, 1969.

[53] K Seeger. *Semiconductor physics. An introduction.* Springer-Verlag, Berlin, 2004.

[54] K. Suzuki, T. Tanaka, Y. Tosaka, H. Horie, and Y. Arimoto. Scaling theory for Double-Gate SOI MOSFET's. *IEEE Trans. Electron Devices*, 40(12):2326 –2329, 1993.

[55] S. M. Sze. *Physics of semiconductor devices.* John Wiley & Sons, 1981.

[56] C. Villani. A review of mathematical topics in collisional kinetic theory. In *Handbook of mathematical fluid dynamics, Vol. I*, pages 71–305. North-Holland, Amsterdam, 2002.

[57] B. Vinter and C. Weisbuch. *Quantum Semiconductor Structures.* Academic Press, 1991.

[58] T. Wenckebach. *Essential of Semiconductor Physics.* Wiley, Chichester, 1999.

Part *I*

A quantum effective mass model for ultra-scaled confined nanostructures

Chapter 2

Model derivation

Nota bene : This chapter as well as the following one resumes and extends a joint work with N. Ben Abdallah and P. Pietra submitted to M^3AS (see also the preprint [5]).

In this chapter, we present the derivation of an effective mass model, describing the quantum motion of electrons in an ultra-scaled confined nanostructure. Due to the strong confinement, the crystal lattice is considered periodic only in the one dimensional transport direction and an atomistic description of the entire cross–section is given. Using an envelope function decomposition, an effective mass approximation is obtained. It consists of a sequence of one dimensional device dependent Schrödinger equations, one for each energy band, in which quantities retaining the effects of the confinement and of the transversal crystal structure are inserted. Both the non–degenerate case and the degenerate case (for the energy bands) are discussed. In view of self–consistent computations, we are also interested in the formal derivation of the charge density.

2.1 Introduction

The extreme miniaturization reached by the electronic devices brings the necessity of using new models to describe the electron transport and to design the device architecture. To a reduced channel length it corresponds also a strong reduced lateral dimension, which induces quantization effects that cannot be captured by classical models. Ultra–scaled strongly confined structures (like nanowires [6, 8] and nanotubes [13, 2]) are becoming promising component in the future nanoelectronics. The numerical modeling of such devices is very important in order to predict their behavior, to access their performance limits and to design new configurations. When the

cross–section diameter is below 3 nm, the strong confinement affects the energy band structure and bulk material properties cannot be used in the simulations (see [9], e.g., and references therein). Atomistic *ab-initio* computations give accurate description of the transport in these innovative devices (see [14], e.g.), but they are computationally too demanding, and cannot be used in a device design framework. The aim of this chapter is to present a new model, that allows for computationally efficient simulations, for describing the transport in ultra–scaled confined devices. The model amounts to a set of one dimensional effective mass Schrödinger equations in the longitudinal direction, one for each energy band, coupled with a 3D Poisson equation for the self–consistent electrostatic potential. The novelty of the chapter lies in the derivation of a new effective mass approximation for nanowires/nanotubes (both in the non–degenerate case and in the degenerate case), and in definition of the 3D electron density needed for self-consistent computations.

Effective mass approximation is a well known approximation in solid state physics (see [3, 18], e.g.) and it received recent attention in the mathematical literature. We recall results for 3D periodic crystals obtained by means of Wigner function techniques [15], two-scale homogenization arguments [1] or envelope function decompositions [4]. We also mention [16], where effective mass results are given for nonlinear Schrödinger equations related to Bose–Einstein condensates on optical lattices, and [7], where the effective mass approximation is performed for a Schrödinger equation singularly perturbed by a confinement potential and a strong magnetic field. For the strongly confined devices considered here, the assumption of infinite periodic structure, which allows to derive the commonly used effective mass approximation, is not valid anymore, and a new setting is required. Indeed, in the case of nanowires or nanotubes, the potential generated by the crystal structure, that fast oscillates in the scale defined by the crystal spacing, can be considered periodic only in the longitudinal direction, since the cross–section comprises only few ions. Therefore, thanks to lateral dimensions comparable to the lattice spacing, the longitudinal effective mass equations are found averaging out not only the lattice potential, but also the lateral dimension.

In this chapter, the formal derivation of the new effective mass model is given for a wire of infinite extension in the longitudinal direction, where the electrons are subject to a lattice potential and to a slowly varying external potential. The key tool to find the asymptotic model is the use of an envelope function decomposition. The approach follows the work of [4], where the effective mass approximation in the case of 3D periodic potentials is obtained using, as orthonormal basis for the decomposition, generalized Bloch waves in the form introduced by [12]. In the case of nanowire/nanotubes, the generalized Bloch waves, that are constructed taking into account the confinement, are "localized" in the transverse direction (see Section 2.3), so that the Brillouin zone in one dimensional, and one dimensional transport problems are obtained when letting the lattice spacing to zero.

As an intermediate step of the asymptotics, the so–called $k \cdot p$ model is derived. Then, perturbation theory allows to diagonalize the $k \cdot p$ Hamiltonian, and filtering the fast oscillations in time gives the final system. In the non–degenerate case (the eigenvalue of the Bloch problem

are all simple), each envelope function has a fast oscillating scale in time related to the corresponding eigenvalue of the Bloch problem, so that adiabatic decoupling occurs, as it is common for fast oscillating system (see [17], e.g., and references therein). An infinite set of decoupled one dimensional effective mass Schrödinger equations, one for each energy band, is obtained (see Proposition 2.4.1). In the degenerate case, the final system is not decoupled anymore. To each multiple eigenvalue corresponds a system of coupled Schrödinger equations with dimension equal to the multiplicity of the eigenvalue. The kinetic part of the limiting effective mass Hamiltonian is diagonal and the coupling occurs through the potential (see Proposition 2.4.2).

The chapter is organized as follows. In Section 2.2, we present the Schrödinger equation which is used as starting point of our work and we write it in a scaled form. Next, in Section 2.3 the envelope function decomposition for confined structure is obtained. Finally, Section 2.4 is devoted to the asymptotic process. The formal derivation of the effective mass model is obtained in the non-degenerate case, as well as in the degenerate case.

2.2 Schrödinger equation and homogenization scaling

In this chapter, we consider a confined nanostructure with infinite longitudinal extension. The structure is characterized by a finite cross–section composed of few ions, so that the lateral dimension is comparable to the typical spacing between lattice sites. The electrons in this nanostructure are subjected to an external potential V and to a bounded potential $W_{\mathcal{L}}$ generated by the crystal lattice, fast oscillating in the scale defined by the crystal spacing. Since the cross-section comprises few ions, $W_{\mathcal{L}}$ is considered periodic only in the longitudinal x-direction. Thus, denoting by γ the lattice spacing and by ω_γ the cross-section, we consider the following Schrödinger equation

$$\begin{aligned} \imath\hbar\partial_t\psi(t,x,z) &= -\frac{1}{2}\frac{\hbar^2}{m_e}\Delta\psi(t,x,z) + W_{\mathcal{L}}(x,z)\psi(t,x,z) + V(x,z)\psi(t,x,z) \quad (x,z)\in\mathbb{R}\times\omega_\gamma, \\ \psi(t,x,z) &= 0 \text{ for } z\in\partial\omega_\gamma. \end{aligned} \tag{2.2.1}$$

We remind that $\hbar$ is the reduced Plank constant ($\hbar = h/2\pi = 1.054\times10^{-34}$ J.s) and m_e is the electron mass ($m_e = 9.109\times10^{-31}$ kg). $W_{\mathcal{L}}(x,z)$ is periodic in the x-direction such that $W_{\mathcal{L}}(x) = W_{\mathcal{L}}(x+\gamma)$, whereas V is considered slowly varying in x. Hence, there are essentially two level of scales in this problem.

First, we have the microscopic length and time scales, denoted respectively λ and τ. It is reasonable to choose λ equal to the lattice spacing γ. So, the lattice potential $W_{\mathcal{L}}$ can be written in the following dimensionless form

$$W_{\mathcal{L}}(x,z) = \frac{m_e\lambda^2}{\tau^2}W'_{\mathcal{L}}\Big(\frac{x}{\lambda},\frac{z}{\lambda}\Big). \tag{2.2.2}$$

It means that a free particle of mass m_e under the influence of $W_{\mathcal{L}}$ will travel a distance λ in a time τ. Moreover, the microscopic time and space scales are linked by the relation

$$\tau = \frac{m_e\lambda^2}{\hbar}. \tag{2.2.3}$$

Secondly, we have the couple of macroscopic scales, L and T. Then, the potential V is rescaled in the following form

$$V(x,z) = \frac{m_e L^2}{T^2} V'\Big(\frac{x}{L}, \frac{z}{\lambda}\Big). \tag{2.2.4}$$

Peculiarly, because the cross section contains only few atoms, the variable z has to be considered in the microscopic scale.

We define two small dimensionless parameters ϵ and δ, being respectively the length and time ratios

$$\epsilon = \frac{\lambda}{L} << 1 \quad \text{and} \quad \delta = \frac{\tau}{T} << 1. \tag{2.2.5}$$

We perform the following change of variables

$$x' = \frac{x}{L}, \quad z' = \frac{z}{\lambda} \quad \text{and} \quad t' = \frac{t}{T}.$$

In the sequel, we omit primes for simplicity, except for the variable z' in order to emphasize that the diameter of ω_γ is comparable to γ and thus that the variable z acts on the microscopic scale, being rescaled as $z' = z/\gamma$. Moreover, ω denotes the scaled cross–section. Consequently, we rescaled the Schrödinger equation (2.2.1) in the following dimensionless form

$$\begin{aligned} \imath\frac{\hbar}{T}\partial_t\psi(t,x,z') &= -\frac{1}{2}\frac{\hbar^2}{L^2 m_e}\partial_{xx}\psi(t,x,z') - \frac{1}{2}\frac{\hbar^2}{\lambda^2 m_e}\Delta_{z'}\psi(t,x,z') \\ &+ \frac{m_e\lambda^2}{\tau^2}W_{\mathcal{L}}\Big(\frac{x}{\epsilon}, z'\Big)\psi(t,x,z') + \frac{m_e L^2}{T^2}V(x,z')\psi(t,x,z') \qquad (x,z') \in \mathbb{R}\times\omega. \end{aligned}$$

We multiply it by $\frac{T^2}{m_e L^2}$ and we obtain

$$\begin{aligned} \imath h\partial_t\psi(t,x,z') &= -\frac{h^2}{2}\partial_{xx}\psi(t,x,z') - \frac{h^2}{2\epsilon^2}\Delta_{z'}\psi(t,x,z') \\ &+ \frac{\epsilon^2}{\delta^2}W_{\mathcal{L}}\Big(\frac{x}{\epsilon}, z'\Big)\psi(t,x,z') + V(x,z')\psi(t,x,z') \qquad (x,z') \in \mathbb{R}\times\omega, \end{aligned}$$

where we introduced the additional dimensionless parameter, that can be interpreted as the Planck constant in macroscopic variables

$$h = \frac{\hbar T}{m_e L^2}. \tag{2.2.6}$$

Here, our focus is not on the semiclassical regime though. So, we work for a fixed h that we choose equal to 1. It means that, in the same way than the microscopic time and space scales, the macroscopic scales are linked by the relation

$$T = \frac{m_e L^2}{\hbar}. \tag{2.2.7}$$

With the relations (2.2.3) and (2.2.7), the two small parameters are related such that $\delta = \epsilon^2$. And consequently, we obtain the dimensionless Schrödinger equation that will be the starting

point for finding our effective mass asymptotic model

$$\begin{aligned} \imath\partial_t\psi(t,x,z') &= -\frac{1}{2}\partial_{xx}\psi(t,x,z') - \frac{1}{2\epsilon^2}\Delta_{z'}\psi(t,x,z') \\ &+ \frac{1}{\epsilon^2}W_{\mathcal{L}}\Big(\frac{x}{\epsilon},z'\Big)\psi(t,x,z') + V(x,z')\psi(t,x,z') \qquad (x,z')\in\mathbb{R}\times\omega, \quad (2.2.8) \\ \psi(t,x,z') &= 0 \text{ for } z'\in\partial\omega. \end{aligned}$$

In the following, we consider that the macroscopic length L is 1. So, ϵ corresponds directly to the space lattice λ and above all the potential $W_{\mathcal{L}}$ is 1-periodic in the x-direction.

Remark 2.2.1. In the physical literature, the most commonly used units are the so called atomic units (a.u.). The fundamental atomic units are the following :

- Length : 1 a.u = a_0 meters, where a_0 is the Bohr radius ($a_0 = 5.292\times10^{-11}m$),
- Energy : 1 a.u = E_h Joules = $\frac{\hbar^2}{a_0^2 m_e}$ Joules, where E_h is the Hartree energy,
- Time : 1 a.u = $\frac{\hbar}{E_h}$ seconds = $\frac{a_0^2 m_e}{\hbar}$ seconds.

Consequently, we perform the following change of variables

$$\widetilde{x} = \frac{x}{a_0}, \quad \widetilde{z} = \frac{z}{a_0}, \quad \widetilde{t} = \frac{\hbar}{a_0^2 m_e}t,$$

$$\widetilde{W}(\widetilde{x},\widetilde{z}) = \frac{a_0^2 m_e}{\hbar^2}W_{\mathcal{L}}(x,z) \quad \text{and} \quad \widetilde{V}(\widetilde{x},\widetilde{z}) = \frac{a_0^2 m_e}{\hbar^2}V(x,z).$$

We omit the tildes and we obtain the following atomic unit Schrödinger equation

$$\begin{aligned} \imath\partial_t\psi(t,x,z) &= -\frac{1}{2}\Delta\psi(t,x,z) + W_{\mathcal{L}}(x,z)\psi(t,x,z) + V(x,z)\psi(t,x,z) \qquad (x,z)\in\mathbb{R}\times\omega_{\gamma/a_0}, \\ \psi(t,x,z) &= 0 \text{ for } z\in\partial\omega_{\gamma/a_0}. \end{aligned} \quad (2.2.9)$$

We finally establish the link between the two scalings concerning the periodic potential $W_{\mathcal{L}}$. We have

$$\frac{\hbar}{a_0^2 m_e}\widetilde{W}_{\mathcal{L}}(\frac{x}{a_0},\frac{z}{a_0}) = \frac{m_e\lambda^2}{\tau^2}W'_{\mathcal{L}}(\frac{x}{\lambda},\frac{z}{\lambda}) = \frac{\hbar}{m_e\lambda^2}W'_{\mathcal{L}}(\frac{x}{\lambda},\frac{z}{\lambda}),$$

using (2.2.3) for the last equality. This expression can be written again

$$W'_{\mathcal{L}}(X,Z) = \frac{\lambda^2}{a_0^2}\widetilde{W}_{\mathcal{L}}(\frac{\lambda}{a_0}X,\frac{\lambda}{a_0}Z). \quad (2.2.10)$$

Consequently, for the numerical simulations (in Chapter 3), the lattice potential, found in the physical literature expressed in a.u., has to be transformed following (2.2.10) to be inserted in our formalism.

2.3 Envelope function decomposition

2.3.1 Bloch problem

The key tool to find the asymptotic model is the use of an envelope function decomposition, which allows to separate the fast and the slow variables. The orthonormal basis for the decomposition is made of generalized Bloch functions, eigenfunctions of the following problem in the unit cell $\mathcal{U} = (-1/2, 1/2) \times \omega$.

$$\begin{cases} -\frac{1}{2}\Delta\chi_n + W_{\mathcal{L}}\chi_n = E_n\chi_n. \\ \chi_n(y, z') = 0 \quad \text{on } \partial\omega, \quad \chi_n \text{ 1-periodic in } y. \\ \int_{\mathcal{U}} |\chi_n|^2 dy dz' = 1. \end{cases} \tag{2.3.1}$$

Physically relevant potential $W_{\mathcal{L}}$ are real-valued and bounded. Therefore, the eigenfunctions χ_n are real-valued and form a complete orthonormal basis of $L^2(\mathcal{U})$. The sequence of the eigenvalues $E_n \in \mathbb{R}$ is not decreasing with $E_n \to +\infty$. Because of the periodic conditions, they are not necessarily distinct.

Remark 2.3.1. The peculiarity of the strongly confined structure is reflected in the choice of the Bloch problem. We point out that the unit cell $\mathcal{U}$ comprises the entire cross–section of the wire. Therefore, the Bloch functions depend on the device under consideration, for instance on the device geometry and on the growing orientation of the wire. Moreover, the homogeneous Dirichlet condition imposes confinement in the transverse directions, while periodicity is considered only in the transport direction. Consequently, the eigenvectors are 3D quantities but the associated energy bands are one dimensional. The energy bands are the eigenvalues $E_n(k)$ of the fibered Hamiltonian, depending on the (here one dimensional) wave vector k

$$H_{\mathcal{L}}(k) = \frac{1}{2}k^2 - \imath k\partial_x - \frac{1}{2}\Delta + W_{\mathcal{L}}, \tag{2.3.2}$$

considered with the same boundary condition as in (2.3.1). The associated eigenvectors are denoted by $\chi_{n,k}(y, z')$. Notice that the operator in problem (2.3.1) coincides with $H_{\mathcal{L}}(0)$, and that $\chi_n = \chi_{n,0}$ and $E_n = E_n(0)$. In particular, E_n is the energy of the n^{th} band at $k = 0$. We refer to Section 1.2.3 for the link with the Bloch problem for 3D crystals.

Definition 2.3.1. *For each pair of Bloch functions, we define averaged quantities on the periodic direction as the functions*

$$g_{nn'}(z') = \int_{-1/2}^{1/2} \chi_n(y, z')\chi_{n'}(y, z')dy. \tag{2.3.3}$$

These quantities will be used throughout this Part to reconstruct 3D functions from 1D wave functions (subject to the transport), and to project a 3D potential to the 1D transport direction.

Notation We shall use the symbol $\widehat{\cdot}$ for the Fourier transform in $L^2(\mathbb{R})$ and, with an abuse of notation, we shall keep the same notation for the Fourier transform in the variable x of a function $\psi(x,z') \in L^2(\mathbb{R}\times\omega)$

$$\widehat{\psi}(k,z') = \frac{1}{\sqrt{2\pi}}\int_{\mathbb{R}} \psi(x,z')e^{-\imath kx}dx. \tag{2.3.4}$$

Moreover, the scalar product in $L^2(\mathcal{U})$ will be denoted by $< f,g >= \int_{\mathcal{U}} f(y,z')\overline{g(y,z')}dydz'$. We also use the notation $\mathbb{1}_{\mathcal{A}}$ to denote the indicator function of the set $\mathcal{A}$.

2.3.2 Envelope functions

The following Theorem is an extension to the nanowire case of the result given in [4] for 3D periodic crystals, considering the variable $z' \in \omega$ as a parameter.

Theorem 2.3.1. *Let $\{\chi_n(x,z')\}$ be the set of orthonormal eigenfunctions given by (2.3.1). For every function $\psi \in L^2(\mathbb{R}\times\omega)$ there exists a unique sequence $\{f_n(x)|n\in\mathbb{N}\}$, with $f_n \in L^2(\mathbb{R})$ and $supp\widehat{f_n} \subset (-\pi,\pi)$, such that*

$$\psi(x,z') = \sum_{n\in\mathbb{N}} f_n(x)\chi_n(x,z')\ . \tag{2.3.5}$$

Moreover, the Parseval identity holds

$$\left\|\psi(x,z')\right\|^2_{L^2(\mathbb{R}\times\omega)} = \sum_{n\in\mathbb{N}} \|f_n(x)\|^2_{L^2(\mathbb{R})}\,. \tag{2.3.6}$$

Finally, the Fourier transform of f_n is given by

$$\widehat{f_n}(k) = \int_{\mathbb{R}\times\omega} \overline{u_{n,k}(x,z')}\psi(x,z')dxdz', \tag{2.3.7}$$

where, for $x\in\mathbb{R}, z'\in\omega, k\in\mathbb{R}, n\in\mathbb{N}$,

$$u_{n,k}(x,z') = \frac{1}{\sqrt{2\pi}}\mathbb{1}_{(-\pi,\pi)}(k)e^{\imath kx}\chi_n(x,z'). \tag{2.3.8}$$

Proof. • *Fourier basis decomposition in the transport direction :* Let us first consider a regular function $\psi \in \mathcal{S}(\mathbb{R}_x; L^2(\omega))$. We can write

$$\begin{aligned}\psi(x,z') &= \frac{1}{\sqrt{2\pi}}\int_{\mathbb{R}_k}\widehat{\psi}(k,z')e^{\imath kx}dk = \frac{1}{\sqrt{2\pi}}\sum_{l\in\mathbb{Z}}\int_{-\pi+2\pi l}^{\pi+2\pi l}\widehat{\psi}(k,z')e^{\imath kx}dk\\ &= \frac{1}{\sqrt{2\pi}}\sum_{l\in\mathbb{Z}} e^{\imath 2\pi lx}\int_{-\pi}^{\pi}\widehat{\psi}(\xi+2\pi l,z')e^{\imath\xi x}d\xi.\end{aligned}$$

Consequently, we obtain the following decomposition

$$\psi(x,z') = \sum_{l\in\mathbb{Z}}\mathcal{G}_l(x,z')e^{\imath 2\pi lx}, \tag{2.3.9}$$

where $\mathcal{G}_l$ is defined as

$$\mathcal{G}_l(x,z') = \frac{1}{\sqrt{2\pi}} \int_{-\pi}^{\pi} \widehat{\psi}(\xi + 2\pi l, z') e^{\imath \xi x} d\xi. \tag{2.3.10}$$

Clearly the Fourier transform (in the first variable) of $\mathcal{G}_l$ has support in $(-\pi, \pi)$. Uniqueness of the decomposition can be easily checked, assuming that (2.3.9) holds for some $\widetilde{\mathcal{G}}_l$ with *supp* $\widehat{\widetilde{\mathcal{G}}}_l(\xi, .) \subset (-\pi, \pi)$. In this case, we get

$$\begin{aligned} \widehat{\psi}(k,z') &= \frac{1}{\sqrt{2\pi}} \int_{\mathbb{R}_x} \psi(x,z') e^{-\imath k x} dx = \frac{1}{\sqrt{2\pi}} \int_{\mathbb{R}_x} \sum_{l\in\mathbb{Z}} \widetilde{\mathcal{G}}_l(x,z') e^{-\imath(k-2\pi l)x} dx \\ &= \sum_{l\in\mathbb{Z}} \widehat{\widetilde{\mathcal{G}}}_l(k-2\pi l, z') = \mathbb{1}_{(-\pi+2\pi l, \pi+2\pi l)}(k) \widehat{\widetilde{\mathcal{G}}}_l(k-2\pi l, z'), \end{aligned}$$

which implies

$$\widehat{\widetilde{\mathcal{G}}}_l(\xi, z') = \mathbb{1}_{(-\pi,\pi)}(\xi) \widehat{\psi}(\xi + 2\pi l, z'), \quad \forall l \in \mathbb{Z}. \tag{2.3.11}$$

Finally, for a fixed z',

$$\begin{aligned} \sum_{l\in\mathbb{Z}} \left\| \mathcal{G}_l(x,z') \right\|^2_{L^2(\mathbb{R}_x)} &= \sum_{l\in\mathbb{Z}} \left\| \widehat{\mathcal{G}}_l(\xi,z') \right\|^2_{L^2(\mathbb{R}_\xi)} \\ &= \sum_{l\in\mathbb{Z}} \int_{\mathbb{R}_\xi} |\widehat{\psi}(\xi + 2\pi l, z') \mathbb{1}_{(-\pi,\pi)}(\xi)|^2 d\xi \\ &= \sum_{l\in\mathbb{Z}} \int_{-\pi+2\pi l}^{\pi+2\pi l} |\widehat{\psi}(k,z')|^2 dk \\ &= \left\| \widehat{\psi}(k,z') \right\|^2_{L^2(\mathbb{R}_k)} = \left\| \psi(x,z') \right\|^2_{L^2(\mathbb{R}_x)}. \end{aligned} \tag{2.3.12}$$

Hence, we obtain

$$\sum_{l\in\mathbb{Z}} \left\| \mathcal{G}_l(x,z') \right\|^2_{L^2(\mathbb{R}_x \times \omega)} = \left\| \psi(x,z') \right\|^2_{L^2(\mathbb{R}_x \times \omega)}. \tag{2.3.13}$$

• *Bloch function decomposition :* For $x \in \mathbb{R}$, $y \in (-1/2, 1/2)$, $z' \in \omega$, let us define

$$F(x,y,z') = \sum_{l\in\mathbb{Z}} \mathcal{G}_l(x,z') e^{\imath 2\pi l y}. \tag{2.3.14}$$

On the one hand, since the sequence $\{e^{\imath 2\pi l y} | l \in \mathbb{Z}\}$ forms an orthonormal basis of $L^2(-1/2, 1/2)$, we have

$$\int_{-1/2}^{1/2} |F(x,y,z')|^2 dy = \sum_{l\in\mathbb{Z}} |\mathcal{G}_l(x,z')|^2,$$

and consequently

$$\left\| F(x,y,z') \right\|^2_{L^2(\mathbb{R}_x \times \mathcal{U})} = \sum_{l\in\mathbb{Z}} \left\| \mathcal{G}_l(x,z') \right\|^2_{L^2(\mathbb{R}_x \times \omega)}. \tag{2.3.15}$$

On the other hand, for fixed x, $F(x,y,z')$ is a 1-periodic function in y, so it can be expanded in terms of $\{\chi_n(y,z')\}$. We get

$$F(x,y,z') = \sum_{n\in\mathbb{N}} f_n(x) \chi_n(y,z'), \tag{2.3.16}$$

where $f_n(x)$ is the Fourier coefficient with respect to $\chi_n(y,z')$, defined by

$$f_n(x) =< F(x,y,z'), \chi_n(y,z') >, \tag{2.3.17}$$

and the Parseval identity holds :

$$\left\|F(x,y,z')\right\|^2_{L^2(\mathcal{U})} = \sum_{n\in\mathbb{N}} |f_n(x)|^2.$$

Integration over $\mathbb{R}_x$ gives

$$\left\|F(x,y,z')\right\|^2_{L^2(\mathbb{R}_x\times\mathcal{U})} = \sum_{n\in\mathbb{N}} \|f_n(x)\|^2_{L^2(\mathbb{R}_x)}\,. \tag{2.3.18}$$

For $y = x$, due to (2.3.9), (2.3.14) reads $\psi(x,z') = F(x,x,z')$. Therefore, (2.3.16) gives the decomposition (2.3.5), and (2.3.18) gives the isometry property (2.3.6). In order to extend the theorem to functions of $L^2(\mathbb{R}_x \times \omega)$ we check the uniqueness.

• *Uniqueness of* $\{f_n | n \in \mathbb{N}\}$ *:* We assume that (2.3.16) holds for some sequence $\{\widetilde{f}_n | n \in \mathbb{N}\}$. For fixed z', we expand $\chi_n(y,z')$ in terms of the Fourier basis of $L^2(-1/2,1/2)$, denoting by

$$c_{n,l}(z') = \int_{-1/2}^{1/2} \chi_n(y,z') e^{-\imath 2\pi l y} dy \tag{2.3.19}$$

the Fourier coefficients of χ_n. We obtain

$$F(x,y,z') = \sum_{l\in\mathbb{Z}} \widetilde{\mathcal{G}}_l(x,z') e^{\imath 2\pi l y},$$

with

$$\widetilde{\mathcal{G}}_l(x,z') = \sum_{n\in\mathbb{N}} \widetilde{f}_n(x) c_{n,l}(z'). \tag{2.3.20}$$

Using the quantities $g_{nn'}$'s defined in (2.3.3), we have

$$\sum_{l\in\mathbb{Z}} \widetilde{\mathcal{G}}_l(x,z')\overline{c_{n',l}(z')} = \sum_{l\in\mathbb{Z}}\sum_{n\in\mathbb{N}} \widetilde{f}_n(x) c_{n,l}(z')\overline{c_{n',l}(z')} = \sum_{n\in\mathbb{N}} \widetilde{f}_n(x) g_{nn'}(z').$$

Finally, integrating over ω and exploiting the orthonormality of the χ_n's on $\mathcal{U}$, we have

$$\widetilde{f}_n(x) = \sum_{l\in\mathbb{Z}} \int_\omega \widetilde{\mathcal{G}}_l(x,z')\overline{c_{n,l}(z')} dz'. \tag{2.3.21}$$

Because of the uniqueness of decomposition (2.3.9) (and in turns of (2.3.14)) $\widetilde{\mathcal{G}}_l = \mathcal{G}_l$ and thus (2.3.21) coincides with (2.3.17).

• *Fourier transform :* The Fourier transform $\widehat{f}_n$ can be easily computed, using the fact that the sequence $\{e^{-\imath 2\pi l y} | l \in \mathbb{Z}\}$ forms an orthonormal basis of $L^2(-1/2,1/2)$. Indeed, from definition (2.3.17), with (2.3.14), we write

$$f_n(x) = \sum_{l\in\mathbb{Z}} \int_\omega \mathcal{G}_l(x,z')\overline{c_{n,l}(z')} dz', \tag{2.3.22}$$

where the notation (2.3.19) for the Fourier coefficients of χ_n is used. Therefore, taking into account (2.3.11), we have

$$\begin{aligned}\widehat{f_n}(k) &= \sum_{l\in\mathbb{Z}} \int_\omega \mathbb{1}_{(-\pi,\pi)}(k)\widehat{\psi}(k+2\pi l, z')\overline{c_{n,l}(z')}dz' \\ &= \frac{1}{\sqrt{2\pi}}\sum_{l\in\mathbb{Z}} \int_\omega \mathbb{1}_{(-\pi,\pi)}(k)\Big(\int_{\mathbb{R}_x} \psi(x,z')e^{-\imath(k+2\pi l)x}dx\Big)\overline{c_{n,l}(z')}dz'.\end{aligned}$$

Noticing that $\chi_n(x,z') = \sum_{l\in\mathbb{Z}} \overline{c_{n,l}(z')}e^{-\imath 2\pi l x}$, we finally obtain

$$\widehat{f_n}(k) = \frac{1}{\sqrt{2\pi}}\mathbb{1}_{(-\pi,\pi)}(k)\int_{\mathbb{R}_x\times\omega} \psi(x,z')e^{-\imath kx}\chi_n(x,z')dxdz'.$$

□

Definition 2.3.2. *The functions f_n of Theorem 2.3.1 will be called the envelope functions of ψ with respect to the basis $\{\chi_n | n\in\mathbb{N}\}$.*

It is immediate to write expressions (2.3.5) and (2.3.6) of Theorem 2.3.1 in terms of the Fourier transform $\widehat{f_n}$. It gives the following Corollary.

Corollary 2.3.2. *Let $\{f_n | n\in\mathbb{N}\}$ be the envelope functions of $\psi\in L^2(\mathbb{R}\times\omega)$ with respect to the basis $\{\chi_n | n\in\mathbb{N}\}$. Then*

$$\psi(x,z') = \sum_{n\in\mathbb{N}} \frac{1}{\sqrt{2\pi}}\int_{-\pi}^{\pi} \widehat{f_n}(k)e^{\imath kx}\chi_n(x,z')dk\ . \tag{2.3.23}$$

And, the following identity holds

$$\big\|\psi(x,z')\big\|^2_{L^2(\mathbb{R}\times\omega)} = \sum_{n\in\mathbb{N}} \Big\|\widehat{f_n}(k)\Big\|^2_{L^2(-\pi,\pi)}. \tag{2.3.24}$$

Remark 2.3.2. The functions (2.3.8) are generalized Bloch waves, in the form introduced by Kohn and Luttinger [12] (used in [4] for obtaining in a rigorous way the effective mass for 3D periodic crystals). As we shall see in the next section, they do not allow to completely diagonalize the periodic part of the Hamiltonian. However, since the wave vector k only appears in the plane wave and not in the periodic part χ_n, they have the advantage of completely separating the oscillating part of the wave function from its slowly varying one. In nanowires/nanotubes, confinement plays an important role and it is reflected in the form of the Bloch waves (2.3.8), which are "localized" in the z' variable, so that scattering is allowed only in the one dimensional longitudinal direction. Indeed, as already pointed out, the wave vector k varies in the 1D domain $(-\pi,\pi)$. It turns out that $(-\pi,\pi)$ is the fundamental domain of the reciprocal lattice, usually called Brillouin zone in solid state physics.

Remark 2.3.3. The Parseval identity (2.3.6) tells that the wave function density can be obtained as superposition of envelope function densities, which depend only on the x variable, the dependence on the variable z' being averaged out. However, in self–consistent computations the

external electrostatic potential is acting on the entire 3D structure, so that explicit dependence on z' has to be kept. A straightforward computation, based on (2.3.14) and (2.3.16), shows that

$$\sum_{l\in\mathbb{Z}} |\mathcal{G}_l(x,z')|^2 = \int_{-1/2}^{1/2} \Big| \sum_{n\in\mathbb{N}} f_n(x)\chi_n(y,z') \Big|^2 dy = \sum_{n,n'} f_n(x)\overline{f_{n'}(x)}g_{nn'}(z'),$$

with $g_{nn'}$ defined in (2.3.3). Therefore, recalling (2.3.12), we obtain, for a fixed z'

$$\int_{\mathbb{R}} |\psi(x,z')|^2 dx = \int_{\mathbb{R}} \Big(\sum_{n,n'} f_n(x)\overline{f_{n'}(x)}g_{nn'}(z') \Big) dx. \tag{2.3.25}$$

We emphasize the presence of the $g_{nn'}$'s that carry the contribution of the confinement.

For any $0 < \epsilon << 1$, the scaled version of the envelope function decomposition is obtained with the same computation as in Theorem 2.3.1 using the fact that to the primitive cell $\mathcal{C}_\epsilon := (-\epsilon/2, \epsilon/2)$ it corresponds the primitive cell of the reciprocal lattice $\mathcal{B}_\epsilon := (-\pi/\epsilon, \pi/\epsilon)$, with $|\mathcal{C}_\epsilon||\mathcal{B}_\epsilon| = 2\pi$. We get

$$\psi(x,z') = \sum_{n\in\mathbb{N}} f_n^\epsilon(x)\chi_n(\frac{x}{\epsilon}, z') \ , \tag{2.3.26}$$

and the Parseval identity holds

$$\big\|\psi(x,z')\big\|^2_{L^2(\mathbb{R}\times\omega)} = \sum_{n\in\mathbb{N}} \|f_n^\epsilon(x)\|^2_{L^2(\mathbb{R})} \, , \tag{2.3.27}$$

together with

$$\int_{\mathbb{R}} |\psi(x,z')|^2 dx = \int_{\mathbb{R}} \Big(\sum_{n,n'} f_n^\epsilon(x)\overline{f_{n'}^\epsilon(x)}g_{nn'}(z') \Big) dx. \tag{2.3.28}$$

Moreover, the Fourier transform $\widehat{f_n^\epsilon}$ has a support in $\mathcal{B}_\epsilon$ and it is defined by

$$\widehat{f_n^\epsilon}(k) = \int_{\mathbb{R}\times\omega} \overline{u_{n,k}^\epsilon(x,z')}\psi(x,z')dxdz', \tag{2.3.29}$$

where the (generalized) scaled Bloch waves are given by

$$u_{n,k}^\epsilon(x,z') = \frac{1}{\sqrt{2\pi}} \mathbb{1}_{\mathcal{B}_\epsilon}(k) e^{\imath kx} \chi_n(\frac{x}{\epsilon}, z'). \tag{2.3.30}$$

The functions f_n^ϵ will be called the ϵ-scaled envelope functions relative to the basis $\{\chi_n | n \in \mathbb{N}\}$. The decomposition of ψ in terms of the Fourier transform $\widehat{f_n^\epsilon}$ is given by

$$\psi(x,z') = \sum_{n\in\mathbb{N}} \frac{1}{\sqrt{2\pi}} \int_{\mathcal{B}_\epsilon} \widehat{f_n^\epsilon}(k) e^{\imath kx} \chi_n(\frac{x}{\epsilon}, z') dk \ . \tag{2.3.31}$$

2.4 Effective mass model derivation

In this section, we shall present the formal derivation of the effective mass approximation used in the next parts of the chapter. The main results can be summarized in the following two Propositions. The first one refers to the non–degenerate case, the second one to the degenerate case.

Proposition 2.4.1. *Assume that all the eigenvalues E_n of the problem (2.3.1) are simple. Then, the effective dynamics is given by an infinite set of 1D Schrödinger equations that in the n^{th} band have the form*

$$\imath\partial_t h_{em,n}(t,x) = -\frac{1}{2m_n^*}\partial_{xx} h_{em,n}(t,x) + V_{nn}(x) h_{em,n}(t,x). \tag{2.4.1}$$

m_n^* denotes the n^{th} band effective mass and it is defined by

$$\frac{1}{m_n^*} = 1 - 2\sum_{n'\neq n} \frac{P_{nn'}P_{n'n}}{E_n - E_{n'}}, \tag{2.4.2}$$

where

$$P_{nn'} = < \partial_y \chi_{n'}(y,z'), \chi_n(y,z') > \tag{2.4.3}$$

are the matrix elements of the first order derivative operator between Bloch functions. Moreover, $V_{nn'}$ is an effective potential given by

$$V_{nn'}(x) = \int_\omega V(x,z') g_{nn'}(z') dz', \tag{2.4.4}$$

constructed by projecting the 3D potential V in the transport direction through the $g_{nn'}$'s defined in (2.3.3).

In the degenerate case, the final set of equations is not decoupled anymore, but to each multiple eigenvalue it corresponds a system of dimension equal to the multiplicity of E_n, as stated in the next Proposition.

Proposition 2.4.2. *Assume that each eigenvalue E_n of the problem (2.3.1) has multiplicity $\alpha_n \geq 1$ and denote by $\chi_{n,\alpha}$, with $1 \leq \alpha \leq \alpha_n$, the α_n eigenvectors associated with E_n. To simplify notations, we say that $\chi_{n,\alpha}$ is the $(n\text{-}\alpha)^{th}$ eigenvector (where $n\text{-}\alpha = \sum_{n'<n}\alpha_{n'} + \alpha$). Let*

$$P_{(n,\alpha\ n',\alpha')} = < \partial_y \chi_{n',\alpha'}(y,z'), \chi_{n,\alpha}(y,z') > \tag{2.4.5}$$

be defined analogously to (2.4.3). Then, the degenerate effective mass dynamics is described by a set of $\alpha_n \times \alpha_n$ system, where the generic $n\text{-}\alpha^{th}$ equation has the form

$$\imath\partial_t h_{em,n,\alpha}(t,x) = -\frac{1}{2m_{n,\alpha}^*}\partial_{xx} h_{em,n,\alpha}(t,x) + \sum_{\alpha'=1}^{\alpha_n} V_{(n,\alpha\ n,\alpha')}(x) h_{em,n,\alpha'}(t,x), \tag{2.4.6}$$

where the effective mass $m^*_{n,\alpha}$ *is now defined by*

$$\frac{1}{m^*_{n,\alpha}} = 1 - 2\sum_{n'\neq n}\sum_{\alpha'=1}^{\alpha_{n'}} \frac{P_{(n,\alpha\ n',\alpha')}P_{(n',\alpha'\ n,\alpha)}}{E_n - E_{n'}} \tag{2.4.7}$$

and the effective potential $V_{(n,\alpha\ n',\alpha')}$ *is defined analogously to (2.4.4).*

In order to derive the asymptotic model, we start from the exact dynamics of the envelope functions (Section 2.4.1). Then, in Section 2.4.2, we formally pass to the limit in the term containing the slowly varying potential V and we obtain a $k\cdot p$ model. Using perturbation techniques, we diagonalize the $k\cdot p$ Hamiltonian and we construct an effective mass operator (Section 2.4.3). Finally, in Section 2.4.4, the effective mass dynamics is obtained filtering the fast oscillations in time. We shall see that, since the wave vector k is a scalar, the use of the asymptotic expansion for the perturbed eigenvalues is justified not only in the non–degenerate case, but also in the degenerate one (see [11]). This leads to a diagonal kinetic part in the limiting Hamiltonian. However, the presence of multiple eigenvalues does not allow to complete separate the time scales and the time averaging process leads to a coupling in the potential term.

Remark 2.4.1. We point out that the effective mass and the effective potential in the model depend on the device structure since they are computed by means of the Bloch functions (2.3.1). This is an important feature of the model, since, as already mentioned in the introduction, simulations with bulk material quantities fail to reproduce the physical experiments [9].

2.4.1 Dynamics of envelope functions

We first derive the exact dynamics of the envelope functions of the solution of Schrödinger equation (2.2.8). It will be given in Fourier space, and in order to simplify notations, we introduce the definition

$$g^\epsilon_n(t,k) = \widehat{f^\epsilon_n}(t,k). \tag{2.4.8}$$

Proposition 2.4.3. *Let* $\psi^\epsilon(t,x,z')$ *be the solution of the Schrödinger equation (2.2.8) and let*

$$\psi^\epsilon(t,x,z') = \sum_{n\in\mathbb{N}} f^\epsilon_n(t,x)\chi_n(\frac{x}{\epsilon},z') \tag{2.4.9}$$

be its ϵ*-scaled envelope function decomposition relative to the basis* $\{\chi_n | n\in\mathbb{N}\}$ *defined in (2.3.1). The exact dynamics of envelope functions is given by*

$$\begin{aligned} \imath\partial_t g^\epsilon_n(t,k) &= \frac{1}{2}k^2 g^\epsilon_n(t,k) + \frac{1}{\epsilon^2}E_n g^\epsilon_n(t,k) - \frac{\imath}{\epsilon}k\sum_{n'\in\mathbb{N}} P_{nn'}g^\epsilon_{n'}(t,k) \\ &+ \sum_{n'\in\mathbb{N}}\int_{\mathbb{R}_{k'}} U^\epsilon_{nn'}(k,k')g^\epsilon_{n'}(t,k')dk', \end{aligned} \tag{2.4.10}$$

where the kernel $U^\epsilon_{nn'}(k,k')$ *is defined by*

$$U^\epsilon_{nn'}(k,k') = \frac{1}{2\pi}\mathbb{1}_{\mathcal{B}_\epsilon}(k')\mathbb{1}_{\mathcal{B}_\epsilon}(k)\int_{\mathbb{R}_x\times\omega} e^{\imath(k'-k)x}\chi_{n'}(\frac{x}{\epsilon},z')V(x,z')\chi_n(\frac{x}{\epsilon},z')dxdz', \tag{2.4.11}$$

and the $P_{nn'}$*'s are defined in (2.4.3).*

The proof of this proposition is postponed to the appendix. In position variables, (2.4.10) reads as follows

$$\imath\partial_t f_n^\epsilon(t,x) = -\frac{1}{2}\partial_{xx} f_n^\epsilon(t,x) + \frac{1}{\epsilon^2} E_n f_n^\epsilon(t,x) - \frac{1}{\epsilon}\sum_{n'\in\mathbb{N}} P_{nn'}\partial_x f_{n'}^\epsilon(t,x) + \left(\mathcal{V}^\epsilon f^\epsilon\right)_n(t,x), \quad (2.4.12)$$

where the non local operator $\mathcal{V}^\epsilon$ is defined component wise, for any element $f^\epsilon = (f_1^\epsilon, f_2^\epsilon, ...)$, such that

$$\widehat{\left(\mathcal{V}^\epsilon f^\epsilon\right)}_n(t,k) = \sum_{n'\in\mathbb{N}} \int_{\mathbb{R}_{k'}} U_{nn'}^\epsilon(k,k') g_{n'}^\epsilon(t,k')dk'. \quad (2.4.13)$$

2.4.2 $k\cdot p$ model

The so-called $k\cdot p$ model is obtained in passing to the limit in the operator $\mathcal{U}^\epsilon$ defined component wise, for any element $g^\epsilon = (g_1^\epsilon, g_2^\epsilon, ...)$, as

$$(\mathcal{U}^\epsilon g^\epsilon)_n(t,k) = \sum_{n'\in\mathbb{N}} \int_{\mathbb{R}_{k'}} U_{nn'}^\epsilon(k,k') g_{n'}^\epsilon(t,k')dk'. \quad (2.4.14)$$

Since the χ_n's are 1-periodic in the first variable, we have

$$\lim_{\epsilon\to 0}\int_{\mathbb{R}} e^{\imath(k'-k)x}\chi_{n'}(\frac{x}{\epsilon},z')V(x,z')\chi_n(\frac{x}{\epsilon},z')dx = \int_{\mathbb{R}} V(x,z')e^{\imath(k'-k)x}dx\int_{-1/2}^{1/2}\chi_n(y,z')\chi_{n'}(y,z')dy.$$

Thus, using definition (2.3.3) for $g_{nn'}(z')$, the formal limit of (2.4.11) is given by

$$\begin{aligned} U_{nn'}(k,k') &= \frac{1}{2\pi}\int_\omega \Big(\int_{\mathbb{R}_x} e^{\imath(k'-k)x}V(x,z')dx\Big)g_{nn'}(z')dz' \quad (2.4.15)\\ &= \frac{1}{\sqrt{2\pi}}\int_\omega \widehat{V}(k-k',z')g_{nn'}(z')dz', \end{aligned}$$

and the formal limit of $\mathcal{U}^\epsilon$ is the operator $\mathcal{U}^0$ defined by

$$\begin{aligned} (\mathcal{U}^0 g_{kp}^\epsilon)_n(t,k) &= \sum_{n'\in\mathbb{N}}\int_{\mathbb{R}_{k'}} U_{nn'}(k,k')g_{kp,n'}^\epsilon(t,k')dk' \quad (2.4.16)\\ &= \sum_{n'\in\mathbb{N}}\int_{\mathbb{R}_{k'}}\left(\frac{1}{\sqrt{2\pi}}\int_\omega \widehat{V}(k-k',z')g_{nn'}(z')dz'\right)g_{kp,n'}^\epsilon(t,k')dk'. \end{aligned}$$

Therefore, the $k\cdot p$ dynamics is summarized in the following Proposition.

Proposition 2.4.4. *The $k\cdot p$ model is given, in Fourier space, by the equations*

$$\imath\partial_t g_{kp,n}^\epsilon(t,k) = \frac{1}{2}k^2 g_{kp,n}^\epsilon(t,k) + \frac{1}{\epsilon^2}E_n g_{kp,n}^\epsilon(t,k) - \frac{\imath}{\epsilon}k\sum_{n'\in\mathbb{N}} P_{nn'}g_{kp,n'}^\epsilon(t,k) + (\mathcal{U}^0 g_{kp}^\epsilon)_n(t,k), \quad (2.4.17)$$

where $\mathcal{U}^0$ is given by (2.4.16).

The back Fourier transform of g^ϵ_{kp}, which will be denoted by f^ϵ_{kp}, is solution of

$$\begin{aligned} \imath\partial_t f^\epsilon_{kp,n}(t,x) &= -\frac{1}{2}\partial_{xx} f^\epsilon_{kp,n}(t,x) + \frac{1}{\epsilon^2} E_n f^\epsilon_{kp,n}(t,x) \\ &- \frac{1}{\epsilon}\sum_{n'\in\mathbb{N}} P_{nn'}\partial_x f^\epsilon_{kp,n'}(t,x) + \sum_{n'\in\mathbb{N}} V_{nn'}(x) f^\epsilon_{kp,n'}(t,x), \end{aligned} \tag{2.4.18}$$

with $V_{nn'}$ defined in (2.4.4). Notice that the $k\cdot p$ model consists of an infinite set of coupled 1D equations for the functions $f^\epsilon_{kp,n}(t,x)$. The effect of confinement is incorporated in the band energy E_n, in the derivative operator between Bloch functions $P_{nn'}$, and in the effective potential matrix $V_{nn'}$.

2.4.3 Diagonalization of the $k\cdot p$ Hamiltonian

Non-degenerate case

In this section, we make the assumption that the eigenvalues E_n of the problem (2.3.1) are simple, and that they are numbered in increasing order, i.e.

$$E_1 < E_2 < ... \tag{2.4.19}$$

Therefore, the diagonalization of the $k\cdot p$ Hamiltonian relies on non-degenerate perturbation theory and leads to the construction of an effective mass operator.

We consider first the case $V(x,z') = 0$ and concentrate on the diagonalization of the $k\cdot p$ Hamiltonian. We rewrite equation (2.4.17) in the form

$$\imath\epsilon^2\partial_t g^\epsilon_{kp,n}(t,k) = \frac{1}{2}\epsilon^2 k^2 g^\epsilon_{kp,n}(t,k) + E_n g^\epsilon_{kp,n}(t,k) - \imath\epsilon k\sum_{n'\in\mathbb{N}} P_{nn'} g^\epsilon_{kp,n'}(t,k). \tag{2.4.20}$$

Choosing $\xi = \epsilon k$, we define the following operators

$$(A^0)_{nn'} = E_n\delta_{nn'}, \quad (A^1)_{nn'} = -\imath P_{nn'} \quad \text{and} \quad (A^2)_{nn'} = \frac{1}{2}\delta_{nn'}. \tag{2.4.21}$$

Introducing also $A(\xi) = A^0 + \xi A^1 + \xi^2 A^2$, we notice that

$$(A(\xi))_{nn'} = E_n\delta_{nn'} - \imath\xi P_{nn'} + \frac{1}{2}\xi^2\delta_{nn'} \tag{2.4.22}$$

corresponds to the operator at the right-hand side of equation (2.4.20). For simplicity, in the following, we consider those operators acting on $l^2 = \{a_n \in \mathbb{C} | \big(\sum_{n\in\mathbb{N}} |a_n|^2\big)^{1/2} < +\infty\}$.

A non-degenerate perturbation technique is applied to approximate the eigenvalues $\lambda_n(\xi)$ of $A(\xi)$:

$$A(\xi)v_n(\xi) = \lambda_n(\xi)v_n(\xi). \tag{2.4.23}$$

Remark 2.4.2. We point out that the operator $A(\xi)$ is nothing but the expression of the fibered Hamiltonian (2.3.2) in the basis $\{\chi_n|\ n \in \mathbb{N}\}$. More precisely, we have $(A(\xi))_{nn'} = < H_{\mathcal{L}}(\xi)\chi_n(y,z'), \chi_{n'}(y,z') >$. Therefore, it is easy to see that $\lambda_n(\xi) = E_n(\xi)$ and $v_n(\xi) = < \chi_{n,\xi}(y,z'), \chi_n(y,z') >$, where $\chi_{n,\xi}(y,z')$ denotes the eigenvector of the fibered Hamiltonian $H_{\mathcal{L}}(\xi)$ as defined in Remark 2.3.1.

We expand $v_n(\xi)$ and $\lambda_n(\xi)$ as

$$v_n(\xi) = v_n^0 + \xi v_n^1 + \xi^2 v_n^2 + ... \qquad \lambda_n(\xi) = \lambda_n^0 + \xi\lambda_n^1 + \xi^2\lambda_n^2 + ... \tag{2.4.24}$$

Inserting this expression into (2.4.23) and collecting terms with the same order of ξ yields

$$A^0 v_n^0 = \lambda_n^0 v_n^0, \tag{2.4.25}$$

$$A^0 v_n^1 + A^1 v_n^0 = \lambda_n^0 v_n^1 + \lambda_n^1 v_n^0, \tag{2.4.26}$$

$$A^0 v_n^2 + A^1 v_n^1 + A^2 v_n^0 = \lambda_n^0 v_n^2 + \lambda_n^1 v_n^1 + \lambda_n^2 v_n^0. \tag{2.4.27}$$

The system (2.4.25) gives directly $\lambda_n^0 = E_n$ and $v_n^0 = e_n$, where e_n is the n^{th} vector of the canonical basis in l^2. Next, we project (2.4.26) on e_n and we obtain

$$E_n v_{n,n}^1 - \imath P_{nn} = E_n v_{n,n}^1 + \lambda_n^1,$$

where $v_{n,n'}^1$ is the $(n')^{th}$ component of v_n^1. Integration by parts in (2.4.3) gives $P_{nn'} = -P_{n'n}$ and thus $P_{nn} = 0$. We conclude that $\lambda_n^1 = 0$.
Projecting (2.4.26) on $e_{n'}$ $(n' \neq n)$ gives

$$v_{n,n'}^1 = -\imath \frac{P_{n'n}}{E_n - E_{n'}}. \tag{2.4.28}$$

Finally, we project (2.4.27) on e_n to get

$$E_n v_{n,n}^2 - \imath \sum_{n'} P_{nn'} v_{n,n'}^1 + \frac{1}{2} = E_n v_{n,n}^2 + \lambda_n^2.$$

Using (2.4.28) and the fact that $P_{nn} = 0$, we obtain

$$\lambda_n^2 = \frac{1}{2}\Big(1 - 2\sum_{n' \neq n} \frac{P_{nn'}P_{n'n}}{E_n - E_{n'}}\Big). \tag{2.4.29}$$

Then, defining m_n^* as in (2.4.2), we conclude saying that

$$\lambda_n \simeq \lambda_n^0 + \xi^2\lambda_n^2 = E_n + \frac{1}{2}\frac{\xi^2}{m_n^*}. \tag{2.4.30}$$

The asymptotic result is formalized in the following Proposition, where the potential terms are incorporated.

Proposition 2.4.5. *The $k \cdot p$ Hamiltonian of equation (2.4.17) is diagonalized in the kinetic part and it leads to the dynamics of $g^\epsilon_{em} = (g^\epsilon_{em,1}, g^\epsilon_{em,2}, ...)$, solution of*

$$\imath \partial_t g^\epsilon_{em,n}(t,k) = (A^\epsilon_{em} g^\epsilon_{em})_n(t,k) + (\mathcal{U}^0 g^\epsilon_{em})_n(t,k). \tag{2.4.31}$$

The operator A^ϵ_{em} is defined by

$$(A^\epsilon_{em} g^\epsilon_{em})_n(t,k) = \left(\frac{E_n}{\epsilon^2} + \frac{1}{2} \frac{k^2}{m^*_n} \right) g^\epsilon_{em,n}(t,k), \tag{2.4.32}$$

where m^*_n is the n^{th} band effective mass given by (2.4.2).

The back Fourier transform of g^ϵ_{em}, which is denoted by f^ϵ_{em}, is solution of

$$\imath \partial_t f^\epsilon_{em,n}(t,x) = -\frac{1}{2m^*_n} \partial_{xx} f^\epsilon_{em,n}(t,x) + \frac{1}{\epsilon^2} E_n f^\epsilon_{em,n}(t,x) + \sum_{n' \in \mathbb{N}} V_{nn'}(x) f^\epsilon_{em,n'}(t,x). \tag{2.4.33}$$

Degenerate case

We now discuss the degenerate case and consider each eigenvalue E_n with its multiplicity $\alpha_n \geq 1$. In the previous section, the unperturbed eigenvalues, as well as the perturbed ones, have been numbered in increasing order. In the degenerate case, crossing of the modes may lead to a loss of regularity of the perturbed eigenvalues. However, as already mentioned at the beginning of section 2.4, one peculiarity of nanowires (with respect to 3D crystals) is that the perturbation parameter ξ is scalar, and Kato's results [11] say that in the neighborhood of $\xi = 0$ there are α_n (not necessarily distinct) eigenvalues which are analytic, together with the corresponding eigenvectors. We denote the perturbed regular eigencouple of (2.4.23) by $(\lambda_{n,\alpha}(\xi), v_{n,\alpha}(\xi))$. Then, in view of Remark 2.4.2 the same numbering is inherited by the eigenvectors $\chi_{n,\alpha}$. Moreover, as in Proposition 2.4.2, we use the notation $n\text{-}\alpha = \sum_{n'<n} \alpha_{n'} + \alpha$.

As in the non–degenerate case, we still can write

$$A^0 v^0_{n,\alpha} = \lambda^0_{n,\alpha} v^0_{n,\alpha}, \tag{2.4.34}$$

$$A^0 v^1_{n,\alpha} + A^1 v^0_{n,\alpha} = \lambda^0_{n,\alpha} v^1_{n,\alpha} + \lambda^1_{n,\alpha} v^0_{n,\alpha}, \tag{2.4.35}$$

$$A^0 v^2_{n,\alpha} + A^1 v^1_{n,\alpha} + A^2 v^0_{n,\alpha} = \lambda^0_{n,\alpha} v^2_{n,\alpha} + \lambda^1_{n,\alpha} v^1_{n,\alpha} + \lambda^2_{n,\alpha} v^0_{n,\alpha}. \tag{2.4.36}$$

The system (2.4.34) gives directly $\lambda^0_{n,\alpha} = E_n$ and $v^0_{n,\alpha} = e_{n,\alpha}$ where $e_{n,\alpha}$ is the $n\text{-}\alpha^{th}$ vector of the canonical basis in l^2.
The projection of (2.4.35) on $e_{n,\alpha}$ implies $\lambda^1_{n,\alpha} = 0$, because integration by parts still implies $P_{(n,\alpha\ n,\alpha)} = 0$. Then, projecting (2.4.35) on $e_{n,\alpha'}$ $(\alpha' \neq \alpha)$ gives

$$P_{(n,\alpha'\ n,\alpha)} = 0. \tag{2.4.37}$$

Also, projecting (2.4.35) on $e_{n',\alpha'}$ $(n' \neq n)$, we obtain

$$-\imath P_{(n',\alpha'\ n,\alpha)} + E_{n'} v^1_{n,\alpha\ n',\alpha'} = E_n v^1_{n,\alpha\ n',\alpha'}$$

where $v^1_{n,\alpha\ n',\alpha'}$ is the $(n'\text{-}\alpha')^{th}$ component of $v^1_{n,\alpha}$. It gives

$$v^1_{n,\alpha\ n',\alpha'} = -\imath \frac{P_{(n',\alpha'\ n,\alpha)}}{E_n - E_{n'}}. \tag{2.4.38}$$

Finally, using $P_{(n,\alpha\ n,\alpha)} = 0$ and (2.4.37), the projection of (2.4.36) on $e_{n,\alpha}$ simplifies to

$$E_n v^2_{n,\alpha\ n,\alpha} - \imath \sum_{n'\neq n} \sum_{\alpha'=1}^{\alpha_{n'}} P_{(n,\alpha\ n',\alpha')} v^1_{n,\alpha\ n',\alpha'} + \frac{1}{2} = E_n v^2_{n,\alpha\ n,\alpha} + \lambda^2_{n,\alpha}.$$

Using (2.4.38), we obtain

$$\lambda^2_{n,\alpha} = \frac{1}{2}\Big(1 - 2 \sum_{n'\neq n} \sum_{\alpha'=1}^{\alpha_{n'}} \frac{P_{(n,\alpha\ n',\alpha')} P_{(n',\alpha'\ n,\alpha)}}{E_n - E_{n'}}\Big). \tag{2.4.39}$$

We conclude saying that

$$\lambda_{n,\alpha} \simeq \lambda^0_{n,\alpha} + \xi^2 \lambda^2_{n,\alpha} = E_n + \frac{1}{2}\frac{\xi^2}{m^*_{n,\alpha}}, \tag{2.4.40}$$

where the effective mass $m^*_{n,\alpha}$ is defined in (2.4.7). Consequently, in this case, the inverse Fourier transform of g^ϵ_{em}, which is still denoted by f^ϵ_{em}, is solution of

$$\begin{aligned} \imath\partial_t f^\epsilon_{em,n,\alpha}(t,x) &= -\frac{1}{2m^*_{n,\alpha}} \partial_{xx} f^\epsilon_{em,n,\alpha}(t,x) + \frac{1}{\epsilon^2} E_n f^\epsilon_{em,n,\alpha}(t,x) \\ &+ \sum_{n'} \sum_{\alpha'=1}^{\alpha_{n'}} V_{(n,\alpha\ n',\alpha')}(x) f^\epsilon_{em,n',\alpha'}(t,x). \end{aligned} \tag{2.4.41}$$

Remark 2.4.3. In the above computations we obtained (2.4.37) thanks to the analyticity of the perturbed eigenvalues and of the corresponding eigenvectors, that allowed to write (2.4.34)–(2.4.36), so that no drift term appears in the approximate equation (2.4.41). Moreover, we can project (2.4.36) on $e_{n,\alpha'}$, with $\alpha' \neq \alpha$ to obtain

$$-\sum_{n''} \sum_{\alpha''=1}^{\alpha_{n''}} \frac{P_{(n,\alpha'\ n'',\alpha'')} P_{(n'',\alpha''\ n,\alpha)}}{E_n - E_{n''}} = 0.$$

Therefore, in the case of nanowires, the effective mass equations have a simpler structure than in the case of 3D crystals reported, for e.g., in [18, 10].

2.4.4 Effective mass dynamics

Non-degenerate case

The equation (2.4.33) involves fast oscillations in time, that can be filtered out by setting $f^\epsilon_{em,n}(t,x) = h^\epsilon_{em,n}(t,x) e^{-\imath E_n \frac{t}{\epsilon^2}}$. Then, h^ϵ_{em} is solution of

$$\imath\partial_t h^\epsilon_{em,n}(t,x) = -\frac{1}{2m^*_n} \partial_{xx} h^\epsilon_{em,n}(t,x) + \sum_{n'\in\mathbb{N}} e^{-\imath(E_{n'}-E_n)\frac{t}{\epsilon^2}} V_{nn'}(x) h^\epsilon_{em,n'}(t,x). \tag{2.4.42}$$

We separate the diagonal part of the Hamiltonian of (2.4.42)

$$(H_0 h)_n = -\frac{1}{2m_n^*}\partial_{xx} h_n(x) + V_{nn}(x) h_n(x), \tag{2.4.43}$$

and the off–diagonal part given by the operator

$$(R^\epsilon(t)h)_n = \sum_{n' \neq n} e^{-\imath(E_{n'}-E_n)\frac{t}{\epsilon^2}} V_{nn'}(x) h_{n'}(x). \tag{2.4.44}$$

Formally, we have that

$$R^\epsilon(t) = \epsilon^2 \frac{d}{dt}\widetilde{R}^\epsilon(t), \tag{2.4.45}$$

where

$$(\widetilde{R}^\epsilon(t)h)_n = \sum_{n' \neq n} \frac{\imath}{(E_{n'}-E_n)} e^{-\imath(E_{n'}-E_n)\frac{t}{\epsilon^2}} V_{nn'}(x) h_{n'}(x). \tag{2.4.46}$$

Since H_0 is the complete Hamiltonian of (2.4.1) of Proposition 2.4.1, using a generalized Duhamel formula for the evolution of h^ϵ_{em} we can formally write

$$h^\epsilon_{em}(t) - h_{em}(t) = \int_0^t S(t-s) R^\epsilon(s) h^\epsilon_{em}(s) ds,$$

where $S(t) = e^{-\imath t H_0}$ is the (diagonal) unitary group generated by H_0. Therefore, thanks to (2.4.45), integration by parts shows that the action of the evolution operator (2.4.44) vanishes in the limit $\epsilon \to 0$ and h^ϵ_{em} formally converges to the solution of the averaged system (2.4.1).

Remark 2.4.4. In view of self–consistent computations, we are now interested in the formal limit $\epsilon \to 0$ of (2.3.28). The transformation $f^\epsilon_n(t,x) = h^\epsilon_n(t,x) e^{-\imath E_n \frac{t}{\epsilon^2}}$, that allows to filter oscillations in time, conserves the modulus $|f^\epsilon_n(t,x)| = |h^\epsilon_n(t,x)|$. Consequently, we can write

$$\begin{aligned} \sum_{n,n'} f^\epsilon_n(t,x)\overline{f^\epsilon_{n'}(t,x)} g_{nn'}(z') &= \sum_{n\in\mathbb{N}} |f^\epsilon_n(t,x)|^2 g_{nn}(z') \\ &+ \sum_{n\in\mathbb{N}} h^\epsilon_n(t,x)\Big(\sum_{n'\neq n} \overline{h^\epsilon_{n'}(t,x)} e^{-\imath(E_n-E_{n'})\frac{t}{\epsilon^2}} g_{nn'}(z')\Big). \end{aligned} \tag{2.4.47}$$

Because of the vanishing average over long time periods of $e^{-\imath(E_{n'}-E_n)\frac{t}{\epsilon^2}}$, we can say that the second term (corresponding to the off–diagonal part) vanishes in the limit $\epsilon \to 0$. Moreover, we previously saw that a formal limiting process allows to pass from the dynamics of f^ϵ_n to the effective mass dynamics of $h_{em,n}$. Therefore, $\int_{\mathbb{R}} |\psi^\epsilon(t,x,z')|^2 dx$ converges formally to the averaged term

$$\int_{\mathbb{R}} \Big(\sum_{n\in\mathbb{N}} |h_{em,n}(t,x)|^2 g_{nn}(z')\Big) dx,$$

where, in the superposition of the densities, the multiplication by g_{nn}'s allows to take into account the effects of the cross-section confinement.

Degenerate case

Again, we can filter oscillations in time of (2.4.41) by setting $f^\epsilon_{em,n,\alpha}(t,x) = h^\epsilon_{em,n,\alpha}(t,x)e^{-\imath E_n \frac{t}{\epsilon^2}}$. Then, $h^\epsilon_{em,n,\alpha}$ is solution of

$$\begin{aligned} \imath\partial_t h^\epsilon_{em,n,\alpha}(t,x) &= -\frac{1}{2m^*_{n,\alpha}}\partial_{xx} h^\epsilon_{em,n,\alpha}(t,x) \\ &+ \sum_{n'\in\mathbb{N}}\sum_{\alpha'=1}^{\alpha_{n'}} e^{-i(E_{n'}-E_n)\frac{t}{\epsilon^2}} V_{(n,\alpha\ n',\alpha')}(x) h^\epsilon_{em,n',\alpha'}(t,x). \end{aligned} \tag{2.4.48}$$

As for the non–degenerate case, we can still define a remainder operator in the form

$$(R^\epsilon(t)h)_{n,\alpha} = \sum_{n'\neq n}\sum_{\alpha'=1}^{\alpha_{n'}} e^{-\imath(E_{n'}-E_n)\frac{t}{\epsilon^2}} V_{(n,\alpha\ n',\alpha')}(x) h_{n',\alpha'}(x). \tag{2.4.49}$$

But, in this case, the H_0 operator is not diagonal anymore

$$(H_0 h)_{n,\alpha} = -\frac{1}{2m^*_{n,\alpha}}\partial_{xx} h_{n,\alpha}(x) + \sum_{\alpha'=1}^{\alpha_n} V_{(n,\alpha\ n,\alpha')}(x) h_{n,\alpha'}(x). \tag{2.4.50}$$

We still can formally pass to the limit when $\epsilon \to 0$ to obtain Proposition 2.4.2. We emphasize that the important difference with the non-degenerate case is that a complete separation of the oscillating time scales is not possible and the final system retains a coupling through the potential.

Remark 2.4.5. In the degenerate case, the first member of (2.4.47) can be restated emphasizing the multiplicity of the eigenvalues as

$$\sum_{n\in\mathbb{N}}\sum_{\alpha=1}^{\alpha_n}\sum_{n'\in\mathbb{N}}\sum_{\alpha'=1}^{\alpha_{n'}} f^\epsilon_{n,\alpha}(t,x)\overline{f^\epsilon_{n',\alpha'}(t,x)} g_{(n,\alpha\ n',\alpha')}(z').$$

Clearly, in this case, the transformation $f^\epsilon_{n,\alpha}(t,x) = h^\epsilon_{n,\alpha}(t,x)e^{-\imath E_n \frac{t}{\epsilon^2}}$, for $\alpha = 1,\dots,\alpha_n$, does not allow to obtain a diagonal density in the $\epsilon \to 0$ limit. Indeed, $\int_{\mathbb{R}} |\psi^\epsilon(t,x,z')|^2 dx$ converges formally to the averaged term

$$\int_{\mathbb{R}} \Big(\sum_{n\in\mathbb{N}}\sum_{\alpha=1}^{\alpha_n}\sum_{\alpha'=1}^{\alpha_n} h_{em,n,\alpha}(t,x)\overline{h_{em,n,\alpha'}(t,x)} g_{(n,\alpha\ n,\alpha')}(z') \Big) dx,$$

where a coupling among bands corresponding to the same eigenvalue is present. Instead, the coupling disappears if we integrate in the variable z', because of the orthogonality of the $\chi_{n,\alpha}$'s. Therefore, $\int_{\mathbb{R}\times\omega} |\psi^\epsilon(t,x,z')|^2 dx dz'$ converges formally to the averaged term

$$\int_{\mathbb{R}} \Big(\sum_{n\in\mathbb{N}}\sum_{\alpha=1}^{\alpha_n} |h_{em,n,\alpha}(t,x)|^2 \Big) dx.$$

Appendix : Proof of Proposition 2.4.3

Proof. The solution $\psi^\epsilon(t,x,z')$ of Schrödinger equation (2.2.8) can be decomposed according to (2.3.31), where the Fourier transform $g_n^\epsilon(t,k)$ of the ϵ-scaled envelope function is given by formula (2.3.29) and the Bloch waves are defined in (2.3.30).

So, multiplying the Schrödinger equation (2.2.8) by $\overline{u_{n,k}^\epsilon(x,z')}$ and integration over $\mathbb{R}_x \times \omega$ leads to the following expression

$$\begin{aligned} &\int_{\mathbb{R}_x\times\omega} \imath\partial_t\psi^\epsilon\overline{u_{n,k}^\epsilon}dxdz' \qquad (2.A.1)\\ =\ &\int_{\mathbb{R}_x\times\omega}\Big(-\frac{1}{2}\partial_{xx}\psi^\epsilon-\frac{1}{2\epsilon^2}\Delta_{z'}\psi^\epsilon+\frac{1}{\epsilon^2}W_{\mathcal{L}}(\frac{x}{\epsilon},z')\psi^\epsilon+V(x,z')\psi^\epsilon\Big)\overline{u_{n,k}^\epsilon}dxdz'. \end{aligned}$$

We treat each term separately. Concerning the first term, formula (2.3.29)gives immediately

$$\int_{\mathbb{R}_x\times\omega}\imath\partial_t\psi^\epsilon(t,x,z')\overline{u_{n,k}^\epsilon(x,z')}dxdz' = \imath\partial_t g_n^\epsilon(t,k). \qquad (2.A.2)$$

In the same way, the last term can be treated easily. We obtain

$$\int_{\mathbb{R}_x\times\omega}V(x,z')\psi^\epsilon(t,x,z')\overline{u_{n,k}^\epsilon(x,z')}dxdz' = \sum_{n'\in\mathbb{N}}\int_{\mathbb{R}_{k'}}U_{nn'}^\epsilon(k,k')g_{n'}^\epsilon(t,k')dk', \qquad (2.A.3)$$

where $U_{nn'}^\epsilon(k,k')$ is defined in (2.4.11).

Differentiation with respect to x of the scaled Bloch wave (2.3.30) gives

$$\partial_x u_{n,k}^\epsilon(x,z') \;=\; \imath k u_{n,k}^\epsilon(x,z')+\frac{1}{\epsilon}\frac{1}{\sqrt{2\pi}}\mathbb{1}_{\mathcal{B}_\epsilon}(k)e^{\imath kx}\partial_y\chi_n(\frac{x}{\epsilon},z'),$$

and

$$\begin{aligned}\partial_{xx}u_{n,k}^\epsilon(x,z') &= -k^2u_{n,k}^\epsilon(x,z')\\ &+\frac{1}{\sqrt{2\pi}}\mathbb{1}_{\mathcal{B}_\epsilon}(k)e^{\imath kx}\left(\frac{2\imath k}{\epsilon}\partial_y\chi_n(\frac{x}{\epsilon},z')+\frac{1}{\epsilon^2}\partial_{yy}\chi_n(\frac{x}{\epsilon},z')\right),\end{aligned}$$

where $\partial_y\chi_n(\frac{x}{\epsilon},z')$ denotes the derivative of χ_n with respect to the first argument.

The second term in (2.A.1) can be rewritten integrating by parts twice and using the above differentiation formulas, obtaining

$$\begin{aligned} &\frac{k^2}{2}\int_{\mathbb{R}_x\times\omega}\psi^\epsilon(t,x,z')\overline{u_{n,k}^\epsilon(x,z')}dxdz' \qquad (2.A.4)\\ +\ &\frac{\imath k}{\epsilon}\frac{1}{\sqrt{2\pi}}\mathbb{1}_{\mathcal{B}_\epsilon}(k)\int_{\mathbb{R}_x\times\omega}\psi^\epsilon(t,x,z')e^{-\imath kx}\partial_y\chi_n(\frac{x}{\epsilon},z')dxdz' \qquad (2.A.5)\\ -\ &\frac{1}{2\epsilon^2}\frac{1}{\sqrt{2\pi}}\mathbb{1}_{\mathcal{B}_\epsilon}(k)\int_{\mathbb{R}_x\times\omega}\psi^\epsilon(t,x,z')e^{-\imath kx}\partial_{yy}\chi_n(\frac{x}{\epsilon},z')dxdz'. \qquad (2.A.6)\end{aligned}$$

The third term in (2.A.1) becomes

$$-\frac{1}{2\epsilon^2}\frac{1}{\sqrt{2\pi}}\mathbb{1}_{\mathcal{B}_\epsilon}(k)\int_{\mathbb{R}_x\times\omega}\psi^\epsilon(t,x,z')e^{-\imath kx}\Delta_{z'}\chi_n(\frac{x}{\epsilon},z')dxdz', \tag{2.A.7}$$

and the fourth term is written as

$$\frac{1}{\epsilon^2}\frac{1}{\sqrt{2\pi}}\mathbb{1}_{\mathcal{B}_\epsilon}(k)\int_{\mathbb{R}_x\times\omega}\psi^\epsilon(t,x,z')e^{-\imath kx}W_{\mathcal{L}}(\frac{x}{\epsilon},z')\chi_n(\frac{x}{\epsilon},z')dxdz'. \tag{2.A.8}$$

Now, we group (2.A.6), (2.A.7) and (2.A.8). It gives

$$\frac{1}{\epsilon^2}\frac{1}{\sqrt{2\pi}}\mathbb{1}_{\mathcal{B}_\epsilon}(k)\int_{\mathbb{R}_x\times\omega}\psi^\epsilon(t,x,z')e^{-\imath kx}\left(-\frac{1}{2}(\partial_{yy}+\Delta_{z'})+W_{\mathcal{L}}\right)\chi_n(\frac{x}{\epsilon},z')dxdz'. \tag{2.A.9}$$

Recalling the eigenvalue problem (2.3.1) and the definition of Bloch waves (2.3.30), (2.A.9) becomes

$$\frac{1}{\epsilon^2}\int_{\mathbb{R}_x\times\omega}\psi^\epsilon(t,x,z')E_n\overline{u^\epsilon_{n,k}(x,z')}dxdz'=\frac{1}{\epsilon^2}E_n g^\epsilon_n(t,k). \tag{2.A.10}$$

To conclude, we need to treat the term (2.A.5). Using (2.3.31), we have

$$\begin{aligned}
&\frac{\imath k}{\epsilon}\frac{1}{\sqrt{2\pi}}\mathbb{1}_{\mathcal{B}_\epsilon}(k)\int_{\mathbb{R}_x\times\omega}\psi^\epsilon(t,x,z')e^{-\imath kx}\partial_y\chi_n(\frac{x}{\epsilon},z')dxdz'\\
=\;&\frac{\imath}{\epsilon}\frac{1}{2\pi}\mathbb{1}_{\mathcal{B}_\epsilon}(k')\mathbb{1}_{\mathcal{B}_\epsilon}(k)\\
&\sum_{n'}\int_{\mathbb{R}_{k'}}g^\epsilon_{n'}(t,k')k\left(\int_{\mathbb{R}_x\times\omega}e^{\imath(k'-k)x}\partial_y\chi_n(\frac{x}{\epsilon},z')\chi_{n'}(\frac{x}{\epsilon},z')dxdz'\right)dk',
\end{aligned} \tag{2.A.11}$$

and

$$\begin{aligned}
&\int_{\mathbb{R}_x\times\omega}e^{\imath(k'-k)x}\partial_y\chi_n(\frac{x}{\epsilon},z')\chi_{n'}(\frac{x}{\epsilon},z')dxdz'\\
=\;&\sum_{l\in\mathbb{Z}}\int_{(-1/2+l)\epsilon}^{(1/2+l)\epsilon}\int_\omega e^{\imath(k'-k)x}\partial_y\chi_n(\frac{x}{\epsilon},z')\chi_{n'}(\frac{x}{\epsilon},z')dz'dx\\
=\;&\sum_{l\in\mathbb{Z}}e^{\imath(k'-k)l\epsilon}\int_{-\epsilon/2}^{\epsilon/2}\int_\omega e^{\imath(k'-k)s}\partial_y\chi_n(\frac{s}{\epsilon},z')\chi_{n'}(\frac{s}{\epsilon},z')dz'ds,
\end{aligned} \tag{2.A.12}$$

with $k,k'\in\mathcal{B}_\epsilon$. We recall that the function

$$\Delta_T(t)=\sum_{r\in\mathbb{Z}}\delta(t-rT)$$

for a given T, usually referred to as the Dirac comb function, is periodic of period T, and it can be represented as a Fourier series, with all Fourier coefficients $1/T$. It holds

$$\Delta_T(t)=\frac{1}{T}\sum_{l\in\mathbb{Z}}e^{\imath 2\pi lt/T}.$$

Therefore, we have

$$\frac{1}{2\pi}\sum_{l\in\mathbb{Z}} e^{\imath(k-k')l\epsilon} = \epsilon^{-1}\sum_{r\in\mathbb{Z}}\delta(k-k'-\frac{2\pi}{\epsilon}r). \tag{2.A.13}$$

Since k and k' in (2.A.11) are both in the scaled Brillouin zone $\mathcal{B}_\epsilon$, $k-k' = \frac{2\pi}{\epsilon}r$ is only possible if $r=0$. Thus, using (2.A.13) with $r=0$ in (2.A.12) yields

$$\begin{aligned} & \epsilon^{-1}\mathbb{1}_{\mathcal{B}_\epsilon}(k')\mathbb{1}_{\mathcal{B}_\epsilon}(k)\delta(k-k')\int_{-\epsilon/2}^{\epsilon/2}\int_\omega \partial_y\chi_n(\frac{s}{\epsilon},z')\chi_{n'}(\frac{s}{\epsilon},z')dz'ds \\ = \;& \mathbb{1}_{\mathcal{B}_\epsilon}(k')\mathbb{1}_{\mathcal{B}_\epsilon}(k)\delta(k-k')\int_{-1/2}^{1/2}\int_\omega \partial_y\chi_n(y,z')\chi_{n'}(y,z')dz'dy. \end{aligned}$$

Defining $P_{nn'}$ as in (2.4.3) and noticing that $P_{n'n} = -P_{nn'}$, the term (2.A.11) becomes finally

$$-\frac{\imath}{\epsilon}k\sum_{n'} P_{nn'}g^\epsilon_{n'}(t,k).$$

Consequently, grouping each term, we obtain (2.4.10).

□

Bibliography

[1] G. Allaire and A. Piatnitski. Homogenization of the Schrödinger equation and effective mass theorems. *Comm. Math. Phys.*, 258(1):1–22, 2005.

[2] J. Appenzeller, J. Knoch, R. Martel, V. Derycke, S.J. Wind, and P. Avouris. Carbon nanotube electronics. *IEEE Trans. Nanotechnol.*, 1(4):184 – 189, 2002.

[3] N.W. Ashcroft and N.D. Mermin. *Solid State Physics*. Saunders College Publishing, 1976.

[4] L. Barletti and N. Ben Abdallah. Quantum Transport in Crystals: Effective Mass Theorem and K·P Hamiltonians. *Comm. Math. Phys.*, 307:567–607, 2011.

[5] N. Ben Abdallah, C. Jourdana, and P. Pietra. An effective mass model for the simulation of ultra-scaled confined devices. Preprint IMATI-CNR 10PV11/7/0.

[6] Y. Cui, Z. Zhong, D. Wang, W. U. Wang, and C. M. Lieber. High performance silicon nanowire field effect transistors. *Nano Letters*, 3(2):149–152, 2003.

[7] F. Delebecque-Fendt and F. Méhats. An effective mass theorem for the bidimensional electron gas in a strong magnetic field. *Comm. Math. Phys.*, 292(3):829–870, 2009.

[8] X. Duan, C. Niu, V. Sahi, J. Chen, J. W. Parce, S. Empedocles, and J. L. Goldman. High-performance thin-film transistors using semiconductor nanowires and nanoribbons. *Nature*, 425:274–278, 2003.

[9] E. Gnani, A. Gnudi, S. Reggiani, M. Luisier, and G. Baccarani. Band effects on the transport characteristics of ultrascaled snw-fets. *IEEE Trans. Nanotechnol.*, 7(6):700 –709, 2008.

[10] A. Jüngel. *Transport equations for semiconductorsSemiconductor equations*. Lecture Notes in Physics No. 773. Springer, Berlin, 2009.

[11] T. Kato. *Perturbation theory for linear operators*. Springer-Verlag, Berlin, second edition, 1976.

[12] J. M. Luttinger and W. Kohn. Motion of electrons and holes in perturbed periodic fields. *Phys. Rev.*, 97(4):869–883, 1955.

[13] P.L. McEuen, M.S. Fuhrer, and H. Park. Single-walled carbon nanotube electronics. *IEEE Trans. Nanotechnol.*, 1(1):78 –85, 2002.

[14] A. Pecchia, L. Salamandra, L. Latessa, B. Aradi, T. Frauenheim, and A. Di Carlo. Atomistic modeling of gate-all-around si-nanowire field-effect transistors. *IEEE Trans. Electron Devices*, 54(12):3159 –3167, 2007.

[15] F. Poupaud and C. Ringhofer. Semi-classical limits in a crystal with exterior potentials and effective mass theorems. *Comm. Partial Differential Equations*, 21(11-12):1897–1918, 1996.

[16] C. Sparber. Effective mass theorems for nonlinear Schrödinger equations. *SIAM J. Appl. Math.*, 66(3):820–842, 2006.

[17] S. Teufel. *Adiabatic perturbation theory in quantum dynamics*, volume 1821 of *Lecture Notes in Mathematics*. Springer-Verlag, Berlin, 2003.

[18] T. Wenckebach. *Essential of Semiconductor Physics*. Wiley, Chichester, 1999.

Chapter 3

Numerical simulations

We present in this chapter numerical simulation of the effective mass model derived in the previous chapter for a bounded ultra-scaled confined nanodevice. The model considered here consists of a sequence of one dimensional device dependent stationary Schrödinger equations, one for each energy band, in which effective quantities retain the atomistic description of the cross section and the strong confinement of the structure. In order to model a gate-all-around Field Effect Transistor, self-consistent computations include the resolution, in the whole 3D domain, of a Poisson equation describing a slowly varying macroscopic potential. A numerical description of the Schrödinger-Poisson system is detailed. Then, simulations of the electron transport in a simplified one wall carbon nanotube are presented.

3.1 Introduction

In this chapter, the effective mass model, obtained in Chapter 2 for an infinite wire, in used to compute the 1D scattering states of electrons moving in a bounded nanodevice under the action of an external applied potential and of the self-consistent potential generated by the electrons in the 3D structure. The 3D Poisson equation for the electrostatic potential requires the definition of the 3D macroscopic charge density, that is obtained coupling the 1D densities carried by each n^{th} band with the 2D confinement densities given by average of the Bloch function densities. To summarize, the model used in the simulations consists of two steps. The first step requires the solution (to be done once, for a given device) of a generalized Bloch problem (on a 3D cell) to provide, in particular, the effective mass for each band. The second step is the resolution of the coupled stationary 1D Schrödinger – 3D Poisson system, where the physical quantities computed in the previous step are incorporated. We refer to [15] (and Chapter 4) for a diffusive transport model that is adapted to the peculiarities of nanowires, where the device dependent physical quantities are defined as here through the solution of a Bloch problem. Finally, we point out that our approach differs from the subband decomposition method ([23, 4], e.g), where the

confinement is taken into account during the Schrödinger-Poisson iterative algorithm, solving at each iteration an eigenvalue problem on slices perpendicular to the transport direction.

In order to assess the capability of the model to describe the transport in a strongly confined structure, numerical experiments are performed for a very simplified one wall carbon nanotube. The model is able to incorporate relevant physical features, such as band effects, providing qualitatively accurate current–voltage characteristics. Moreover, the dimension reduction for the transport problem allows for computationally efficient simulations. A similar approach, that amounts to 1D transport problems in each band and 3D electrostatic computations, has been used in [18], where simulation of transport in a silicon nanowire are given in the non degenerate case. We also mention that in [11] and [12], the band effects are taken into account using a high order approximation of the dispersion relation in a subband decomposition framework.

This chapter is organized as follows. A self–consistent Schrödinger–Poisson model is presented in Section 3.2. Section 3.3 collects the equations actually used in the simulation of transport in a nanotube and describes the iterative algorithm. Finally, the numerical experiments are presented in Section 3.4.

3.2 The stationary 1D Schrödinger - 3D Poisson problem

A FET (Field Effect Transistor) based on a nanowire or a nanotube is described by a bounded 3D domain defined as $\Omega = (x_L, x_R) \times \omega_\epsilon$ where (x_L, x_R) denotes the bounded longitudinal section and ω_ϵ denotes the 2D cross-section. The longitudinal direction of the FET is described by a sequence of 1D Schrödinger equations of the form (2.4.1) on (x_L, x_R). The system is considered as an open quantum system : electrons are injected from the leads considered as reservoirs, they travel through the channel (active region) and they leave the device through another reservoir. Transparent Boundary Conditions TBCs [10, 17, 2] are used to complete the system. More precisely, TBCs are computed assuming that in the leads the potential V_{nn} is constant, equal to $V_{nn}(x_L)$ in the left lead (Source contact) and equal to $V_{nn}(x_R)$ in the right lead (Drain contact). Then, the plane waves, solutions in the leads, are linked to the solution inside (x_L, x_R) via continuity conditions (for the wave function and its derivative).

For each n^{th} band and for each wave vector k, we consider the stationary Schrödinger equation

$$-\frac{1}{2m_n^*}\partial_{xx}\psi_n^k(x) + V_{nn}(x)\psi_n^k(x) = \mathcal{E}_n^k\psi_n^k(x), \qquad x \in (x_L, x_R), \tag{3.2.1}$$

with $\mathcal{E}_n^k = \frac{k^2}{2m_n^*} + V_{nn}(x_L)$ if $k > 0$ and with $\mathcal{E}_n^k = \frac{k^2}{2m_n^*} + V_{nn}(x_R)$ if $k < 0$. The TBCs take the form

$$\partial_x\psi_n^k(x_L) + \imath k\psi_n^k(x_L) = 2\imath k \quad \text{and} \quad \partial_x\psi_n^k(x_R) = \imath p_+(k)\psi_n^k(x_R) \quad \text{for} \quad k > 0, \tag{3.2.2}$$

$$\partial_x\psi_n^k(x_R) + \imath k\psi_n^k(x_R) = 2\imath k \quad \text{and} \quad \partial_x\psi_n^k(x_L) = -\imath p_-(k)\psi_n^k(x_L) \quad \text{for} \quad k < 0, \tag{3.2.3}$$

where

$$p_{\pm}(k) = \sqrt{k^2 \mp 2m_n^*(V_{nn}(x_R) - V_{nn}(x_L))}$$

We point out that the "memory" of the cross-section is encoded in the effective mass m_n^* given by (2.4.2) and in the effective potential $V_{nn}(x)$ defined in (2.4.4).

In the degenerate case, if E_n has multiplicity α_n, a system of dimension α_n, in the form (2.4.6) has to be considered. Accordingly, TBC's for systems must be introduced. As in the scalar case, plane wave solutions in the leads are computed, assuming constant potential. From the dispersion relation the group velocity is obtained and comparison of the sign of the group velocities with those of the wave vectors allows to identify the ingoing and the outgoing waves. Finally, the TBC's are derived, as in the single Schrödinger equation case, by eliminating the reflection and the transmission coefficients, giving a system of dimension α_n, which turns out to be a matrix form of equations (3.2.2) or (3.2.3). In Appendix A, we present the derivation of TBC's for a double eigenvalue with two positive effective masses. We also refer to [3] for the derivation in the case of a two-band Schrödinger model with a coupling in the kinetic part.

Next, in an open system electrons are considered in mixed states and the 1D density carried by the n^{th} band N_{1D}^n is given superimposing the densities of states injected from the reservoirs, that is

$$N_{1D}^n(x) = \int_{\mathbb{R}} \phi_n(k)|\psi_n^k(x)|^2 dk, \tag{3.2.4}$$

where $\phi_n(k)$ characterizes the electron injection from the reservoirs. In the subsequent simulation, the Boltzmann statistics is used (see Section 3.3.4).

The electrostatic behavior of the device is described by the self-consistent electrostatic potential solution of a Poisson equation in the 3D device. In view of Remarks 2.3.3 and 2.4.4, the 3D macroscopic charge density $\rho(x,z)$ (entering in the second member of the Poisson equation) is computed as superposition of densities in each band by means of the relation

$$\rho(x,z) = \sum_{n\in\mathbb{N}} N_{1D}^n(x) g_{nn}(\frac{z}{\epsilon}) \qquad (x,z) \in (x_L, x_R) \times \omega_\epsilon, \tag{3.2.5}$$

where the $g_{nn}(z)$, defined in (2.3.3), takes into account the confinement part of the wave function and $N_{1D}^n(x)$ is the 1D density carried by n^{th} band given by (3.2.4). In the degenerate case, the 3D charge density is computed by

$$\rho(x,z) = \sum_{n\in\mathbb{N}} \sum_{\alpha=1}^{\alpha_n} \sum_{\alpha'=1}^{\alpha_n} N_{1D}^{(n,\alpha\ n,\alpha')}(x) g_{(n,\alpha\ n,\alpha')}(\frac{z}{\epsilon}) \qquad (x,z) \in (x_L, x_R) \times \omega_\epsilon, \tag{3.2.6}$$

where $g_{(n,\alpha\ n',\alpha')}$ and $N_{1D}^{(n,\alpha\ n,\alpha')}$ are respectively defined analogously to (2.3.3) and (3.2.4). In this case, a coupling occurs between the energy bands corresponding to the same eigenvalue (see Remark 2.4.5).

Finally, the total current density is given by

$$J(x) = \sum_{n\in\mathbb{N}} J_n(x), \qquad x \in (x_L, x_R), \tag{3.2.7}$$

where the current density in the n^{th} band is expressed by

$$J_n(x) = \frac{1}{m_n^*} \int_{\mathbb{R}} \phi_n(k) \Im m\Big(\overline{\psi_n^k(x)} \partial_x \psi_n^k(x)\Big) dk, \tag{3.2.8}$$

where $\Im m$ denotes the imaginary part. Due to the TBCs, the continuity equation is satisfied for the 1D stationnary Schrödinger equation (3.2.1) and it gives immediately that the current density J_n is independent of position. In the degenerate case, since the system (2.4.6) has a diagonal kinetic part, the conserved quantity associated with the multiple eigenvalue E_n is $\sum_{\alpha=1}^{\alpha_n} J_{n,\alpha}(x)$, where the current density $J_{n,\alpha}$ is analogous to (3.2.8). Indeed, going back to the degenerate effective mass dynamics in Chapter 2, we multiply (2.4.6) by $\overline{h_{em,n,\alpha}}$ and we take the imaginary part, obtaining

$$\frac{1}{2}\partial_t |h_{em,n,\alpha}|^2 = \Im m\Big(- \frac{1}{2m_{n,\alpha}^*} \partial_{xx} h_{em,n,\alpha} \overline{h_{em,n,\alpha}} + \sum_{\alpha'=1}^{\alpha_n} V_{(n,\alpha\ n,\alpha')} h_{em,n,\alpha'} \overline{h_{em,n,\alpha}} \Big).$$

Summing on each band, since $\Im m\big(h_{em,n,\alpha}\overline{h_{em,n,\alpha'}} + h_{em,n,\alpha'}\overline{h_{em,n,\alpha}}\big) = 0$ and $V_{(n,\alpha\ n,\alpha')} = V_{(n,\alpha'\ n,\alpha)}$, it gives the conservation law

$$\sum_{n\in\mathbb{N}} \sum_{\alpha=1}^{\alpha_n} \left(\partial_t |h_{em,n,\alpha}|^2 + \partial_x \Big(\frac{1}{m_{n,\alpha}^*} \Im m(\overline{h_{em,n,\alpha}} \partial_x h_{em,n,\alpha}) \Big) \right) = 0.$$

We point out that the density which enters in this conservation law is the one associated with the transport and it is not the 3D density used for seft-consistent computations (see Remark 2.4.5). Therefore, the total current density in the degenerate case is defined by

$$J(x) = \sum_{n\in\mathbb{N}} \sum_{\alpha=1}^{\alpha_n} J_{n,\alpha}(x), \qquad x \in (x_L, x_R). \tag{3.2.9}$$

To summarize, the model consists of two steps (see Fig.3.1). The first step requires the resolution of the generalized Bloch problem (2.3.1) in the primitive cell, and it provides the energies, the effective masses and the functions (2.3.3). This computation is done only once for a given device. We point out that these quantities depend not only on the material, but also on the given device, e.g on the geometrical structure and on the growing orientation of the wire. We also emphasize that the model relies on an atomistic computation in the primitive cell and not in the entire structure. Then, the second step consists of the resolution of the coupled Schrödinger-Poisson system, where the physical quantities computed in the previous step are included. The 1D Schrödinger equations with open boundary conditions describe the electron transport along the wire, whereas the 3D Poisson equation models the electrostatic potential in the entire structure. The reduced dimensionality of the Schrödinger equations greatly decreases the computational time in the simulations.

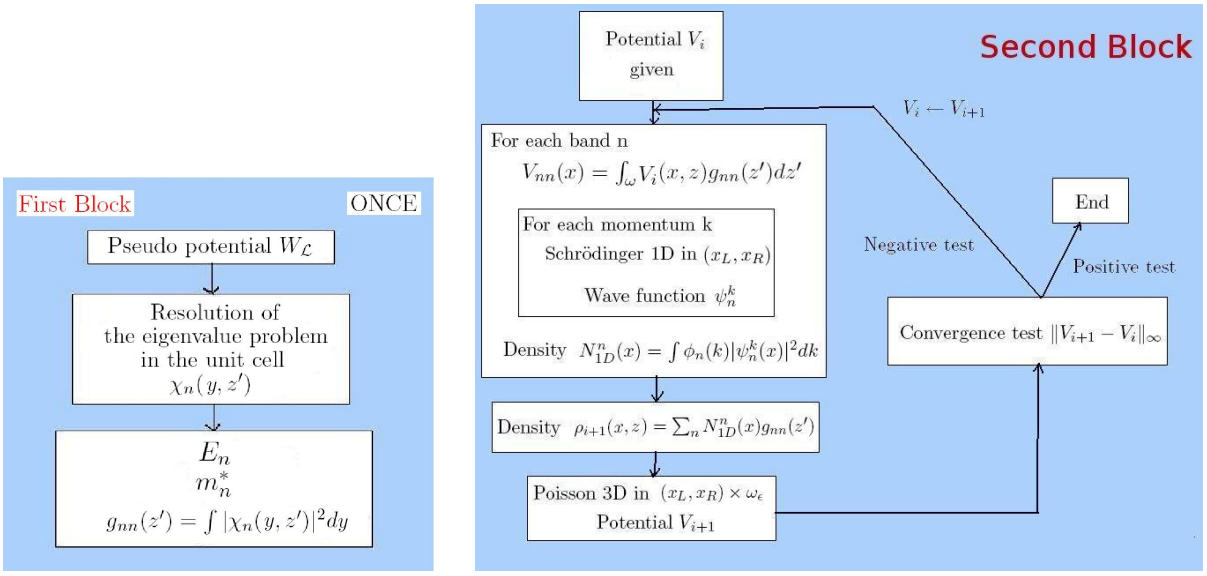

Figure 3.1: General organization of the effective mass model.

3.3 Numerical implementation for a nanotube

3.3.1 Modeled device

The numerical simulations that will be presented in Section 3.4 aim at testing the capability of the model to describe the electron transport in an ultra-scaled confined structure and they will be carried out in a very simplified case, a one–wall carbon nanotube with a cross-section made of 12 atoms disposed on a squared frame, surrounded by one atom layer of dielectric acting like an insulator.

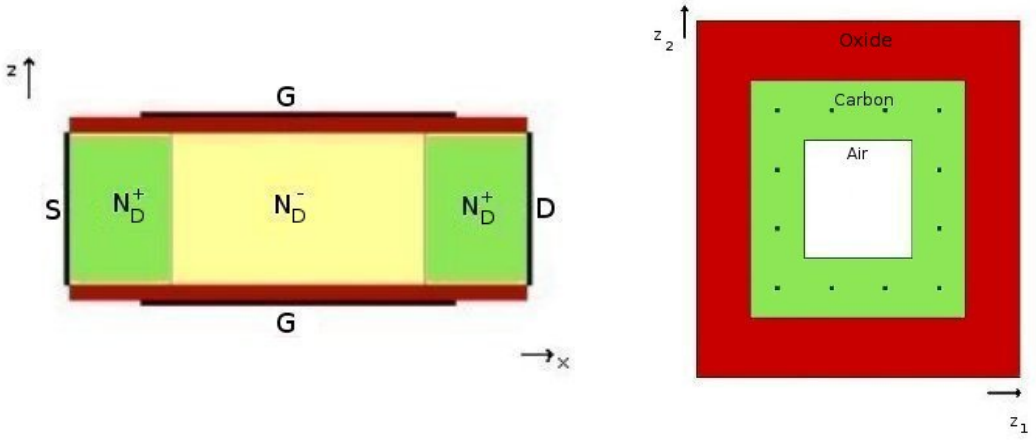

Figure 3.2: Longitudinal section (left) and transversal cross-section (right) of the simplified carbon nanotube with a squared transversal cross-section containing 12 atoms.

The transport problem is solved for a gate-all-around FET (Field Effect Transistor) with channel length equal to 10 nm doped with a donor concentration equal to $N_D^- = 10^{21}$ m^{-3}, with Source and Drain regions 10 nm long, largely doped ($N_D^+ = 10^{26}$ m^{-3}). A schematic representation of the device is given in Fig.3.2. The x variable corresponds to the transport direction, whereas (z_1, z_2) describes the 2D cross-section. The lattice spacing ϵ for carbon is equal to 3.57 Å. Therefore, the wire cross-section edge l (equal to $6\epsilon \approx 2nm$) is tiny compared to the longitudinal length L equals to 30 nm.

3.3.2 Pseudo-potential

The potential $W_{\mathcal{L}}$ generated by the crystal lattice and used to compute the Bloch functions (2.3.1) is visualized in Fig.3.3. It is a pseudo-potential used by [25] for *ab-initio* atomistic-based electronic density calculations for carbon nanotubes. In correspondence of each nucleus, we take $W_{\mathcal{L}}(r) = \sum_{i=1}^{3} A_i \exp(-a_i r)$, where r is the distance to the nucleus and the coefficients A_i and a_i have been defined in [19] to reproduce the band structure of the carbon nanotube. A large potential barrier (we chose 15 eV) is used at the boundaries of the nanotube to take in account the dielectric layer.

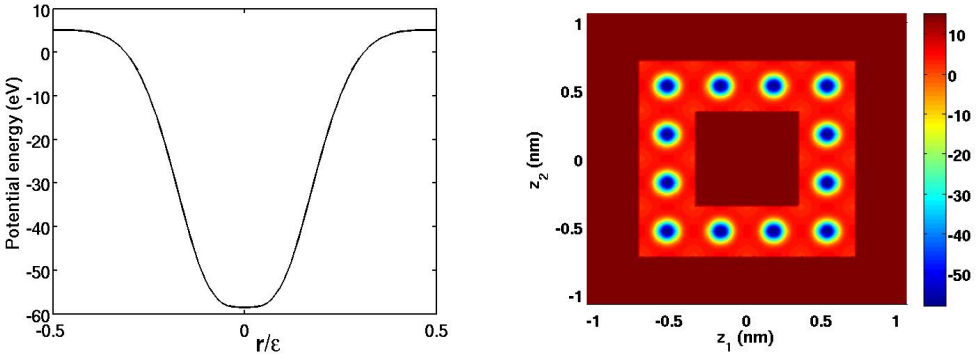

Figure 3.3: Pseudo-potential energy (eV) : 1D $W_{\mathcal{L}}(r)$ (left) and $W_{\mathcal{L}}(x = 0, z)$ (right).

3.3.3 Implemented equations

For the sake of completeness, we recall the equations which are used in the simulations, writing them in unscaled form. First, the Bloch waves $\chi_n^\epsilon(x, z')$ are the normalized eigenfunctions of the following problem in the cell $\mathcal{U}_\epsilon = (-\epsilon/2, \epsilon/2) \times \omega$,

$$\begin{cases} -\frac{\hbar^2}{2m_e}\Delta\chi_n^\epsilon + W_{\mathcal{L}}\chi_n^\epsilon = E_n\chi_n^\epsilon. \\ \chi_n^\epsilon(x, z') = 0 \quad \text{on } \partial\omega, \quad \chi_n^\epsilon \ \epsilon\text{-periodic in } x, \end{cases} \tag{3.3.1}$$

where ϵ is the lattice spacing, $\hbar$ is the reduced Planck constant and m_e is the electron mass. Although not all the eigenvalues of (3.3.1) are simple in the present case, still a decoupled

system can be considered. Actually, it turns out that, for the problem under consideration with the gate-all-around, the off-diagonal terms in the potential matrix ($V_{(n,\alpha\ n,\alpha')}$ with $\alpha \neq \alpha'$) are negligible. Then, the transport is described by a set of 1D Schrödinger equations with TBCs, which can be expressed, for a positive wave vector $k > 0$ (see (3.2.1) with (3.2.2)), as follows

$$\begin{cases} -\dfrac{\hbar^2}{2m_n^*}\partial_{xx}\psi_n^k(x) + V_{nn}(x)\psi_n^k(x) = \Big(\dfrac{\hbar^2k^2}{2m_n^*} + V_{nn}(x_L)\Big)\psi_n^k(x), \quad x \in (x_L, x_R), \\ \partial_x\psi_n^k(x_L) + \imath k\psi_n^k(x_L) = 2\imath k, \\ \hbar\partial_x\psi_n^k(x_R) = \imath\sqrt{\hbar^2k^2 - 2m_n^*\big(V_{nn}(x_R) - V_{nn}(x_L)\big)}\psi_n^k(x_R), \end{cases} \tag{3.3.2}$$

where

$$\frac{m_e}{m_n^*} = 1 - \frac{2\hbar^2}{m_e}\sum_{q\neq n}\frac{P_{nq}P_{qn}}{E_n - E_q} \quad \text{with} \quad P_{nq} = \int_{\mathcal{U}_\epsilon} \partial_x\chi_q^\epsilon\ \overline{\chi_n^\epsilon}dxdz', \tag{3.3.3}$$

and

$$V_{nn}(x) = \int_\omega V(x, \epsilon z')g_{nn}(z')dz' \quad \text{with} \quad g_{nn}(z') = \int_{-\epsilon/2}^{\epsilon/2}|\chi_n^\epsilon(x, z')|^2dx. \tag{3.3.4}$$

For negative wave vector $k < 0$, the equations are similar (see (3.2.1) with (3.2.3)).

Next, we compute the 1D charge densities (3.2.4) for each band n and then the macroscopic 3D charge density ρ (3.2.5). Finally, the electrostatic potential V_P is solution of the following 3D Poisson equation

$$-\nabla\big(\epsilon_r(z)\nabla V_P(x,z)\big) = \frac{q}{\epsilon_0}\big(N_D(x,z) - \rho(x,z)\big), \qquad (x,z) \in (x_L, x_R)\times\omega_\epsilon. \tag{3.3.5}$$

q is the elementary charge, ϵ_0 the permittivity in vacuum, ϵ_r the relative permittivity and N_D the prescribed doping density (null in the oxide and the air regions, and given as in Section 3.3.1 in the carbon region). Equation (3.3.5) is supplemented by boundary conditions that will be made explicit in Section 3.3.5. Notice that this equation gives the potential V_P (expressed in Volts), instead the Schrödinger equation (3.3.2) is written in terms of an energy V (expressed in Joules). They are linked by the relation $V = -qV_P$.

Finally, the current density in physical variables is given by

$$J(x) = \sum_{n\in\mathbb{N}}\frac{q\hbar}{m_n^*}\int_{\mathbb{R}}\phi_n(k)\Im m\Big(\overline{\psi_n^k(x)}\partial_x\psi_n^k(x)\Big)dk, \qquad x \in (x_L, x_R). \tag{3.3.6}$$

3.3.4 Distribution function and Fermi level

In this work, we choose the Boltzmann statistic to describe the distribution ϕ_n used to compute the 1D charge densities (3.2.4). It is typically defined by

$$\phi_n(k) = \frac{C}{\sqrt{m_n^*}}e^{-\left(\frac{\hbar^2k^2}{2m_n^*} + E_n - \mu_{eq}\right)/(k_BT)} \tag{3.3.7}$$

where C is a physical constant independent of the band index, k_B the Boltzmann constant, T the lattice temperature and μ_{eq} the Fermi level at thermal equilibrium.

Remark 3.3.1. We notice that $\phi_n(k)$ does not depend on the contact lead under consideration, and it is the same in the non equilibrium case. To be precise, we should write $\phi_n(k) = \phi_n^L(k)$ for $k > 0$ and $\phi_n(k) = \phi_n^R(k)$ for $k < 0$, being respectively the statistics of the electrons injected at $x = x_L$ and at $x = x_R$. These statistics correspond to

$$\phi_n^{L,R}(k) = \frac{C}{\sqrt{m_n^*}} e^{-\left(\frac{\hbar^2 k^2}{2m_n^*} + V_{nn}(x_{L,R}) + E_n - \mu_n^{L,R}\right)/(k_B T)}$$

where $\mu_n^{L,R} = \mu_{eq} + V_{nn}(x_{L,R})$. However, a cancellation occurs in the exponent, since both the energy $\mathcal{E}_n^k$ and the Fermi level μ_{eq} are shifted by the same potential energy V_{nn}. It gives (3.3.7).

Next, we have to determine the Fermi level at thermal equilibrium. More precisely, we compute directly the constant term $Ce^{\mu_{eq}/(k_B T)}$. It is obtained under the hypothesis of quasi-neutrality at the boundaries

$$\int_{\omega_\epsilon} \Big(\rho(x_c, z) - N_D(x_c, z)\Big) dz = 0, \tag{3.3.8}$$

where $x_c = x_L$ or $x_c = x_R$. We suppose that the potential V is constant along the transport direction and consequently all the wave functions ψ_n^k contributing to ρ have unitary modulus. After calculations, we obtain the explicit formula

$$Ce^{\mu_{eq}/(k_B T)} = \frac{\int_{\omega_\epsilon} N_D(x_c, z) dz}{\sum_n \int_{\mathbb{R}} \frac{1}{\sqrt{m_n^*}} e^{-\left(\frac{\hbar^2 k^2}{2m_n^*} + E_n\right)/(k_B T)} dk}. \tag{3.3.9}$$

3.3.5 Poisson boundary conditions

In this subsection, we discuss the choice of boundary conditions for the 3D Poisson equation (3.3.5). The boundary $\partial\Omega$ of the computational domain is split in three parts: $\partial\Omega = \Gamma_C \cup \Gamma_G \cup \Gamma_N$.

Γ_C corresponds to the ohmic Source and Drain contacts i.e. $\Gamma_C = \{(x, z) \in \partial\Omega \text{ such that } x = x_c\}$. On Γ_C, we impose a Robin boundary condition

$$\partial_x V_P + \alpha_c \Big(V_P - (V_{Applied} + V_b)\Big) = 0$$

in order to control at the same time the value and the slope of the potential. The sign of α_c is chosen to have coercivity of the bilinear form and the value of α_c is of order of $\frac{1}{L}$. $V_{Applied}$ corresponds to the applied potential at ohmic contacts. Finally, V_b is the *built-in* potential defined, solving at the contacts, a 2D Poisson equation

$$\begin{cases} -\nabla(\epsilon_r \nabla V_b(z)) = \frac{q}{\epsilon_0} N_D(x_c, z) - \frac{q}{\epsilon_0} \rho_{2D}(z), & z \in \omega_\epsilon, \\ \partial_\nu V_b = 0, \quad \int_{\omega_\epsilon} V_b(z) dz = 0. \end{cases} \tag{3.3.10}$$

We notice that V_b is the same at Source and Drain contact because of the same doping density. Moreover, the density ρ_{2D} does not depend on the potential. Indeed, we make the same

assumption than for the Fermi level calculation (i.e. V constant in the transport direction) and thus the density can be expressed explicitly (using (3.2.5), (3.2.4), (3.3.7) and (3.3.9)). Fig.3.4 displays the shape of the 2D *built-in* potential for our nanotube device.

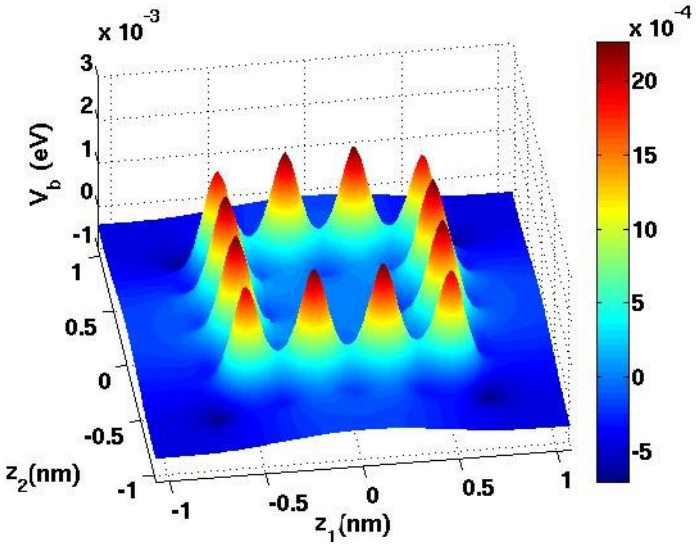

Figure 3.4: Shape of the 2D built-in potential energy V_b (eV).

Next, Γ_G corresponds to the gate, that is chosen here all–around (see Fig.3.2), and a gate potential V_G is applied on Γ_G to modulate the number of free electrons. Finally, we impose homogeneous Neumann boundary conditions in the remain boundary domain $\Gamma_N = \partial\Omega\backslash(\Gamma_C \cup \Gamma_G)$. To sum up, we supplement the Poisson equation (3.3.5) with the following boundary conditions

$$\begin{cases} \partial_x V_P + \alpha_c\Big(V_P - (V_{Applied} + V_b)\Big) = 0 & \text{on } \Gamma_C, \\ V_P = V_G & \text{on } \Gamma_G, \\ \partial_\nu V_P = 0 & \text{on } \Gamma_N. \end{cases} \tag{3.3.11}$$

3.3.6 Algorithm

We now discuss the implementation of the entire problem (3.3.1)-(3.3.5) emphasizing the delicate numerical points.

First block : to solve the eigenvalue problem in the primitive cell

The starting point is to solve the eigenvalue problem (3.3.1) to compute the smallest eigenvalues (corresponding to the bands with the lowest energies). It is discretized with Q_1 finite elements

on parallelepipeds. This choice is motivated by the fact that the mesh should preserve the symmetries of the device structure. Also, the use of tensorial basis functions makes easier the computation and the assembling of matrices. Moreover, a tensorial mesh between the 2D cross section and the 1D longitudinal domain is essential for our model. At different steps of the algorithm, we need to transform a 3D quantity into a 1D one, or inversely. With a tensorial mesh, the numerical transformations (in particular numerical integrations) are more accurate. Finally, due to the fine pattern of the pseudo-potential (see Fig.3.3), a fine mesh is necessary. The 1D lattice spacing (of length ϵ) must be decomposed by a minimum of 20 discretization points, which gives, for a 3D uniform mesh, about 250 000 degrees of freedom for the finite element space.

Thus, the problem (3.3.1) is reduced to a generalized eigenvalue problem of the form $Au = \lambda Bu$, solved using the library Arpack [16]. This software is based upon an algorithmic variant of the Arnoldi process called the Implicitly Restarted Arnoldi Method [24]. When the matrix A is symmetric, it is reduced to a variant of the Lanczos process called the Implicitly Restarted Lanczos Method. These variants may be viewed as a synthesis of the Arnoldi/Lanczos process with the Implicitly Shifted QR technique that is suitable for large problems. An advantage of this library is that it has a reverse communication interface. The user has to specify a routine for the matrix-vector multiplication and another one to solve a linear system. Consequently, users can work with any matrix storage format and in particular with sparse matrix storage format. In our Fortran90 code, we use the CSR (Compressed Sparse Row) format which is adequate for the manipulation of very large sparse matrices since it is less demanding in memory. Of course, the matrix assembling procedure (linked to the finite element method) as well as other matrix operations are implemented to be compatible with this format.

Second block : to solve the Schrödinger-Poisson problem

The previous block, done only once for the given device, provides the energies E_n, the effective masses m_n^* and the functions g_{nn}'s. These quantities are inserted in the Schrödinger-Poisson problem (3.3.2)-(3.3.5). The first step is to compute the solution of (3.3.10) to get the *built-in* potential V_b at the ohmic contacts. The procedure is then initialized by taking $V(., z) = V_b(z)$. Next, we consider the whole system (3.3.2)-(3.3.5) at thermal equilibrium (for zero applied Drain–Source voltage). Finally, we consider the resolution of the Schrödinger-Poisson system when a Drain-Source voltage V_{DS} is applied. We start from the obtained potential at thermal equilibrium and we increment the voltage by steps of 0.02 V. At each outer iteration, the computed potential is used to initialize the inner iteration algorithm. To conclude, all this procedure (initialization, thermal equilibrium solution and Drain–Source voltage continuation) is repeated for different gate voltage V_G.

Here we detail the discretization schemes and the iterative algorithm for the inner solution of the Schrödinger–Poisson problem (3.3.2)-(3.3.5). Because of the highly nonlinear coupling

between the density and the potential equations, the inner iteration procedure is done by an iterative method of Gummel type. It is described in the following steps :

1) For a given 3D potential V_P^{old}, we compute a 1D potential V_{nn} for each n^{th} band using (3.3.4).

2) The 1D Schrödinger equation with TBCs is solved for each n^{th} band and each wave vector k. For $k > 0$, equation (3.3.2) is transformed into an initial value problem

$$\begin{cases} -\dfrac{\hbar}{2m_n^*}\partial_{xx}\varphi_n^k(x) + V_{nn}(x)\varphi_n^k(x) = \Big(\dfrac{\hbar^2k^2}{2m_n^*} + V_{nn}(x_L)\Big)\varphi_n^k(x), \\ \varphi_n^k(x_R) = 1, \\ \partial_x\varphi_n^k(x_R) = \imath\sqrt{\hbar^2k^2 - 2m_n^*\big(V_{nn}(x_R) - V_{nn}(x_L)\big)}. \end{cases} \tag{3.3.12}$$

It suffices to normalize $\varphi^k(x)$ by $2\imath k/\big[\partial_x\varphi_n^k(x_L) + 2\imath k\varphi_n^k(x_L)\big]$ to recover $\psi_n^k(x)$. The negative wave vector case is treated analogously. The ODE is then discretized with a Crank-Nicolson scheme, which is a conservative scheme and it avoids numerical dissipation for large k's. Indeed, in Fig.3.5, we present the modulus $|\psi_n^k(x)|^2$ obtained for $k = 1.10^{10}$ m^{-1} and for a constant potential $V_{nn}(x)$, with a fourth-order Runge-Kutta scheme (left) and a Crank-Nicolson scheme (right). The space step is chosen relatively large (200 discretization points) in order to show how the lack of conservation properties for the Runge-Kutta scheme affects the results. It results that the modulus stays constant equal to 1 with the Crank-Nicolson scheme instead the solution blows-up with the Runge-Kutta scheme.

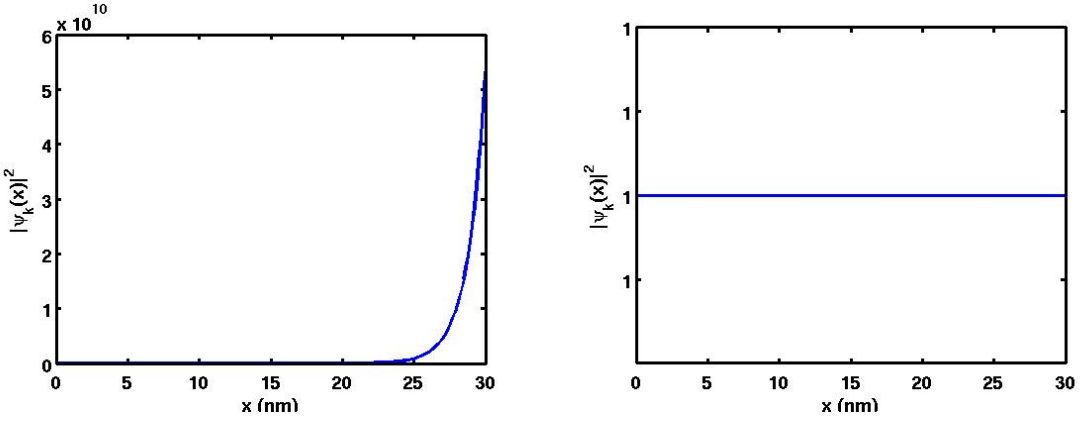

Figure 3.5: $|\psi_n^k(x)|^2$ obtained with a Runge-Kutta (left) and a Crank-Nicolson (right) scheme.

Numerous efficient schemes have been studied for the resolution of the stationary Schrödinger equation. We mention e.g. the recent works [20, 5, 1] where a WKB approximation enables the use of coarser space grids to compute with accuracy the highly oscillating wave functions. Another approach (see [7, 8, 6] e.g.) consists to derive an asymptotic reduced model by considering the regime of a finite number of resonant states. Nevertheless, we focus in this chapter to

the implementation of our entire Schrödinger-Poisson model, where the computation of the 1D Schrödinger equations is not so expensive compared to the resolution of the 3D Poisson equation. That is the reason why we prefer to use a simple Crank-Nicolson scheme.

3) We can compute the 1D charge density N_{1D}^n (3.2.4) for each n^{th} band and, afterwards, the 3D charge density ρ (3.2.5). To calculate the density (3.2.4), we use a numerical integration method. For our work, the trapezoidal rule is adequate. A k_{max} is fixed such that the exponential in ϕ_n (3.3.7) is small enough for this k_{max}. Since there are not resonant energies for our simplified device, we use here a constant momentum step Δk, enough refined to take into account the contribution of each significant energy. Nevertheless, it is possible to implement an adaptative momentum mesh size method (as it is developed in [22] for example) detecting peaks in the transmission coefficients. It allows to optimize the number of Schrödinger equations to be solved. Finally, we point out that it is not necessary to store in memory all the wave functions since the trapezoidal numerical integration can be computed progressively inside the loop on the wave vectors.

4) We solve the 3D Poisson equation (3.3.5) with the boundary conditions (3.3.11) using Q_1 finite elements on parallelepipeds and we obtain a new potential V_P^{new}. To solve the linear system for the Poisson equation, we choose the routine MI26 of the HSL library [14]. It implements the BiCGStab (BiConjugate Gradient Stabilized) method which is an efficient iterative method for sparse matrices.

The high nonlinearity of the coupled Schrödinger–Poisson system is the most delicate step of the procedure. A simple–minded iterative algorithm fails to converge and a Newton-Raphson method is computationally expensive. We use an iterative method of Gummel type, which consists to introduce in the Poisson equation (3.3.5) a function $\mathcal{T}$ depending exponentially of V_P

$$-\nabla\big(\epsilon_r \nabla V_P(x,z)\big) = \frac{q}{\epsilon_0} N_D(x,z) - \frac{q}{\epsilon_0}\rho[V_P](x,z)\frac{\mathcal{T}[V_P]}{\mathcal{T}[V_P]}.$$

A natural choice (because of the Boltzmann statistics) is to take $\mathcal{T}[V_P] = \exp(\frac{qV_P}{k_{\mathcal{B}}T})$. Then the iterative scheme is given by

$$-\nabla\big(\epsilon_r \nabla V_P^{new}(x,z)\big) = \frac{q}{\epsilon_0} N_D(x,z) - \frac{q}{\epsilon_0}\rho[V_P^{old}](x,z)\exp\Big(\frac{q}{k_{\mathcal{B}}T}(V_P^{new} - V_P^{old})\Big). \tag{3.3.13}$$

Intuitively, when the difference between the new potential V_P^{new} and the old potential V_P^{old} becomes important, the contribution of the density ρ is less significant for the calculation of V_P^{new}. Numerically, we use a linear version of this method which is obtained by a Taylor expansion

$$-\nabla\big(\epsilon_r \nabla V_P^{new}(x,z)\big) = \frac{q}{\epsilon_0} N_D(x,z) - \frac{q}{\epsilon_0}\rho[V_P^{old}](x,z)\Big(1 + \frac{q}{k_{\mathcal{B}}T}(V_P^{new} - V_P^{old})\Big). \tag{3.3.14}$$

The Gummel iterative algorithm has been introduced in [13] for the Drift-Diffusion model and it has been extended to the present form for a Schrödinger-Poisson system [9]. We also refer to

[23] where this method is used in the simulation of a 2D ballistic Schrödinger-Poisson system. The choice of the initial potential is essential to obtain the convergence of the Gummel method.

5) We repeat the four previous steps until the difference $\|V_P^{new} - V_P^{old}\|_{L^\infty}$ becomes sufficiently small (inferior to 10^{-5} in the presented simulations).

This entire procedure gives computationally efficient simulations upon condition that the choice of meshes is judicious. Since the high energy wave functions are strongly oscillating, a fine mesh size is needed to solve the 1D Schrödinger equations. On the contrary, the Poisson equation is solved in the whole domain and a larger mesh size is allowed in the transport direction. Therefore, in the simulations performed in Section 3.4, we solve the Schrödinger equations with 400 discretization points, whereas the mesh used for the Poisson equation contains only 50 points in the transport direction. The transition between the large discretization and the refined one is done by a linear interpolation, since the Poisson equation is solved with Q_1 finite elements. Concerning the 2D cross section, the computed quantities have always a fine pattern (see Fig.3.4, e.g.) and we use for the Poisson equation the same 2D mesh used to solve the eigenvalue problem (see Section 3.3.6). It gives a 3D finite element method for the Poisson equation with about 660 000 degrees of freedom.

3.4 Numerical results

We present in this part some results obtained for the simplified one-wall carbon nanotube described in Section 3.3.1, aiming at reproducing the qualitative behavior of the device. Therefore, the Schrödinger-Poisson system is solved only in the first three "conduction" bands. Looking at the energies E_n, the most significant gap is observed between the 40^{th} and the 41^{th}band. Consequently, we choose to consider the 41^{th}, 42^{th} and the 43^{th} bands.

In the present simulation, mode 42^{th} and mode 43^{th} coincide. Nevertheless, as already pointed out in Section 3.3.3, the computed off-diagonal potential term $V_{42,43}$ is virtually zero and the coupling of these two bands can be neglected. In Fig.3.6 the 2D quantities $g_{nn}(z)$'s are presented. We notice that the 12 ion cores of the cross–section clearly appear, showing that the g_{nn}'s retain information of the confinement and of the cross–section structure. Moreover, we point out that the two bottom pictures, corresponding to the multiple eigenvalue, coincide up to a rotation. In Appendix B, other g_{nn}'s are displayed for an artistic parenthesis. These g_{nn}'s, corresponding to large modes, are not significant from a mathematical point of view, but they have fascinating shapes.

These g_{nn}'s (as well as effective masses m_n^* and energies E_n) are included in the transport problem solved for a gate-all-around FET. We start to compute the thermal equilibrium. Then, we apply a Drain–Source voltage V_{DS}. To visualize the results, we first present 1D curves instead of 3D plots. 1D profiles of the density and of the potential are presented for a fixed gate voltage

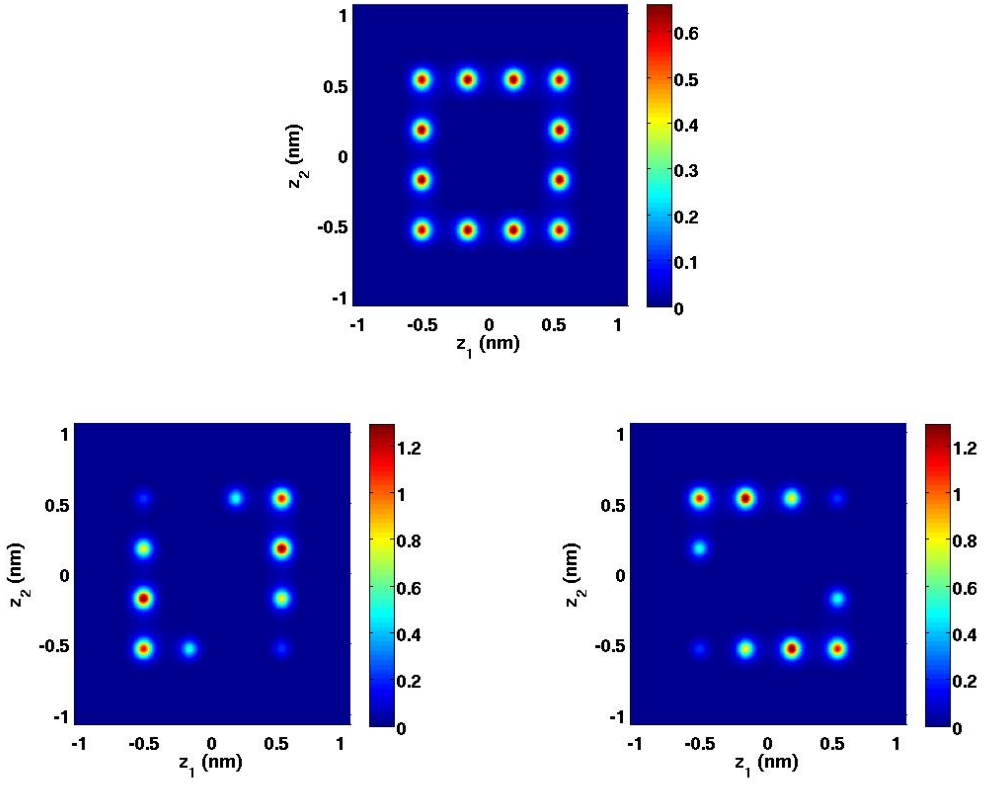

Figure 3.6: $g_{nn}(z)$ for 41^{th} mode (top), 42^{th} and 43^{th} mode (bottom, from left to right).

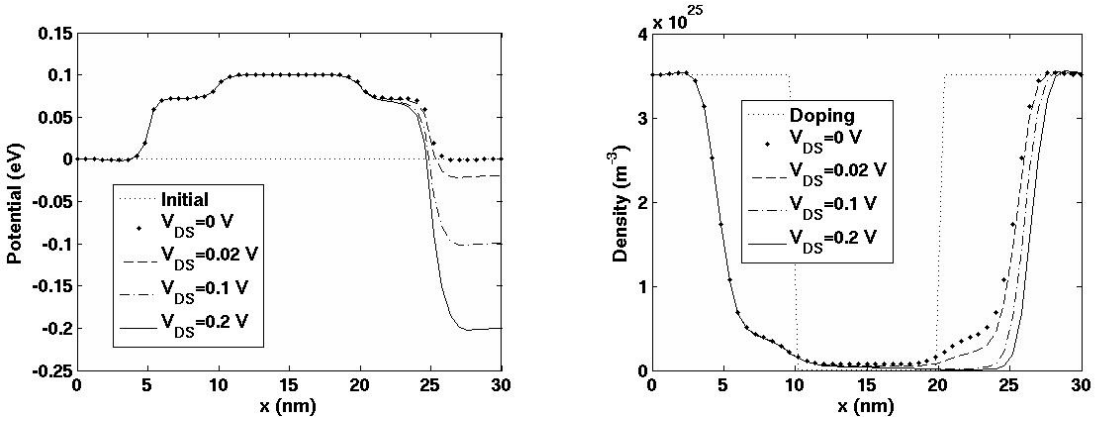

Figure 3.7: 1D potential energies (eV) (left) and 1D densities (m^{-3})(right) for different V_{DS}, with $V_G = -0.1$ V.

$V_G = -0.1$ V in Fig.3.7. These 1D curves are results of an integration of 3D quantities over the 2D wire section. In the left figure, variations at $x = 5$ nm and $x = 25$ nm are due to the gate, instead variations at $x = 10$ nm and $x = 20$ nm are consequences of the doping. We remark that the 1D potential in the channel has a value close to V_G, confirming that the transport is mainly controlled by the gate.

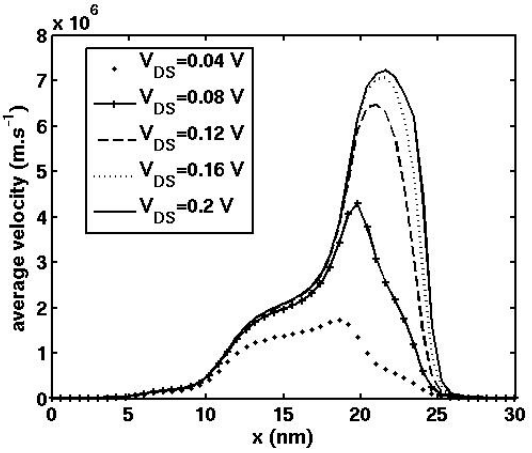

Figure 3.8: Average velocity (ms^{-1}) for $V_G = -0.1$ V.

In order to show the changes due to the voltage, that are not clearly visible from the 1D density pictures, it is interesting to plot the average velocity, defined as $v(x) = J/[q \sum_n N^n_{1D}(x)]$. Fig.3.8 illustrates how the average velocity increases with the applied Drain–Source voltage V_{DS}. It is also apparent that, for larger values of the Drain–Source voltage, velocities tend to a saturation regime (see also Fig.3.13).

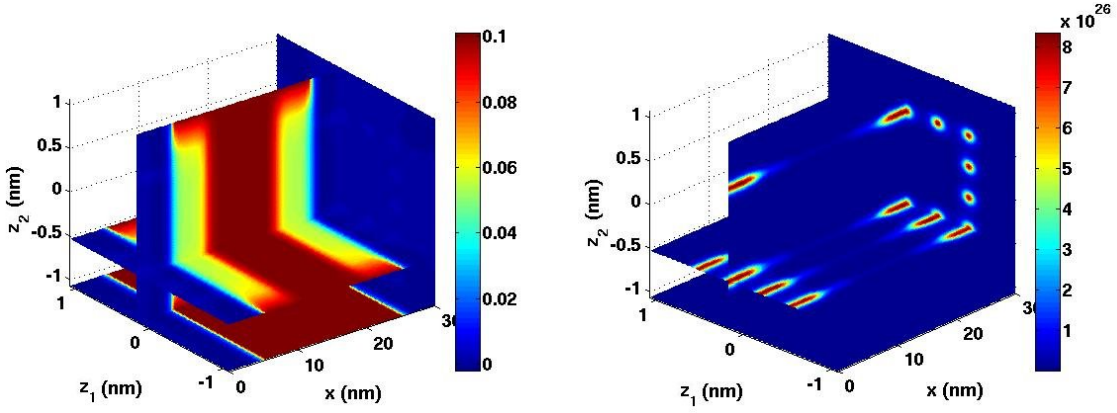

Figure 3.9: 3D potential energy (eV) (left) and 3D density (m^{-3}) (right) at thermal equilibrium for $V_G = -0.1$ V.

The description of the entire 3D device is visualized in Fig.3.9, where the 3D potential energy (left) and the 3D density (right) are plotted at thermal equilibrium for $V_G = -0.1$ V. In the

left picture of Fig.3.9 the structure of the FET is apparent, with the Source, Drain and channel regions and a clear influence of the gate. Fig.3.9 does not allow to appreciate the fine structure of the potential, that seems to be constant in the cross–section. Only at the logarithmic scale, that is used in Fig.3.12 to represent the 2D potential in the central slice ($x = 15$ nm), we can recognize the cross–section influence. The fine pattern exhibited by the plot confirm the need of the 660 000 dof's, used for the Poisson computation.

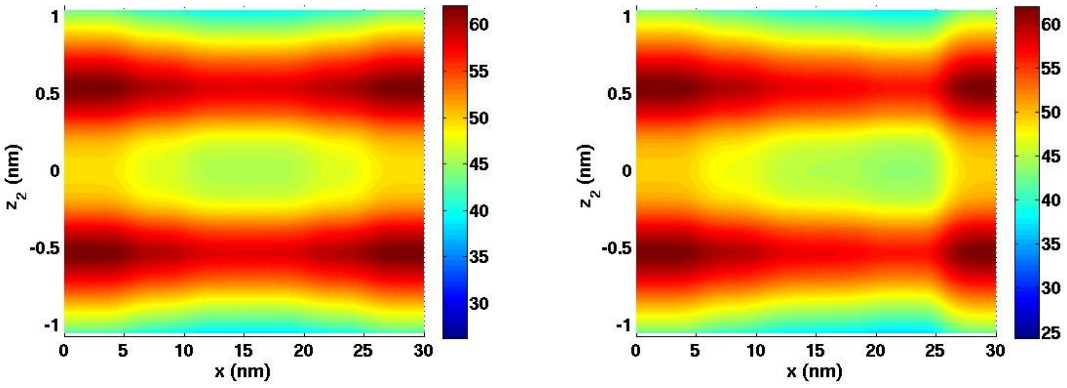

Figure 3.10: 2D slice (crossing 2 nuclei) of density in logarithmic scale at equilibrium (left) and for $V_{DS} = 0.2$ V (right), with $V_G = -0.1$ V. x-axis is the transport direction.

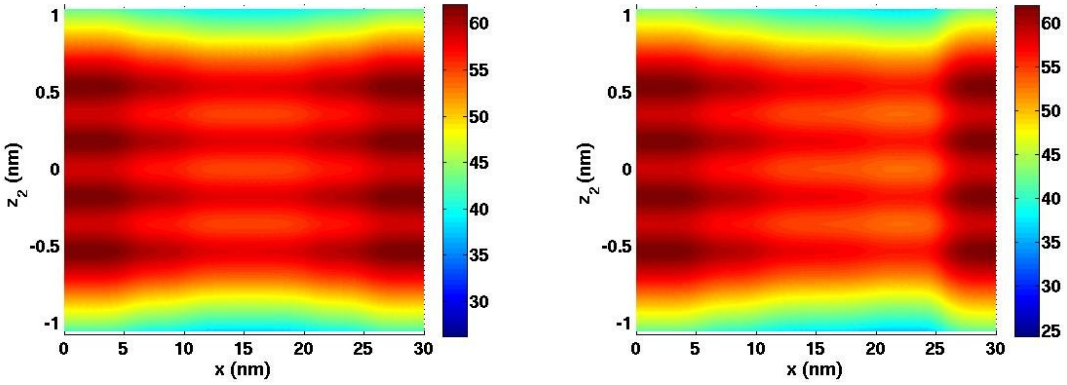

Figure 3.11: 2D slice (crossing 4 nuclei) of density in logarithmic scale at equilibrium (left) and for $V_{DS} = 0.2$ V (right), with $V_G = -0.1$ V. x-axis is the transport direction.

The right picture of Fig.3.9 allows to visualize the formation of a channel for each nucleus. The transport from Source to Drain is illustrated by Figs.3.10 and 3.11, that represent the density, in logarithmic scale, in a 2D slice along the transport direction (x-axis in the pictures). Fig.3.10 shows a slice that crosses two ions and Fig.3.11 corresponds to a slice that crosses four ions. Comparing the thermal equilibrium pictures (left) with the ones for $V_{DS} = 0.2$ V (right), we observe the electron motion from the left to the right. Also, the different sharpness of the

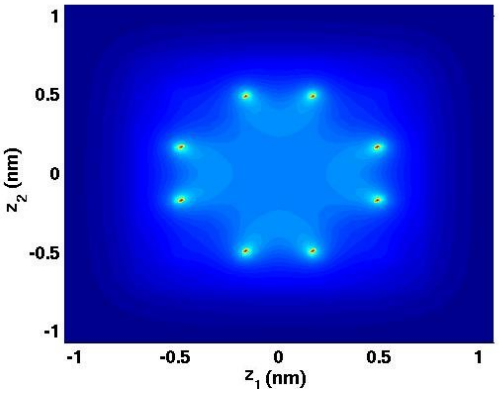

Figure 3.12: 2D cross-section at $x = 15$ nm of the potential energy in logarithmic scale at equilibrium for $V_G = -0.1$ V.

density around the ion cores in Figs.3.10 and 3.11 shows the influence of the neighboring ions.

Finally, in Fig.3.13, the output current–voltage characteristics of our simulated device (for the fixed gate voltage $V_G = -0.1$ V) are presented, plotting the total current, as well as the partial current carried by each band. As expected, the current in the first band is larger than the one in the other two bands. The second band and the third band, which correspond to the same eigenvalue, carry virtually the same current. We notice that the qualitative behavior of these curves is similar to that of the conventional MOSFETs with two typical regimes: an ohmic regime for small values of Drain-Source voltage and a quasi-saturation regime for $V_{DS} > 0.12V$.

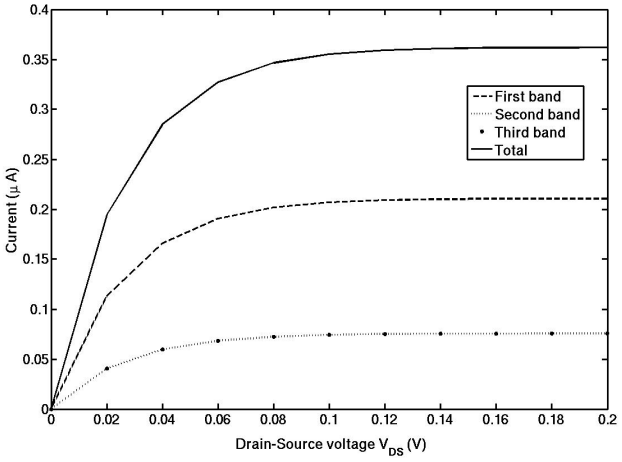

Figure 3.13: Current-voltage characteristics for $V_G = -0.1$ V.

We conclude saying that, even for this simplified problem, our model is able to capture the qualitative behavior of the most relevant physical quantities, well describing the electron transport in an ultra-scaled confined nanostructure.

Appendix A : Derivation of transparent boundary conditions for a two band system

In the case where an eigenvalue E_n has a multiplicity $\alpha_n = 2$, the stationnary Schrödinger problem is a system of the following form

$$\begin{pmatrix} -a_n\partial_{xx} & 0 \\ 0 & -b_n\partial_{xx} \end{pmatrix} \vec{\boldsymbol{\psi}}_{\boldsymbol{n}} + \begin{pmatrix} V_{(n,1\ n,1)} & V_{(n,1\ n,2)} \\ V_{(n,2\ n,1)} & V_{(n,2\ n,2)} \end{pmatrix} \vec{\boldsymbol{\psi}}_{\boldsymbol{n}} = E_n \vec{\boldsymbol{\psi}}_{\boldsymbol{n}}, \tag{3.A.1}$$

where $\vec{\boldsymbol{\psi}}_{\boldsymbol{n}} = \begin{pmatrix} \psi_{n,1} \\ \psi_{n,2} \end{pmatrix}$. $V_{(n,\alpha\ n,\alpha')}$ are the effective potentials defined analogously to (2.4.4). We remind that $V_{(n,\alpha\ n,\alpha')} = V_{(n,\alpha'\ n,\alpha)}$. Moreover, a_n and b_n are the coefficients

$$a_n = \frac{1}{2m^*_{n,1}} \qquad \text{and} \qquad b_n = \frac{1}{2m^*_{n,2}}, \tag{3.A.2}$$

where $m^*_{n,\alpha}$ are the effective masses defined in (2.4.7). By definition, $a_n \neq 0$ and $b_n \neq 0$. To simplify, in the sequel we omit index n and above all we study only the case $a_n > 0$ and $b_n > 0$ which is the more relevant case for our applications.

3.A.1. Dispersion relation

The first point is to find the dispersion relation. The idea is to look for plane wave solutions of (3.A.1) when V_{11}, V_{22} and V_{12} are constants. Thus, we suppose

$$\vec{\boldsymbol{\psi}} = e^{ik(E)x}\vec{\boldsymbol{e}}, \tag{3.A.3}$$

where $\vec{\boldsymbol{e}}$ is a unitary vector. We obtain that $\vec{\boldsymbol{\psi}}$ is solution of (3.A.1) if and only if

$$\begin{pmatrix} ak^2 + V_{11} & V_{12} \\ V_{12} & bk^2 + V_{22} \end{pmatrix} \vec{\boldsymbol{e}} = E\vec{\boldsymbol{e}}. \tag{3.A.4}$$

It is an eigenvalue problem which leads to the following dispersion relation

$$\Big(ak^2 + V_{11} - E\Big)\Big(bk^2 + V_{22} - E\Big) - V_{12}^2 = 0. \tag{3.A.5}$$

3.A.1.1. Expression of E in terms of k

First, with (3.A.5), we can express E in terms of k. So,

$$E^2 - E\Big((a+b)k^2 + V_{11} + V_{22}\Big) + abk^4 + (aV_{22} + bV_{11})k^2 + V_{11}V_{22} - V_{12}^2 = 0.$$

To simplify notations, we choose

$$A(k) = \frac{(a-b)k^2 + (V_{11} - V_{22})}{2}. \tag{3.A.6}$$

It gives, after calculations,

$$E_1(k) = bk^2 + V_{22} + A(k) + \sqrt{A(k)^2 + V_{12}^2} = ak^2 + V_{11} - A(k) + \sqrt{A(k)^2 + V_{12}^2}, \tag{3.A.7}$$

$$E_2(k) = bk^2 + V_{22} + A(k) - \sqrt{A(k)^2 + V_{12}^2} = ak^2 + V_{11} - A(k) - \sqrt{A(k)^2 + V_{12}^2}. \tag{3.A.8}$$

We point out that here E_1 and E_2 are chosen such that $E_1(k) \geq E_2(k)$. We can also compue the corresponding normalized eigenvectors. Two cases have to be distinguished. When $A(k) > 0$, we obtain

$$\vec{e_1}(k) = \sqrt{\frac{A(k) + \sqrt{A(k)^2 + V_{12}^2}}{2\sqrt{A(k)^2 + V_{12}^2}}} \begin{pmatrix} 1 \\ \frac{V_{12}}{A(k)+\sqrt{A(k)^2+V_{12}^2}} \end{pmatrix}, \tag{3.A.9}$$

$$\vec{e_2}(k) = \sqrt{\frac{A(k) + \sqrt{A(k)^2 + V_{12}^2}}{2\sqrt{A(k)^2 + V_{12}^2}}} \begin{pmatrix} \frac{-V_{12}}{A(k)+\sqrt{A(k)^2+V_{12}^2}} \\ 1 \end{pmatrix}, \tag{3.A.10}$$

and when $A(k) < 0$,

$$\vec{e_1}(k) = \sqrt{\frac{A(k) - \sqrt{A(k)^2 + V_{12}^2}}{-2\sqrt{A(k)^2 + V_{12}^2}}} \begin{pmatrix} \frac{-V_{12}}{A(k)-\sqrt{A(k)^2+V_{12}^2}} \\ 1 \end{pmatrix}, \tag{3.A.11}$$

$$\vec{e_2}(k) = \sqrt{\frac{A(k) - \sqrt{A(k)^2 + V_{12}^2}}{-2\sqrt{A(k)^2 + V_{12}^2}}} \begin{pmatrix} 1 \\ \frac{V_{12}}{A(k)-\sqrt{A(k)^2+V_{12}^2}} \end{pmatrix}. \tag{3.A.12}$$

Remark 3.A.1. *If we assume that $V_{12} = 0$, the problem (3.A.4) is diagonal and eigenvalues are trivial. In the case $A(k) > 0$ for example, (3.A.7) and (3.A.8) correctly give $E_1(k) = ak^2 + V_{11}$ and $E_2(k) = bk^2 + V_{22}$. Moreover, (3.A.9) and (3.A.10) give the canonical eigenvectors $\vec{e_1}(k) = \begin{pmatrix} 1 \\ 0 \end{pmatrix}$ and $\vec{e_2}(k) = \begin{pmatrix} 0 \\ 1 \end{pmatrix}$.*

Remark 3.A.2. *The case $A(k) = 0$ $\left(\text{possible for all } k \text{ if } a = b \text{ and } V_{11} = V_{22}, \text{ for } k = 0 \text{ if only } V_{11} = V_{22}, \text{ or just for a specific } k \text{ such that } k^2 = -\frac{V_{11}-V_{22}}{a-b}\right)$ gives two different possibilities. When $V_{12} = 0$, we have only one eigenvalue $E(k) = ak^2 + V_{11} = bk^2 + V_{22}$ of multiplicity 2 and normalized eigenvectors are the canonical vectors. On the contrary, when $V_{12} \neq 0$, the eigenvalues are $E_1(k) = bk^2 + V_{22} + |V_{12}|$ and $E_2(k) = bk^2 + V_{22} - |V_{12}|$ and both formulations (3.A.9)-(3.A.10) or (3.A.11)-(3.A.12) can be used to find eigenvectors $\vec{e_1}(k) = \pm\frac{1}{\sqrt{2}} \begin{pmatrix} \frac{V_{12}}{|V_{12}|} \\ 1 \end{pmatrix}$ and $\vec{e_2}(k) = \pm\frac{1}{\sqrt{2}} \begin{pmatrix} -\frac{V_{12}}{|V_{12}|} \\ 1 \end{pmatrix}$.*

3.A.1.2. Sign of $A(k)$

The sign of the term $A(k)$ (introduced in (3.A.6)) is significant and we study here the possible cases :

- Case $a = b$ and $V_{11} = V_{22}$: $A(k) = 0$,
- Case $a = b$ and $V_{11} \neq V_{22}$: $A(0) = 0$ and $A(k) = \frac{V_{11}-V_{22}}{2}$ for all $k \neq 0$, thus the sign of $A(k)$ is the sign of $(V_{11} - V_{22})$,
- Case $a \neq b$ and $V_{11} = V_{22}$: $A(k) = \frac{(a-b)k^2}{2}$, thus the sign of $A(k)$ is the sign of $(a - b)$,
- Case $a \neq b$ and $V_{11} \neq V_{22}$: two subcases are possible :

* $sign(a - b) = sign(V_{11} - V_{22})$, the sign of $A(k)$ is the sign of $(V_{11} - V_{22})$ and $(a - b)$,
* $sign(a - b) \neq sign(V_{11} - V_{22})$: the sign of $A(k)$ is the sign of $(V_{11} - V_{22})$ if $k^2 < -\frac{V_{11}-V_{22}}{a-b}$ and the sign of $(a - b)$ if $k^2 > -\frac{V_{11}-V_{22}}{a-b}$. This case is illustrated in Fig.3.14 where we plot the two eigenvalues E_1 and E_2 in function of k. In fact, we remind that we defined $E_1 \geq E_2$. Consequently, $E_1(k)$ and $E_2(k)$ are not the parabola but the continuous and the dash curves. They coincide when $k^2 = -\frac{V_{11}-V_{22}}{a-b}$.

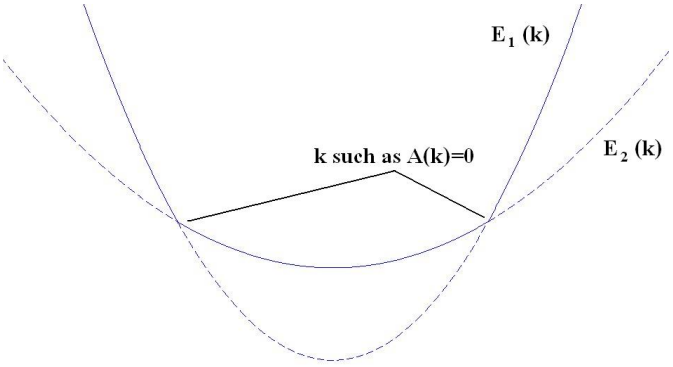

Figure 3.14: Illustration of the case $A(k) = 0$ for a specific k.

3.A.1.3. Expression of k in terms of E

Another way to invert the dispersion relation (3.A.5) is to express k in terms of E. It gives

$$abk^4 - k^2\Big((a+b)E - (aV_{22} + bV_{11})\Big) + E^2 - (V_{11} + V_{22})E + V_{11}V_{22} - V_{12}^2 = 0.$$

Again, to simplify notations, we introduce

$$B(E) = \frac{(a-b)E - (aV_{22} - bV_{11})}{2}. \tag{3.A.13}$$

After calculations, we obtain the following wave vectors

$$k_1(E) = \pm\sqrt{\frac{a(E - V_{22}) - B(E) - \sqrt{B(E)^2 + abV_{12}^2}}{ab}} = \pm\sqrt{\frac{b(E - V_{11}) + B(E) - \sqrt{B(E)^2 + abV_{12}^2}}{ab}}, \tag{3.A.14}$$

$$k_2(E) = \pm\sqrt{\frac{a(E - V_{22}) - B(E) + \sqrt{B(E)^2 + abV_{12}^2}}{ab}} = \pm\sqrt{\frac{b(E - V_{11}) + B(E) + \sqrt{B(E)^2 + abV_{12}^2}}{ab}}. \tag{3.A.15}$$

$\sqrt[+]{x}(x \in \mathbb{R})$ is the complex square root of x, having a positive real part ($x \geq 0$) or a positive imaginary part ($x \leq 0$).

3.A.1.4. Identity relations

In order to define the group velocities, it is essential to determine the relations between $E_{1,2}$ and $k_{1,2}$. Defining the following coefficients

$$C^+(k) = (a-b)A(k) + (a+b)\sqrt{A(k)^2 + V_{12}^2}, \tag{3.A.16}$$

$$C^-(k) = (a-b)A(k) - (a+b)\sqrt{A(k)^2 + V_{12}^2}, \tag{3.A.17}$$

we can prove the results presented in Table 3.15.

	$C^-(k) > 0$	$C^-(k) < 0$
$C^+(k) > 0$	$k_1^2(E_1(k)) = k^2$ $k_1^2(E_2(k)) = k^2$	$k_1^2(E_1(k)) = k^2$ $k_2^2(E_2(k)) = k^2$
$C^+(k) < 0$	$k_2^2(E_1(k)) = k^2$ $k_1^2(E_2(k)) = k^2$	$k_2^2(E_1(k)) = k^2$ $k_2^2(E_2(k)) = k^2$

Figure 3.15: Table given relations between E and k^2 in function of C^+ and C^- signs.

In a similar way, defining

$$D^+(E) = \frac{(a-b)B(E) + (a+b)\sqrt{B(E)^2 + abV_{12}^2}}{2ab}, \tag{3.A.18}$$

$$D^-(E) = \frac{(a-b)B(E) - (a+b)\sqrt{B(E)^2 + abV_{12}^2}}{2ab}, \tag{3.A.19}$$

we can prove the results presented in Table 3.16.

	$D^-(E) > 0$	$D^-(E) < 0$
$D^+(E) > 0$	$E_2(k_1(E)) = E$ $E_2(k_2(E)) = E$	$E_1(k_1(E)) = E$ $E_2(k_2(E)) = E$
$D^+(E) < 0$	$E_2(k_1(E)) = E$ $E_1(k_2(E)) = E$	$E_1(k_1(E)) = E$ $E_1(k_2(E)) = E$

Figure 3.16: Table given relations between E and k^2 in function of D^+ and D^- signs.

Proof. First, we find after calculations that

$$B(E_1(k)) = \frac{(a+b)A(k) + (a-b)\sqrt{A(k)^2 + V_{12}^2}}{2},$$

$$B(E_2(k)) = \frac{(a+b)A(k) - (a-b)\sqrt{A(k)^2 + V_{12}^2}}{2}.$$

Using these expressions in (3.A.14)-(3.A.15), we finally obtain

$$k_1^2(E_1(k)) = k^2 + \frac{C^+(k) - |C^+(k)|}{2ab} \quad \text{and} \quad k_2^2(E_1(k)) = k^2 + \frac{C^+(k) + |C^+(k)|}{2ab}, \tag{3.A.20}$$

$$k_1^2(E_2(k)) = k^2 + \frac{C^-(k) - |C^-(k)|}{2ab} \quad \text{and} \quad k_2^2(E_2(k)) = k^2 + \frac{C^-(k) + |C^-(k)|}{2ab}. \tag{3.A.21}$$

In an analogous way, we have

$$A(k_1(E)) = \frac{(a+b)B(E) - (a-b)\sqrt{B(E)^2 + abV_{12}^2}}{2ab},$$

$$A(k_2(E)) = \frac{(a+b)B(E) + (a-b)\sqrt{B(E)^2 + abV_{12}^2}}{2ab}.$$

Using these expressions in (3.A.7)-(3.A.8), it gives

$$E_1(k_1(E)) = E + D^-(E) + |D^-(E)| \quad \text{and} \quad E_2(k_1(E)) = E + D^-(E) - |D^-(E)|, \tag{3.A.22}$$

$$E_1(k_2(E)) = E + D^+(E) + |D^+(E)| \quad \text{and} \quad E_2(k_2(E)) = E + D^+(E) - |D^+(E)|. \tag{3.A.23}$$

□

3.A.1.5. Sign of $C^+(k)$, $C^-(k)$, $D^+(E)$ and $D^-(E)$

In the previous subsection, we have seen the importance of $C^{\pm}(k)$ and $D^{\pm}(E)$ signs to determine the relations between $E_{1,2}$ and $k_{1,2}$. We remind that we consider here only the case $a > 0$ and $b > 0$. When $V_{12} \neq 0$, we can easily show that

$$\forall k, C^+(k) > 0 \text{ and } C^-(k) < 0, \tag{3.A.24}$$

and

$$\forall E, D^+(E) > 0 \text{ and } D^-(E) < 0. \tag{3.A.25}$$

These results are in accordance together since, referring to tables Fig.3.15 and Fig.3.16, we obtain on the one hand

$$k_1^2(E_1(k)) = k^2 \quad \text{and} \quad k_2^2(E_2(k)) = k^2, \tag{3.A.26}$$

and on the other hand

$$E_1(k_1(E)) = E \quad \text{and} \quad E_2(k_2(E)) = E. \tag{3.A.27}$$

3.A.1.6. Group velocities

We have now all the elements to define the group velocities. These velocities are essential to identify the waves traveling to the right and to the left. Since we obtained the relations (3.A.26) and (3.A.27), the group velocities are given by the following formulae

$$V_1(E) = \mathcal{V}_1(k_1(E)) = \frac{dE_1(k)}{dk}\bigg|_{k=k_1(E)} \qquad \text{and} \qquad V_2(E) = \mathcal{V}_2(k_2(E)) = \frac{dE_2(k)}{dk}\bigg|_{k=k_2(E)}. \tag{3.A.28}$$

Because $A'(k) = (a-b)k$, we obtain

$$V_1(E) = (a+b)k_1(E) + \frac{(a-b)k_1(E)A(k_1(E))}{\sqrt{A(k_1(E))^2 + V_{12}^2}} = \frac{k_1(E)C^+(k_1(E))}{\sqrt{A(k_1(E))^2 + V_{12}^2}}, \tag{3.A.29}$$

$$V_2(E) = (a+b)k_2(E) - \frac{(a-b)k_2(E)A(k_2(E))}{\sqrt{A(k_2(E))^2 + V_{12}^2}} = -\frac{k_2(E)C^-(k_2(E))}{\sqrt{A(k_2(E))^2 + V_{12}^2}}. \tag{3.A.30}$$

$C^{\pm}(k)$ are the coefficients defined in (3.A.16) and (3.A.17). Consequently, we can say that the group velocities have same sign as wave vectors k. This is called a direct mode.

Remark 3.A.3. *In other cases ($a < 0$ and $b < 0$ for example), the relations between $E_{1,2}$ and $k_{1,2}$ may be different to (3.A.26) and (3.A.27). It is possible to obtain group velocities which have the unlike sign of wave vectors k. This is called a reverse mode.*

3.A.2. Different modes and boundary conditions

We define

$$\boldsymbol{e_1^{\pm}}(E) = \boldsymbol{e_1}(\pm k_1(E)) \quad \text{and} \quad \boldsymbol{e_2^{\pm}}(E) = \boldsymbol{e_2}(\pm k_2(E)). \tag{3.A.31}$$

We consider the left injected mode. Equation (3.A.1) can be solved explicitly in the region $x < x_L$, assuming V_{11}, V_{22} and V_{12} to be constant equals to $V_{11}(x_L)$, $V_{22}(x_L)$ and $V_{12}(x_L)$. We find

$$\begin{aligned}\boldsymbol{\psi} = \quad & a_L e^{ik_{1,L}(E)(x-x_L)}\boldsymbol{e^+_{1,L}}(E) + b_L e^{-ik_{1,L}(E)(x-x_L)}\boldsymbol{e^-_{1,L}}(E) \\ & + c_L e^{ik_{2,L}(E)(x-x_L)}\boldsymbol{e^+_{2,L}}(E) + d_L e^{-ik_{2,L}(E)(x-x_L)}\boldsymbol{e^-_{2,L}}(E),\end{aligned} \tag{3.A.32}$$

where we use the notations $k_{1,L}$, $k_{2,L}$, $\boldsymbol{e^{\mp}_{1,L}}$ and $\boldsymbol{e^{\mp}_{2,L}}$ to emphasize the dependence on potentials $V_{11}(x_L)$, $V_{22}(x_L)$ and $V_{12}(x_L)$. Because we are in a direct mode, the first and third term correspond to the wave traveling to the right, while the second and fourth term correspond to the wave traveling to the left. We assume that electrons are injected with amplitude 1 in both bands. Therefore, $a_L = 1$ and $c_L = 1$ while b_L and d_L are the left reflection coefficients that we denote by r_1 and r_2. Then, we obtain

$$\begin{aligned}\boldsymbol{\psi} = \quad & e^{ik_{1,L}(E)(x-x_L)}\boldsymbol{e^+_{1,L}}(E) + r_1 e^{-ik_{1,L}(E)(x-x_L)}\boldsymbol{e^-_{1,L}}(E) \\ & + e^{ik_{2,L}(E)(x-x_L)}\boldsymbol{e^+_{2,L}}(E) + r_2 e^{-ik_{2,L}(E)(x-x_L)}\boldsymbol{e^-_{2,L}}(E).\end{aligned} \tag{3.A.33}$$

In the region $x > x_R$, we assume V_{11}, V_{22} and V_{12} are constant equals to $V_{11}(x_R)$, $V_{22}(x_R)$ and $V_{12}(x_R)$ and we find

$$\begin{aligned}\boldsymbol{\psi} = \quad & a_R e^{ik_{1,R}(E)(x-x_R)}\boldsymbol{e^+_{1,R}}(E) + b_R e^{-ik_{1,R}(E)(x-x_R)}\boldsymbol{e^-_{1,R}}(E) \\ & + c_R e^{ik_{2,R}(E)(x-x_R)}\boldsymbol{e^+_{2,R}}(E) + d_R e^{-ik_{2,R}(E)(x-x_R)}\boldsymbol{e^-_{2,R}}(E). \end{aligned} \tag{3.A.34}$$

The first and the third waves are outgoing (or vanishing) and the second and the fourth are ingoing (or exponentially increasing). We make the assumption that these two last have zero amplitude. It gives $b_R = 0$ and $d_R = 0$. a_R and c_R are the right transmission coefficients that we denote by t_1 and t_2. We obtain

$$\boldsymbol{\psi} = t_1 e^{ik_{1,R}(E)(x-x_R)}\boldsymbol{e^+_{1,R}}(E) + t_2 e^{ik_{2,R}(E)(x-x_R)}\boldsymbol{e^+_{2,R}}(E). \tag{3.A.35}$$

Next, the boundary conditions for $\boldsymbol{\psi}$ are obtained like in the single band model by eliminating coefficients r_1, r_2, t_1 and t_2. Indeed, this can be done through an algebraic manipulation which gives

$$\frac{d\boldsymbol{\psi}}{dx}(x_L) - \imath\mathbb{K}_L(E)\boldsymbol{\psi}(x_L) = \imath\Big(k_{1,L}(E)\mathbb{I}_2 - \mathbb{K}_L(E)\Big)\boldsymbol{e^+_{1,L}}(E) + \imath\Big(k_{2,L}(E)\mathbb{I}_2 - \mathbb{K}_L(E)\Big)\boldsymbol{e^+_{2,L}}(E), \tag{3.A.36}$$

$$\frac{d\boldsymbol{\psi}}{dx}(x_R) - \imath\mathbb{K}_R(E)\boldsymbol{\psi}(x_R) = 0. \tag{3.A.37}$$

$\mathbb{I}_2$ is the 2×2 identity matrix and $\mathbb{K}_{L/R}(.)$ are also 2×2 matrices (again "L" stand for "left" and "R" for "right"), defined by

$$\mathbb{K}_{L/R}(E) = \mathbb{B}_{L/R}(E)\mathbb{D}_{L/R}(E)\mathbb{B}^{-1}_{L/R}(E). \tag{3.A.38}$$

$\mathbb{B}_{L/R}(E)$ are the 2×2 matrices transforming the canonical basis on to the basis vectors respectively $(\boldsymbol{e^-_{1,L}}(E), \boldsymbol{e^-_{2,L}}(E))$ and $(\boldsymbol{e^+_{1,R}}(E), \boldsymbol{e^+_{2,R}}(E))$. $\mathbb{B}^{-1}_{L/R}(E)$ their inverse matrices. $\mathbb{D}_{L/R}(E)$ are diagonal matrices defined by

$$\mathbb{D}_L(E) = \begin{pmatrix} -k_{1,L}(E) & 0 \\ 0 & -k_{2,L}(E) \end{pmatrix} \quad \text{and} \quad \mathbb{D}_R(E) = \begin{pmatrix} k_{1,R}(E) & 0 \\ 0 & k_{2,R}(E) \end{pmatrix}. \tag{3.A.39}$$

Appendix B : Examples of amazing g_{nn} for large modes

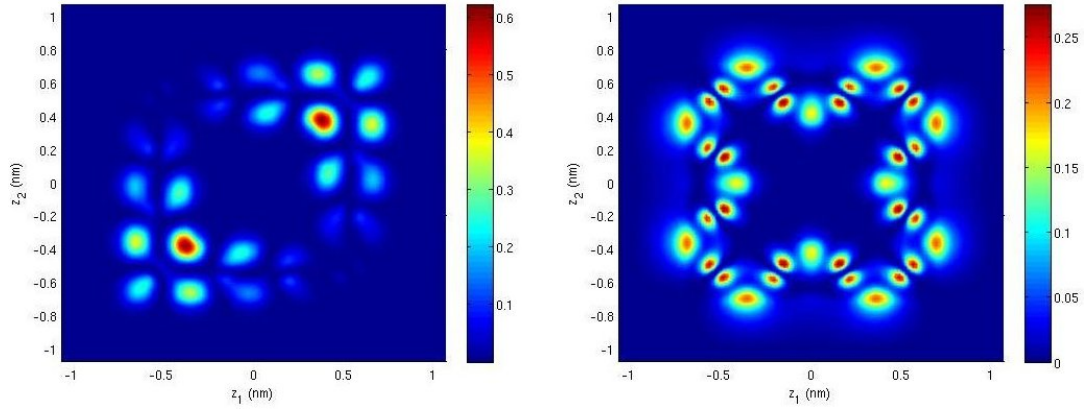

Figure 3.17: $g_{nn}(z)$ for 63^{th} mode (left) and 73^{th} mode (right).

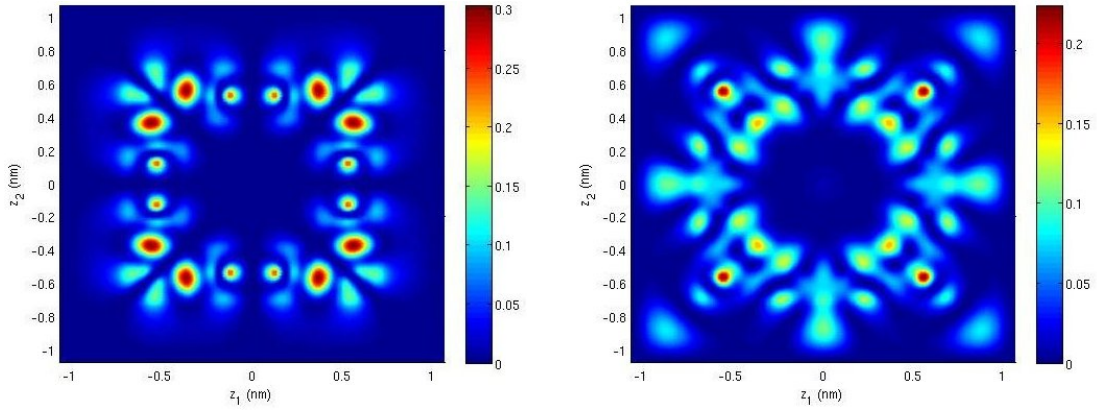

Figure 3.18: $g_{nn}(z)$ for 88^{th} mode (left) and 129^{th} mode (right).

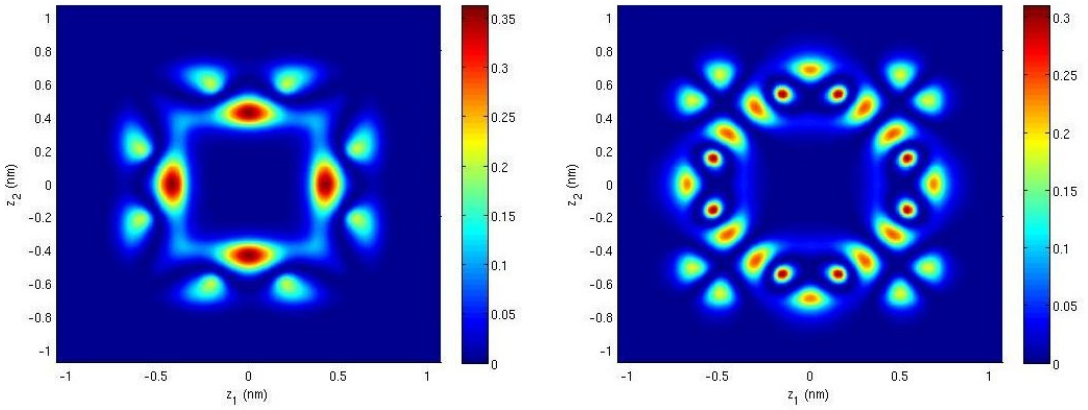

Figure 3.19: $g_{nn}(z)$ for 141^{th} mode (left) and 224^{th} mode (right).

Bibliography

[1] A. Arnold, N. Ben Abdallah, and C. Negulescu. WKB-based schemes for the oscillatory 1D Schrödinger equation in the semiclassical limit. *SIAM J. Numer. Anal.*, 49(4):1436–1460, 2011.

[2] N. Ben Abdallah, P. Degond, and P. A. Markowich. On a one-dimensional Schrödinger-Poisson scattering model. *Z. Angew. Math. Phys.*, 48(1):135–155, 1997.

[3] N. Ben Abdallah and J. Kefi-Ferhane. Mathematical analysis of the two-band Schrödinger model. *Math. Methods Appl. Sci.*, 31(10):1131–1151, 2008.

[4] N. Ben Abdallah, M. Mouis, and C. Negulescu. An accelerated algorithm for 2D simulations of the quantum ballistic transport in nanoscale MOSFETs. *J. Comput. Phys.*, 225(1):74–99, 2007.

[5] N. Ben Abdallah and O. Pinaud. Multiscale simulation of transport in an open quantum system: resonances and WKB interpolation. *J. Comput. Phys.*, 213(1):288–310, 2006.

[6] V. Bonnaillie-Noël, F. Nier, and Y. Patel. Computing the steady states for an asymptotic model of quantum transport in resonant heterostructures. *J. Comput. Phys.*, 219(2):644–670, 2006.

[7] V. Bonnaillie-Noël, F. Nier, and Y. Patel. Far from equilibrium steady states of 1D-Schrödinger-Poisson systems with quantum wells. I. *Ann. Inst. H. Poincaré Anal. Non Linéaire*, 25(5):937–968, 2008.

[8] V. Bonnaillie-Noël, F. Nier, and Y. Patel. Far from equilibrium steady states of 1D-Schrödinger-Poisson systems with quantum wells. II. *J. Math. Soc. Japan*, 61(1):65–106, 2009.

[9] Ph. Caussignac, B. Zimmermann, and R. Ferro. Finite element approximation of electrostatic potential in one-dimensional multilayer structures with quantized electronic charge. *Computing*, 45(3):251–264, 1990.

[10] W. R. Frensley. Boundary conditions for open quantum systems driven far from equilibrium. *Rev. Mod. Phys.*, 62(3):745–791, 1990.

[11] E. Gnani, A. Gnudi, S. Reggiani, M. Luisier, and G. Baccarani. Band effects on the transport characteristics of ultrascaled snw-fets. *IEEE Trans. Nanotechnol.*, 7(6):700 –709, 2008.

[12] E. Gnani, S. Reggiani, A. Gnudi, P. Parruccini, R. Colle, M. Rudan, and G. Baccarani. Band-structure effects in ultrascaled silicon nanowires. *IEEE Trans. Electron Devices*, 54(9):2243 –2254, 2007.

[13] H.K. Gummel. A self-consistent iterative scheme for one-dimensional steady state transistor calculations. *IEEE Trans. Electron Devices*, 11(10):455 – 465, 1964.

[14] HSL (2011). *A collection of Fortran codes for large scale scinetific computation.* http://www.hsl.rl.ac.uk/hsl2011.

[15] C. Jourdana and N. Vauchelet. Analysis of a diffusive effective mass model for nanowires. Kinet. Relat. Models (to appear).

[16] R. Lehoucq, D. Sorensen, and C. Yang. *ARPACK User's Guide: Solution of Large Scale Eigenvalue Problems with Implicitly Restarted Arnoldi Methods.*

[17] C. S. Lent and D. J. Kirkner. The quantum transmitting boundary method. *J. Appl. Phys.*, 67(10):6353–6359, 1990.

[18] P. Marconcini, G. Fiori, M. Macucci, and G. Iannaccone. Hierarchical simulation of transport in silicon nanowire transistors. *J. Comput. Electron.*, 7:415–418, 2008.

[19] A. Mayer. Band structure and transport properties of carbon nanotubes using a local pseudopotential and a transfer-matrix technique. *Carbon*, 42(10):2057 – 2066, 2004.

[20] C. Negulescu. Numerical analysis of a multiscale finite element scheme for the resolution of the stationary Schrödinger equation. *Numer. Math.*, 108(4):625–652, 2008.

[21] P. Pietra and N. Vauchelet. Modeling and simulation of the diffusive transport in a nanoscale double-gate mosfet. *J. Comput. Electron.*, 7:52–65, 2008.

[22] O. Pinaud. Transient simulations of a resonant tunneling diode. *J. Appl. Phys.*, 92(4):1987–1994, 2002.

[23] E. Polizzi and N. Ben Abdallah. Subband decomposition approach for the simulation of quantum electron transport in nanostructures. *J. Comput. Phys.*, 202(1):150 – 180, 2005.

[24] D. Sorensen. Implicitly restarted Arnoldi/Lanczos methods for large scale eigenvalue calculations. Technical report, Institute for Computer Applications in Science and Engineering (ICASE), 1996.

[25] D. Zhang and E. Polizzi. Efficient modeling techniques for atomistic-based electronic density calculations. *J. Comput. Electron.*, 7:427–431, 2008.

Part *II*

Transport models with collisions for ultra-scaled confined structures

Chapter 4

Analysis of a diffusive effective mass model

Nota bene : This chapter largely corresponds to an article [12] (to appear in KRM) which is a joint work with N. Vauchelet.

We propose in this chapter to derive and analyze a self-consistent model describing the diffusive transport in a nanowire. From a physical point of view, it describes the electron transport in an ultra-scaled confined structure, taking into account the interactions of charged particles with phonons. The transport direction is assumed to be large compared to the wire section and is described by a drift-diffusion equation including effective quantities computed from a Bloch problem in the crystal lattice. The electrostatic potential solves a Poisson equation where the particle density couples on each energy band a two dimensional confinement density with the monodimensional transport density given by the Boltzmann statistics. On the one hand, we study the derivation of this Nanowire Drift-Diffusion Poisson model from a kinetic level description. On the other hand, we present an existence result for this model in a bounded domain.

4.1 Introduction

A quantum wire is an electronic component made of a periodic ion packing. The transport direction is large compared to the wire section, which includes only few atoms. So, the assumption of infinite periodic structure in the wire cross-section, which allows to derive the usual effective mass theorem [1, 22], cannot be used anymore.

In [5], a new quantum model for nanowires is derived. Using an envelope function decomposition, [3] is extended to nanowires and a longitudinal effective mass model is obtained. However, in many applications such that FETs (Field Effect Transistors) for example, semiconductor devices contains largely doped regions. In these regions, collisions play an important role in the transport. Usually, quantum models do not include collisions of charged particles. That is the reason why a diffusive model has to be developed.

In this chapter, a Nanowire Drift-Diffusion Poisson NDDP model is derived following [8] by performing a diffusive limit from a sequence of 1D Boltzmann equations in the transport direction, one for each energy band. Similarly to [5], this model takes into account the ultra-scaled confinement and retains information of the nanowire cross-section. Moreover, a self-consistent model includes the resolution of the Poisson equation in the entire device.

It is worth noting that the model derived and analyzed in this chapter is not specific to nanowires. It can also be used to describe the transport in other ultra-scaled confined nanostructures, in particular in nanotubes.

4.1.1 Nanowire quantities

In order to define the effective masses and the other physical quantities used in the NDDP model, we need to recall the model derived in [5]. We consider an infinite wire defined in a physical domain $\mathbb{R} \times \omega_{z_\epsilon}$, where ϵ is the typical spacing between lattice sites. The transport is described by a scaled Schrödinger equation in $\mathbb{R}\times\omega_{z_\epsilon}$ containing a potential $W_{\mathcal{L}}$ generated by the crystal lattice, fast oscillating in the scale defined by the crystal spacing, and a slowly varying potential V computed self-consistently through the resolution of a Poisson equation in the whole domain. Since the 2D cross-section ω_{z_ϵ} comprises few ions, $W_{\mathcal{L}}$ is considered periodic only in the longitudinal x-direction, also called transport direction. The variable z of the transverse section can be considered as fast variable, and it can be rescaled as $z' = \frac{z}{\epsilon}$. To simplify notations, we now omit the primes. Then, ω_z will denote the scaled cross-section and we assume to work in rescaled quantities such that the periodicity is set to 1 in the transport direction.

As usual in quantum mechanics, we assign to the structure a Bloch problem. For our nanowire, we define the generalized Bloch functions as the eigenfunctions of the following eigenvalue problem in the 3D unit cell $\mathcal{U} = (-1/2, 1/2) \times \omega_z$:

$$\begin{cases} -\frac{1}{2}\Delta\chi_n + W_{\mathcal{L}}\chi_n = E_n\chi_n. \\ \chi_n(y,z) = 0 \ \text{ on } \partial\omega_z, \quad \chi_n \text{ 1-periodic in } y. \\ \int_{\mathcal{U}} |\chi_n|^2 dydz = 1. \end{cases} \tag{4.1.1}$$

We use here the notation y to emphasize we consider only one period $(-1/2, 1/2)$. This definition of the Bloch problem is peculiar to the strongly confined structure. First, the unit cell $\mathcal{U}$ comprises the entire cross-section ω_z. So, the Bloch functions depend on the device under consideration (geometry, growing orientation...). Second, the boundary conditions are representative

of the nanowire problem since we consider the periodicity only in the transport direction and we choose homogeneous Dirichlet conditions in other directions in order to impose confinement. Consequently, the eigenvectors are 3D quantities but the lattice space and the energy bands have to be seen as 1D objects.

Assumption 4.1.1. *We assume that $W_{\mathcal{L}}$ is a nonnegative potential given in $L^{\infty}(\mathcal{U})$.*

Under Assumption 4.1.1, verified by physically relevant potentials, it is well-known that the eigenfunctions χ_n, solutions of (4.1.1), form an orthonormal basis of $L^2(\mathcal{U})$ (see e.g. [11]), with real eigenvalues which satisfies

$$E_1 \leq E_2 \leq ..., \qquad \lim_{n\to+\infty} E_n = +\infty. \tag{4.1.2}$$

Assumption 4.1.2. *We assume that the eigenvalues E_n are all simple.*

In [5], authors perform an asymptotic process, using an envelope function decomposition, in order to average out not only the lattice potential but also the lateral dimension. This process brings into play some relevant averaged quantities, based on the Bloch functions. In particular, a n^{th} band effective mass m_n^* is given by

$$\frac{1}{m_n^*} = 1 - 2\sum_{n'\neq n} \frac{P_{nn'}P_{n'n}}{E_n - E_{n'}}, \tag{4.1.3}$$

where

$$P_{nn'} = \int_{\mathcal{U}} \partial_y \chi_{n'}(y,z)\chi_n(y,z)\,dydz \tag{4.1.4}$$

are the matrix elements of the gradient operator between Bloch functions. Also, an effective potential V_{nn} is defined by

$$V_{nn}(t,x) = \int_{\omega_z} V(t,x,z)g_{nn}(z)\,dz = \langle V(t,x,\cdot), g_{nn}\rangle, \tag{4.1.5}$$

with

$$g_{nn}(z) = \int_{-1/2}^{1/2} \chi_n^2(y,z)\,dy, \tag{4.1.6}$$

where we make use of the notation $\langle f, g\rangle = \int_{\omega_z} f(z)g(z)\,dz$.

Finally, the asymptotic quantum model obtained in [5] consists of an infinite set of one dimensional device dependent Schrödinger equations, that in the n^{th} band have the form :

$$\imath\partial_t\psi_n(t,x) = -\frac{1}{2m_n^*}\partial_{xx}\psi_n(t,x) + V_{nn}(t,x)\psi_n(t,x). \tag{4.1.7}$$

Moreover, self-consistent computations include the resolution of a Poisson equation in the three dimensional structure to compute the slowly varying potential V. The peculiarity comes in

the definition of the macroscopic charge density ρ, entering in the second member of the Poisson equation, which combines the confinement information of the cross-section with the one dimensional transport density. It is given by

$$\rho(t,x,z) = \sum_{n=1}^{+\infty} N_n(t,x) g_{nn}(z). \tag{4.1.8}$$

Here N_n is the 1D density carried by the n-th band, given in function of ψ_n. We point out that g_{nn}'s are crucial quantities that retain the atomistic description of the cross-section. They allow to link the one dimensional transport direction to the entire nanowire (and inversely) since they are used to define on the one hand the effective potential V_{nn} and on the other hand the macroscopic density ρ. The drift-diffusion Poisson model for nanowires presented in this chapter is based on the same mechanism. The difference is that we discuss here how to insert the effective quantities in a diffusive transport model.

Assumption 4.1.2 is restrictive. In [5], the degenerate case is also discussed. Then, to each multiple eigenvalue corresponds a system of coupled Schrödinger equations with dimension equal to the multiplicity of the eigenvalue. The kinetic part of the effective mass Hamiltonian is diagonal and the coupling occurs through the potential. Nevertheless, the derivation of a diffusive model in this case is far from the scope of this chapter and is not discussed here.

4.1.2 Diffusive transport description

In this chapter, we mainly consider a finite wire in the transport direction x defined in the bounded rescaled domain $\omega_x = [0, L]$ such that $L >> 1$. We denote $\Omega = [0, L] \times \omega_z$ this bounded device. Since L is large compared to the size of ω_z, the crystal lattice can be assumed periodic only in the transport direction as presented in the above subsection. Moreover, we will consider that the evolution of charged particles is mainly driven by collisions with phonons which represent lattice vibrations. A widely used model to describe such kind of transport in various area such as plasmas or semiconductors is the drift-diffusion equation. It consists in a conservation equation of the particle density in the transport direction which is called here the surface density $N_s(t,x)$ and which corresponds to the integral in the direction z of the total density. The current is the sum of a drift term and of a diffusion term [13, 15, 17]. The equation reads

$$\partial_t N_s - \partial_x \Big(D(\partial_x N_s + N_s \partial_x V_s) \Big) = 0, \tag{4.1.9}$$

where D is a diffusion coefficient and $V_s(t,x)$ is the effective potential. This potential is self-consistant and takes into account the quantum confinement in the nanowire. Its derivation will be specified in Section 4.2 ; in particular, we will show that its expression is given by

$$V_s = -\ln \mathcal{Z} \quad \text{with} \quad \mathcal{Z} = \sum_{n=1}^{+\infty} e^{-\left(E_n + V_{nn}\right)}, \tag{4.1.10}$$

where E_n are the eigenvalues of the problem (4.1.1) and $V_{nn}(t,x)$ are the potential energies defined by (4.1.5). It is also usual to introduce the quasi-fermi variable $\varphi(t,x)$ and the Slotboom variable $u(t,x)$ defined by

$$u = e^{\varphi} = N_s e^{V_s} = \frac{N_s}{\mathcal{Z}}. \tag{4.1.11}$$

Then, the current $J(t,x)$ can be expressed as

$$J = -D(\partial_x N_s + N_s \partial_x V_s) = -D N_s \partial_x \varphi = -D e^{-V_s} \partial_x u.$$

The electrostatic potential $V(t,x,z)$ is solution of the Poisson equation

$$-\Delta_{x,z} V = \rho. \tag{4.1.12}$$

The three dimensional macroscopic charge density $\rho(t,x,z)$ takes into account the contribution of all energy bands ; As it is justified in [5] (and reminded in (4.1.8)), ρ is defined as follows

$$\rho = \sum_{n=1}^{+\infty} N_n g_{nn}, \tag{4.1.13}$$

where $g_{nn}(z)$ is given by (4.1.6) and $N_n(t,x)$ is the charge density in the transport direction which is now expressed in the approximation of the Boltzmann statistics by

$$N_n = e^{\varphi - \left(E_n + V_{nn}\right)} = \frac{N_s}{\mathcal{Z}} e^{-\left(E_n + V_{nn}\right)}. \tag{4.1.14}$$

We complete this system with the following boundary conditions

$$N_s(t,x) = N_b \qquad \text{for} \quad x \in \partial\omega_x, \tag{4.1.15}$$

$$V(t,x,z) = V_b(z) \qquad \text{for} \quad x \in \partial\omega_x, \tag{4.1.16}$$

$$\partial_z V(t,x,z) = 0 \qquad \text{for} \quad z \in \partial\omega_z. \tag{4.1.17}$$

These boundary conditions do not correspond to the mixed type boundary conditions necessary for physical applications (taking in account source and drain contacts, gate...). It is chosen for the mathematical convenience and in particular for the elliptic regularity properties of the Poisson equation (4.1.12) on our domain.

To simplify notations, we define the functional $\mathcal{S}[V](t,x,z)$ such that

$$\mathcal{S}[V] = \sum_{n=1}^{+\infty} \frac{e^{-\left(E_n + V_{nn}\right)}}{\mathcal{Z}} g_{nn}. \tag{4.1.18}$$

With this notation, we have

$$\rho = N_s \mathcal{S}[V]. \tag{4.1.19}$$

4.1.3 Main results

In [8, 10, 20], the authors propose transport models for confined structures using the subband description which allows to reduce the 3D problem to a 2D transport equation. The transport coefficients have then to be computed by solving eigenvalue problems for the steady-state Schrödinger equation in the confinement direction, which is therefore one dimensional. Compared to [8, 20], the NDDP model presented in this chapter, involved the resolution of the Bloch problem in all directions and the confinement is two-dimensional.

The main results in this chapter concern the coupled Nanowire Drift-Diffusion Poisson NDDP system (4.1.9)–(4.1.17) and are divided into three parts. In a first part we study the derivation of the model (4.1.9)–(4.1.14) in a wire with infinite extension from a kinetic level description. This latter model describes the interaction of charged particles with phonons at thermal equilibrium. Assuming that the potential V is given, we are able to state in Theorem 4.2.3 the convergence of this model towards the NDDP model.

In a second part, we focus on the study of the NDDP model in the bounded device $\Omega = [0, L] \times \omega_z$. We will make the following assumptions :

Assumption 4.1.3. *The function D is assumed to be a $\mathcal{C}^1$ function on $\overline{\omega_x}$ and there exists two nonnegative constants D_1 and D_2 such that $0 < D_1 \leq D \leq D_2$.*

Assumption 4.1.4. *The initial condition satisfies $N_s^0 \ln N_s^0 \in L^1(\omega_x)$ and $N_s^0 \geq 0$ a.e. And we denote $\mathcal{N}_I = \int_{\omega_x} N_s^0 dx$.*

Assumption 4.1.5. *The boundary data for the surface density N_b is a positive constant. The Dirichlet boundary condition for the potential satisfies $V_b \in C^2(\partial\omega_x \times \omega_z)$ and the compatibility condition $\partial_z V_b(z) = 0$ for all $z \in \partial\omega_z$.*

The main result is the following existence theorem :

Theorem 4.1.1. *Let $T > 0$. Under Assumptions 4.1.3, 4.1.4 and 4.1.5, the Nanowire Drift-Diffusion Poisson system (4.1.9)–(4.1.17) admits a weak solution such that*

$$N_s \ln N_s \in L^\infty([0,T]; L^1(\omega_x)) \qquad \text{and} \qquad \sqrt{N_s} \in L^2([0,T]; H^1(\omega_x)),$$

$$V \in L^\infty([0,T]; H^1(\Omega)).$$

To prove this result, we follow the idea proposed in [20] which relies strongly on the estimate on the relative entropy that we will prove in Section 4.3.3. The main difficulty is due to the quantum confinement for which we need some sharp estimates on the quantities provided by the Bloch problem. Such estimates are given in Section 4.3.1. Then a priori estimates give a functional framework for the quantities N_s and V. Since N_s will be defined only in $L \log L$, we need to regularized the system. For the regularized system we obtain existence of solutions such as in [20] and we recover a solution of the non-regularized system by passing to the limit in the regularization.

Finally, in a third part, we study the stationary Nanowire Drift-Diffusion Poisson problem in the case of thermodynamic equilibrium boundary data. On the one hand, we prove the existence of a unique stationary solution. On the other hand, we demonstrate the convergence of a transient solution towards this stationary solution when the time grows to infinity, using again the relative entropy.

This chapter is organized as follows. In Section 4.2, we describe the derivation of the model from a kinetic model taking into account the interactions of the charged particles with phonons. Section 4.3 is devoted to the proof of Theorem 4.1.1. We first state estimates on the eigen-elements defining the Nanowire quantities. Then, we define the regularization of the model. We prove a priori estimates for this regularized system. Next, the regularized Nanowire Poisson system is analyzed. Finally, we prove Theorem 4.1.1 by passing to the limit in the regularization. In Section 4.4, we study the stationary problem and the convergence of a transient solution when the times grows to infinity.

4.2 Diffusive limit

4.2.1 Kinetic description

The drift-diffusion model can be derived from kinetic theory when the mean free path related to particle interactions with a thermal bath is small compared to the system length-scale [4, 19]. In this section, we present the derivation of this model from the Boltzmann equation describing collisions of charged particles with phonons at thermal equilibrium. This equation governs the evolution of the distribution function $f_n(t,x,p)$ on the n^{th} band whose energy is given by $E_n + V_{nn}$. Here and in the following, we shall use the notation f_n for a function depending on the n^{th} band, and the notation $f = (f_n)_{n\geq 1}$ when the entire set of bands is taken into account. The time variable t is nonnegative, the position variable is denoted x and the momentum variable p. The equation writes [19, 21]

$$\partial_t f_n^\eta + \frac{1}{\eta}\Big(v_n \partial_x f_n^\eta - \partial_x V_{nn} \partial_p f_n^\eta\Big) = \frac{1}{\eta^2}\mathcal{Q}_B(f^\eta)_n, \tag{4.2.1}$$

where η is the scaled mean free path, assumed to be small. In this equation, v_n is the velocity given by $v_n(p) = \frac{p}{m_n^*}$, m_n^* the n^{th} band effective mass (4.1.3) and $V_{nn}(t,x)$ the effective potential energy associated with the n^{th} band (4.1.5). This equation is completed by the initial data denoted f^0.

Up to our knowledge, it is actually an open question to derive the Boltzmann equation (4.2.1) from a purely quantum model (in our case from (4.1.7)). Nevertheless the derivation of the collisionless Vlasov equation from a semi-classical limit of the Schrödinger equation is known (see e.g. [7]). Then we assume in this work that we can describe the collisions by adding heuristically a collision operator in the kinetic model describing the classical direction. Such a idea has been already used in [8, 21]. Focusing on the scattering between electrons and phonons,

the collision operator $\mathcal{Q}_B$ is assumed to be in the linear BGK approximation for Boltzmann statistics. It reads

$$\mathcal{Q}_B(f)_n = \sum_{n'=1}^{+\infty} \int_{\mathbb{R}} \alpha_{n,n'}(p,p') \Big(\mathcal{M}_n(p) f_{n'}(p') - \mathcal{M}_{n'}(p') f_n(p) \Big) dp' \tag{4.2.2}$$

where the function $\mathcal{M}_n$ is the Maxwellian

$$\mathcal{M}_n(t,x,p) = \frac{1}{\sqrt{2\pi m_n^* \mathcal{Z}(t,x)}} e^{-\left(\frac{p^2}{2m_n^*} + E_n + V_{nn}(t,x)\right)} \tag{4.2.3}$$

normalized such that

$$\sum_{n=1}^{+\infty} \int_{\mathbb{R}} \mathcal{M}_n dp = 1. \tag{4.2.4}$$

The repartition function $\mathcal{Z}$ is thus given by

$$\mathcal{Z}(t,x) = \sum_{n=1}^{+\infty} e^{-\left(E_n + V_{nn}(t,x)\right)}. \tag{4.2.5}$$

The energies E_n correspond to the eigenvalues of the problem (4.1.1). We notice that Assumption 4.1.1 allows us to give a sense to this definition of $\mathcal{Z}$ since $\mathcal{Z} \leq \sum_n e^{-E_n} \leq \sum_n e^{-\Lambda_n} < \infty$, where Λ_n are the eigenvalues of the Laplacian operator (see Section 4.3.1).

Assumption 4.2.1. *The cross-section α is symmetric and bounded from above and below :*

$$\exists \alpha_1, \alpha_2 > 0,\ 0 < \alpha_1 \leq \alpha_{n,n'}(p,p') \leq \alpha_2,\ \forall n, n' \geq 1,\ \forall p \in \mathbb{R},\ \forall p' \in \mathbb{R}.$$

In the diffusion approximation, boundary layers appears at the frontier of the domain. Since the study of this phenomena is far from the scope of this chapter, we consider the limit in the case where the spatial domain is $\mathbb{R}$, assuming that there is no charged carriers at infinity such that $\lim_{x \to \pm\infty} f_n^\eta(t,x,p) = 0$. For the rigorous analysis of boundary layers in the diffusion approximation, we refer the reader to [19, 16].

Let us recall an existence result for our problem. It is a direct corollary of well known existence results on the Boltzmann equation (see e.g. [9, 19] and references therein).

Theorem 4.2.1. *Let us assume that the potential $V \geq 0$ is given in $L^\infty([0,T]; H^2(\mathbb{R} \times \omega_z))$ and that the initial data satisfies $f^0 \in l^1(L^\infty(\mathbb{R} \times \mathbb{R}))$ and $f^0 \geq 0$. For fixed $\eta > 0$, under Assumption 4.2.1, the problem (4.2.1)-(4.2.5) admits a unique weak solution $f^\eta \in L^\infty_{loc}(\mathbb{R}^+, l^1(L^1(\mathbb{R} \times \mathbb{R})))$ and $f^\eta \geq 0$.*

4.2.2 Properties of the collision operator

We present some well known properties of the collision operator $\mathcal{Q}_B$ defined by (4.2.2). In this section, the time variable t and the position variable x are considered as parameters, thus we omit to write the dependence on t and x. We define the weighted space

$$L^2_{\mathcal{M}} = \{ f = (f_n)_{n \geq 1} \text{ such that } \sum_{n=1}^{+\infty} \int_{\mathbb{R}} \frac{f_n^2}{\mathcal{M}_n} dp < +\infty \}, \tag{4.2.6}$$

which is a Hilbert space with the scalar product

$$\langle f, g\rangle_{\mathcal{M}} = \sum_{n=1}^{+\infty} \int_{\mathbb{R}} \frac{f_n g_n}{\mathcal{M}_n} dp. \tag{4.2.7}$$

We have the following properties for $\mathcal{Q}_B$ whose proofs can be found in [18] (section 3.1).

Proposition 4.2.2. *We assume that the cross-section α satisfies Assumption 4.2.1. Then the following properties hold for $\mathcal{Q}_B$:*

(i) $\sum_{n\geq 1} \int_{\mathbb{R}} \mathcal{Q}_B(f)_n dp = 0$.

(ii) $\mathcal{Q}_B$ is a linear, selfadjoint and negative bounded operator on $L^2_{\mathcal{M}}$.

(iii) $Ker\ \mathcal{Q}_B = \{f \in L^2_{\mathcal{M}},\ such\ that\ \exists N_s \in \mathbb{R}, f_n = N_s \mathcal{M}_n\}$ *and* $(Ker\ \mathcal{Q}_B)^{\perp} = Im\ \mathcal{Q}_B$.

(iv) If $\mathcal{P}$ is the orthogonal projection on $Ker\ \mathcal{Q}_B$ with the scalar product $\langle ., .\rangle_{\mathcal{M}}$, then

$$-\langle \mathcal{Q}_B(f), f\rangle_{\mathcal{M}} \geq \alpha_1 \|f - \mathcal{P}(f)\|^2_{\mathcal{M}}.$$

The third point of Proposition 4.2.2 implies that the equation $\mathcal{Q}_B(f) = h$ admits a solution in $L^2_{\mathcal{M}}$ iff $h \in (Ker\ \mathcal{Q}_B)^{\perp}$. Moreover, this solution is unique if we impose $f \in (Ker\ \mathcal{Q}_B)^{\perp}$ where $(Ker\ \mathcal{Q}_B)^{\perp} = \{f$ such that $\sum_{n=1}^{+\infty} \int_{\mathbb{R}} f_n dp = 0\}$. As a consequence, we can define :

Definition 4.2.1. *There exists $\Theta \in L^2_{\mathcal{M}}$ such that for all $n \geq 1$,*

$$\mathcal{Q}_B(\Theta)_n = -\frac{p}{m_n^*}\mathcal{M}_n \qquad and \qquad \sum_{n=1}^{+\infty} \int_{\mathbb{R}} \Theta_n dp = 0. \tag{4.2.8}$$

We define the nonnegative diffusion coefficient by

$$D = \sum_{n=1}^{+\infty} \int_{\mathbb{R}} \frac{p}{m_n^*} \Theta_n dp. \tag{4.2.9}$$

Remark 4.2.1. Particular case when α is constant.
Let us assume that for all n, n', k, k', $\alpha(n, n', k, k') = 1/\tau$, where τ is a relaxation time. After calculations,

$$\Theta_n(p) = \tau \frac{p}{m_n^*}\mathcal{M}_n(p) \qquad \text{and} \qquad D = \tau \sum_{n=1}^{+\infty} \frac{e^{-(E_n + V_{nn})}}{m_n^* \sum_{m=1}^{+\infty} e^{-(E_m + V_{mm})}}.$$

We emphasize that this expression is slightly different to the formula used in [18] for example where D is defined as τ/m.

4.2.3 Asymptotic expansion for the diffusive limit

Let us consider a solution f_n^{η} of the Boltzmann equation (4.2.1) and assume that it admits a Hilbert expansion

$$f_n^{\eta} = f_{0,n} + \eta f_{1,n} + \eta^2 f_{2,n} + ...$$

Inserting this decomposition in (4.2.1) and identifying with respect to powers of η, we obtain

$$\mathcal{Q}_B(f_0)_n = 0. \tag{4.2.10}$$

$$v_n \partial_x f_{0,n} - \partial_x V_{nn} \partial_p f_{0,n} = \mathcal{Q}_B(f_1)_n. \tag{4.2.11}$$

$$\partial_t f_{0,n} + v_n \partial_x f_{1,n} - \partial_x V_{nn} \partial_p f_{1,n} = \mathcal{Q}_B(f_2)_n. \tag{4.2.12}$$

With (4.2.10), we get $f_0 \in Ker\ \mathcal{Q}_B$. Thus, (iii) of Proposition 4.2.2 gives

$$f_{0,n} = N_s \mathcal{M}_n. \tag{4.2.13}$$

Injecting this expression in (4.2.11) it follows, after calculations

$$\mathcal{Q}_B(f_1)_n = H_n := v_n \mathcal{M}_n \Big(\partial_x N_s + N_s \partial_x V_s \Big),$$

where $V_s = -\ln \mathcal{Z}$. By Proposition 4.2.2, f_1 exists iff $H \in (Ker\ \mathcal{Q}_B)^{\perp}$. Because we have $\int v_n \mathcal{M}_n dp = 0$ ($v_n \mathcal{M}_n$ is an odd function), this condition is true. We choose Θ as proposed in Definition 4.2.1. Thus,

$$f_{1,n} = -\Theta_n \Big(\partial_x N_s + N_s \partial_x V_s \Big). \tag{4.2.14}$$

By Proposition 4.2.2, (4.2.12) has a solution iff,

$$\sum_{n=1}^{+\infty} \int_{\mathbb{R}} \Big(\partial_t f_{0,n} + v_n \partial_x f_{1,n} - \partial_x V_{nn} \partial_p f_{1,n} \Big) dp = 0.$$

Using (4.2.13), (4.2.14) and (4.2.9) we have formally obtained the drift-diffusion equation (4.1.9).

4.2.4 A convergence proof of the derivation

In this Section, we investigate the rigorous diffusive limit of the Boltzmann equation (4.2.1) as $\eta \to 0$. This study is proposed in the simplified case where the potential V is given and regular. The diffusive limit of a coupled Boltzmann transport equation with the Poisson equation is studied in [16] and with quantum confinement in [21]. The main result is the following theorem :

Theorem 4.2.3. *Let us assume that the potential $V \geq 0$ is given in $L^\infty([0,T]; H^2(\mathbb{R} \times \omega_z))$ and $\partial_t V$ is bounded in $L^\infty([0,T] \times \mathbb{R} \times \omega_z)$ and that the initial data satisfies $f^0 \in l^1(L^\infty(\mathbb{R}^2))$ and $f^0 \geq 0$. Moreover, let $T > 0$ and let $(f_n^\eta)_{n \geq 1}$ be a solution of the Boltzmann equation (4.2.1)-(4.2.5). Then, up to the extraction of a subsequence and under Assumption 4.2.1, N_s^η defined by $N_s^\eta := \sum_{n \geq 1} \int_{\mathbb{R}} f_n^\eta dp$ converges weakly towards $N_s \in L^2([0,T] \times \mathbb{R})$ solution of the drift-diffusion equation :*

$$\partial_t N_s - \partial_x \Big(D(\partial_x N_s + N_s \partial_x V_s) \Big) = 0,$$

where $V_s(t,x) = -\ln \Big(\sum_n e^{-\left(E_n + V_{nn}(t,x)\right)} \Big)$, with the initial data $N_s^0(x) = \sum_n \int_{\mathbb{R}} f_n^0(x,p)\, dp$.

Notation For the proof, we introduce the function $M_n = \frac{1}{\sqrt{2\pi m_n^*}} e^{-\left(\frac{p^2}{2m_n^*}+E_n+V_{nn}\right)}$ which is such that

$$v_n \partial_x M_n - \partial_x V_{nn} \partial_p M_n = 0.$$

Moreover, for $T > 0$, we consider the Banach spaces $X = L^\infty([0,T]; L^2_{M(t)})$ and $Y = L^2([0,T]; L^2_{M^{-1}(t)})$.

Lemma 4.2.4. *Assume $f^0 \in l^1(L^1_{x,p}) \cap L^2_{M(t=0)}$ and V is given such as in Theorem 4.2.3. Then, the unique solution f^η of the Boltzmann equations (4.2.1) in $L^\infty([0,T]; l^1(L^1_{x,p}))$ is in X. Moreover, f^η is bounded in X independently of η.*

Proof. Assuming that all the functions are regular enough, we multiply (4.2.1) by f_n^η/M_n and integrate. We obtain

$$\frac{d}{dt}\sum_{n=1}^{+\infty} \iint \frac{(f_n^\eta)^2}{2M_n}\, dxdp - \sum_{n=1}^{+\infty} \iint \partial_t V_{nn} \frac{(f_n^\eta)^2}{2M_n}\, dxdp = \frac{1}{\eta^2}\sum_{n=1}^{+\infty} \iint \mathcal{Q}_B(f^\eta)_n \frac{f_n^\eta}{M_n}\, dxdp. \tag{4.2.15}$$

By assumption there exists $\mu \geq 0$ such that $|\partial_t V_{nn}| \leq \mu$ on $[0,T] \times \mathbb{R}$. We define

$$X^\eta(t) = \sum_{n=1}^{+\infty} \iint \frac{(f_n^\eta)^2}{2M_n}\, dxdp \quad \text{and} \quad S^\eta(t) = -\frac{1}{\eta^2}\sum_{n=1}^{+\infty} \iint \mathcal{Q}_B(f^\eta)_n \frac{f_n^\eta}{M_n} dxdp. \tag{4.2.16}$$

Since $\mathcal{Q}_B$ is negative, $S^\eta(t) \geq 0\ \forall t \in [0,T]$. So, (4.2.15) gives

$$\frac{dX^\eta}{dt} - \mu X^\eta \leq -S^\eta. \tag{4.2.17}$$

Integrating this inequality allows to conclude the proof.

To justify all calculations, we regularized the problem and consider f_R a solution of the regularized truncated problem, $f_R \in \mathcal{D}([0,T] \times \mathbb{R}^2)$. Thus f_R satisfies (4.2.15) and

$$\frac{d}{dt}\sum_{n=1}^{+\infty} \iint \frac{f_R^2}{2M_n}\, dxdp \leq \mu \sum_{n=1}^{+\infty} \iint \frac{f_R^2}{2M_n}\, dxdp.$$

Thus f_R is bounded in X independently of R. We can extract a subsequence converging towards a function $g \in X$ in X-weak*. We know moreover that f_R satisfies the Cauchy criterion in $L^\infty([0,T], l^1(L^1_{x,p}))$ as a solution of the truncated problem. Thus, f_R converges strongly towards f in this space. By uniqueness of the weak* limit, $g = f$ a.e. □

Lemma 4.2.5. *Under the assumption of Lemma 4.2.4, there exists $f \in X$ and $N_s \in L^2([0,T] \times \mathbb{R})$ such that, up to an extraction :*
(i) $f^\eta \rightharpoonup f$ in X-weak*.
(ii) $N_s^\eta \rightharpoonup N_s$ in $L^2_{t,x}$-weak.
(iii) If we define the current by

$$J^\eta = \frac{1}{\eta}\sum_{n=1}^{+\infty} \int_{\mathbb{R}} v_n f_n^\eta dp, \tag{4.2.18}$$

then $J^\eta \rightharpoonup J$ in $L^2_{t,x}$-weak. Moreover, $f_n = N_s \mathcal{M}_n$ a.e. for all n.

Proof. We integrate (4.2.17) between 0 and t, for all $t \in [0,T]$. It gives

$$X^\eta(t) - \mu \int_0^t X^\eta(s)ds + \int_0^t S^\eta(s)ds \leq X^\eta(0).$$

Thus, there exists a constant $C > 0$ such that

$$0 \leq \int_0^T S^\eta(s)ds \leq C. \tag{4.2.19}$$

If $\mathcal{P}$ is the orthogonal projection on $Ker\ \mathcal{Q}_B$ defined as in Proposition 4.2.2, there exists $N^\eta(t,x)$ such that $\mathcal{P}(f^\eta)_n = N^\eta \mathcal{M}_n$. Moreover, $f^\eta - \mathcal{P}(f^\eta) \in (Ker\ \mathcal{Q}_B)^\perp$ that is to say that $\sum_{n\geq 1} \int \big(f_n^\eta - \mathcal{P}(f^\eta)_n\big)dp = 0$. We conclude, using (4.2.4), that

$$N^\eta(t,x) = \sum_{n=1}^{+\infty} \int_{\mathbb{R}} f_n^\eta(t,x,p)dp := N_s^\eta(t,x). \tag{4.2.20}$$

We can easily show that (iv) of Proposition 4.2.2 is also true for the scalar product $\langle .,. \rangle_M$. We obtain the bound

$$\sum_{n=1}^{+\infty} \int_0^T \iint \frac{(f^\eta - N_s^\eta \mathcal{M}_n)^2}{M_n} dxdpdt \leq \frac{\eta^2}{\alpha_1} \int_0^T S^\eta(s)\, ds \leq C\eta^2. \tag{4.2.21}$$

We verify that $\|f^\eta\|_X$ is bounded. Thus, we can extract a subsequence satisfying (i).

Then, from (4.2.21), we have

$$\sum_{n=1}^{+\infty} \int_0^T \iint \frac{(N_s^\eta \mathcal{M}_n)^2}{M_n} dxdpdt = \sum_{n=1}^{+\infty} \int_0^T \iint \Big(\frac{N_s^\eta}{\mathcal{Z}}\Big)^2 M_n\, dxdpdt \leq C.$$

It provides that $\|N_s^\eta/\mathcal{Z}\|_Y$ is bounded. Thus there exists $\rho \in Y$ such that, up to an extraction, for all $\phi \in L_t^2 L^2_{M^{-1}}$,

$$\sum_{n=1}^{+\infty} \int_0^T \iint \frac{N_s^\eta}{\mathcal{Z}} M_n \phi_n\, dxdpdt \to \sum_{n=1}^{+\infty} \int_0^T \iint \rho M_n \phi_n\, dxdpdt. \tag{4.2.22}$$

For $\xi \in L^2([0,T]\times\mathbb{R})$ take $\phi_n(t,x,p) = \xi(t,x)$ for all $n \geq 1$, we easily verify that $\phi \in L_t^2 L^2_{M^{-1}}$. So, if we define $N_s := \rho\mathcal{Z} \in L^2([0,T]\times\mathbb{R})$, we find

$$\int_0^T \int N_s^\eta \xi \left(\sum_{n=1}^{+\infty} \int \frac{M_n}{\mathcal{Z}} dp \right) dxdt \to \int_0^T \int \rho\mathcal{Z}\xi \left(\sum_{n=1}^{+\infty} \int \frac{M_n}{\mathcal{Z}} dp \right) dxdt.$$

This proves (ii). Moreover, from (4.2.22), $N_s^\eta \frac{M_n}{\mathcal{Z}} = N_s^\eta \mathcal{M}_n \rightharpoonup \rho M_n$ in X-weak*. From (4.2.21), f^η and $N_s^\eta \mathcal{M}_n$ have the same weak limit. So, for all $n \geq 1$,

$$f = \rho M_n = N_s \mathcal{M}_n \quad \text{a.e.} \tag{4.2.23}$$

Finally, we have

$$J^\eta = \frac{1}{\eta} \sum_{n=1}^{+\infty} \int_{\mathbb{R}} v_n f_n^\eta dp = \frac{1}{\eta} \sum_{n=1}^{+\infty} \int_{\mathbb{R}} v_n \big(f_n^\eta - N_s \mathcal{M}_n\big) dp.$$

Applying the Cauchy-Schwarz inequality

$$J^\eta \leq \left(\sum_{n=1}^{+\infty}\int_{\mathbb{R}} v_n^2 M_n dp\right)^{1/2}\left(\sum_{n=1}^{+\infty}\int_{\mathbb{R}}\frac{(f_n^\eta - N_s\mathcal{M}_n)^2}{\eta^2 M_n}dp\right)^{1/2}. \tag{4.2.24}$$

With (4.2.21), we deduce that J^η is bounded in $L^2_{t,x}$. □

Proof of Theorem 4.2.3. Integrating the Boltzmann equation (4.2.1) with respect to p, we find the conservation law

$$\partial_t N_s^\eta + \partial_x J^\eta = 0 \tag{4.2.25}$$

where J^η is the current defined in (4.2.18). Considering the function Θ defined in (4.2.8), we have

$$J^\eta = \frac{1}{\eta}\sum_{n=1}^{+\infty}\int_{\mathbb{R}} v_n f_n^\eta dp = \frac{1}{\eta}\langle v_n\mathcal{M}_n, f_n^\eta\rangle_{\mathcal{M}} = -\frac{1}{\eta}\langle \mathcal{Q}_B(\Theta)_n, f_n^\eta\rangle_{\mathcal{M}}.$$

The selfadjointness of $\mathcal{Q}_B$ gives

$$-J^\eta = \frac{1}{\eta}\langle \Theta_n, \mathcal{Q}_B(f^\eta)_n\rangle_{\mathcal{M}} = \sum_{n=1}^{+\infty}\int_{\mathbb{R}}\frac{\Theta_n\mathcal{Q}_B(f^\eta)_n}{\eta\mathcal{M}_n}dp. \tag{4.2.26}$$

Now, to establish the rigorous limit $\eta \to 0$, we use the weak formulation of (4.2.1) and (4.2.25) : for all $\psi \in \mathcal{C}^1([0,T]\times\mathbb{R}^2)$ compactly supported and for all $\phi \in \mathcal{C}^1([0,T]\times\mathbb{R})$ compactly supported :

$$\iiint f_n^\eta\big(-\eta\partial_t\psi - v_n\partial_x\psi + \partial_x V_{nn}\partial_p\psi\big)dxdpdt - \frac{1}{\eta}\iiint \mathcal{Q}_B(f^\eta)_n\psi dxdpdt = 0, \tag{4.2.27}$$

and

$$-\iint N_s^\eta\partial_t\phi dxdt - \iint J^\eta\partial_x\phi dxdt = 0. \tag{4.2.28}$$

At this point we use Lemmas of Appendix A. On the one hand, from Lemma 4.A.1, we can substitute ψ by ϕ in (4.2.27). Summing with respect to n, we immediately obtain (4.2.28). On the other hand, Lemmas 4.A.1 and 4.A.2 prove that we can choose $\psi = \phi\frac{\Theta_n}{\mathcal{M}_n}$ in (4.2.27) for all $\phi \in \mathcal{C}^1([0,T]\times\mathbb{R})$ compactly supported. Summing with respect to n and using (4.2.26), we find after calculations

$$\begin{aligned}
&-\eta\sum_{n=1}^{+\infty}\iiint f_n^\eta\partial_t\Big(\phi\frac{\Theta_n}{\mathcal{M}_n}\Big)dxdpdt - \sum_{n=1}^{+\infty}\iiint v_n\frac{f_n^\eta}{\mathcal{M}_n}\partial_x\big(\Theta_n\phi\big)dxdpdt\\
&+\sum_{n=1}^{+\infty}\iiint \phi\frac{f_n^\eta}{\mathcal{M}_n}\big(\partial_x V_{nn}\partial_p\Theta_n - v_n\Theta_n\partial_x\ln\mathcal{Z}\big)dxdpdt + \iint J^\eta\phi dxdt = 0.
\end{aligned} \tag{4.2.29}$$

Using Lemma 4.2.5, we have the weak convergence of f_n^η, N_s^η and J^η. Moreover, we have that $f_n^\eta \in L^2_{\mathcal{M}}$ thus the limit of the first term vanishes thanks to Lemma 4.A.2. Moreover, this same Lemma proves that $v_n\frac{\Theta_n}{\mathcal{M}_n}$ and $v_n\frac{\partial_s\Theta_n}{\mathcal{M}_n}$ (for $s = t$, x and p) are in X. Finally, since by assumption V_{nn} is bounded in $L^\infty([0,T];H^2(\mathbb{R}))$, we can pass to the limit and we obtain

$$\iint J\phi\, dxdt = \sum_{n=1}^{+\infty}\iiint\left(v_n N_s\partial_x\big(\Theta_n\phi\big) - N_s\phi\big(\partial_x V_{nn}\partial_p\Theta_n - v_n\Theta_n\partial_x\ln\mathcal{Z}\big)\right)dxdpdt,$$

which is the weak formulation of $J = -D(\partial_x N_s + N_s\partial_x V_s)$. □

4.3 Analysis of the Nanowire Drift-Diffusion-Poisson system

4.3.1 Spectral properties

In this Section, we investigate some technical Lemmas concerning spectral properties of the Hamiltonian defined in (4.1.1). As in Section 4.2.1 we denote by Λ_n the eigenvalues of the Laplacian, i.e.

$$\begin{cases} -\Delta u_n = \Lambda_n u_n, & \text{on} \quad \mathcal{U} = (-1/2, 1/2) \times \omega_z, \\ u_n(-1/2, z') = u_n(1/2, z'), & u_n(y, z') = 0 \quad \text{on } (-1/2, 1/2) \times \partial\omega_z. \end{cases}$$

From the min-max principle it is clear that for nonnegative potential $W_{\mathcal{L}}$, we have $E_n \geq \Lambda_n$. Moreover, the eigenfunctions u_n satisfy $u_n = u_n^1 u_n^2$ where $(u_n^1)_{n\in\mathbb{N}}$ are eigenvectors of the Laplacian in the y-direction with periodic boundary conditions and $(u_n^2)_{n\in\mathbb{N}}$ are eigenvectors of the Laplacian in the z-direction with Dirichlet boundary conditions. From well-known properties of eigenvalues of the Laplacian-Dirichlet [11], we deduce that for all $\lambda > 0$, $\sum_{n\geq 1} e^{-\lambda\Lambda_n} < +\infty$. Thus

$$\forall\, \lambda > 0, \quad \sum_{n=1}^{+\infty} e^{-\lambda E_n} < \infty. \tag{4.3.1}$$

In the following we will make use of the notation : $L_z^p L_x^q(\Omega) = \{u \in L^1_{loc}(\Omega) \text{ s.t. } \|u\|_{L_z^p L_x^q(\Omega)} = (\int_{\omega_z} \|u(\cdot, z)\|^p_{L^q(\omega_x)}\, dz)^{1/p} < +\infty\}$. We recall that we have the Sobolev embedding $H^1(\Omega) \hookrightarrow L_z^2 L_x^\infty(\Omega)$ where $\Omega = \omega_x \times \omega_z \subset \mathbb{R} \times \mathbb{R}^2$ (see [6]).

Lemma 4.3.1. *Under Assumption 4.1.1 we have that for all $n \in \mathbb{N}$*

$$\|\chi_n\|_{L^\infty(\mathcal{U})} = \|\chi_n\|_{L^\infty(\Omega)} \leq C(E_n + \|W_{\mathcal{L}}\|_{L^\infty}), \tag{4.3.2}$$

where C stands for a nonnegative constant. Therefore we have

$$\|g_{nn}\|_{L^\infty(\omega_z)} \leq C(E_n + \|W_{\mathcal{L}}\|_{L^\infty})^2, \tag{4.3.3}$$

$$\|V_{nn}\|_{L^\infty(\omega_x)} \leq C\|V\|_{H^1(\Omega)}(E_n + \|W_{\mathcal{L}}\|_{L^\infty})^2. \tag{4.3.4}$$

Proof. We notice first that since $W_{\mathcal{L}}$ (and χ_n) is 1-periodic in x. So, we have that $\|W_{\mathcal{L}}\|_{L^\infty(\mathcal{U})} = \|W_{\mathcal{L}}\|_{L^\infty(\Omega)}$. From (4.1.1), we deduce that $\Delta\chi_n \in L^2(\Omega)$ and

$$\|\Delta\chi_n\|_{L^2} \leq 2(E_n + \|W_{\mathcal{L}}\|_{L^\infty}).$$

Using the elliptic regularity for the Laplacian operator, we deduce (4.3.2) thanks to the Sobolev embedding $H^2(\Omega) \hookrightarrow L^\infty(\Omega)$. The estimates (4.3.3) and (4.3.4) follows directly from a Cauchy-Schwarz inequality and the Sobolev embedding $H^1(\Omega) \hookrightarrow L_z^2 L_x^\infty(\Omega)$. □

Lemma 4.3.2. Properties of $\mathcal{S}[V]$. *Let us assume that $V \in H^1(\Omega)$ with $V \geq 0$. Then the function $\mathcal{S}[V]$, defined in (4.1.18), satisfies :*
(i) $\mathcal{S}[V]$ is bounded i.e. $|\mathcal{S}[V]| < +\infty$.
(ii) If moreover $\widetilde{V} \in H^1(\Omega)$ with $\widetilde{V} \geq 0$, then there exists a nonnegative constant C such that :

$$\|\mathcal{S}[V] - \mathcal{S}[\widetilde{V}]\|_{L^2(\Omega)} \leq C\|V - \widetilde{V}\|_{L^2(\Omega)}. \tag{4.3.5}$$

Proof. **(i)** First, we study the coefficient $\mathcal{Z}$. We have

$$\mathcal{Z}(x) = \sum_{n=1}^{+\infty} e^{-\left(E_n + V_{nn}(x)\right)} \geq e^{-\left(E_1 + \|V_{11}\|_{L^\infty(\omega_x)}\right)}.$$

Then from Lemma 4.3.1, when $V \in H^1(\Omega)$, there exists a constant $C > 0$ such that $\mathcal{Z}(x) > C$. Using the fact that $V_{nn} \geq 0$ when $V \geq 0$, we get

$$|\mathcal{S}[V](x,z)| \leq C\sum_{n=1}^{+\infty} e^{-E_n}\|g_{nn}\|_{L^\infty(\omega_z)} \leq C\sum_{n=1}^{+\infty} e^{-E_n}(E_n + \|W_{\mathcal{L}}\|_{L^\infty})^2,$$

where we use (4.3.3) for the last inequality. A direct consequence of (4.3.1) is that $\sum_{n\geq 1} E_n^2 e^{-E_n}$ is finite. Then $\mathcal{S}[V]$ is bounded.

(ii) We use the fact that

$$\mathcal{S}[V] - \mathcal{S}[\widetilde{V}] = \int_0^1 \partial_s S[\widetilde{V} + s(V - \widetilde{V})]ds.$$

We define $\mathcal{E}(s) = e^{-\left(E_n + \langle \widetilde{V} + s(V-\widetilde{V}), g_{nn}\rangle\right)}$. So,

$$\partial_s \mathcal{S}[\widetilde{V} + s(V - \widetilde{V})] = \frac{\left(\sum_{n\geq 1}\mathcal{E}'(s)g_{nn}\right)\left(\sum_{n\geq 1}\mathcal{E}(s)\right) - \left(\sum_{n\geq 1}\mathcal{E}(s)g_{nn}\right)\left(\sum_{n\geq 1}\mathcal{E}'(s)\right)}{\left(\sum_{n\geq 1}\mathcal{E}(s)\right)^2}.$$

We have $\mathcal{E}'(s) = -\langle V - \widetilde{V}, g_{nn}\rangle\mathcal{E}(s)$. The first term becomes

$$\left|\frac{\sum_{n\geq 1}\mathcal{E}'(s)g_{nn}}{\sum_{n\geq 1}\mathcal{E}(s)}\right| = \left|\frac{\sum_{n\geq 1}\mathcal{E}(s)\langle V - \widetilde{V}, g_{nn}\rangle g_{nn}}{\sum_{n\geq 1}\mathcal{E}(s)}\right| \leq C\sum_{n=1}^{+\infty} e^{-E_n} g_{nn}|\langle V - \widetilde{V}, g_{nn}\rangle|.$$

Finally,

$$\left|\frac{\sum_{n\geq 1}\mathcal{E}'(s)g_{nn}}{\sum_{n\geq 1}\mathcal{E}(s)}\right| \leq C\|V - \widetilde{V}\|_{L^2(\omega_z)}\sum_{n=1}^{+\infty} e^{-E_n} g_{nn}\|g_{nn}\|_{L^2(\omega_z)} \leq C\|V - \widetilde{V}\|_{L^2(\omega_z)},$$

where we use (4.3.3) and (4.3.1) for the last inequality. We can treat the second term in a similar way

$$\left|\frac{\left(\sum_{n\geq 1}\mathcal{E}(s)g_{nn}\right)\left(\sum_{n\geq 1}\mathcal{E}(s) < V - \widetilde{V}, g_{nn} >\right)}{\left(\sum_{n\geq 1}\mathcal{E}(s)\right)^2}\right| \leq C\sum_{n=1}^{+\infty} e^{-E_n}|\langle V - \widetilde{V}, g_{nn}\rangle|.$$

Consequently, we deduce (4.3.5). □

4.3.2 Regularized system

We define the linear regularization operator by

$$\begin{aligned} \mathcal{R}^\delta : L^1(\Omega) &\to C^\infty(\overline{\Omega}) \\ \mathcal{V} &\mapsto \mathcal{R}^\delta[\mathcal{V}](x,z) = (\overline{\mathcal{V}} * \xi_{\delta,x} * \xi_{\delta,z})|_{\overline{\Omega}}, \end{aligned} \tag{4.3.6}$$

where $\overline{\mathcal{V}}$ is the extension of $\mathcal{V}$ by zero outside Ω and $\xi_{\delta,x}$ and $\xi_{\delta,z}$ are C^∞ nonnegative compactly supported even approximations of the unity, respectively on $\mathbb{R}$ and $\mathbb{R}^2$. We can prove the following properties, using convolution results :

Lemma 4.3.3. Properties of $\mathcal{R}^\delta$:
(i) $\mathcal{R}^\delta$ is a bounded operator on $L^p_x L^q_z(\Omega)$ for $1 \le p,q \le +\infty$ and satisfies for all $\mathcal{V} \in L^p_x L^q_z(\Omega)$,

$$\|\mathcal{R}^\delta[\mathcal{V}]\|_{L^p_x L^q_z(\Omega)} \le \|\mathcal{V}\|_{L^p_x L^q_z(\Omega)} \quad \text{and} \quad \lim_{\delta\to 0} \|\mathcal{R}^\delta[\mathcal{V}] - \mathcal{V}\|_{L^p_x L^q_z(\Omega)} = 0.$$

(ii) $\mathcal{R}^\delta$ is selfadjoint on $L^2(\Omega)$.

(iii) For all $\mathcal{V} \in H^1(\Omega)$,

$$\nabla_x \mathcal{R}^\delta[\mathcal{V}] = \mathcal{R}^\delta[\nabla_x \mathcal{V}] \quad \text{and} \quad \lim_{\delta\to 0} \|\nabla_x \mathcal{R}^\delta[\mathcal{V}] - \nabla_x \mathcal{V}\|_{L^2(\Omega)} = 0.$$

Then the regularized Nanowire Drift-Diffusion Poisson NDDP$_\delta$ system is defined for $\delta \in [0,1]$ by

$$\partial_t N_s^\delta - \partial_x\Big(D(\partial_x N_s^\delta + N_s^\delta \partial_x V_s^\delta)\Big) = 0 \tag{4.3.7}$$

and

$$-\Delta V^\delta = \mathcal{R}^\delta\Big[\frac{N_s^\delta}{\mathcal{Z}^\delta}\sum_{n=1}^{+\infty} e^{-\left(E_n + V_{nn}^\delta\right)} g_{nn}\Big] = \mathcal{R}^\delta\Big[N_s^\delta \mathcal{S}^\delta\Big] \tag{4.3.8}$$

where the regularized quantities are defined by

$$V_{nn}^\delta(x) = \int_{\omega_z} \mathcal{R}^\delta[V^\delta(x,z)] g_{nn}(z) dz = < \mathcal{R}^\delta[V^\delta], g_{nn} >, \tag{4.3.9}$$

$$V_s^\delta = -\ln \mathcal{Z}^\delta \quad \text{with} \quad \mathcal{Z}^\delta[V^\delta] = \sum_{n=1}^{+\infty} e^{-\left(E_n + V_{nn}^\delta\right)}, \tag{4.3.10}$$

and

$$\mathcal{S}^\delta[V^\delta] = \sum_{n\ge 1} \frac{e^{-\left(E_n + V_{nn}^\delta\right)}}{\mathcal{Z}^\delta} g_{nn}. \tag{4.3.11}$$

As above, we denote $N_n^\delta = u^\delta e^{-(E_n + V_{nn}^\delta)}$ where u^δ is the Slotboom variable $u^\delta = N_s^\delta/\mathcal{Z}^\delta$. The initial regularized density $N_s^{\delta,0}$ is chosen such that $N_s^{\delta,0} = \min(N_s^0, \delta^{-1})$. Moreover, the regularized boundary conditions are

$$N_s^\delta(t,x) = N_b \qquad \text{for} \quad x \in \partial\omega_x, \tag{4.3.12}$$

$$V^\delta(t,x,z) = V_b(z) \qquad \text{for} \quad x \in \partial\omega_x, \tag{4.3.13}$$

$$\partial_z V^\delta(t,x,z) = 0 \qquad \text{for} \quad z \in \partial\omega_z. \tag{4.3.14}$$

Remark 4.3.1. When $\delta \to 0$, $\mathcal{R}^\delta \to Id$ and the regularized system (4.1.9)–(4.1.17) tends to the unregularized problem (4.3.7)–(4.3.14).

4.3.3 A priori estimates

Let us consider a weak solution (N_s^δ, V^δ) of the regularized problem (4.3.7)–(4.3.11). We introduce two extensions $\underline{N_s}$ and $\underline{V}$ of the boundary data. These extensions are respectively defined on ω_x and Ω and chosen such that :

- $\underline{N_s} \in C^2(\omega_x)$, $0 < \underline{N_1} \leq \underline{N_s}(x) \leq \underline{N_2}$ where $\underline{N_1}$ and $\underline{N_2}$ are two constants, and $\underline{N_s}|_{\partial\omega_x} = N_b$.
- $\underline{V} \in C^2(\Omega)$ and satisfies the boundary conditions $\underline{V}|_{\partial\omega_x\times\omega_z} = V_b(z)$ and $\partial_z\underline{V}|_{\omega_x\times\partial\omega_z} = 0$.

For regular enough domains, these functions exist. From (4.1.5) with $\underline{V}$ instead of V^δ, we define $V_{nn}[\underline{V}]$ denoted by $\underline{V_{nn}}$. In the same way, we denote $\underline{\mathcal{Z}}$, $\underline{\mathcal{S}}$, $\underline{N_n}$, $\underline{\rho}$ and $\underline{u}$ the quantities associated with $\underline{N_s}$ and $\underline{V}$.

Proposition 4.3.4. *Let $T > 0$ and $\delta \in [0,1]$. Let (N_s^δ, V^δ) be a weak solution of the regularized system NDDP$_\delta$ (4.3.7)–(4.3.14), such that $N_s^\delta \ln N_s^\delta \in L^\infty([0,T], L^1(\omega_x))$, $V^\delta \in L^\infty([0,T], H^1(\Omega))$ and $\sqrt{N_s^\delta} \in L^2([0,T], H^1(\omega_x))$. Then, there exists a nonnegative constant C_T depending only on T such that*

$$\forall t \in [0,T], \qquad 0 \leq W(t) \leq C_T, \tag{4.3.15}$$

where W is the relative entropy defined by

$$W = \sum_{n=1}^{+\infty} \int_{\omega_x} \Big(N_n^\delta \ln\Big(\frac{N_n^\delta}{\underline{N_n}}\Big) - N_n^\delta + \underline{N_n} \Big) dx + \frac{1}{2}\int_\Omega |\nabla(V^\delta - \underline{V})|^2 dxdz. \tag{4.3.16}$$

Proof. We remark that

$$\frac{d}{dt}\sum_{n=1}^{+\infty} \int_{\omega_x} \Big(N_n^\delta \ln\Big(\frac{N_n^\delta}{\underline{N_n}}\Big) - N_n^\delta + \underline{N_n} \Big) dx = \sum_{n=1}^{+\infty} \int_{\omega_x} \partial_t N_n^\delta \ln\Big(\frac{N_n^\delta}{\underline{N_n}}\Big) dx.$$

By definition, we have $\ln N_n^\delta = \ln u^\delta - E_n - V_{nn}^\delta$. Using (4.3.7), it leads to

$$\begin{aligned}\sum_{n=1}^{+\infty} \int_{\omega_x} \partial_t N_n^\delta \ln\Big(\frac{N_n^\delta}{\underline{N_n}}\Big) dx \;&=\; \int_{\omega_x} \partial_x\big(De^{-V_s^\delta}\partial_x u^\delta\big) \ln\Big(\frac{u^\delta}{\underline{u}}\Big) dx \\ &\quad - \frac{d}{dt}\sum_{n=1}^{+\infty} \int_{\omega_x} N_n^\delta\Big(V_{nn}^\delta - \underline{V_{nn}}\Big) dx + \sum_{n=1}^{+\infty} \int_{\omega_x} N_n^\delta \partial_t (V_{nn}^\delta - \underline{V_{nn}}) dx.\end{aligned}$$

Integrating by parts, the first right hand side term gives

$$\int_{\omega_x} \partial_x\big(De^{-V_s^\delta}\partial_x u^\delta\big) \ln\Big(\frac{u^\delta}{\underline{u}}\Big) dx = -\int_{\omega_x} De^{-V_s^\delta} \frac{(\partial_x u^\delta)^2}{u^\delta} dx + \int_{\omega_x} De^{-V_s^\delta} \frac{\partial_x u^\delta \partial_x \underline{u}}{\underline{u}} dx.$$

Using the definition (4.3.9) of V_{nn}^δ, the last right hand side term gives

$$\sum_{n=1}^{+\infty} \int_{\omega_x} N_n^\delta \partial_t (V_{nn}^\delta - \underline{V_{nn}}) dx = \sum_{n=1}^{+\infty} \int_{\omega_x} N_n^\delta \partial_t < \mathcal{R}^\delta[V^\delta] - \mathcal{R}^\delta[\underline{V}], g_{nn} > dx.$$

At this point, the linearity and the selfadjointness of the regularization operator $\mathcal{R}^\delta$ and the regularized Poisson equation (4.3.8) imply

$$\sum_{n=1}^{+\infty}\int_\Omega N_n^\delta \partial_t \mathcal{R}^\delta[V^\delta - \underline{V}]g_{nn}dxdz = \frac{1}{2}\frac{d}{dt}\int_\Omega |\nabla(V^\delta - \underline{V})|^2 dxdz.$$

In the same way, we can write

$$\frac{d}{dt}\sum_{n=1}^{+\infty}\int_{\omega_x} N_n^\delta(V_{nn}^\delta - \underline{V_{nn}})dx = \frac{d}{dt}\int_\Omega |\nabla(V^\delta - \underline{V})|^2 dxdz.$$

Thus, defining W as in (4.3.16), we finally find

$$\frac{dW}{dt} = -\int_{\omega_x} De^{-V_s^\delta}\frac{(\partial_x u^\delta)^2}{u^\delta}dx + \int_{\omega_x} De^{-V_s^\delta}\frac{\partial_x u^\delta \partial_x \underline{u}}{\underline{u}}dx. \tag{4.3.17}$$

We denote

$$\mathcal{D}^\delta(t) = \int_{\omega_x} De^{-V_s^\delta}\frac{(\partial_x u^\delta)^2}{u^\delta}dx \tag{4.3.18}$$

the term which can be seen as an entropy dissipation rate. We also define $\beta = \|\partial_x \underline{u}/\underline{u}\|_{L^\infty(\omega_x)}$, $\beta < +\infty$. Consequently,

$$\frac{dW}{dt} + \mathcal{D}^\delta \leq \beta\|De^{-V_s^\delta}\partial_x u^\delta\|_{L^1(\omega_x)} \leq \beta\sqrt{\mathcal{D}^\delta}\sqrt{D\|N_s^\delta\|_{L^1(\omega_x)}}.$$

Using the inequality $2ab \leq \kappa^2 a^2 + \frac{b^2}{\kappa^2}$ for $\kappa > 0$ small enough and Assumption 4.1.3, we get,

$$\frac{dW}{dt} \leq \frac{dW}{dt} + C_1\mathcal{D}^\delta \leq C_2\|N_s^\delta\|_{L^1(\omega_x)}, \tag{4.3.19}$$

where C_1 and C_2 are two nonnegative constants. Finally, using the inequality $\ln(x) - x + 1 \geq x + (1 - e)$, for $x > 0$, we have

$$W \geq \sum_{n=1}^{+\infty}\int_{\omega_x}\underline{N_n}\Big(\frac{N_n^\delta}{\underline{N_n}} + 1 - e\Big)dx \geq \int_{\omega_x} N_s^\delta dx - (e-1)\int_{\omega_x}\underline{N_s}dx.$$

With (4.3.19), it leads to

$$\frac{dW}{dt} \leq C_2\|N_s^\delta\|_{L^1(\omega_x)} \leq C(W + C_0),$$

where C and C_0 are two nonnegative constants. We conclude thanks to a Gronwall's inequality and the fact that Assumption 4.1.4 and $V \in H^1(\Omega)$ imply that the initial entropy $W(0)$ is bounded. Moreover, we get the bound on the mass

$$\forall\, t \in [0,T], \qquad \int_{\omega_x} N_s^\delta\, dx \leq C. \tag{4.3.20}$$

□

Corollary 4.3.5. *Let $T > 0$ and $\delta \in [0,1]$. Under assumptions of Proposition 4.3.4, there exist C_1 and C_2 two nonnegative constants such that*

$$\forall t \in [0,T], \qquad \int_0^t \int_{\omega_x} |\partial_x \sqrt{N_s^\delta}|^2 dx ds \leq C_1, \tag{4.3.21}$$

$$\forall t \in [0,T],\ \forall p \in [1,+\infty) \qquad \int_0^t \|N_s^\delta\|_{L^p(\omega_x)} ds \leq C_2. \tag{4.3.22}$$

Proof. In this proof, the letter C is used to denote nonnegative constants. We can express the coefficient $\mathcal{D}^\delta$ defined in (4.3.18) in terms of N_s^δ and V_s^δ

$$\mathcal{D}^\delta(t) = \int_{\omega_x} D\Big(4|\partial_x \sqrt{N_s^\delta}|^2 + 2\partial_x N_s^\delta \partial_x V_s^\delta + N_s^\delta |\partial_x V_s^\delta|^2\Big) dx.$$

After an integration by parts on the second term of the right hand side, we deduce

$$4\|\partial_x \sqrt{N_s^\delta}\|^2_{L^2(\omega_x)} \leq C\left(\mathcal{D}^\delta(t) + 2\int_{\omega_x} N_s^\delta \partial_{xx} V_s^\delta dx - 2\Big(N_s^\delta(L)\partial_x V_s^\delta(L) + N_s^\delta(0)\partial_x V_s^\delta(0)\Big)\right). \tag{4.3.23}$$

On the one hand, after calculations, we find

$$\partial_{xx} V_s^\delta = \frac{\sum_n e^{-\left(E_n + V_{nn}^\delta\right)} \partial_{xx} V_{nn}^\delta}{\mathcal{Z}^\delta} + \left(\frac{\sum_n e^{-\left(E_n + V_{nn}^\delta\right)} \partial_x V_{nn}^\delta}{\mathcal{Z}^\delta}\right)^2 - \frac{\sum_n e^{-\left(E_n + V_{nn}^\delta\right)} (\partial_x V_{nn}^\delta)^2}{\mathcal{Z}^\delta}.$$

By the Cauchy-Schwarz inequality, the sum of the last two terms is nonpositive. Moreover, from the regularized Poisson equation (4.3.8)

$$\begin{aligned} \partial_{xx} V_{nn}^\delta = < \partial_{xx} \mathcal{R}^\delta[V^\delta], g_{nn} > &= < -\Delta_z \mathcal{R}^\delta[V^\delta], g_{nn} > - < \mathcal{R}^\delta[\rho^\delta], g_{nn} > \\ &\leq \|\mathcal{R}^\delta[V^\delta]\|_{L^2(\omega_z)} \|\chi_n\|_{L^\infty(\Omega)} \|\chi_n\|_{H^2(\Omega)}. \end{aligned}$$

To obtain the last inequality, we remark that the second term is nonpositive and to treat the first term, we make an integration by parts and we use the fact that

$$\|\Delta_z g_{nn}\|_{L^2(\omega_z)} \leq 2\|\chi_n\|_{L^\infty(\Omega)} \|\chi_n\|_{H^2(\Omega)}.$$

Using the property (i) of Lemma 4.3.3 and (4.3.1), we conclude that

$$\int_{\omega_x} N_s^\delta \partial_{xx} V_s^\delta dx \leq C\|N_s^\delta\|_{L^2(\omega_x)} \|V^\delta\|_{L^2(\Omega)}. \tag{4.3.24}$$

On the other hand, we have

$$N_s^\delta \partial_x V_s^\delta\,|_{\partial\omega_x} = N_b \frac{\sum_n < \partial_x \mathcal{R}^\delta[V^\delta], g_{nn} > e^{-(E_n + V_{nn}^\delta)}}{\sum_n e^{-(E_n + V_{nn}^\delta)}} \leq C N_b \int_{\omega_z} |\partial_x \mathcal{R}^\delta[V^\delta]_{|\partial\omega_x}| dz.$$

Thanks to the trace Theorem and Lemma 4.3.3, we obtain

$$N_s^\delta \partial_x V_s^\delta|_{\partial\omega_x} \leq C N_b \|V^\delta\|_{H^2(\Omega)} \leq C N_b \|N_s^\delta\|_{L^2(\omega_x)},$$

where we use the elliptic regularity and Lemma 4.3.2 and 4.3.3 for the last inequality. With (4.3.23) and (4.3.24), we conclude that

$$4\|\partial_x\sqrt{N_s^\delta}\|^2_{L^2(\omega_x)} \leq C\Big(\mathcal{D}^\delta(t) + \|N_s^\delta\|_{L^2(\omega_x)}\Big).$$

Applying the Gagliardo-Nirenberg inequality to the function $\sqrt{N_s^\delta}$ and using the bound on $\|N_s^\delta\|_{L^1(\omega_x)}$ (4.3.20), we obtain

$$\forall t \in [0,T], \qquad \int_{\omega_x} |\partial_x\sqrt{N_s^\delta}|^2 dx \leq C(1+\mathcal{D}^\delta(t)). \tag{4.3.25}$$

With (4.3.19), we can say that $\int_0^t \mathcal{D}^\delta(s)ds \leq C(W(0)+\mathcal{N}_I t)$ for all $t \in [0,T]$ and consequently we obtain (4.3.21). Finally, (4.3.22) is a consequence of (4.3.21) with the Gagliardo-Nirenberg inequality. □

4.3.4 Analysis of the regularized Nanowire Poisson system

In this section, the surface density N_s is assumed to be given and we only consider the resolution of the regularized Nanowire Poisson equation (4.3.8) with boundary conditions (4.3.13)–(4.3.14) for $\delta \in [0,1]$.

We introduce the functional space

$$H^1_{\omega_x} = \{V \in H^1(\Omega), \quad \text{s. t. } \forall x \in \partial\omega_x,\ \forall z \in \omega_z,\ V(x,z) = 0\}.$$

Let us also take $V_0 \in H^1(\Omega)$ such that $V_0 = V_b$ on $\partial\omega_x \times \omega_z$ and $\partial_z V_0(x,z) = 0$ for all $z \in \partial\omega_z$. A possibility is to take $V_0 = \underline{V}$. Most of the results presented here can be obtained by a straightforward adaptation of [8, 20]. Thus we will not detail the proofs. We first state the following existence result :

Proposition 4.3.6. *Let $T > 0$ and $\delta \in [0,1]$. We assume $N_s \in L^\infty([0,T];L^1(\omega_x))$ such that $N_s \geq 0$ a.e. Then the regularized Nanowire Poisson equation (4.3.8) with boundary conditions (4.3.13)–(4.3.14) admits a unique solution $V^\delta \in V_0 + H^1_{\omega_x}$ with a bound independent of δ.*

Proof. Using the selfadjointness of the regularization operator, a weak solution of (4.3.8) is a critical point in the space $V_0 + H^1_{\omega_x}$ of the functional

$$\begin{aligned} J(V,N_s) &= J_0(V) + J_1(V,N_s) \\ &= \frac{1}{2}\int_\Omega |\nabla V|^2 dxdz + \int_{\omega_x} N_s \ln\Big(\sum_{n=1}^{+\infty} e^{-\left(E_n + <\mathcal{R}^\delta[V], g_{nn}>\right)}\Big)dx. \end{aligned} \tag{4.3.26}$$

Following the proof of Proposition 3.1 in [20] and using Lemma 4.3.1, we show that J is a continuous, convex and coercive functional on $V_0 + H^1_{\omega_x}$. Thus J admits a unique minimizer V and we have a bound on V in H^1 only depending on the L^1 norm of N_s. □

Then, we have the following continuity result :

Proposition 4.3.7. *Let $T > 0$ and $\delta \in [0,1]$. Assume N_s and $\widetilde{N}_s$ are given in $L^\infty([0,T];L^1(\omega_x))$ such that $N_s \geq 0$ and $\widetilde{N}_s \geq 0$ a.e. Then, the corresponding solutions V^δ and $\widetilde{V}^\delta$ of the regularized Nanowire Poisson equation (4.3.8) with boundary conditions (4.3.13)–(4.3.14) verify*

$$\forall t \in [0,T], \quad \|V^\delta - \widetilde{V}^\delta\|_{H^1(\Omega)} \leq C\|N_s - \widetilde{N}_s\|_{L^1(\omega_x)}. \tag{4.3.27}$$

Moreover, if N_s and $\widetilde{N}_s$ belongs to $L^\infty([0,T];L^2(\omega_x))$, we have

$$\forall t \in [0,T], \quad \|V^\delta - \widetilde{V}^\delta\|_{H^2(\Omega)} \leq C\|N_s - \widetilde{N}_s\|_{L^2(\omega_x)}, \tag{4.3.28}$$

where C stands for a nonnegative constant not depending on δ.

Proof. Multiplying the regularized Poisson equation (4.3.8) by $V^\delta - \widetilde{V}^\delta$ and integrating, we obtain

$$\int_\Omega |\nabla(V^\delta - \widetilde{V}^\delta)|^2 dxdz = \int_\Omega \Big((N_s - \widetilde{N}_s)\mathcal{S}^\delta[V^\delta] + \widetilde{N}_s\big(\mathcal{S}^\delta[V^\delta] - \mathcal{S}^\delta[\widetilde{V}^\delta]\big)\Big)\mathcal{R}^\delta[V^\delta - \widetilde{V}^\delta]dxdz.$$

Because the functional $V \mapsto \mathcal{S}[V]$ is decreasing with respect to V, term $(\mathcal{S}^\delta[V^\delta] - \mathcal{S}^\delta[\widetilde{V}^\delta])\mathcal{R}^\delta[V^\delta - \widetilde{V}^\delta]$ is nonpositive. We deduce

$$\int_\Omega |\nabla(V^\delta - \widetilde{V}^\delta)|^2 dxdz \quad \leq \quad \|N_s - \widetilde{N}_s\|_{L^1(\omega_x)}\| < \mathcal{R}^\delta[V^\delta - \widetilde{V}^\delta], \mathcal{S}^\delta[V^\delta] > \|_{L^\infty(\omega_x)}. \tag{4.3.29}$$

Then, (i) of Lemma 4.3.2 and a Cauchy-Schwarz inequality gives

$$\int_\Omega |\nabla(V^\delta - \widetilde{V}^\delta)|^2 dxdz \leq C\|N_s - \widetilde{N}_s\|_{L^1(\omega_x)}\|\mathcal{R}^\delta[V^\delta - \widetilde{V}^\delta]\|_{L^2_z L^\infty_x(\Omega)}.$$

We use the property (i) of Lemma 4.3.3 and the embedding $H^1 \hookrightarrow L^2_z L^\infty_x$. We obtain

$$\int_\Omega |\nabla(V^\delta - \widetilde{V}^\delta)|^2 dxdz \leq C\|N_s - \widetilde{N}_s\|_{L^1(\omega_x)}\|V^\delta - \widetilde{V}^\delta\|_{H^1(\Omega)}.$$

Finally, thanks to the Poincaré inequality, we get (4.3.27).

For the H^2 estimate, we have

$$-\Delta(V^\delta - \widetilde{V}^\delta) = \rho^\delta - \widetilde{\rho}^\delta = \mathcal{R}^\delta\Big[(N_s - \widetilde{N}_s)\mathcal{S}^\delta[V^\delta] + \widetilde{N}_s\big(\mathcal{S}^\delta[V^\delta] - \mathcal{S}^\delta[\widetilde{V}^\delta]\big)\Big].$$

Then we bound the L^2 norm of the right hand side as above using the spectral properties in Section 4.3.1. We finally get the H^2 estimate (4.3.28) from the elliptic regularity.

□

Finally, a straightforward adaptation of Proposition 3.2 of [20] gives the following convergence result as δ goes to 0.

Proposition 4.3.8. *As $\delta \to 0$, the solution V^δ of the regularized Nanowire Poisson system converges, uniformly with respect to $N_s \in L^\infty([0,T];L^1(\omega_x))$ such that $N_s \geq 0$ a.e, to the solution V of the unregularized problem in $L^\infty([0,T];H^1(\Omega))$.*

4.3.5 Existence of solutions for the regularized system

Proposition 4.3.9. *Let $T > 0$ and $\delta \in [0,1]$ be fixed. Then the regularized problem NDDP$_\delta$ admits a unique solution (N_s^δ, V^δ) with $N_s^\delta \in C([0,T];L^2(\omega_x)) \cap L^2([0,T];H^1(\omega_x))$ and $V^\delta \in L^\infty([0,T];H^1(\Omega))$.*

Proof. The proof of this result follows closely the proof of Theorem 1.2 of [8]. Thus we will not detail it and only give the main steps. The proof relies on a fixed point argument on the map F defined by :
Step 1 : For a given $N_s^\delta \geq 0$, we solve the regularized Nanowire Poisson equation (4.3.8) with boundary conditions (4.3.13)–(4.3.14) and we define V_s^δ by (4.3.10) which belongs to $L^\infty([0,T];H^1(\omega_x))$.
Step 2 : The effective potential V_s^δ being known, we solve the following drift-diffusion equation for the unknown $\widehat{N}_s^\delta$

$$\partial_t \widehat{N}_s^\delta - \partial_x\Big(D(\partial_x \widehat{N}_s^\delta + \widehat{N}_s^\delta \partial_x V_s^\delta)\Big) = 0,$$

with the boundary condition $\widehat{N}_s^\delta|_{\partial\omega_x} = N_b$ and the initial value $\widehat{N}_s^\delta(0,x) = N_s^0(x)$. The map F is then defined after these two steps by $F(N_s^\delta) = \widehat{N}_s^\delta$.

Then we can prove that for T small enough, F is a contraction on the space $M_{a,T}$ defined by $M_{a,T} = \{n, \|n\|_T \leq a\}$ where the norm is

$$\|n\|_T = \Big[\max_{0\leq t\leq T} \|n(t)\|^2_{L^2(\omega_x)} + \int_0^T \|n(t)\|^2_{H^1(\omega_x)} dt\Big]^{1/2}. \tag{4.3.30}$$

We have then constructed a unique solution on a small time interval $[0,T_0]$. Using the a priori estimate, we can iterate this procedure to construct a solution on $[T_0, 2T_0]$ that extend the previous one. We iterate this construction until covering the interval $[0,T]$. □

4.3.6 Passing to the limit $\delta \to 0$

We construct a solution of the non-regularized Nanowire drift-diffusion Poisson system by passing to the limit $\delta \to 0$ in the regularization. First, we recall a statement of an Aubin-Lions lemma [2, 14] :

Lemma 4.3.10. *Take $T > 0$, $q \in (1, +\infty)$ and let $(f_n)_{n\in\mathbb{N}}$ be a bounded sequence of functions in $L^q([0,T];H)$ where H is a Banach space. If $(f_n)_{n\in\mathbb{N}}$ is bounded in $L^q([0,T];V)$ where V is compactly embedded in H and $\partial f_n/\partial t$ is bounded in $L^q([0,T];V')$ uniformly with respect to $n \in \mathbb{N}$, then, $(f_n)_{n\in\mathbb{N}}$ is relatively compact in $L^q([0,T];H)$.*

Proof of Theorem 4.1.1. We fix $T > 0$. From Proposition 4.3.9, there exists N_s^δ and V^δ solution of the regularized system NDDP$_\delta$ with the initial data $N_s^{\delta,0}$. The bound on $\|N_s^\delta\|_{L^1(\omega_x)}$ (4.3.20) and the dissipation estimate (Corollary 4.3.5) furnish a bound of $\sqrt{N_s^\delta}$ in $L^\infty([0,T];L^2(\omega_x))$ and in $L^2([0,T];H^1(\omega_x))$. Thus, N_s^δ is bounded uniformly with respect to

δ in $L^2([0,T];W^{1,1}(\omega_x))$ (since we have the equality $\partial_x N_s^\delta = 2\sqrt{N_s^\delta}\partial_x\sqrt{N_s^\delta}$). Next, using the Cauchy-Schwarz inequality and Assumption 4.1.3, we obtain

$$\int_0^T \Big(\int_{\omega_x} |\partial_x N_s^\delta + N_s^\delta \partial_x V_s^\delta| dx \Big)^2 dt \leq C \int_0^T \mathcal{D}^\delta(t) dt$$

where $\mathcal{D}^\delta$ is the entropy dissipation rate defined in (4.3.18) which is bounded in $L^1([0,T])$ uniformly with respect to δ. From the drift-diffusion equation (4.3.7), we conclude that $\partial_t N_s^\delta$ is bounded in $L^2([0,T];W^{-1,1}(\omega_x))$ uniformly with respect to δ. Therefore, we can apply the Aubin Lemma 4.3.10 for $q=2$, $H=L^1(\omega_x)$ and $V=W^{1,1}(\omega_x)$. There exists a subsequence (that we still denote abusively N_s^δ) such that $N_s^\delta \to N_s$ strongly in $L^2([0,T];L^1(\omega_x))$. Finally, for this function N_s, we solve the unregularized Nanowire Poisson system and construct V such that $V \in L^\infty([0,T];H^1(\Omega))$ (Proposition 4.3.6) and $\lim_{\delta\to 0}\|V^\delta - V\|_{L^2([0,T];H^1(\Omega))} = 0$ (thanks to Proposition 4.3.8).

The last step is to pass to the limit $\delta \to 0$ in the drift-diffusion equation. We have

$$\int_0^T \int_{\omega_x} N_s^\delta \partial_x V_s^\delta dx dt \quad \leq \quad C\|N_s^\delta\|_{L^1([0,T];L^2(\omega_x))}\|V^\delta\|_{L^\infty([0,T];H^1(\Omega))}.$$

Corollary 4.3.5 shows that $\|N_s^\delta\|_{L^1([0,T];L^2(\omega_x))}$ is bounded independently of δ and we conclude that there exists a nonnegative constant C independent of δ such that

$$\int_0^T \int_{\omega_x} N_s^\delta \partial_x V_s^\delta dx dt \leq C. \tag{4.3.31}$$

It gives a sense to the drift-diffusion equation when $\delta \to 0$. Finally, using (4.3.4), we immediately deduce that $V_{nn}^\delta \to V_{nn}$ in $L^2([0,T];H^1(\omega_x))$ and that

$$\partial_x V_s^\delta = \frac{\sum_n \partial_x V_{nn}^\delta e^{-\left(E_n + V_{nn}^\delta\right)}}{\mathcal{Z}^\delta}$$

converges in $L^2([0,T]\times\omega_x)$. It is enough to prove that

$$N_s^\delta \partial_x V_s^\delta \rightharpoonup N_s \partial_x V_s \quad \text{in} \quad \mathcal{D}'([0,T]\times\omega_x).$$

Thus, up to an extraction, (N_s, V) is a solution of the NDDP system. Moreover, by semicontinuity, we can pass in the limit in the a priori estimates such that we still have the relative entropy estimation of Proposition 4.3.4 for (N_s, V). □

4.4 Long time behavior

Finally, in the last part of this chapter, we prove the existence of a unique stationary solution in the case of thermodynamic equilibrium boundary data. Moreover, the relative entropy allows to prove the convergence of a transient solution towards this stationary solution when the time grows to infinity.

4.4.1 Stationary problem

The stationary problem that we consider reads

$$-\partial_x\Big(D(x)\big(\partial_x N_s^\infty(x) + N_s^\infty(x)\partial_x V_s^\infty(x)\big)\Big) = 0, \tag{4.4.1}$$

where the stationary effective potential V_s^∞ is given by

$$V_s^\infty(x) = -\ln \mathcal{Z}^\infty(x) \quad \text{with} \quad \mathcal{Z}^\infty(x) = \sum_{n=1}^{+\infty} e^{-\left(E_n + <V^\infty(x,z), g_{nn}(z)>\right)}. \tag{4.4.2}$$

The potential V^∞ is solution of the following Poisson equation

$$-\Delta_{x,z} V^\infty(x,z) = \sum_{n=1}^{+\infty} N_n^\infty(x) g_{nn}(z), \tag{4.4.3}$$

with

$$N_n^\infty(x) = \frac{N_s^\infty(x)}{\mathcal{Z}^\infty(x)} e^{-\left(E_n + <V^\infty(x,z), g_{nn}(z)>\right)}. \tag{4.4.4}$$

The boundary conditions are similar to those of the non stationary problem

$$N_s^\infty(x) = N_b \qquad \text{for} \quad x \in \partial\omega_x, \tag{4.4.5}$$

$$V^\infty(x,z) = V_b(z) \qquad \text{for} \quad x \in \partial\omega_x, \tag{4.4.6}$$

$$\partial_z V^\infty(x,z) = 0 \qquad \text{for} \quad z \in \partial\omega_z. \tag{4.4.7}$$

By analogy to (4.1.11), we define the Slotboom variable $u^\infty = N_s^\infty e^{V_s^\infty} = N_s^\infty / \mathcal{Z}^\infty$.

Assumption 4.4.1. *We assume that the boundaries are at the thermal equilibrium that is to say that the Slotboom variable is the same for all $x \in \partial\omega_x$.*

Considering Assumption 4.4.1, we denote u_b^∞ the positive real number such that $u_b^\infty = N_b e^{V_s^b}$ where V_s^b is defined by

$$V_s^b = -\ln\Big(\sum_{n=1}^{+\infty} e^{-(E_n + <V_b(z), g_{nn}(z)>)}\Big).$$

Proposition 4.4.1. *Under Assumptions 4.1.3, 4.1.5 and 4.4.1, the stationary problem (4.4.1)–(4.4.7) admits a unique solution such that $N_s^\infty \in \mathcal{C}^2(\omega_x)$ and $V^\infty \in \mathcal{C}^2(\Omega)$.*

Proof. First, we remark that the stationary drift-diffusion equation can be written

$$-\partial_x\big(De^{-V_s^\infty}\partial_x u^\infty\big) = 0, \tag{4.4.8}$$

with, thanks to Assumption 4.4.1, the boundary condition

$$u^\infty = u_b^\infty \quad \text{for } x \in \partial\omega_x. \tag{4.4.9}$$

The uniqueness of this problem implies immediately that $u^\infty = u_b^\infty \ \forall x \in \omega_x$. Then, the problem (4.4.1)–(4.4.4) is reduced to

$$-\Delta_{x,z} V^\infty = u_b^\infty \sum_{n=1}^{+\infty} e^{-\left(E_n + <V^\infty, g_{nn}>\right)} g_{nn}, \tag{4.4.10}$$

and the solution is the minimum of the convex functional

$$J(V) = \frac{1}{2}\int_\Omega |\nabla V|^2 dxdz + \int_{\omega_x} u_b^\infty \sum_{n=1}^{+\infty} e^{-\left(E_n + <V, g_{nn}>\right)}. \tag{4.4.11}$$

□

4.4.2 Convergence of the relative entropy

To finish, the study of the convergence of a transient solution towards the stationary solution is established proving the decreasing and the convergence towards 0 as t goes to $+\infty$ of the relative entropy defined by

$$W^\infty(t) = \sum_{n=1}^{+\infty} \int_{\omega_x} \left(N_n \ln\left(\frac{N_n}{N_n^\infty}\right) - N_n + N_n^\infty \right) dx + \frac{1}{2}\int_\Omega |\nabla(V - V^\infty)|^2 dxdz. \tag{4.4.12}$$

Proposition 4.4.2. *Under Assumptions 4.1.3, 4.1.5 and 4.4.1, a solution of the Nanowire Drift-Diffusion Poisson system (4.1.9)–(4.1.17) is such that :*
(i) The relative entropy W^∞ defined in (4.4.12) is decreasing and $W^\infty(t) \to 0$ as $t \to +\infty$,
(ii) We have $N_s - N_s^\infty \to 0$ in $L^1(\omega_x)$ and $V - V^\infty \to 0$ in $H^1(\Omega)$ as $t \to +\infty$.

Proof. Let (N_s^∞, V^∞) the solution of the stationary problem (4.4.1)–(4.4.4). We deduce from (4.3.17), since u^∞ is constant, that

$$\frac{dW^\infty}{dt} = -\mathcal{D}(t),$$

where $\mathcal{D}$ is defined in (4.3.18). Thus, for all $t > 0$, we have

$$W^\infty(t) + \int_0^t \mathcal{D}(s) ds = W^\infty(0).$$

It implies that there exists a sequence $t_j \to 0$ such that

$$\mathcal{D}(t_j) \to 0 \quad \text{as} \quad j \to +\infty. \tag{4.4.13}$$

Next, as we have seen in the proof of Corollary 4.3.5 (4.3.25), we have the following inequality

$$\|\partial_x \sqrt{N_s}\|_{L^2}^2 \leq C\big(\mathcal{D}(t) + 1\big), \tag{4.4.14}$$

where C is a nonnegative constant. Evaluating (4.4.13) and (4.4.14) at $t = t_j$, we deduce that the sequence $(\sqrt{N_s(t_j)})_j$ is bounded in $H^1(\omega_x)$. Because of the compactness embedding of

$H^1(\omega_x)$ into $L^4(\omega_x)$, we can say that there exists a $\overline{N_s}$ in $L^2(\omega_x)$ such that $\sqrt{\overline{N_s}} \in H^1(\omega_x)$ and $N_s(t_j) \to \overline{N_s}$ in $L^2(\omega_x)$ as $j \to +\infty$.

With Proposition 4.3.7, it follows that it exists a $\overline{V}$ in $H^2(\Omega)$ such that $V(t_j) \to \overline{V}$ in $H^2(\Omega)$ as $j \to +\infty$. As above, thanks to (4.3.4), we can say it exists also a $\overline{V_s}$ in $H^1(\omega_x)$ such that $V_s(t_j) \to \overline{V_s}$ in $H^1(\omega_x)$ as $j \to +\infty$ and consequently we deduce that

$$u(t_j) = N_s(t_j)e^{V_s(t_j)} \to \overline{N_s}e^{\overline{V_s}} \quad \text{in } L^2(\omega_x). \tag{4.4.15}$$

Now, we write, for any $h \in L^4(\omega_x)$,

$$\Big| \int_{\omega_x} \partial_x\big(N_s(t_j)e^{V_s(t_j)}\big)h dx \Big| = \Big| \int_{\omega_x} \partial_x u(t_j) h dx \Big|.$$

A Cauchy-Schwarz inequality gives

$$\Big| \int_{\omega_x} \partial_x\big(N_s(t_j)e^{V_s(t_j)}\big)h dx \Big| \leq \Big(\int_{\omega_x} e^{-V_s(t_j)} \frac{|\partial_x u(t_j)|^2}{u(t_j)} dx \Big)^{1/2} \|N_s(t_j)e^{2V_s(t_j)}\|^{1/2}_{L^2(\omega_x)} \|h\|_{L^4(\omega_x)}.$$

Using (4.4.15), (4.4.13) and Assumption 4.1.3, we deduce that

$$\Big| \int_{\omega_x} \partial_x\big(N_s(t_j)e^{V_s(t_j)}\big)h dx \Big| \to 0 \quad \text{as} \quad j \to +\infty, \tag{4.4.16}$$

and thus that $\overline{N_s}e^{\overline{V_s}}$ is constant in ω_x.

As we already said, $(\sqrt{N_s(t_j)})_j$ is bounded in $H^1(\omega_x)$ and $N_s(t_j) \to \overline{N_s}$ in $L^2(\omega_x)$ as $j \to +\infty$. Consequently, the properties of the trace of $H^1(\omega_x)$ functions and the embedding of $H^1(\partial\omega_x)$ into $L^2(\partial\omega_x)$ give that $\overline{N_s}|_{\partial\omega_x} = N_b$. In the same way, we have $\overline{V_s}|_{\partial\omega_x} = V_s^b$. It implies that $\overline{N_s}e^{\overline{V_s}} = u_b^\infty$. Thus, $(\overline{N_s}, \overline{V})$ can be identified as the unique solution of the stationary Nanowire Drift-Diffusion Poisson problem

$$\overline{N_s} = N_s^\infty \quad \text{and} \quad \overline{V} = V^\infty \quad \text{as } j \to +\infty. \tag{4.4.17}$$

With the definitions (4.1.14) and (4.4.4), we deduce that $N_n(t_j) \to N_n^\infty$ for each band n and thus $W^\infty(t_j) \to 0$. Since the function W is decreasing, we finally obtain

$$\lim_{t\to+\infty} W^\infty(t) = \lim_{j\to+\infty} W^\infty(t_j) = 0. \tag{4.4.18}$$

Consequently, $\|V(t) - V^\infty\|_{H^1(\Omega)} \to 0$ as $t \to +\infty$. Moreover, we remind that $N_s = \sum_{n=1}^{+\infty} N_n$ and we conclude that $\|N_s(t) - N_s^\infty\|_{L^1(\omega_x)} \to 0$ as $t \to +\infty$.

□

Appendix : Technical lemmas for the diffusive limit

Lemma 4.A.1. *For all function $p \mapsto \gamma(p)$ polynomially increasing as well as all its derivative and for all $\phi \in \mathcal{C}^\infty([0,T]\times\mathbb{R})$ compactly supported, the function $\psi = \gamma\phi$ can be taken as test function in the weak formulation (4.2.27) of the Boltzmann equation.*

Proof. Let $p \mapsto \xi_R(p)$ such that $\xi_R \in \mathcal{D}([-R,R])$, $0 \le \xi_R \le 1$, $|\partial_p \xi_R| \le 1$ and $\xi_R \to 1$ a.e. when $R \to +\infty$. We set $\psi_R = \phi\gamma\xi_R$, function with which we can write the weak formulation (4.2.27). To pass to the limit $R \to +\infty$, it suffices from a Lebesgue theorem that $\gamma f_n^\eta \in L^1_p(\mathbb{R})$ and $p\gamma f_n^\eta \in L^1_p(\mathbb{R})$ as well as for $\partial_p\gamma$. However, with the Cauchy-Schwarz inequality,

$$\int_{\mathbb{R}} |\gamma f_n^\eta|(1+|p|)dp \le \left(\int_{\mathbb{R}} (1+|p|)^2 M_n(p)\gamma^2(p)dp\right)^{1/2}\left(\int_{\mathbb{R}} \frac{(f_n^\eta)^2}{M_n(p)}dp\right)^{1/2} < \infty,$$

because γ is polynomially increasing. □

Lemma 4.A.2. *Let Θ be defined in (4.2.8). There exist nonnegative constants C_0, C_1 and C_2 such that $\forall (t,x) \in [0,T]\times\mathbb{R}$:*

$$C_1(1+|p|) \le \left|\frac{\Theta_n}{\mathcal{M}_n}\right| \le C_2(1+|p|), \tag{4.A.1}$$

$$\left|\frac{\partial_s \Theta_n}{\mathcal{M}_n}\right| \le C_0(1+|p|^2) \quad \textit{for } s{=}t,\ x \textit{ and } p. \tag{4.A.2}$$

Proof. By the definition (4.2.8), we have

$$\lambda_n \Theta_n = \mathcal{Q}_B^+(\Theta)_n + \frac{p}{m_n^*}\mathcal{M}_n. \tag{4.A.3}$$

where we denote $\mathcal{Q}_B^+(\Theta)_n = \mathcal{M}_n \sum_{n'\ge 1}\int \alpha_{n,n'}\Theta_{n'}dp'$ and $\lambda_n = \sum_{n'\ge1}\int \alpha_{n,n'}\mathcal{M}_{n'}dp'$. Using Assumption 4.2.1, we immediately find $\alpha_1 \le \lambda_n \le \alpha_2$. Applying a Cauchy-Schwarz inequality,

$$|\mathcal{Q}_B^+(\Theta)_n| \le \alpha_2\mathcal{M}_n \sum_{n'=1}^{+\infty}\int |\Theta_{n'}(p')|dp' \le \alpha_2\mathcal{M}_n\left(\sum_{n'=1}^{+\infty}\int \frac{\left(\Theta_{n'}(p')\right)^2}{\mathcal{M}_{n'}(p')}dp'\right)^{1/2}.$$

Since $\Theta \in L^2_{\mathcal{M}}$, (4.A.1) follows directly from (4.A.3) and we differentiate it to obtain (4.A.2). □

Bibliography

[1] N.W. Ashcroft and N.D. Mermin. *Solid State Physics*. Saunders College Publishing, 1976.

[2] J.-P. Aubin. Un théorème de compacité. *C. R. Acad. Sci. Paris*, 256:5042–5044, 1963.

[3] L. Barletti and N. Ben Abdallah. Quantum Transport in Crystals: Effective Mass Theorem and K·P Hamiltonians. *Comm. Math. Phys.*, 307:567–607, 2011.

[4] N. Ben Abdallah and P. Degond. On a hierarchy of macroscopic models for semiconductors. *J. Math. Phys.*, 37(7):3306–3333, 1996.

[5] N. Ben Abdallah, C. Jourdana, and P. Pietra. An effective mass model for the simulation of ultra-scaled confined devices. Preprint IMATI-CNR 10PV11/7/0.

[6] N. Ben Abdallah and F. Méhats. On a Vlasov-Schrödinger-Poisson model. *Comm. Partial Differential Equations*, 29(1-2):173–206, 2004.

[7] N. Ben Abdallah and F. Méhats. Semiclassical analysis of the Schrödinger equation with a partially confining potential. *J. Math. Pures Appl. (9)*, 84(5):580–614, 2005.

[8] N. Ben Abdallah, F. Méhats, and N. Vauchelet. Diffusive transport of partially quantized particles: existence, uniqueness and long-time behaviour. *Proc. Edinb. Math. Soc. (2)*, 49(3):513–549, 2006.

[9] N. Ben Abdallah and M. L. Tayeb. Diffusion approximation for the one dimensional Boltzmann-Poisson system. *Discrete Contin. Dyn. Syst. Ser. B*, 4(4):1129–1142, 2004.

[10] C. Heitzinger and Ringhofer C. A transport equation for confined structures derived from the Boltzmann equation. *Comm. Math. Sci.*, 9(3):829–857, 2011.

[11] A. Henrot. *Extremum problems for eigenvalues of elliptic operators*. Frontiers in Mathematics. Birkhäuser Verlag, Basel, 2006.

[12] C. Jourdana and N. Vauchelet. Analysis of a diffusive effective mass model for nanowires. Kinet. Relat. Models (to appear).

[13] A. Jüngel. *Transport equations for semiconductorsSemiconductor equations*. Lecture Notes in Physics No. 773. Springer, Berlin, 2009.

[14] J.-L. Lions. *Équations différentielles opérationnelles et problèmes aux limites.* Die Grundlehren der mathematischen Wissenschaften, Bd. 111. Springer-Verlag, Berlin, 1961.

[15] P.A. Markowich, C.A. Ringhofer, and C. Schmeiser. *Semiconductor equations.* Springer-Verlag, Vienna, 1990.

[16] N. Masmoudi and M. L. Tayeb. Diffusion limit of a semiconductor Boltzmann-Poisson system. *SIAM J. Math. Anal.*, 38(6):1788–1807 (electronic), 2007.

[17] M. S. Mock. *Analysis of mathematical models of semiconductor devices*, volume 3 of *Advances in Numerical Computation Series.* Boole Press, Dún Laoghaire, 1983.

[18] P. Pietra and N. Vauchelet. Modeling and simulation of the diffusive transport in a nanoscale double-gate mosfet. *J. Comput. Electron.*, 7:52–65, 2008.

[19] F. Poupaud. Diffusion approximation of the linear semiconductor Boltzmann equation: analysis of boundary layers. *Asymptotic Anal.*, 4(4):293–317, 1991.

[20] N. Vauchelet. Diffusive transport of partially quantized particles: $L \log L$ solutions. *Math. Models Methods Appl. Sci.*, 18(4):489–510, 2008.

[21] N. Vauchelet. Diffusive limit of a two dimensional kinetic system of partially quantized particles. *J. Stat. Phys.*, 139(5):882–914, 2010.

[22] T. Wenckebach. *Essential of Semiconductor Physics.* Wiley, Chichester, 1999.

Chapter 5

Hybrid classical-quantum approach : modeling and simulations

Nota bene : A short summary of this chapter has been submitted as a proceeding of the conference SMAI 2011, published in ESAIM Proceedings. It is a joint work with N. Ben Abdallah, P. Pietra and N. Vauchelet.

In this chapter, we propose a hybrid classical-quantum model to study the motion of electrons in ultra-scaled confined nanostructures. The transport of charged particles is considered as one dimensional. It is described by a quantum effective mass model in the active zone (where quantum effects are strong) coupled directly with a drift-diffusion system in the rest of the device (since collisions with phonons play an important role in these regions). The connection conditions are obtained by writing the continuity of the current at interfaces. In this chapter, we explain how the model takes into account the peculiarities due to the strong confinement. Then, we describe the implemention algorithm, discussing also the scalability of the code. We also present numerical simulations for a simplified one wall carbon nanotube.

5.1 Introduction

In the recent semiconductor devices, and specially in ultra-scaled confined nanostructures, quantum effects play an important role in the particle transport due to the extremely small dimensions. Nevertheless, these quantum effects generally take place in a localized region whereas in the rest of the device domain the transport can be described by classical models. Thus, it can be interesting to follow a hybrid strategy : use a quantum model in regions where quantum effects are strong and couple it to a classical model in the rest of the device domain.

The hybrid strategy is motivated by different points of view. First, the quantum transport simulations are complex and above all computationally expensive. Secondly, quantum models usually do not include collisions of charged particles. For example, in FETs, an active zone is sandwiched between two largely doped regions (Source and Drain) considered as electron reservoirs. The electron-phonon collisions are important in these zones and thus, the transport is expected to be in a highly collisional regime. Thirdly, boundary conditions are not easily imposed in quantum models. Specially for large gate potentials, many waves are reflected and the transparent boundary conditions do not take them into account correctly. This issue will be made more precise in the presentation of numerical results. For all these reasons, we study in this chapter a one-dimensional coupled stationary Schrödinger drift-diffusion model and we present numerical simulations for an ultra-scaled confined nanostructure in which the transport can be seen as acting only in one dimension.

This spatial coupling is in the continuity of other works. In [6], a coupled kinetic-quantum model has been introduced. A Boltzmann equation is used in the classical zones instead a Schrödinger equation is chosen in the quantum domain. So, the transport in the quantum region is considered ballistic, whereas the classical regions can be high collisional with an appropriate collision operator. At interfaces, reflection-transmission coefficients are defined to give the boundary conditions of the Boltzmann equation. Inversely, the distribution function is used as an alimentation function to construct the quantum density. In this paper, the author proves that the reflection-transmission conditions preserve the current.

Next, in [14], the Boltzmann equation and the reflection-transmission conditions are replaced by a drift-diffusion equation and interface conditions. These connection conditions are derived from those of [6] through a diffusive approximation and a boundary layer analysis. In [5], the strategy to couple the drift-diffusion Schrödinger system is quite different since the coupling is direct and authors get an analytic expression of the connection conditions by writing the exact continuity of the current at the interfaces. Differently, in [14], due to the diffusion approximation, the continuity of the classical and the quantum current is only preserved up to an order α where α is the small parameter of the diffusion approximation. We also mention [15] where a hybrid strategy is studied with a quantum drift-diffusion equation.

Here, we follow the method of [5], coupling directly our classical model with the quantum one. The difference is that we have to take in account different bands. We preserve the continuity of the total current. Also, in [14, 5], numerical simulations are performed for a resonant tunneling diode. Here, we have in mind a gate-all-around FET, with a three dimensional self-consistent potential. Due to the gate in particular, the system is more sensitive to the boundary conditions and numerical simulations have to be implemented with caution. Simulations presented in this chapter are done for a simplified one wall carbon nanotube. An effort has been also done in the parallelization of the code in order to perform high-performance computations decreasing the overall computational cost.

This chapter is organized as follows. In the first part, we present the hybrid strategy for

ultra-scaled confined nanostructures. In Section 5.2, we remind the equations in the classical regions (introduced in [19] and in this thesis in Chapter 4), those in the quantum zone (obtained in [8] and in this thesis in Chapter 3) and we finish explaining the interface conditions. Again, self–consistent computations required that the transport equations are coupled with a 3D Poisson equation. In Section 5.3, we describe the numerical method, based on mixed finite elements, to solve the drift-diffusion and we present some numerical results obtained for our simplified carbon nanotube. Section 5.4 is devoted to the implementation of the hybrid classical-quantum strategy. After an explanation of the algorithm, we present numerical results for this approach and we discuss advantages of this approach with respect to the drift-diffusion or the fully quantum one presented in Chapter 3. Finally, Section 5.5 is dedicated to high-performance computations, with a discussion about the parallelization of the code.

5.2 Presentation of the hybrid strategy

As in the previous chapters, we study an ultra-scaled confined nanostructure defined in a bounded domain $\Omega = (x_L, x_R) \times \omega_\epsilon$, where (x_L, x_R) is the transport domain and ω_ϵ is the two dimensional cross section containing only few atoms. Some important quantities have already been introduced in this PhD thesis to describe such structures. We only remind here their expressions (in physical variables), and we refer to the previous chapters for more explanations. So, we still denote by V the slowly varying potential defined in Ω and computed through the resolution of a Poisson equation. Again, the variable z of the transversal section can be considered as fast variable, and it can be rescaled as $z' = \frac{z}{\epsilon}$, where ϵ is the lattice spacing. Then, ω denotes the scaled cross-section. Also, we consider the Bloch functions $\chi_n^\epsilon(x, z')$'s, generated by the lattice potential $W_\mathcal{L}$ periodic only in the longitudinal direction, which are solutions of the following eigenvalue problem in the cell $\mathcal{U}_\epsilon = (-\epsilon/2, \epsilon/2) \times \omega$

$$\begin{cases} -\frac{\hbar^2}{2m_e}\Delta\chi_n^\epsilon + W_\mathcal{L}\chi_n^\epsilon = E_n\chi_n^\epsilon. \\ \chi_n^\epsilon(x, z') = 0 \quad \text{on } \partial\omega, \quad \chi_n^\epsilon \ \epsilon\text{-periodic in } x. \end{cases} \tag{5.2.1}$$

$\hbar$ is the reduced Planck constant and m_e is the electron mass. In this chapter, we still make the following assumption :

Assumption 5.2.1. *We assume that the eigenvalues E_n of (5.2.1) are all simple.*

Then, we can define the n^{th} band effective mass m_n^* by

$$\frac{m_e}{m_n^*} = 1 - \frac{2\hbar^2}{m_e}\sum_{q\neq n}\frac{P_{nq}P_{qn}}{E_n - E_q} \quad \text{with} \quad P_{nq} = \int_{\mathcal{U}_\epsilon} \partial_x\chi_q^\epsilon\ \overline{\chi_n^\epsilon} dxdz'. \tag{5.2.2}$$

Moreover, the one dimensional n^{th} band effective potential V_{nn} is given by

$$V_{nn}(x) = \int_\omega V(x, \epsilon z')g_{nn}(z')dz', \tag{5.2.3}$$

where the quantities g_{nn}'s, which allow to make the link between the 1D transport direction to the 3D confined structure, are

$$g_{nn}(z') = \int_{-\epsilon/2}^{\epsilon/2} |\chi_n^\epsilon(x, z')|^2 dx. \tag{5.2.4}$$

Now, we present the hybrid strategy to couple, spatially in the transport direction, the Schrödinger system with the drift-diffusion equation. We assume that the device domain in the transport direction x is divided into a quantum zone $\omega_Q = (x_1, x_2)$, with $x_L < x_1 < x_2 < x_R$ and a classical zone $\omega_C = (x_L, x_R) \backslash \omega_Q$. The different regions of the domain (x_L, x_R) are illustrated in Fig.5.1.

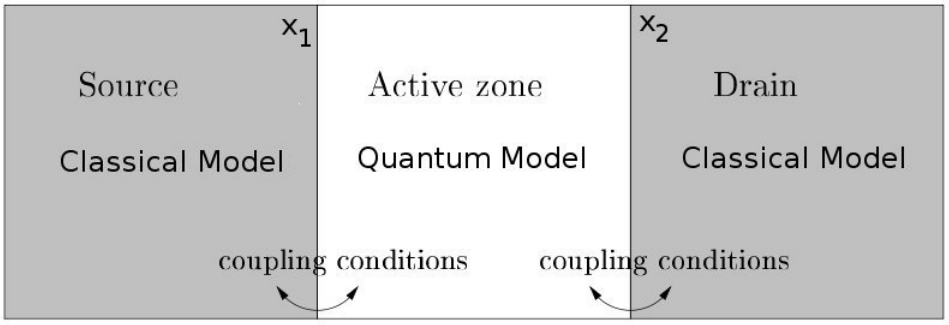

Figure 5.1: Schematic representation of hybrid model regions.

For the sake of completeness, we start to remind the transport equations in the classical regions (already presented in Chapter 4) as well as the equations in the quantum region (already detailled in Chapter 3). We assume at this point that the electrostatic potential V is given (and consequently also the n^{th} band effective potential V_{nn}). Afterward, we describe the interface conditions which preserve the continuity of the total current between the classical and the quantum domains. Finally, we present the self-consistent Poisson equation.

5.2.1 The classical regions

Contrary to Chapter 4, we are interested in numerical simulations and we write the equations in unscaled form. We consider the stationary drift-diffusion model on the disconnected domain ω_C

$$\frac{d}{dx} J_C(x) = 0, \tag{5.2.5}$$

where the classical current density is written in the following form

$$J_C(x) = -\mu(x)\ \partial_x \varphi(x)\ F\big(V_s(x) - \varphi(x)\big). \tag{5.2.6}$$

μ is the electron mobility coefficient (in physical variables, it is linked to the diffusive coefficient D, used in the previous chapter, by the Einstein relation $D = k_B T\mu$) and V_s is the effective potential defined by

$$V_s(x) = -k_B T \ln \mathcal{Z}(x) \quad \text{with} \quad \mathcal{Z}(x) = \sum_{n=1}^{+\infty} e^{-\left(E_n + V_{nn}(x)\right)/(k_B T)}. \tag{5.2.7}$$

k_B is the Boltzmann constant and T is the lattice temperature. Finally, φ is the unknown quasi-fermi energy. The choice to write the current density in function of the quasi-fermi energy variable is motivated by the fact that we want to find an analytic expression of the interface conditions, as we will explain in the following. As in the previous chapter, we work with the Boltzmann statistics. So, F is defined by

$$F(s) = n_i e^{-s/(k_B T)}, \tag{5.2.8}$$

where n_i is the intrinsic density.

Next, we impose the following boundary conditions

$$\varphi(x_L) = \varphi_L \qquad \text{and} \qquad \varphi(x_R) = \varphi_R \tag{5.2.9}$$

where φ_L and φ_R are imposed under the hypothesis of quasi-neutrality at the boundaries. Denoting by x_c the abscissa at the boundary ($x_c = x_L$ or $x_c = x_R$), the quasi-neutrality is written as

$$\int_{\omega_\epsilon} N_D(x_c, z) dz = F\big(V_s(x_c) - \varphi(x_c)\big), \tag{5.2.10}$$

where N_D is the prescribed doping density. For the Boltzmann statistics, it leads to

$$\varphi(x_c) = k_B T \ln \left(\frac{\int_{\omega_\epsilon} N_D(x_c, z) dz}{n_i} \right) + V_s(x_c). \tag{5.2.11}$$

Finally, the two classical regions are connected by means of the condition

$$J_C(x_1) = J_C(x_2) = h(\varphi(x_1)) - h(\varphi(x_2)). \tag{5.2.12}$$

h is a real-valued and monotonously increasing function which will be determined in the following subsections by the quantum expression for the current. We remark that, at the thermal equilibrium, $\varphi(x_1) = \varphi(x_2)$ and thus $J_C = 0$. We also see that $\varphi(x_1) > \varphi(x_2)$ gives a positive current and inversely. The system (5.2.5), (5.2.6), (5.2.9) and (5.2.12) is well posed (see [5] and references therein).

As in Chapter 4, in preparation for self-consistent computations, we need to define, from the surface density $N_s = F(V_s - \varphi)$, a charge density for each n^{th} band. We proceed as in the previous chapter (4.1.14) and we obtain

$$N_C^n(x) = F\big(V_s(x) - \varphi(x)\big) \frac{e^{-\left(E_n + V_{nn}(x)\right)/(k_B T)}}{\mathcal{Z}(x)}. \tag{5.2.13}$$

5.2.2 The quantum region

We consider the potential energy $\widetilde{V}_{nn}$ defined by

$$\widetilde{V}_{nn}(x) = \begin{cases} V_{nn}(x_1) =: V_{nn}^L, & \text{for } x \leq x_1, \\ V_{nn}(x), & \text{for } x \in \omega_Q, \\ V_{nn}(x_2) =: V_{nn}^R, & \text{for } x \geq x_2. \end{cases}$$

$\widetilde{V}_{nn}$ is a continuous extension of V_{nn} to the entire real line, with a constant potential energy outside the quantum region ω_Q. To fix ideas, we study here the case where $V_{nn}^L \geq V_{nn}^R$ (the other case can be treated exactly in the same way).

Then, for each n^{th} band and for each wave vector k, we consider the following scattering states Schrödinger equation in the entire real line ($x \in \mathbb{R}$)

$$-\frac{\hbar^2}{2m_n^*}\partial_{xx}\psi_n^k(x) + \widetilde{V}_{nn}(x)\psi_n^k(x) = \mathcal{E}_{n,k}\psi_n^k(x), \tag{5.2.14}$$

with

$$\mathcal{E}_{n,k} = \begin{cases} \mathcal{E}_{n,k}^L = \frac{\hbar^2 k^2}{2m_n^*} + V_{nn}^L & \text{if } k > 0, \\ \mathcal{E}_{n,k}^R = \frac{\hbar^2 k^2}{2m_n^*} + V_{nn}^R & \text{if } k < 0. \end{cases}$$

We remind that $\hbar$ is the reduced Planck constant. In the regions $x < x_1$ and $x > x_2$, the potential energy is constant and the solutions of (5.2.14) are given by a superposition of plane waves. We define the coefficients

$$p_n^{\pm}(k) = \sqrt{\hbar^2 k^2 \mp 2m_n^*(V_{nn}^R - V_{nn}^L)}. \tag{5.2.15}$$

Then, for a positive wave vector $k > 0$, we obtain

$$\begin{aligned} \psi_n^k(x) &= e^{ik(x-x_1)} + r_n(k)e^{-ik(x-x_1)} && \text{for all } x < x_1, \\ \psi_n^k(x) &= t_n(k)e^{ip_n^+(k)(x-x_2)/\hbar} && \text{for all } x > x_2. \end{aligned}$$

Analogously, for a negative wave vector $k < 0$, we have

$$\begin{aligned} \psi_n^k(x) &= e^{ik(x-x_2)} + r_n(k)e^{-ik(x-x_2)} && \text{for all } x > x_2, \\ \psi_n^k(x) &= t_n(k)e^{-ip_n^-(k)(x-x_1)/\hbar} && \text{for all } x < x_1. \end{aligned}$$

Moreover, as done in Chapter 3 in Section 3.2, one can derive Transparent Boundary Conditions (TBCs) (see [7], e.g.) at the boundaries x_1 and x_2. For $k > 0$, the TBCs are written as

$$\partial_x\psi_n^k(x_1) + ik\psi_n^k(x_1) = 2ik \quad \text{and} \quad \hbar\partial_x\psi_n^k(x_2) = ip_n^+(k)\psi_n^k(x_2), \tag{5.2.16}$$

and for $k < 0$, we have

$$\partial_x\psi_n^k(x_2) + ik\psi_n^k(x_2) = 2ik \quad \text{and} \quad \hbar\partial_x\psi_n^k(x_1) = -ip_n^-(k)\psi_n^k(x_1). \tag{5.2.17}$$

The reflection and transmission amplitudes $r_n(k)$ and $t_n(k)$ (which are not prescribed coefficients but deduced from the solution) are, respectively, determined by

$$r_n(k) = \frac{1}{2}\psi_n^k(x_1) + \frac{i}{2k}\partial_x\psi_n^k(x_1) \quad \text{and} \quad t_n(k) = \psi_n^k(x_2) \quad \text{for} \quad k > 0,$$
$$r_n(k) = \frac{1}{2}\psi_n^k(x_2) + \frac{i}{2k}\partial_x\psi_n^k(x_2) \quad \text{and} \quad t_n(k) = \psi_n^k(x_1) \quad \text{for} \quad k < 0.$$

Finally, we define the reflexion coefficients as $R_n(k) = |r_n(k)|^2$ and the transmission coefficients $T_n(k)$, corresponding to the proportion of incident electrons which are transmitted, as

$$T_n(k) = \begin{cases} \frac{p_n^+(k)}{\hbar k}|t_n(k)|^2 & \text{if } k > 0, \\ -\frac{\mathfrak{Re}\left(p_n^-(k)\right)}{\hbar k}|t_n(k)|^2 & \text{if } k < 0. \end{cases} \tag{5.2.18}$$

As it can be visualized in Fig.5.2, the transmission coefficients have the following properties

$$T_n(k) + R_n(k) = 1 \qquad \text{for all } k \in \mathbb{R}, \tag{5.2.19}$$
$$T_n(k) = T_n\Big(-\tfrac{p_n^+(k)}{\hbar}\Big) \qquad \text{for all } k > 0, \tag{5.2.20}$$
$$T_n(k) = T_n\Big(\tfrac{p_n^-(k)}{\hbar}\Big) \qquad \text{for all } \hbar k < -p_n^+(0), \tag{5.2.21}$$
$$T_n(k) = 0 \qquad \text{for all } -p_n^+(0) < \hbar k < 0, \tag{5.2.22}$$

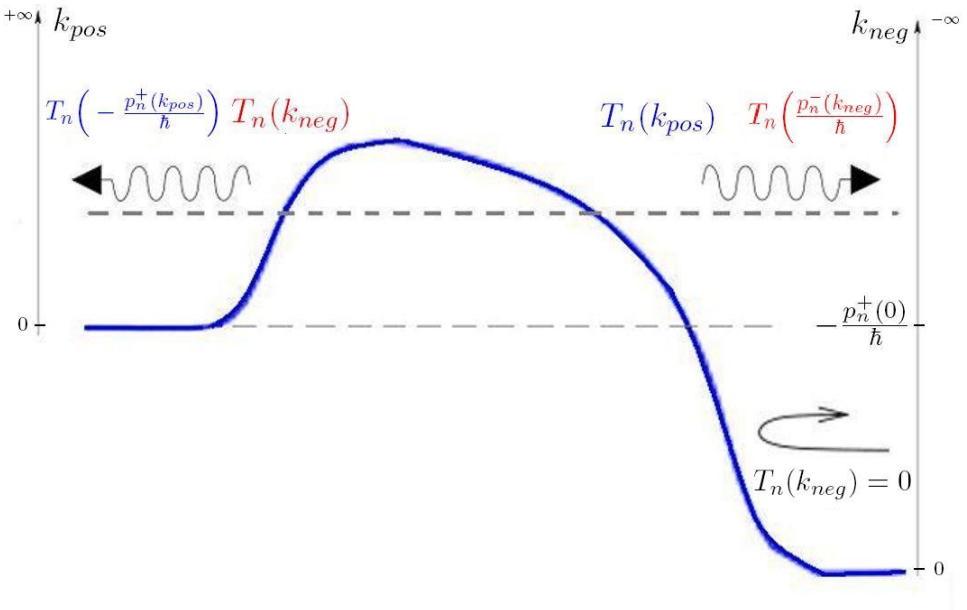

Figure 5.2: Illustration of the transmission coefficient properties.

Next, the 1D density carried by the n^{th} band N_{1D}^n in the region ω_Q is given superimposing the densities of states injected from the reservoirs, that is

$$N_Q^n(x) = \int_{\mathbb{R}} \phi_n(k)|\psi_n^k(x)|^2 dk, \qquad x \in \omega_Q, \tag{5.2.23}$$

where $\phi_n(k)$ is a given distribution function. This distribution function $\phi_n(k)$ can be expressed in term of the quasi-fermi energy variable at the boundaries

$$\phi_n(k) = \begin{cases} f_n\Big(E_n + \mathcal{E}^L_{n,k} - \varphi(x_1)\Big) & \text{if } k > 0, \\ f_n\Big(E_n + \mathcal{E}^R_{n,k} - \varphi(x_2)\Big) & \text{if } k < 0. \end{cases}$$

In the case of the Boltzmann statistics, f_n is defined by

$$f_n(s) = \frac{n_i \hbar}{\sqrt{2\pi k_B T m^*_n}} e^{-s/(k_B T)}. \tag{5.2.24}$$

Finally, the current density is defined by

$$J_Q(x) = \sum_{n=1}^{+\infty} J^n_Q(x), \tag{5.2.25}$$

where the n^{th} band current density is given by

$$J^n_Q(x) = \frac{q\hbar}{m^*_n} \int_{\mathbb{R}} \phi_n(k) \Im m\Big(\overline{\psi^k_n(x)} \partial_x \psi^k_n(x)\Big) dk, \qquad x \in \omega_Q. \tag{5.2.26}$$

It can be easily seen that the current density does not depend on x. Furthermore, using the TBCs of the Schrödinger equation (5.2.16) and (5.2.17), as well as the expression of the transmission coefficients (5.2.18), J^n_Q can be expressed in the following form

$$J^n_Q = \frac{q\hbar}{m^*_n} \int_0^{+\infty} \left(f_n\Big(E_n + \mathcal{E}^L_{n,k} - \varphi(x_1)\Big) - f_n\Big(E_n + \mathcal{E}^L_{n,k} - \varphi(x_2)\Big) \right) k T_n(k) dk. \tag{5.2.27}$$

For the sake of completeness, we present in the following the computation which allows to derive (5.2.27) from

$$J^n_Q(x) = \frac{q\hbar}{m^*_n} \left(\int_0^{+\infty} \phi_n(k) \Im m\Big(\overline{\psi^k_n(x)} \partial_x \psi^k_n(x)\Big) dk + \int_{-\infty}^0 \phi_n(k) \Im m\Big(\overline{\psi^k_n(x)} \partial_x \psi^k_n(x)\Big) dk \right).$$

Using the TBCs (5.2.16), for $k > 0$, we find immediately

$$\hbar \Im m\Big(\overline{\psi^k_n(x)} \partial_x \psi^k_n(x)\Big) = \Im m\Big(\imath p^+_n(k) |\psi^k_n(x_2)|^2\Big) = p^+_n(k) |\psi^k_n(x_2)|^2 = \hbar k T_n(k). \tag{5.2.28}$$

On the other hand, using (5.2.17) for $k < 0$, we find

$$\begin{aligned} \hbar \Im m\Big(\overline{\psi^k_n(x)} \partial_x \psi^k_n(x)\Big) &= \Im m\Big(- \imath p^-_n(k) |\psi^k_n(x_1)|^2\Big) \\ &= 0 \qquad \text{if } \hbar^2 k^2 < -2m^*_n(V^R_{nn} - V^L_{nn}) \\ &= -p^-_n(k) |\psi^k_n(x_1)|^2 = \hbar k T_n(k) \quad \text{if } \hbar^2 k^2 > -2m^*_n(V^R_{nn} - V^L_{nn}). \end{aligned} \tag{5.2.29}$$

Moreover, we remark that for $k < 0$ the condition $\hbar^2 k^2 < -2m^*_n(V^R_{nn} - V^L_{nn})$ is equivalent to $\hbar k > -p^+_n(0)$. Thus, we can write

$$\int_{-\infty}^0 \phi_n(k) \Im m\Big(\overline{\psi^k_n(x)} \partial_x \psi^k_n(x)\Big) dk = \int_{-\infty}^{-p^+_n(0)/\hbar} f_n\Big(E_n + \mathcal{E}^R_{n,k} - \varphi(x_2)\Big) k T_n(k) dk.$$

At this point, we make the following change of variables : $\hbar k' = p_n^-(k)$. It gives immediately $k' > 0$, $kdk = k'dk'$, $\hbar k = -p_n^+(k')$ and $\mathcal{E}_{n,k}^R = \mathcal{E}_{n,k'}^L$. We obtain

$$\int_{-\infty}^{0} \phi_n(k)\Im m\Big(\overline{\psi_n^k(x)}\partial_x\psi_n^k(x)\Big)dk = -\int_0^{+\infty} f_n\Big(E_n + \mathcal{E}_{n,k'}^L - \varphi(x_2)\Big)k'T_n\Big(-\frac{p_n^+(k')}{\hbar}\Big)dk'.$$

We use the reciprocity relation of the transmission coefficients (5.2.18) and we finally find

$$\int_{-\infty}^{0} \phi_n(k)\Im m\Big(\overline{\psi_n^k(x)}\partial_x\psi_n^k(x)\Big)dk = -\int_0^{+\infty} f_n\Big(E_n + \mathcal{E}_{n,k'}^L - \varphi(x_2)\Big)k'T_n(k')dk'. \tag{5.2.30}$$

Grouping (5.2.28) and (5.2.30), it leads to (5.2.27).

For the Boltzmann statistics, (5.2.27) can be written again as

$$J_Q^n = \frac{q\hbar}{m_n^*}\int_0^{+\infty} kT_n(k)f(E_n + \mathcal{E}_{n,k}^L)\Big(e^{\varphi(x_1)/(k_BT)} - e^{\varphi(x_2)/(k_BT)}\Big)dk. \tag{5.2.31}$$

Notice that the term containing the Fermi energy variables enters (5.2.31) as a multiplication factor, and this is crucial to write the interface conditions in an explicit way.

5.2.3 The interface conditions

Now, it is time to couple the transport equations of the classical and the quantum regions presented in Subsection 5.2.1 and 5.2.2. As we expected in (5.2.12), we can write the quantum current as the difference of a increasing function h of the quasi-fermi energy variable φ at the boundaries x_1 and x_2.

Immediately, with (5.2.27), we find

$$h(\varphi) = \sum_{n=1}^{+\infty}\frac{q\hbar}{m_n^*}\int_0^{+\infty} f_n\Big(E_n + \mathcal{E}_{n,k}^L - \varphi\Big)kT_n(k)dk. \tag{5.2.32}$$

In the case where f is given by the Boltzmann statistics (5.2.24), the function h can be expressed explicitly thanks to (5.2.31). We get

$$h(\varphi) = \Theta^{-1}e^{\varphi/(k_BT)}, \tag{5.2.33}$$

where Θ is a positive number defined by

$$\Theta^{-1} = \sum_{n=1}^{+\infty}\frac{q\hbar}{m_n^*}\int_0^{+\infty} f(E_n + \mathcal{E}_{n,k}^L)kT_n(k)dk. \tag{5.2.34}$$

Consequently, we obtain the final interface conditions

$$J_C(x_1) = J_C(x_2) := J_C, \tag{5.2.35}$$

and

$$e^{\varphi(x_1)/(k_BT)} - e^{\varphi(x_2)/(k_BT)} = \Theta J_C. \tag{5.2.36}$$

Remark 5.2.1. The interface conditions (5.2.35) and (5.2.36) preserve the continuity between the classical and the quantum current density. It does not mean that the coupling assures the continuity of the charge density, as we will observe in the numerical results.

This charge density of the hybrid model in the n^{th} band N_{1D}^n is defined by

$$N_{1D}^n(x) = \begin{cases} N_Q^n(x) & \text{for } x \in \omega_Q, \\ N_C^n(x) & \text{for } x \in \omega_C. \end{cases}$$

As in Chapter 3 and Chapter 4, the transformation from the one dimensional transport direction to the entire nanowire is done by the quantities g_{nn}'s (5.2.4). It leads

$$\rho(x,z) = \sum_{n\in\mathbb{N}} N_{1D}^n(x) g_{nn}(\frac{z}{\epsilon}) \qquad (x,z) \in (x_L, x_R) \times \omega_\epsilon. \tag{5.2.37}$$

Again, to take into account many particle effects, it is necessary to consider self-consistent computations. So, we couple the transport equations with the following Poisson equation on the electrostatic potential V_P

$$-\nabla\big(\epsilon_r(z)\nabla V_P(x,z)\big) = \frac{q}{\epsilon_0}\Big(N_D(x,z) - \rho(x,z)\Big), \qquad (x,z) \in (x_L, x_R) \times \omega_\epsilon. \tag{5.2.38}$$

We remind that q is the elementary charge, ϵ_0 the permittivity in vacuum, ϵ_r the relative permittivity and N_D the prescribed doping density. Equation (5.2.38) is supplemented by boundary conditions, similarly to Chapter 3, Section 3.3.5.

Remark 5.2.2. In Section 3.3.5, the built-in potential V_b was defined, solving at the contacts x_c, the following 2D Poisson equation

$$\begin{cases} -\nabla(\epsilon_r \nabla V_b(z)) = \frac{q}{\epsilon_0} N_D(x_c, z) - \frac{q}{\epsilon_0}\rho_{2D}(z), & z \in \omega_\epsilon, \\ \partial_\nu V_b = 0, \quad \int_{\omega_\epsilon} V_b(z)dz = 0, \end{cases}$$

where ρ_{2D} was given by

$$\rho_{2D}(z) = \frac{\sum_n e^{-E_n/(k_BT)} g_{nn}(\frac{z}{\epsilon})}{\sum_n e^{-E_n/(k_BT)}} \int_{\omega_\epsilon} N_D(x_c, z)dz, \tag{5.2.39}$$

assuming that the potential V is constant along the transport direction and consequently all the wave functions ψ_n^k contributing to ρ have unitary modulus. Differently, for the drift-diffusion model, using (5.2.37), (5.2.13) and (5.2.10), we obtain

$$\rho_{2D}(z) = \frac{\sum_n e^{-\left(E_n + V_{nn}(x_c)\right)/(k_BT)} g_{nn}(\frac{z}{\epsilon})}{\sum_n e^{-\left(E_n + V_{nn}(x_c)\right)/(k_BT)}} \int_{\omega_\epsilon} N_D(x_c, z)dz. \tag{5.2.40}$$

The density ρ_{2D} depends now on the potential V. Nevertheless, in simulations obtained in Chapter 3 for our simplified device, V_{nn}'s are almost equals at contacts for all the considered bands. In this case, the two formulations (5.2.39) and (5.2.40) coincide. That is the reason why we decide in the sequel to compute the built-in potential V_b only with (5.2.39).

5.3 Implementation of the drift-diffusion model

The algorithm is similar to Chapter 3 (Section 3.3.6), and it is summarized in Fig.5.3. We still have two separate blocks. The first block consists of solving the eigenvalue problem of the Bloch functions in the primitive cell (5.2.1). The second block couples, by means of an iterative method of Gummel type the transport equations with the Poisson equation, incorporating the physical quantities computed in the first block. For this second block, we first consider the whole system at thermal equilibrium (zero applied Drain-Source voltage) and then we apply a Drain-Source voltage V_{DS}, incremented by steps. Finally, this procedure is repeated for different gate voltage V_G.

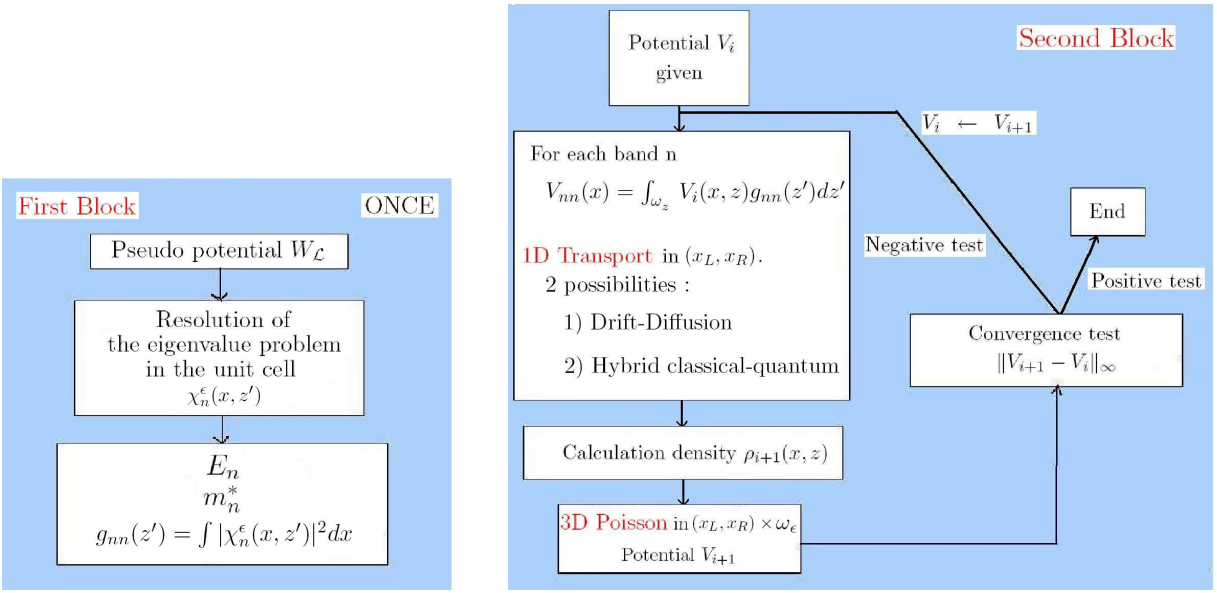

Figure 5.3: General organization of the effective mass models.

Consequently, the only difference considered in this chapter is the approach used for the transport in the second block. In this section, we describe the numerical method used to solve the classical transport (drift-diffusion equation) in the entire transport domain. In the next section, we present the algorithm used to implement the hybrid strategy (just described in the previous section). In both cases, we consider that the distribution function is given by the Boltzmann statistics, and we present some numerical results for our simplified one-wall carbon nanotube.

5.3.1 Discretization with mixed finite elements

In this part, we present the numerical method used to solve the drift-diffusion equation

$$\frac{d}{dx} J(x) = 0, \qquad x \in (x_L, x_R), \tag{5.3.1}$$

with

$$J(x) = -\mu(x)\ \partial_x\varphi(x)\ F\big(V_s(x) - \varphi(x)\big), \tag{5.3.2}$$

and with Dirichlet boundary conditions in x_L and x_R (5.2.9).

In order to guarantee conservation properties for the current, we use a mixed finite element scheme. We refer to [9] and references therein, for a general presentation on mixed finite elements, to [10, 11, 12], for mixed finite elements for the drift–diffusion equation in density formulation, and to [16, 17], for the quasi-fermi level formulation. Let us first describe the mixed finite element scheme in the linear case, considering

$$J(x) = -a(x)\ \partial_x\varphi(x), \tag{5.3.3}$$

together with equation (5.3.1).

We consider the 1D domain $[x_L, x_R]$ and we define the following partition

$$x_L \equiv x_0 < x_1 < ... < x_{N-1} < x_N \equiv x_R.$$

We also denote by I_i the interval $]x_{i-1}, x_i[$ $(i = 1, \ldots, N)$. We choose the mixed finite elements of lowest order (introduced for 2D problems in [23]) and we write the system in hybrid form (see [1] for the theoretical study) introducing the following finite dimensional spaces

$$\begin{aligned} X_h &= \{\sigma \in L^2(x_L, x_R) \,:\, \sigma(x) \text{ is linear in } I_i,\ i = 1, \ldots, N\}, \\ W_h &= \{\xi \in L^2(x_L, x_R) \,:\, \xi \text{ is constant in } I_i,\ i = 1, \ldots, N\}, \\ \Lambda_{h,\chi} &= \{q \text{ is defined at the nodes } x_0, \ldots, x_N; q(x_0) = \chi(x_L)\, q(x_N) = \chi(x_R)\}. \end{aligned}$$

The mixed–hybrid approximation of equations (5.3.1) and (5.3.3) is then:

$$\text{Find } J_h \in X_h,\ \overline{\varphi}_h \in W_h,\ \varphi_h \in \Lambda_{h,\varphi},\ \text{such that :}$$

$$\int_{x_L}^{x_R} a^{-1}(x) J_h \sigma dx - \sum_{i=1}^{N} \int_{I_i} \overline{\varphi}_h \sigma_x dx + \sum_{i=1}^{N} \Big[\varphi_h \sigma\Big]_{x_{i-1}}^{x_i} \Bigg) = 0, \tag{5.3.4}$$

$$\sum_{i=1}^{N} \left(\int_{I_i} (J_h)_x \xi dx \right) = 0 \tag{5.3.5}$$

$$\sum_{i=1}^{N} \big[q J_h\big]_{x_{i-1}}^{x_i} = 0, \tag{5.3.6}$$

for all $\sigma \in X_h$, $\xi \in W_h$, $q \in \Lambda_{h,0}$. Notice that the first equation (5.3.4) is obtained from a weak version of (5.3.3), using integration by parts and summation over all I_i. The second equation (5.3.5) is a discrete weak version of (5.3.1), and the third equation (5.3.6) implies continuity of the current J_h at the nodes. As usual for this formulation, the variables J_h and $\overline{\varphi}_h$ can be eliminated by static condensation, leading to a final algebraic system in the variable φ_h. In the particular case under consideration, since the right hand side of (5.3.5) is null, the static condensation procedure is very simple. It is very easy to see that (5.3.5) implies that J_h is

constant in each I_i. Moreover, thanks to (5.3.6), we can conclude that J_h is globally constant. Then, if we choose $\sigma = 1$ on I_i and $\sigma = 0$ elsewhere, we obtain

$$J_{h|I_i} = -(\varphi_i - \varphi_{i-1}) / \int_{x_{i-1}}^{x_i} a^{-1}(x)dx \ . \tag{5.3.7}$$

Since J_h is constant, and therefore independent of i, (5.3.7) gives in particular

$$-(\varphi_{i+1} - \varphi_i) / \int_{x_i}^{x_{i+1}} a^{-1}(x)dx = -(\varphi_i - \varphi_{i-1}) / \int_{x_{i-1}}^{x_i} a^{-1}(x)dx, \tag{5.3.8}$$

which is a tridiagonal system in the unknowns φ_i. Here we use the notation φ_i for the value of the function φ_h in the node x_i. Then, the (constant) current J_h can be computed using formula (5.3.7). Moreover, from equation (5.3.4), taking $\sigma = x - (x_{i-1} + x_i)/2$ on I_i and $\sigma = 0$ elsewhere, we obtain $\overline{\varphi}_{h|I_i} = (\varphi_{i-1} + \varphi_i)/2$.

Notice that (5.3.8) could be obtained approximating directly the second order elliptic problem $-\frac{d}{dx}\big(a(x)\frac{d}{dx}\varphi(x)\big) = 0$ (+BC's) by means of piece–wise linear continuous finite elements, taking a piece–wise constant approximation of the coefficient $a(x)$ given by the harmonic average on the interval I_i

$$\overline{a}_{|I_i} = (x_i - x_{i-1}) / \int_{x_{i-1}}^{x_i} a^{-1}(x)dx \ .$$

We emphasize that the use of harmonic average (that comes out naturally in the mixed finite element setting) has been proved (in the one dimensional case) to provide better results than the use of the mean value, in particular when $a(x)$ exhibits sharp variations (see [2, 9]).

Now we go back to the discretization of problem (5.3.1)-(5.3.2) by taking

$$a(x) = \mu(x)\ F\big(V_s(x) - \varphi(x)\big). \tag{5.3.9}$$

in (5.3.8). To simplify the computation, in (5.3.9) we use, as approximation of $\varphi(x)$, the function $\overline{\varphi}_h \in W_h$. Within the iterative algorithm that will allow to solve the coupled drift–diffusion Poisson system, $\mu(x)$ is a given function, and $V_s(x)$ is a given piece-wise linear continuous function. The vectors of their values in the nodes, with a slight abuse of notation, will be denoted by $\mu = (\mu_0, \mu_1, ..., \mu_N)^T$, $V_s = (V_{s,0}, V_{s,1}, ..., V_{s,N})^T$. In order to completely define the discretization scheme, we need to approximate the integrals in (5.3.8) when $a(x)$ is given by (5.3.9), and we choose

$$\int_{x_{i-1}}^{x_i} a^{-1}(x)dx \sim \frac{2}{\mu_i + \mu_{i-1}} \int_{x_{i-1}}^{x_i} F^{-1}\big(V_s(x) - \overline{\varphi}_h\big)dx. \tag{5.3.10}$$

In the case of Boltzmann statistics, the function F is given by (5.2.8), and an explicit expression of (5.3.10) gives

$$\int_{x_{i-1}}^{x_i} a^{-1}(x)dx \sim {n_i}^{-1} \frac{2}{\mu_i + \mu_{i-1}} e^{-\left(\frac{\varphi_i + \varphi_{i-1}}{2k_BT}\right)} \mathcal{I}(V_s/k_BT), \tag{5.3.11}$$

where we recall that n_i is the constant intrinsic density as in (5.2.8), and $\mathcal{I}(u)$ represents, for a function u, linear in the interval I_i, the exact integral $\int_{x_{i-1}}^{x_i} e^{u(x)}dx$, given by the formula

$$\mathcal{I}(u) = \frac{x_i - x_{i-1}}{u_i - u_{i-1}}(e^{u_i} - e^{u_{i-1}}). \tag{5.3.12}$$

To summarize, using (5.3.11) we introduce the coefficients

$$D_0^i = D_0^i(\varphi_h) = -n_i \frac{\mu_i + \mu_{i-1}}{2} e^{\left(\frac{\varphi_i + \varphi_{i-1}}{2k_B T}\right)} / \mathcal{I}(V_s/k_B T), \tag{5.3.13}$$

that, inserted in (5.3.8), give

$$-D_0^i \varphi_{i-1} + \left(D_0^i + D_0^{i+1}\right)\varphi_i - D_0^{i+1}\varphi_{i+1} = 0. \tag{5.3.14}$$

The current is then given by

$$J_i = D_0^i * \left(\varphi_i - \varphi_{i-1}\right). \tag{5.3.15}$$

Consequently, the equations (5.3.14) together with the boundary conditions form a $N+1$ nonlinear system in the unknown φ that we can write in the form $G(\varphi) = 0$. To treat the nonlinearity, we solve this problem using a Newton algorithm. It means that for a given φ^{old}, the iteration step consists of solving

$$J_G\left(\varphi^{old}\right)\ \delta\varphi = -G\left(\varphi^{old}\right), \tag{5.3.16}$$

and then of defining $\varphi^{new} = \varphi^{old} + \delta\varphi$. We repeat the iterations until the convergence threshold is reached. In general, only few iterations are necessary since the convergence is quadratic.

In (5.3.16), J_G corresponds to the $(N+1) \times (N+1)$ Jacobian matrix. Some examples of entries of the Jacobian matrix evaluated at φ^{old} are presented in the following in the case where F is described by the Boltzmann statistics (5.2.8). It gives

$$\frac{\partial G}{\partial \varphi_{i-1}^{old}} = -D_0^i\left(1 + \frac{\varphi_{i-1}^{old} - \varphi_i^{old}}{2k_B T}\right), \tag{5.3.17}$$

$$\frac{\partial G}{\partial \varphi_i^{old}} = D_0^i\left(1 - \frac{\varphi_{i-1}^{old} - \varphi_i^{old}}{2k_B T}\right) + D_0^{i+1}\left(1 - \frac{\varphi_{i+1}^{old} - \varphi_i^{old}}{2k_B T}\right), \tag{5.3.18}$$

and

$$\frac{\partial G}{\partial \varphi_{i+1}^{old}} = -D_0^{i+1}\left(1 + \frac{\varphi_{i+1}^{old} - \varphi_i^{old}}{2k_B T}\right). \tag{5.3.19}$$

It is important to say that care has to be taken when dealing with the exponentials. We have to do by hand all the possible simplifications before to implement it, in order to avoid possible blow-up of the exponentials.

Moreover, the boundary conditions are now given by $\delta\varphi = 0$. So, we obtain, at each Newton iteration, a linear system with a tridiagonal matrix. It is easily solved using a LU decomposition and calculating explicitly each coefficient. Once we obtain φ_i for all $i = 0, ..., N$, we calculate the current J_i with the expression (5.3.15). Finally, an important point of the Newton method is the initialization in order to guarantee the convergence. For the first Gummel iteration at

thermal equilibrium, we initialize the Newton method taking $\varphi_i^0 = \varphi(x_C)$ (see (5.2.11)) for all $i = 0, ..., N$. Then, at each Gummel iteration, we initialize the Newton method with the quasi-fermi energy variable found in the previous iteration. Finally, when we increment a new Source-Drain voltage V_{DS}, if the incrementation step is enough small (around 0.02 V), we can use the quasi-fermi energy found for the previous V_{DS} to initialize the Newton algorithm at the first Gummel iteration.

5.3.2 Numerical results

In order to check the implementation approach that we just described and the model detailled in Section 5.2.1, we present in this subsection some numerical results obtained solving the transport problem with the drift-diffusion model in the entire longitudinal domain.

An important point of these simulations is the determination of the electron mobility coefficient μ. As it was already motivated in the Remark 4.2.1, we choose

$$\mu(x) = q\tau \sum_{n=1}^{+\infty} \frac{e^{-\left(E_n + V_{nn}(x)\right)/(k_B T)}}{m_n^* \sum_{m=1}^{+\infty} e^{-\left(E_m + V_{mm}(x)\right)/(k_B T)}}, \tag{5.3.20}$$

where τ is the relaxation time. It can be determined with the usual formulation

$$\tau = \frac{m_e \widetilde{\mu}}{q}, \tag{5.3.21}$$

where $\widetilde{\mu}$ is the electron mobility constant, which should be found in the semiconductor literature. However, we have to say that our physical understanding concerning this parameter is limited. For our simplified carbon nanotube, the semiconductor literature is of little help and it is difficult to figure out the suitable value. Consequently, we prefer to adjust it numerically in order to obtain a current comparable with the one of the fully quantum approach. In fact, for the drift-diffusion model, the current is exactly proportional to the mobility constant. So, one reasonable possibility is to choose $\widetilde{\mu}$ adjusting its value to the one obtained with the quantum model. In Fig.5.4, the obtained current-voltage characteristic is shown (and it can be compared with Fig.3.13 in Chapter 3).

On the contrary, the shape of the mobility coefficient $\mu(x)$ is much more significant than the value $\widetilde{\mu}$. In Fig.5.5, we present $\mu(x)$ for different Drain-Source voltages V_{DS}, for a fixed gate voltage $V_G = -0.1$ V. The spatial variations are due to the variations of V_{nn} (see formula (5.3.20)). An analogy can be done with the field dependent mobility (see i.e. [21, 20]) where the effective electric field is inserted in the definition of the mobility.

Finally, another quantity is interesting to be studied for the drift-diffusion model : the quasi-fermi energy φ. In Figs.5.6 and 5.7, each figure corresponds to a fixed gate voltage V_G where the quasi-fermi energy is plotted for different Source-Drain voltages V_{DS}. In order to visualize the variations in function of the gate voltage, we also represent in Fig.5.8 the gate dependent curves for a fixed applied voltage $V_{DS} = 0.08$ V (left figure, red curves) and $V_{DS} = 0.2$ V (right figure,

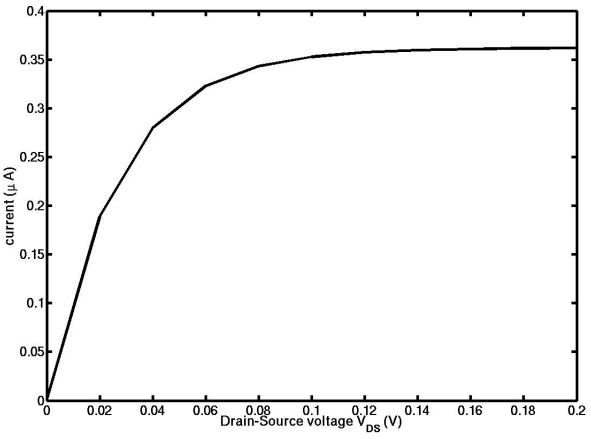

Figure 5.4: Current-Voltage characteristic for the drift-diffusion model with $V_G = -0.01$ V.

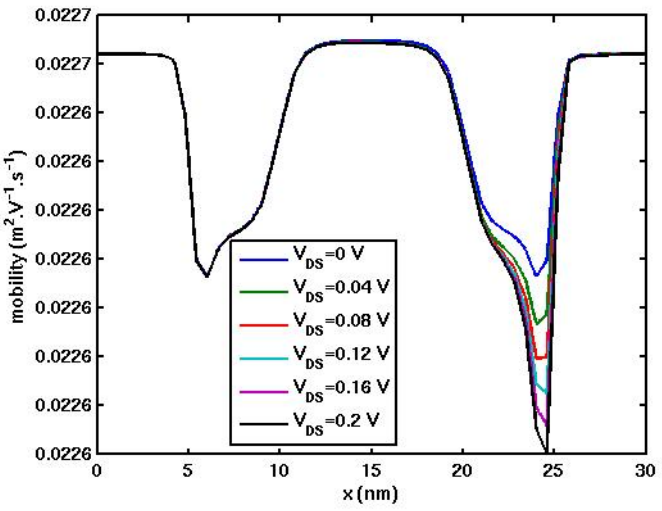

Figure 5.5: Mobility $\mu(x)$ for different Drain-Source voltages V_{DS}.

black curves). Obviously, φ decreases with the potential energy. At the drain contact, it is close to be a translation proportional to the potential energy, instead in the channel region, variations seems more complex and largely influenced by the gate. More precisely, when the gate voltage increases, the quasi-fermi energy tends to become linear between the Source and the Drain contacts. Here we consider the quasi-fermi energy as a variable in the entire domain. In the quantum approach, we only compute the fermi level at boundaries for the thermal equilibrium and we just translate it when we consider an applied voltage.

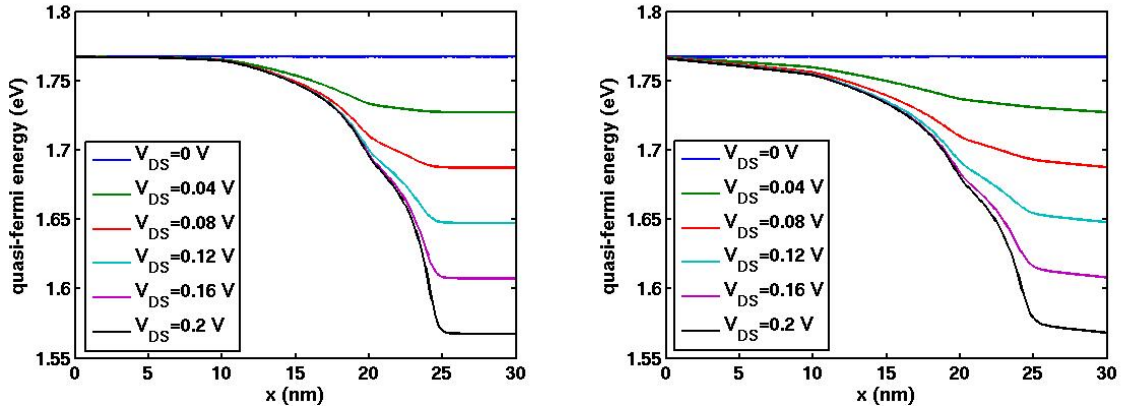

Figure 5.6: Quasi-fermi energy $\varphi(x)$ (eV) for different Drain-Source voltages V_{DS}, with fixed $V_G = -0.1$ V (left) and $V_G = 0$ V (right).

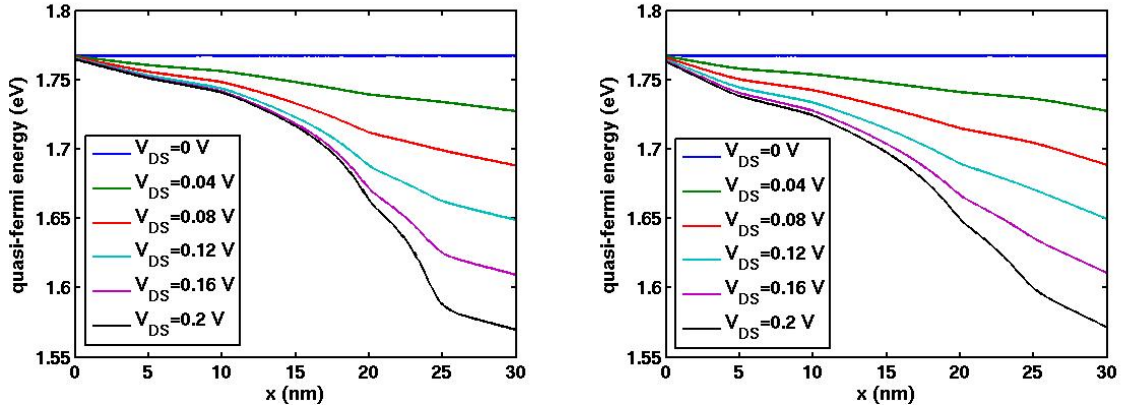

Figure 5.7: Quasi-fermi energy $\varphi(x)$ (eV) for different Drain-Source voltages V_{DS}, with fixed $V_G = 0.05$ V (left) and $V_G = 0.1$ V (right).

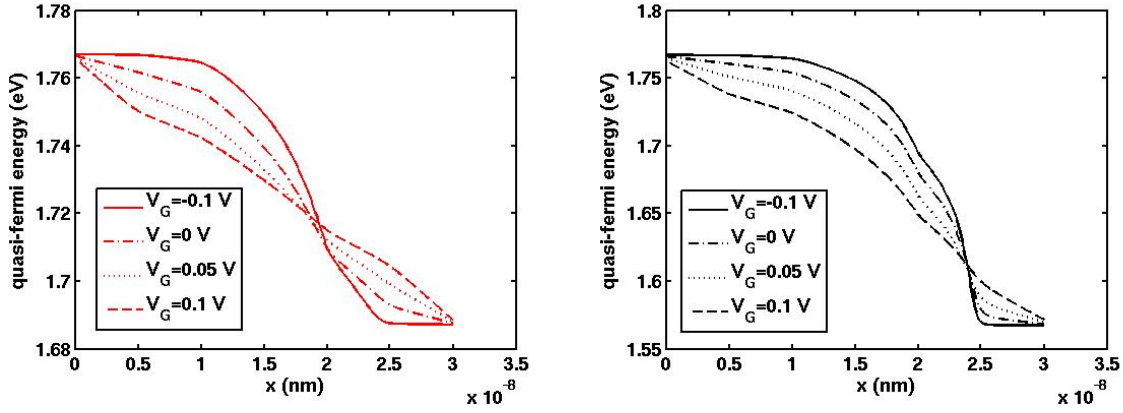

Figure 5.8: Quasi-fermi energy $\varphi(x)$ (eV) for a fixed Drain-Source voltage $V_{DS} = 0.08$ V (left) and $V_{DS} = 0.2$ V (right), for different V_G.

5.4 Treatment of the hybrid transport strategy

5.4.1 Implemented algorithm

We are now interested in the implementation of the hybrid strategy. We remind that it consists of using the Schrödinger system in the quantum zone ω_Q and the drift-diffusion model in the classical region ω_C. The solutions in the two domains are connected by the interface conditions. To present this hybrid strategy, we detail the different steps of a Gummel iteration. So, for a given potential V, we compute the quantities V_{nn} (5.2.3) and then $\mathcal{Z}$ and V_s (5.2.7) as well as μ (5.3.20). Next, we solve the Schrödinger equations for each band n and each wave vector k (5.2.14) on ω_Q with the TBCs (5.2.16) or (5.2.17). We obtain the wave vectors ψ_n^k and thus the transmission coefficients T_n (5.2.18). It allows to compute the number Θ (5.2.34). Solving the stationary drift-diffusion equation (5.2.5) on ω_C with the boundary conditions (5.2.9) and the two connection conditions (5.2.35) and (5.2.36), we obtain the quasi-fermi energy φ and consequently the classical density on each band N_C^n (5.2.13). Moreover, φ in x_1 and x_2 allow also to determine the quantum density on each band N_Q^n (5.2.23). Finally, as usual, we compute the three dimensional density ρ (5.2.37) and we solve the Poisson equation (5.2.38), modified according to the Gummel iteration algorithm as in (3.3.14), to obtain the new value of the potential V.

We refer to Chapter 3 for the resolution of the Schrödinger equations or of the Poisson equation. The drift-diffusion equation is solved with the method described in the previous subsection. The only difference is that we have to insert one line in the matrix generated during the Newton algorithm. This line corresponds to the interface condition (5.2.36). Again, it is important to care for exponentials to avoid blow-up, making simplification by hands. A consequence of this interface condition is that the matrix is not anymore tridiagonal. It is also not symmetric. Consequently, to solve the associated linear systems, we choose a routine which uses the generalized minimum residual (GMRES) iterative method with incomplete LU factorization preconditioner.

5.4.2 Numerical results

It is now time to present numerical results for this hybrid classical-quantum method. As in Chapter 3 (for the quantum model) and in Section 5.3 (for the drift-diffusion model), we study the simplified one-wall carbon nanotube described in Section 3.3.1 and we consider only three energy bands again (the 41^{th}, 42^{th} and the 43^{th} bands). The interfaces are located at $x_1 = 10$ nm and $x_2 = 20$ nm, which correspond to the doping discontinuities.

First, we present in Fig.5.9 1D profiles of the density and of the potential for a fixed gate voltage $V_G = -0.1$ V. These 1D curves are results of an integration of 3D quantities over the 2D wire section. As expected, we recover profiles of Fig.3.7 with the same influence of the gate and the doping. In the sequel, we will try to point out the differences between the different models.

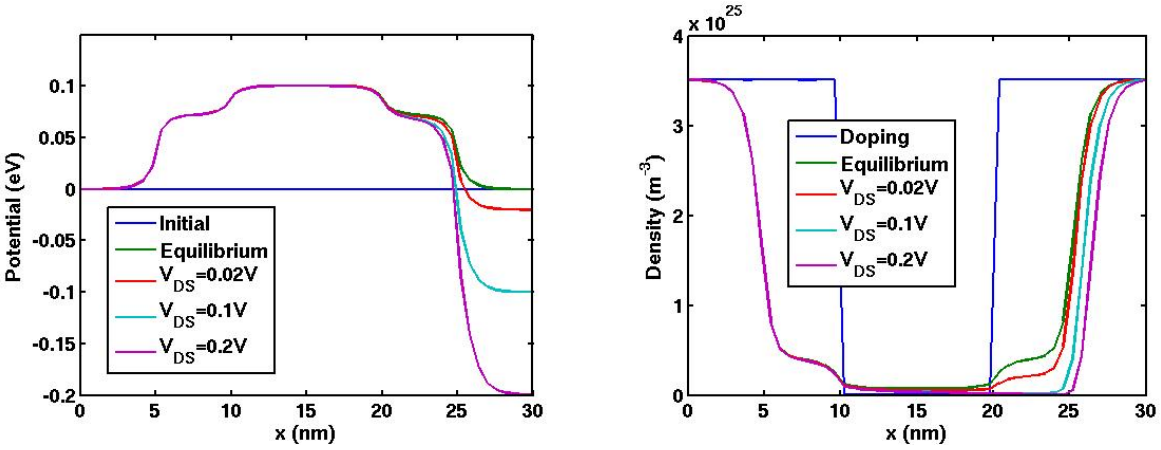

Figure 5.9: 1D potential energies (eV) (left) and 1D densities (m^{-3})(right) for different V_{DS}, with $V_G = -0.1$ V.

From a computational point of view, we present in Table 5.1 the total execution time and the number of Gummel iterations necessary for computing the thermal equilibrium solution with the three methods on a single processor. The drift-diffusion and the hybrid method need half of the iterations compared to the quantum one to reach convergence. This is probably due to the boundary conditions, as we will discuss more precisely in the next paragraph. Moreover, the quantum iterations take longer since the resolution of the large number of Schrödinger equations is more expensive than the resolution of the single drift-diffusion equation. That is also why the drift-diffusion method is less demanding than the hybrid one.

	Quantum	Classical	Hybrid
Time (s)	1934	1139	1303
Nb. Gummel iteration	12	5	6

Table 5.1: Comparison of the three methods at thermal equilibrium with $V_G = -0.1$.

Comparison with the quantum effective mass model (Chapter 3)

First, we point out that the hybrid approach allows to perform computation of the current-voltage characteristic for large gate voltages. In Table 5.2, we describe the total execution time and the number of Gummel iterations necessary for computing the thermal equilibrium solution with the hybrid model for different gate voltages V_G. It proves that the Gummel iterative method is converging in few iterations for all the considered gates. However, we emphasize that already at thermal equilibrium the number of required iterations increases with the gate voltage. It means that the solution is more complicate to be obtained.

On the contrary, the Gummel method used to implement the quantum model considered in Chapter 3 breaks up for large gate voltages. We reach convergence only for negative gate

	$V_G = -0.1$ V	$V_G = 0$ V	$V_G = 0.05$ V	$V_G = 0.1$ V
Time (s)	1303	1565	1657	1651
Nb. Gummel iterations	5	7	8	8

Table 5.2: Comparison for different gate voltage V_G at thermal equilibrium with the hybrid strategy.

voltages and already for $V_G = 0$ V the algorithm fails. If we run a case close to $V_G = 0$ V, which is still converging, we obtain the results shown in Fig.5.10. It represents 1D profiles of the density for $V_G = -0.01$ V (left) as well as a zoom at the source contact (right). We clearly observe a non constant density at the boundaries and the variation is amplified with the applied voltage. For $V_G = 0$ V, this problem gets out of control and the Gummel iterative method breaks.

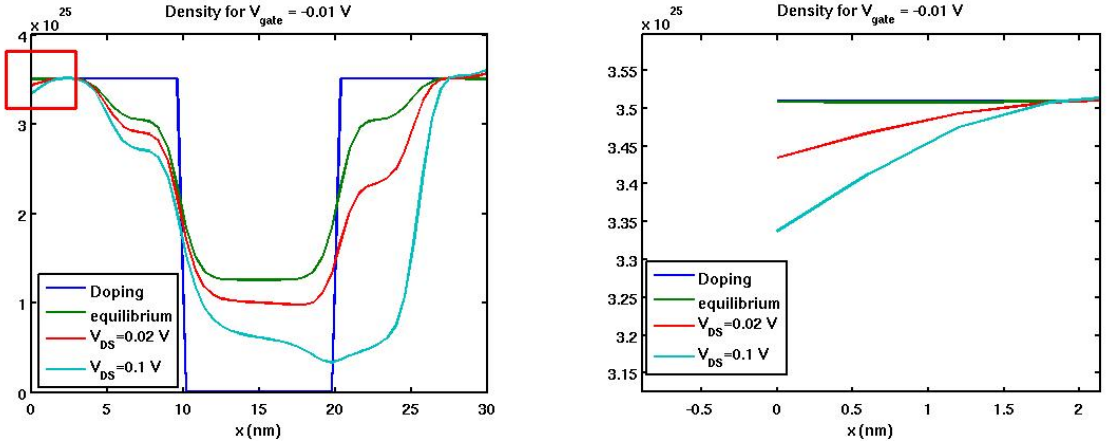

Figure 5.10: 1D densities (m^{-3})(left) and zoom at boundary (right) with the quantum method, for different V_{DS}, with $V_G = -0.01$ V.

We precise that in our opinion this problem is not due to the Fourier boundary condition used for the Poisson equation since the algorithm breaks even sooner (for smaller V_{DS}) with a Dirichlet condition. We believe that the lack of quasi-neutrality at the boundary induces a wrong behavior of the 3D potential.

In the drift-diffusion and the hybrid case, Dirichlet conditions are imposed for the quasi-fermi energy (which immediately gives quasi-neutral conditions for the 1D density) while in the Schrödinger equations quasi-neutrality at the boundary is obtained superimposing all the waves. When many waves are reflected, the transparent boundary conditions do not take them into account correctly.

Moreover, for the computation of the 1D density in the fully quantum model, the statistical function ϕ_n requires the knowledge of the fermi level at equilibrium (through (3.3.9)). Instead, in the hybrid approach, the quasi-fermi energy is computed as a variable and it is used in (5.2.23)

without invoking quasi-neutrality.

To conclude, the hybrid model has a better control on boundary conditions and allows to perform computation for much larger range of gate voltage than the fully quantum one.

Comparison with the drift-diffusion effective mass model (Section 5.3)

In Fig.5.11, we compare the current-voltage characteristic obtained with the drift-diffusion method and with the hybrid one for a fixed mobility. Since the collisions are taken into account in the entire longitudinal region with the fully classical model, it seems correct to observe a larger current than with the hybrid approach.

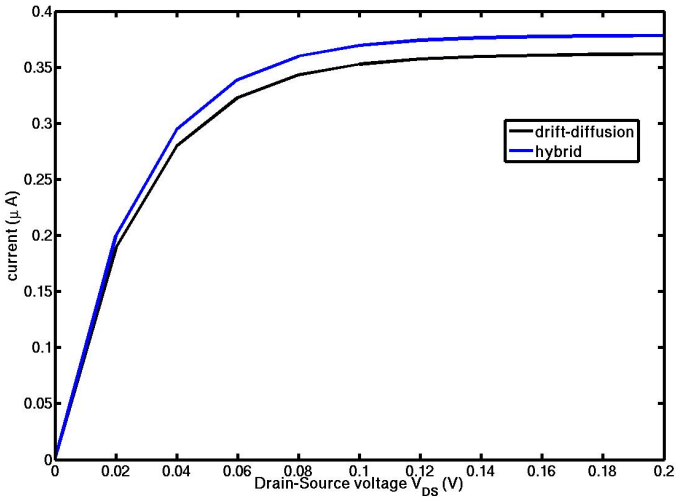

Figure 5.11: Comparison of the Current-Voltage characteristics between the drift-diffusion model and the hybrid approach for $V_G = -0.1$ V.

Nevertheless, this is not always true and things are slightly more complex. As we already pointed out, in the drift-diffusion case the current is proportional to the mobility constant. For the hybrid model, the behavior is completely different as it is presented in Fig.5.12. The blue curve corresponds to a mobility constant that we called "reference" (since it is the one used to plot Figs.5.4 and 5.11). If we multiply this reference mobility by 2, 10 or 100, we obtain respectively the cyan, the magenta and the yellow curves which are really close. In any case, the current has not been multiplied by 2, 10 or 100. It means that the quantum model used in the channel region has a real influence on the current. On the contrary, if we divide the reference mobility by 2 or by 10, we obtain respectively the green and the red curves. In this case, the behavior is different. Indeed, the red curve is much smaller than the green and the blue ones (even if the corresponding current is far to be divided by 10). The model is thus able to capture the phenomenon that for small mobility the particles are driven by numerous collisions and the

transport is limited. It is one of the reason why the hybrid classical-quantum model is preferable to the drift-diffusion one.

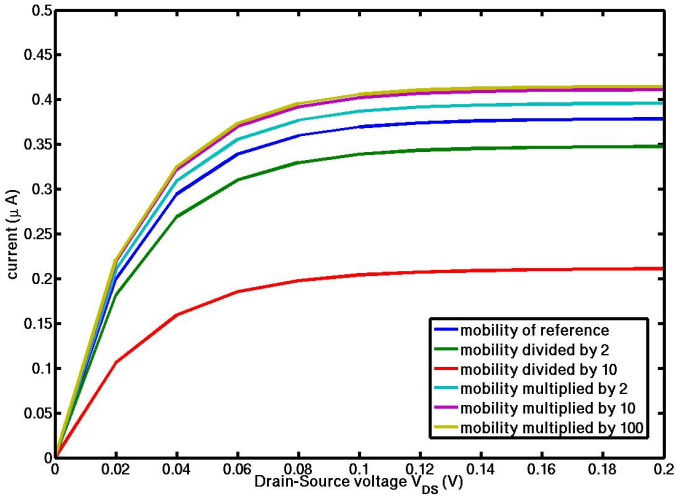

Figure 5.12: Influence of the mobility on the Current-Voltage characteristics for the hybrid approach with $V_G = -0.1$ V.

Study of the gate voltage influence

As in Fig.5.9, in Figs.5.13, 5.14 and 5.15, we present 1D profiles of the density and of the potential obtained with the mobility of reference (see previous paragraph) for a fixed gate voltage respectively $V_G = 0$ V, $V_G = 0.05$ V and $V_G = 0.1$ V. As previously, we clearly observe the important influence of the gate and the doping. We notice that the potential energy decreases when the gate voltage becomes larger. In the channel region, it tries to reach the gate voltage value. Also, for large gate voltages, the influence of the applied Drain-Source voltage in the channel region is very significant. It is less pronounced for $V_G = 0$ V and completely insignificant for $V_G = -0.1$ V. Finally, we point out that, for large applied potential, the 1D density at the level of interfaces (and specially in the one close to the drain) is discontinuous. It was announced in Remark 5.2.1 since the interface conditions are built to preserve only the continuity of the current. We emphasize that this discontinuity is unchanged if we double the number of discretization points in the transport direction (for the Poisson mesh and for the drift-diffusion/Schrödinger one). It seems also that numerically the presence of the discontinuity gives a little bit of flexibility to the system and it allows to reach convergence easier.

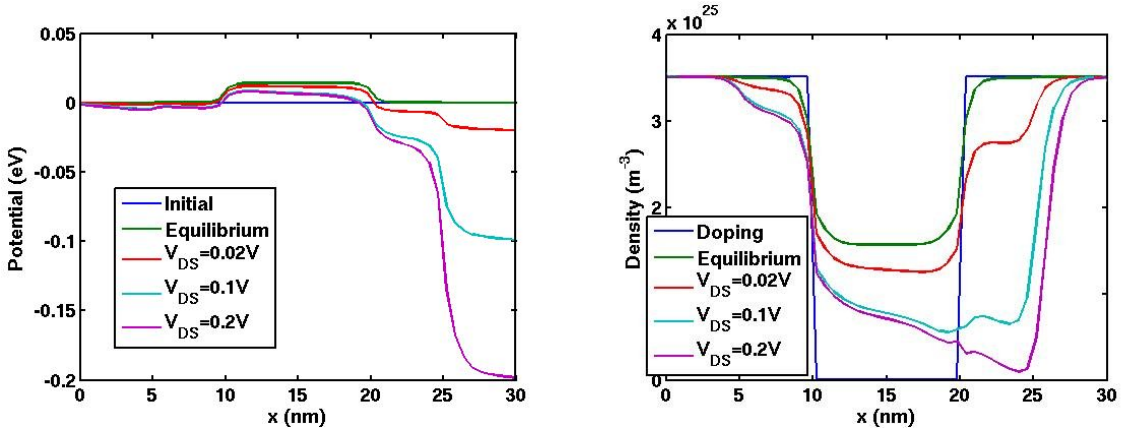

Figure 5.13: 1D potential energies (eV) (left) and 1D densities (m^{-3})(right) for different V_{DS}, with $V_G = 0$ V.

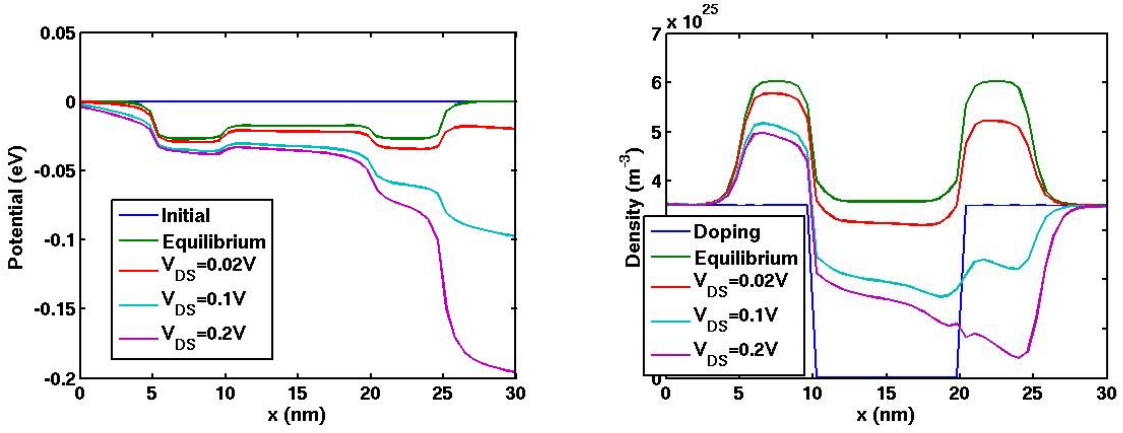

Figure 5.14: 1D potential energies (eV) (left) and 1D densities (m^{-3})(right) for different V_{DS}, with $V_G = 0.05$ V.

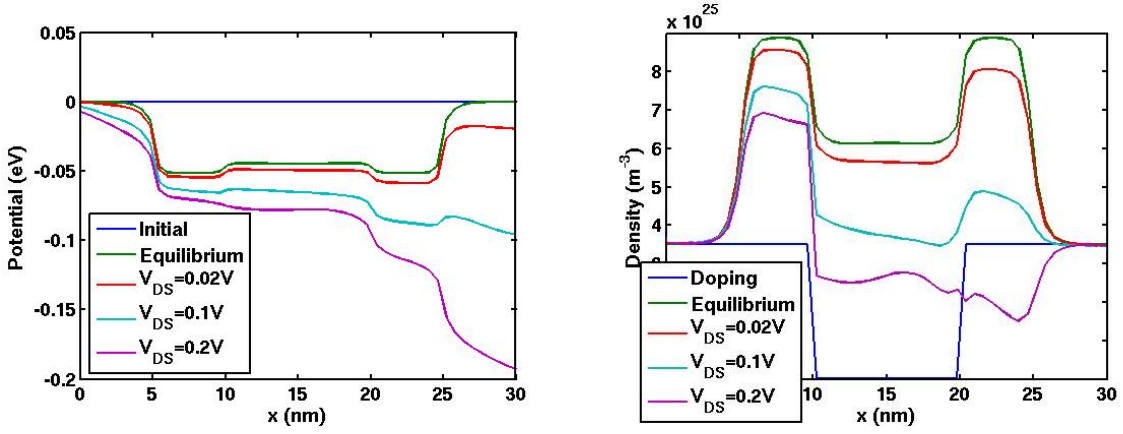

Figure 5.15: 1D potential energies (eV) (left) and 1D densities (m^{-3})(right) for different V_{DS}, with $V_G = 0.1$ V.

Finally, in Fig.5.16, we represents the output characteristics for five different gate voltages. As expected in view of physical experiments, the current in the transistor increases with the gate potential V_G. We still notice the two typical regimes: an ohmic regime for small values of Drain-Source voltage and a quasi-saturation regime for larger V_{DS}. This saturation regime is established for larger Drain-Source voltages when the gate voltage increases. Indeed, for $V_G = 0$ V, the current is already stabilized for $V_{DS} = 0.1$ V, instead it is necessary to reach up to around $V_{DS} = 0.18$ V for $V_G = 0.05$ V. All these observations are in accordance with the behavior of conventional MOSFETs.

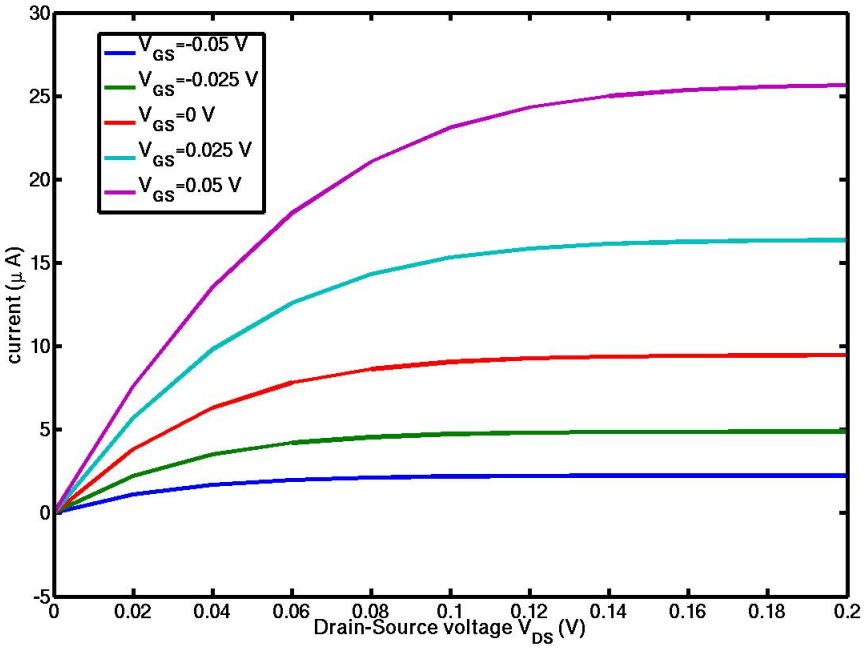

Figure 5.16: Current-Voltage characteristics for five gate voltages V_G.

Study of the interface positions

We now study the influence of the interface positions on the current. We remind that in the previous simulations the interfaces were located at $x_1 = 10$ nm and $x_2 = 20$ nm (doping discontinuities). In Fig.5.17, we present the output characteristics obtained when we move the left interface position x_1. This test is run for a gate voltage $V_G = -0.1$ V and with the mobility of reference. We observe that the current has pretty much the same behavior for every interface positions, except for $x_1 = 12$ nm.. In this case, the interface is placed well inside the active zone and the perceptible lowering of the current confirms that the transport in the channel has to be simulated with the quantum model.

In Fig.5.18, the same test is presented, but we now move the right interface position x_2 for

fixed $x_1 = 10$ nm. Results are very similar since the current stays almost unchanged except for $x_2 = 18$ nm (i.e. when the right interface is largely inside the channel). Consequently, for this simplified device, it seems that the two interfaces play an equivalent role.

Looking more precisely at the current behavior in the saturation regime zooming on the IV curves for large Drain-Source voltages V_{DS} (right pictures of Figs.5.17 and 5.18), we observe a non monotonic behavior of the current saturation value with respect to the interface position. In addition, the order of these values is not specular moving the left interface or the right one.

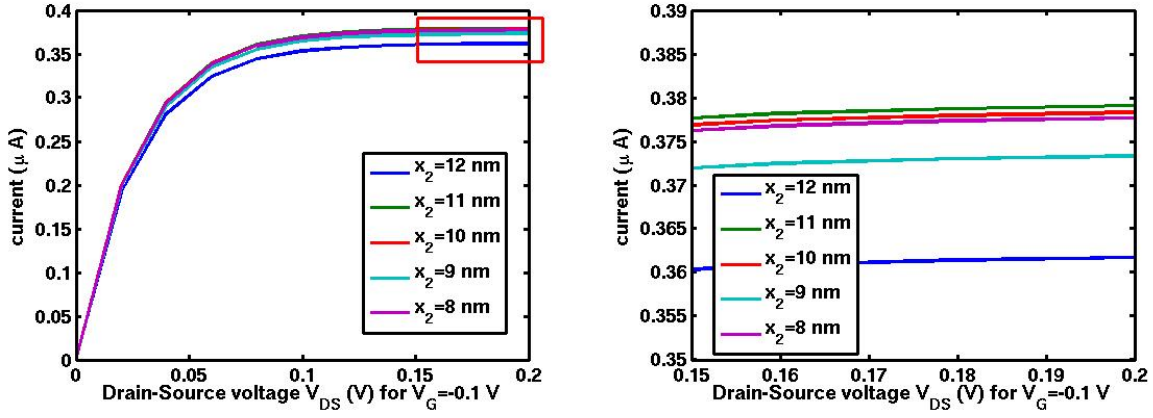

Figure 5.17: Current-Voltage characteristics (left) and zoom for larger V_{DS} (right), moving the left interface position x_1, obtained with the mobility of reference.

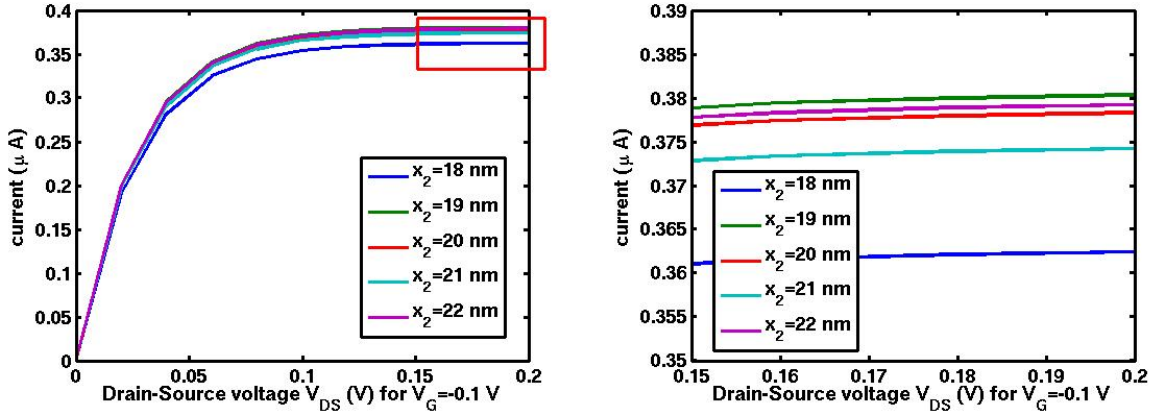

Figure 5.18: Current-Voltage characteristics (left) and zoom for larger V_{DS} (right), moving the right interface position x_2, obtained with the mobility of reference.

As we already mentioned, the choice of the mobility constant is a delicate issue. So far, we have chosen the mobility (called mobility of "reference") in order to match the current obtained with the drift-diffusion model with the one given by the fully quantum approach. Another reasonable possibility is to take a smaller mobility. That is the reason why we also analyze the influence of the interface positions for a mobility equals to the half of the mobility of reference.

We obtain Fig.5.19 when we move the left interface x_1 (in the left picture) and the right one x_2 (in the right picture). In this case, we observe a monotonic behavior of the saturation value in function of the interface position. However, the influence of the interface positions is more pronounced than in Figs.5.17 and 5.18, in accordance with the fact that for this mobility the current given by the drift-diffusion system is smaller than the one obtained with the fully quantum model.

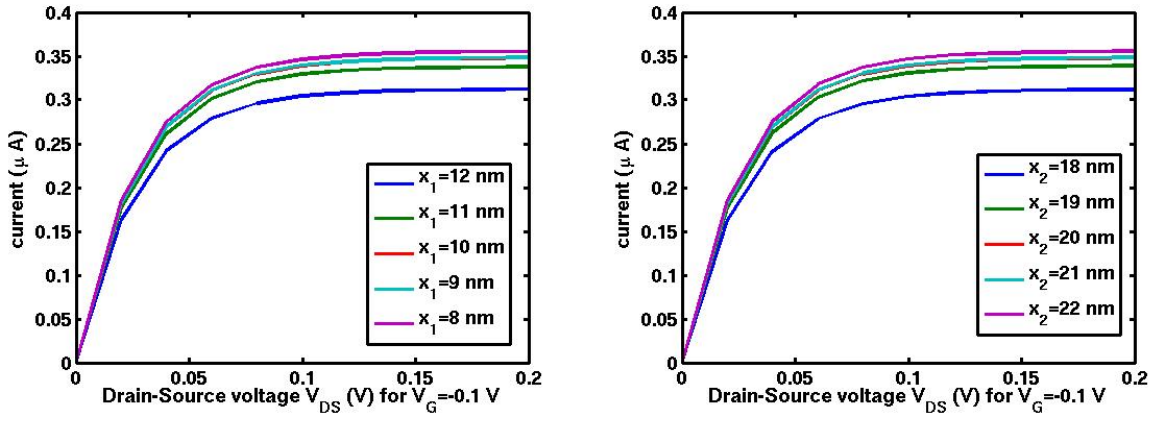

Figure 5.19: Current-Voltage characteristics, moving the left interface position x_1 (left) or the right one x_2 (right), obtained with the mobility of reference divided by 2.

Finally, we would like to mention another interesting experimental test. Locating the interfaces at the gate extremities ($x_1 = 5$ nm and $x_2 = 25$ nm), the Gummel method breaks up for large gate voltages, similarly to the pathological behavior of the fully quantum model considered in Chapter 3. Thus, it seems that the classical model is essential in the entire high doping zone (and not only in electron reservoirs). We conclude saying that the choice of the mobility constant or of the interface positions requires more investigations. In the future, further experiments should be done for a more relevant physical device.

5.5 High-performance computations

The last part of this chapter is devoted to high-performance computations. On the one hand, we point out that parallelization can be used in several instances of the procedure in order to decrease the overall computational cost. On the other hand, we explain the creation of an interface to use in our programs sophisticated meshes created by COMSOL Multiphysics (a software specialized in the modeling process). These improvements allows to increase both the quantity and the quality (more relevant physically) of the simulated tests.

5.5.1 Parallelization of the code

First, we took an interest in parallelization. Parallel computing is a form of computation in which many calculations are carried out simultaneously, operating on the principle that large problems can often be divided into smaller ones, which are then solved concurrently with different processors. It allows to decrease simulation times even if communication and synchronization between the different subtasks are typically one of the greatest obstacles to getting good parallel program performance.

The aim of this work is the parallel implementation of our Fortran90 code on a Beowulf cluster. Cluster is a widely-used term meaning independent computers, combined into a unified system through software and networking, and typically used to provide greater computational power than a single computer. Beowulf clusters are scalable performance clusters based on commodity hardware, on a private system network, with an open source software (Linux) infrastructure.

In our case, numerical experiments have been carried out on the Beowulf cluster "Topsy" at IMATI-CNR in Pavia. The cluster consists of 14 nodes. Each single node is a 2 AMD-Opteron 64 bit dual core. It means that each node has 2 processors and each processor 2 cores. So, a computation may be divided simultaneously into 56 subtasks. Moreover, the total amount of memory on a single node is of 8GB of RAM (Random Access Memory).

We discuss here both the implementation strategies and the performance of the parallel code. The performance is determined by analyzing the execution time in function of the number of processors (more correctly the number of cores), assuming that we are the only users on the system. Different times could be considered (elapsed time, CPU time...), but to simplify we study only the total execution time spent by the algorithm. So, we calculate the speed-up defined by

$$\text{Speed-up} = \frac{\text{Execution time for entire task without using the enhancement}}{\text{Execution time for entire task using the enhancement when possible}}.$$

It represents the increase in performance. Usually, the maximum obtainable speed-up $S(n_{proc})$ using n_{proc} processors is n_{proc} (linear speed-up). It exists various definition of the speed-up, more or less representative of the performance. Since the scope of this part is a general presentation of our parallelization strategy and not an extreme analysis of the performance, we use in the sequel the following simple expression

$$S(n_{proc}) = \frac{t_s}{t_p(n_{proc})},$$

where t_s is the execution time on a single processor and $t_p(n_{proc})$ is the execution time on n_{proc} processors. For a more precise analysis, we should also study the difference of execution times between the sequential code and the parallel one used with one processor, the parallelization performance of local parts of the code, the communication times, the synchronization points...

Computation of the effective mass

The first interesting point to parallelize our algorithm is the computation of the effective mass (5.2.2). It requires the calculation of P_{nq}'s which are obtained integrating over the 3D unit cell. In presented simulations, the eigenvalue problem (5.2.1) is solved for a discretization containing about 250 000 degrees of freedom (dof). And probably, this number has to be larger for more relevant physical devices. It can be parallelized, using the MPI standard, dividing the initial domain into subdomains and summing up the partial results. The domain decomposition, based on the splitting of the computational domain into subregions of smaller size forming a partition of the original domain, became essential in the last decades with the development of parallel computing platforms. To summarize, we divide here the initial domain into subdomains, we calculate the integrations in each subdomain and we sum up results to obtain the final integrals and thus the P_{nq}'s and the effective masses. The main difficulty is to manipulate the data structure used to describe the mesh.

We obtain Tables 5.3 and 5.4, which show the total execution time spent by the algorithm in function of the number of processors for three different meshes. Figs.5.20 and 5.21 are the corresponding speed-up curves, respectively to Tables 5.3 and 5.4. In Mesh 1, the 1D lattice spacing (of length ϵ) is decomposed by 20 discretization points, which gives, for the 3D uniform mesh, about 250 000 degrees of freedom for the finite element space. In Mesh 2 and 3, there are respectively 30 and 40 discretization points, which gives about 900 000 and 2 200 000 dof.

In Table 5.3 and Fig.5.20, we consider only the computation of P_{nq}'s and the speed-up is almost linear. In Table 5.4 and Fig.5.21, we consider the entire procedure of the effective mass computation: loading of eigenvectors and eigenvalues, calculation of P_{nq}'s, computation of the sum to obtain the effective masses and finally saving of results in a file. The performance of the parallelization is quite good (around 15 for 32 processors), but far from the linear speed-up. It can be explained by the presence of non scalable parts like the loading of initial data or the saving of results. These results prove the efficiency to parallelize the effective mass computation. An execution time divided by 15 is far too be negligible. Finally, the performance is independent of the mesh size, which is a good news in view of larger tests for realistic physical problems.

nb. proc.		1	2	3	4	6	8	12	16	20	24	32
time (s)	mesh 1	562.8	282.9	189.7	142.0	95.3	71.8	48.2	36.5	29.5	24.6	19.37
	mesh 2	2014	1005	674	508	341	257	172	130	105	88	67
	mesh 3	4874	2453	1639	1239	835	644	419	317	261	216	164

Table 5.3: Execution times curves for the calculation of P_{nq}'s.

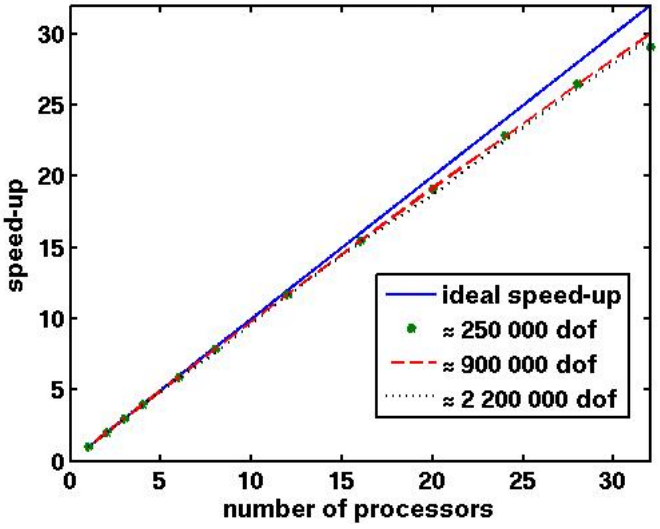

Figure 5.20: Speed-up curves for the calculation of P_{nq}'s.

nb. proc.		1	2	3	4	6	8	12	16	20	24	32
time (s)	mesh 1	581.7	300.9	210.6	160.3	114.1	90.3	66.9	55.3	48.2	43.3	37.9
	mesh 2	2078	1066	735	571	404	320	235	193	169	152	131
	mesh 3	5026	2603	1793	1436	1001	860	585	490	434	385	345

Table 5.4: Execution times for the calculation of effective masses.

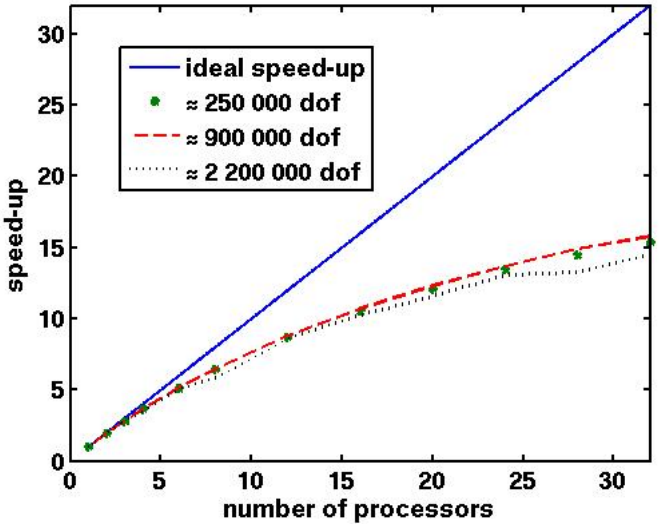

Figure 5.21: Speed-up curves for the calculation of effective masses.

Resolution of the Schrödinger equations

Secondly, in the transport part, we solve a large number of Schrödinger equations (5.2.14) since we have to consider each band n and above all each wave vector k. All these equations are

independent from each other and can be treated simultaneously. Using the MPI standard, we parallelize it and we group results together to calculate, in the case of the hybrid strategy, the transmission coefficients (5.2.18) and the number Θ (5.2.34).

In Table 5.5, we present the obtained total execution time in function of the number of processors. Results are really close to be linear. It confirms that this part of the algorithm is highly scalable. Since the transport is unidimensional, the discretization contains only few hundreds of points. It is all the more true for the hybrid strategy since the quantum zone represents only a part of the entire domain. Consequently, the resolution of one Schrödinger equation is not so expensive, the manipulated structures are not huge and the communication times between processors are limited. It explain the almost linear behavior of the speed-up.

nb. proc.	1	2	3	4	6	8	12	16	20	24	32
time (s)	5.12	2.58	1.72	1.29	0.87	0.65	0.43	0.32	0.26	0.22	0.19

Table 5.5: Execution times for the resolution of the Schrödinger equations.

Resolution of the 3D Poisson equation using PETSc to solve the linear system

Finally, the most expensive part in terms of computational time for our algorithm is the resolution of the linear system for the 3D Poisson equation (usually, more than one million degrees of freedom are needed). In addition, this procedure has to be done a lot of times because of the Gummel iterative method. To parallelize it, we use the PETSc library [3, 4], from Argonne National Laboratory. It is a package which contains a set of advanced data structures and routines for the parallel solution of scientific applications modeled by partial differential equations. In particular, this library based on MPI, BLAS and LAPACK, contains routines, well suited for parallel codes, for standard operations with matrices and vectors. Also, a large part called KSP is dedicated to linear solvers (preconditioners, direct solvers, iterative methods...).

The experiments on “Topsy ” have been performed using PETSc 2.3.2 compiled with mpif90 and installed on the top of both mvapich-0.9.5-mxl1.0.3 and BLAS and LAPACK implementations provided with the acml 3.6.0 distribution.

	Approximate number of d.o.f. (in millions)		
	0.6	1.2	2.0
HSL MI26	136.73	243.24	375.10
PETSc KSPBCGS	60.35	92.93	275.47

Table 5.6: Comparison of the execution time to solve a linear system with two different libraries.

First, in Table 5.6, we consider only one core and we study the execution time to solve the linear system for the Poisson equation at the first Gummel iteration of thermal equilibrium.

We compare the library used in the sequential code with PETSc, for three different meshes (which give respectively about 670 000, 1 200 000 and 2 000 000 degrees of freedom). In the sequential code, we use the library [18], and more precisely, in the category "iterative methods for sparse matrices", the routine MI26 which implements the BiCGStab (BiConjugate Gradient Stabilized) method. In PETSc library, we choose the same BiCGStab method that is the module KSPBCGS. Table 5.6 clearly shows that, for our problem, PETSc is more efficient. Thus, even without running the code simultaneously on various processors, the simple fact to use PETSc is a big improvement. In fact, HSL seems optimized to solve really large problems. The ratio of execution times obtained between the second and the third mesh is much better with HSL than with PETSc.

We now study the scalability of the PETSc linear system solver. In Table 5.7, we still study the execution time to solve the linear system for the Poisson equation at the first Gummel iteration of thermal equilibrium. Here, we analyze it in function of the number of processors, for two different gate voltages V_G. Fig.5.22 is the corresponding speed-up curve. We obtain a correct performance, close enough to the linear regime. For example, with 8 processors the speed-up is about 6, with 16 processors it is about 11 and with 32 processors it is about 24. It is due to the fact that the PETSc library optimally manages both the communication among processors and the algebraic computational kernels. Also, the performance is almost independent to the gate voltage and thus to the values of the non zero entries in the sparse matrix.

nb. proc.		1	2	3	4	6	8	12	16	20	24	32
time (s)	V_G =-0.1V	60.35	36.64	34.82	21.41	16.71	9.82	8.66	6.37	4.67	3.69	2.44
	$V_G = 0\ V$	70.33	50.81	35.71	22.24	16.66	11.10	9.75	7.18	5.54	3.78	3.14

Table 5.7: Execution times for the resolution of a linear system for the 3D Poisson equation.

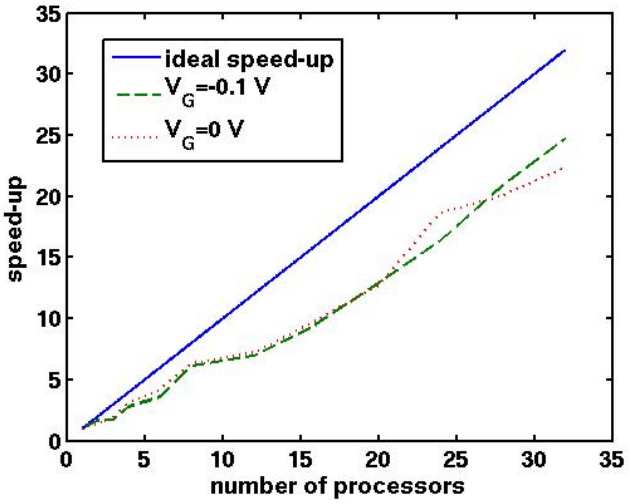

Figure 5.22: Speed-up curves for the resolution of a linear system for the 3D Poisson equation.

Computation of the 1D hybrid transport - 3D Poisson problem

Finally, it is time to consider the entire 1D hybrid transport - 3D Poisson problem. Previously, we have seen that the part corresponding to the resolution of the Schrödinger equations and the one related to the Poisson equation are highly scalable. We repeat that this last point is essential since the Poisson equation is three dimensional and that the procedure has to be done a lot of times because of the Gummel iterative method. So, Table 5.8 represents the execution times and Fig.5.23 the speed-up curves in function of the number of processors for the resolution of the entire 1D hybrid transport - 3D Poisson problem at thermal equilibrium for two different gate voltages V_G. As expected, the performance is not perfect. The curves are far to the linear speed-up. It can be explained by the fact that some parts of the algorithm (the resolution of the drift-diffusion equation, the calculation of the 3D density...) are not (or not much) parallelized. For few processors, the scalable part is proportionately important and the performance is very good. On the contrary, when the number of processors is superior to 8, the non scalable part becomes predominant and the performance is deteriorated. Nevertheless, a decreasing of the total execution time by 10 or 15 is really precious. For instance, for $V_G = 0$ V, we obtain results in 110 seconds instead of waiting 26 minutes.

nb. proc.		1	2	3	4	6	8	12	16	24	32
time (s)	V_G =-0.1V	1303.2	766.6	729.8	438.2	263.7	176.9	146.4	116.6	97.7	80.2
	$V_G = 0$ V	1564.8	920.5	549.7	519.6	298.0	218.0	179.0	151.0	132.5	109.5

Table 5.8: Execution times for the entire 1D hybrid transport - 3D Poisson problem.

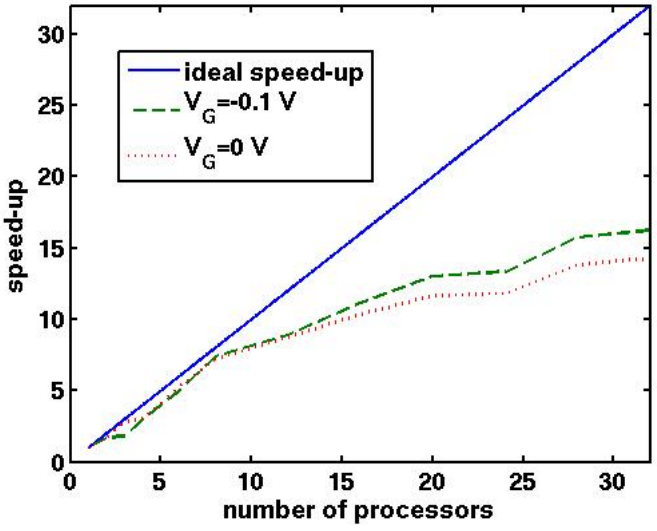

Figure 5.23: Speed-up curves for the entire 1D hybrid transport - 3D Poisson problem.

To conclude, we can say that our algorithm contains many parts interesting to parallelize. Even if the non scalable parts are not negligible, it allows to decrease substantially the execution

time and thus it gives the possibility to carry out more simulations. In the future, an issue to take under consideration is to improve the data storing strategy in order to reduce as much as possible the communication time. Also, it would be interesting to parallelize the resolution of the eigenvalue problem (5.2.1). It seems not easy to parallelize the algorithm implemented by ARPACK, based on a variant of the Arnoldi method. Nevertheless, this package has a reverse communication interface. It means that the user has to specify a routine for the matrix-vector multiplication and a solver for linear systems. At least this part could be parallelize using PETSc. Finally, we would like to mention the library FEAST [22], developed by E. Polizzi, which is a package to solve eigenvalue problems. The algorithm seems to offer important capabilities for achieving scalability on parallel architectures. However, it manipulates complex hermitian matrices and it requires to have an efficient linear solver for such matrices.

5.5.2 Interface to import meshes

Finally, it is important to have the possibility to use sophisticated meshes (as in Fig.5.24 for example) in our programs. In particular, it allows us to test our model with more realistic physical wires (and not just for a toy device). To do this, we decided to use COMSOL Multiphysics [13]. The COMSOL Multiphysics simulation software is an environment which facilitates all steps in the modeling process : defining the geometry, meshing, specifying physics, solving, and then visualizing results. In our case, we do not use all these functionalities but we only take advantage of the meshing.

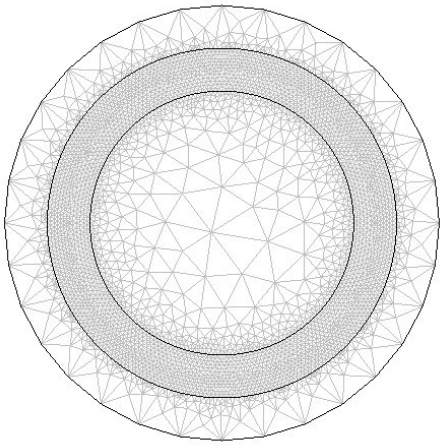

Figure 5.24: An example of COMSOL mesh for a circular nanotube cross section.

In COMSOL, a mesh is defined by a data structure (containing informations about points, edges, elements...). The idea is to get possession this data structure and then to implement few lines of code to create an interface which allows us to use directly the data structure in our Fortran program already implemented. At the end, we create a geometry and a mesh with

COMSOL, we save the defined data structure in a file, we open this file in the Fortran program and we use information of the COMSOL mesh as required by our program.

This interface has been implemented and numerical tests are in progress. A first conclusion is that the created mesh has to preserve symmetries of the cross section geometry. In particular, the resolution of the eigenvalue problem is really sensitive to the mesh and the numerical detection of multiple eigenvalues is a difficult problem.

Bibliography

[1] D. N. Arnold and F. Brezzi. Mixed and nonconforming finite element methods: implementation, postprocessing and error estimates. *RAIRO Modél. Math. Anal. Numér.*, 19(1):7–32, 1985.

[2] I. Babuška and J. E. Osborn. Generalized finite element methods: their performance and their relation to mixed methods. *SIAM J. Numer. Anal.*, 20(3):510–536, 1983.

[3] S. Balay, J. Brown, K. Buschelman, V. Eijkhout, W. D. Gropp, D. Kaushik, M. G. Knepley, L. Curfman McInnes, B. F. Smith, and H. Zhang. PETSc users manual. Technical Report ANL-95/11 - Revision 3.1, Argonne National Laboratory, 2010.

[4] S. Balay, W. D. Gropp, L. Curfman McInnes, and B. F. Smith. Efficient management of parallelism in object oriented numerical software libraries. In E. Arge, A. M. Bruaset, and H. P. Langtangen, editors, *Modern Software Tools in Scientific Computing*, pages 163–202. Birkhäuser Press, 1997.

[5] M. Baro, N. Ben Abdallah, P. Degond, and A. El Ayyadi. A 1d coupled Schrödinger drift-diffusion model including collisions. *J. Comput. Phys.*, 203(1):129 – 153, 2005.

[6] N. Ben Abdallah. A hybrid kinetic-quantum model for stationary electron transport. *J. Statist. Phys.*, 90(3-4):627–662, 1998.

[7] N. Ben Abdallah, P. Degond, and P. A. Markowich. On a one-dimensional Schrödinger-Poisson scattering model. *Z. Angew. Math. Phys.*, 48(1):135–155, 1997.

[8] N. Ben Abdallah, C. Jourdana, and P. Pietra. An effective mass model for the simulation of ultra-scaled confined devices. Preprint IMATI-CNR 10PV11/7/0.

[9] F. Brezzi and M. Fortin. *Mixed and hybrid finite element methods*, volume 15 of *Springer Series in Computational Mathematics*. Springer-Verlag, New York, 1991.

[10] F. Brezzi, L. D. Marini, and P. Pietra. Méthodes d'éléments finis mixtes et schéma de Scharfetter-Gummel. *C. R. Acad. Sci. Paris Sér. I Math.*, 305(13):599–604, 1987.

[11] F. Brezzi, L. D. Marini, and P. Pietra. Numerical simulation of semiconductor devices. In *Proceedings of the Eighth International Conference on Computing Methods in Applied Sciences and Engineering (Versailles, 1987)*, volume 75, pages 493–514, 1989.

[12] F. Brezzi, L. D. Marini, and P. Pietra. Two-dimensional exponential fitting and applications to drift-diffusion models. *SIAM J. Numer. Anal.*, 26(6):1342–1355, 1989.

[13] COMSOL Multiphysics. *COMSOL Multiphysics, a simulation software environment facilitating all steps in the modeling process.* http://www.comsol.com/products/multiphysics/.

[14] P. Degond and A. El Ayyadi. A coupled Schrödinger drift-diffusion model for quantum semiconductor device simulations. *J. Comput. Phys.*, 181(1):222–259, 2002.

[15] A. El Ayyadi and A. Jüngel. Semiconductor simulations using a coupled quantum drift-diffusion Schrödinger-Poisson model. *SIAM J. Appl. Math.*, 66(2):554–572, 2005.

[16] F. Hecht and A. Marrocco. Mixed finite element simulation of heterojunction structures including a boundary layer model for the quasi-fermi levels. *COMPEL*, 13(4):757–770, 1994.

[17] F. Hecht, A. Marrocco, E. Caquot, and M. Filoche. Semiconductor device modelling for heterojunctions structures with mixed finite elements. *COMPEL*, 10(4):425–438, 1991.

[18] HSL (2011). *A collection of Fortran codes for large scale scinetific computation.* http://www.hsl.rl.ac.uk/hsl2011.

[19] C. Jourdana and N. Vauchelet. Analysis of a diffusive effective mass model for nanowires. Kinet. Relat. Models (to appear).

[20] P.A. Markowich, C.A. Ringhofer, and C. Schmeiser. *Semiconductor equations.* Springer-Verlag, Vienna, 1990.

[21] P. Pietra and N. Vauchelet. Modeling and simulation of the diffusive transport in a nanoscale double-gate mosfet. *J. Comput. Electron.*, 7:52–65, 2008.

[22] E. Polizzi. Density-matrix-based algorithm for solving eigenvalue problems. *Phys. Rev. B*, 79(11):115112, 2009.

[23] P.-A. Raviart and J. M. Thomas. A mixed finite element method for 2nd order elliptic problems. In *Mathematical aspects of finite element methods (Proc. Conf., Consiglio Naz. delle Ricerche (C.N.R.), Rome, 1975)*, pages 292–315. Lecture Notes in Math., Vol. 606. Springer, Berlin, 1977.

Part *III*

On a model of magnetization switching driven by a spin-current

Chapter 6

Modeling and numerical simulations

Nota bene : This chapter largely corresponds to
a joint work with N. Ben Abdallah, E. Fouassier and D. Sanchez
submitted to SIAM MMS (see also the preprint [1]).

We study a model of magnetization switching driven by a spin current: the magnetization reversal can be induced without applying an external magnetic field. We first write our one dimensional model in an adimensionalized form, using a small parameter ε. We then explain the various time and space scales involved in the studied phenomena. Taking into account these scales, we first construct an appropriate numerical scheme, that allows us to recover numerically various results of physical experiments. We then perform a formal asymptotic study as ε tends to 0, using a multiscale approach and WKB type asymptotic expansions. We thus obtain approximate limit models that we compare with the original model via numerical simulations.

6.1 Introduction

In this chapter, we are concerned with a model of magnetization reversal induced by a spin polarized current. The idea is of switching the magnetization of a ferromagnetic material without applying an external magnetic field. The magnetization is rather reversed by an additional spin transfer torque. This concept was discovered by Slonczewski [6] and Berger [2] in 1996. Spin transfer appears to be a turning point in spintronics and is the subject of an extensive research in physics. The particular phenomenon we study here is of great interest to construct magnetic memories.

The physical device proposed by [6] and [2] is a *magnetic multilayer* mainly composed of two ferromagnetic layers separated by a nonmagnetic spacer layer (see Fig.6.1). In a schematic

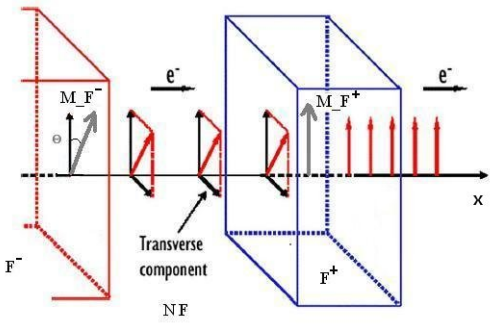

Figure 6.1: A multilayered ferromagnetic device proposed by Slonczewski.

way, it works as follows: the first ferromagnet F^-, being thick, acts as a polarizer, the second ferromagnet F^+, being thin, is to be switched. Initially, the two magnetizations $\vec{M}^-(t=0)$ and $\vec{M}^+(t=0)$ respectively in F^- and F^+ are polarized in a different direction (θ is the angle between $\vec{M}^-(t=0)$ and $\vec{M}^+(t=0)$, see Fig.6.1). This is done by taking two ferromagnetic materials with different anisotropy directions. Roughly, we can say that a ferromagnetic material is a material having a preferred direction for the magnetization (an anisotropy direction): when there is no external field applied at equilibrium), the magnetization is parallel to this anisotropy direction.

In order to induce the switching of the magnetization in the thin layer, an electric current is injected in the device at the left end of the thick layer F^-, *perpendicularly to the layers* (along the x axis). The first ferromagnetic layer F^- is thick (around 100 nm), so that it acts as a polarizer. Its magnetization does not move under the spin current influence, whereas the spin density is polarized in the direction of the magnetization when passing through the F^- layer. On the contrary, the second ferromagnetic layer F^+ is thin (around 1-5 nm). Its magnetization can move driven by the spin current. Indeed, the spin density, which is polarized along $\vec{M}^-$ crossing F^-, reaches F^+ with a transverse component with respect to $\vec{M}^+$. Then, a torque is established between this transverse component and the magnetization $\vec{M}^+$. When the spin transfer is enough intense (that is to say when the injected current is enough important), $\vec{M}^+$ can be completely switched. Physical experiments request a very intense current to observe the switching. Last, another non ferromagnetic layer is at the right end of the device. It allows to reduce the spin density (acting like a "sandbox").

The mathematical model we study here is a simplified version of that introduced by Zhang, Levy and Fert [9] (see also Shpiro, Levy and Zhang [5] for details). In each layer, we write a system of coupled PDEs on the spin density and the local magnetization. The local magnetization satisfies a Landau-Lifshitz equation with an additional term in the effective field. For the spin density, the main particularity of this model lies in the description of spin transport using macroscopic *spin diffusion* in the *entire structure*, the treatment of interfaces scattering being done *via* boundary conditions. The equation satisfied by the spin density is thus a diffusion

equation with an additional torque term where the magnetization appears. All the details are written in the next section.

As noticed in [9], [5], there are various scales for the different phenomena involved in the magnetization reversal process. Rather than making a priori approximations such as in [9], in order to study these different scales, we introduce a small parameter, and we write adimensionalized equations. A natural parameter in our context is the ratio between the thicknesses of the magnetic layers (the thin one and the thick one), denoted by ε. We then perform a study of the adimensionalized equations (see (6.2.12)-(6.2.13)-(6.2.14)-(6.2.15)), in particular an asymptotic study as $\varepsilon \to 0$. The several aspects of our results are the following:

1. we first explain in a schematic framework the different scales that appear in the model. The first important point is the existence of a boundary layer of thickness ε at the right end of the thick layer. The second (even more) important point is the existence of very fast temporal oscillations at scale t/ε^4 for the spin density. More precisely, there is a transverse component of the spin density in the thick layer that is purely oscillating, whereas the thick layer should act as a polarizer.

2. for the phenomenon we are interested in (namely the magnetization reversal), the very fast oscillations are not significant. So we construct a numerical scheme, adapted to our problem, that does not resolve the very fast oscillations. This will be done by two ways: first, we merely use an implicit scheme for the temporal discretization of the equation on the spin density (with a time step much bigger than ε^4) that allows us to "filter" the oscillations; second, we use an averaged spin density (with respect to the fast time variable) to compute the magnetization. At some point, we could make a parallel between our work and what can be done in geophysics, when one wants to avoid the calculation of the non significant waves for the study of a precise phenomenon.

3. we then perform a formal asymptotic study as ε tends to 0 in order to recover a simplified asymptotic model (that will be in particular much easier to handle numerically for small ε). We use a multiscale approach, introducing the variable x/ε to treat the boundary layer. Again, we do not want to compute the oscillating part, so we omit this time scale. The first idea is then to use a basic WKB ansatz: we develop each quantity as a sum of powers of ε, and we compute the first profiles. Our limit model shows the "right" properties with respect to physical experiments. But there is a main restriction on this first model: to derive it, we make an assumption that is not satisfied anymore when the magnetization is switched. In order to avoid this restriction, we then look for a second model, using a "Chapman-Enskog" approach. Roughly, we want to derive first profiles that still depend on the parameter ε, which can be done by considering together quantities such as $M_0+\varepsilon M_1$ and obtaining approximate equations on them. In this chapter, we only discuss the validity of our limit models by making numerical comparisons with the full system.

A previous work by Garcia-Cervera and Wang [3] proposed a numerical scheme for the model of magnetization reversal we consider here. They gave three dimensional simulations but they were not interested in asymptotic analysis, the parameter ε was not small with the data they considered ($\varepsilon = 0.3$).

This chapter is organized as follows. We first explain in details how is derived the model introduced in [9], and we write adimensionalized equations using the small parameter ε. In Section 3 and 4, we present our numerical results for the model we described in the previous section. Then, in section 5 we present our formal derivation of two asymptotic models, and we give some numerical comparisons between the original model and the limit models.

6.2 The spin transfer model

6.2.1 The model proposed by Zhang, Levy and Fert

In this section, we detail the model proposed by Zhang, Levy and Fert [9] for the phenomenon of magnetization-switching we have described in the introduction. More precisely, we detail a slightly simplified model. We do not discuss here other kinds of models that have been proposed for the magnetization reversal, we refer to [9], [5] and the references therein. Let us just mention a more kinetic approach by Stiles and Zangwill [7]. Our aim is to perform both a numerical study and an asymptotic study of the model proposed by [9] in order to recover the experimental results.

Let us consider a magnetic multilayer with the current perpendicular to the plane of the layer (defined as the x-direction). Due to this geometry, we assume in the sequel that all the quantities only depend on the x-space variable (the direction perpendicular to the layers). Hence, the model we present is a one dimensional model (with respect to the space variable).

As suggested by Zhang, Levy and Fert [9], we make the two following simplifications. First, we assume that the non-magnetic spacer layer (NF) is infinitely thin so that the quantities related to the spin current are conserved in this region. That is to say that we replace this layer by an interface, and put some continuity conditions on the spin density at this interface. Second, we assume that the thin ferromagnetic layer F^+ is backed by an ideal paramagnetic layer (some adequate boundary conditions at the right end of the device will be imposed), and we neglect the spin reflection at the interfaces.

Notation Let L be the thickness of the thick ferromagnetic layer F^- and l the thickness of the thin ferromagnetic layer F^+. We assume that F^- corresponds to $x \in (-L, 0)$, F^+ to $x \in (0, l)$, and that the interface separating the layers is at $x = 0$.

The quantities we are interested in are the charge density $\rho : \mathbb{R}^+ \times [-L, l] \to \mathbb{R}$, $(t, x) \mapsto \rho(t, x)$, the spin density $\vec{m} : \mathbb{R}^+ \times [-L, l] \to \mathbb{R}^3$, $(t, x) \mapsto \vec{m}(t, x)$ and the local magnetization

$\vec{M} : \mathbb{R}^+ \times [-L, l] \to \mathbb{R}^3$, $(t, x) \mapsto \vec{M}(t, x)$.

For $\vec{u}$ and $\vec{v}$ two vectors in $\mathbb{R}^3$, we denote by $\vec{u} \cdot \vec{v}$ their scalar product, $\vec{u} \times \vec{v}$ their vector product and $|\vec{u}|$, $|\vec{v}|$ their Euclidean norms. We recall that $\vec{u} \times \vec{v} \cdot \vec{w} = \vec{v} \times \vec{w} \cdot \vec{u} = \vec{w} \times \vec{u} \cdot \vec{v}$.

In the sequel, ∂_t, ∂_x, ∂_x^2 denote the first derivative with respect to the t-variable, the first and second derivatives with respect to the x-variable respectively.

The equations in one ferromagnetic layer

Let us first focus on the equations written in one ferromagnetic layer, in order to describe the interaction between the spin accumulation and the local magnetization. The main aspect, compared to previous models, is that the model proposed by Zhang, Levy and Fert takes into account the effects of spin diffusion. In this model, on one hand, the spin density satisfies a diffusion equation with a term corresponding to a precession phenomenon around the magnetization. On the other hand, the magnetization is solution of a Landau-Lifshitz equation with an additional spin torque.

The equations on the charge density and the spin density. The system of equations on the charge density ρ and the spin density vector $\vec{m}$ is derived from a diffusion equation satisfied by the 2×2 matrix distribution function $\hat{n}(t, x)$ depending on the time variable t and the space variable x. The matrix $\hat{n}(t, x)$ is hermitian. If we denote by I_2 the 2×2 identity matrix and by $\vec{\sigma}$, the vector of Pauli matrices

$$\sigma_1 = \begin{pmatrix} 0 & 1 \\ 1 & 0 \end{pmatrix} \quad , \quad \sigma_2 = \begin{pmatrix} 1 & 0 \\ 0 & -1 \end{pmatrix} \quad \text{and} \quad \sigma_3 = \begin{pmatrix} 0 & -i \\ i & 0 \end{pmatrix},$$

we decompose the matrix distribution function $\hat{n}$ in the basis $(I_2, \sigma_1, \sigma_2, \sigma_3)$ of the space of 2×2 hermitian matrices as

$$\hat{n} = \rho I_2 + \vec{m} \cdot \vec{\sigma},$$

where $\rho(t, x) \in \mathbb{R}$ denotes the charge density and $\vec{m}(t, x) \in \mathbb{R}^3$ the spin density vector.

Let $\hat{\jmath}$, $\hat{C}$, $\hat{D}$ be the matrices representing the current, the conductivity and the diffusion constant. We write

$$\begin{aligned} \hat{C} &= C_0 I_2 + \vec{C} \cdot \vec{\sigma}, \\ \hat{D} &= D_0 I_2 + \vec{D} \cdot \vec{\sigma}, \\ \hat{\jmath} &= j_e I_2 + \vec{\jmath}_m \cdot \vec{\sigma}, \end{aligned}$$

where j_e and $\vec{\jmath}_m$ are respectively the electric current and the magnetic current.

Then for diffusive transport, the current is given by

$$\hat{\jmath} = \hat{C} E(x) - \hat{D} \partial_x \hat{n},$$

where E is the electric field. From this, we get

$$\begin{aligned} j_e &= \mathfrak{Re}\big[\mathrm{Tr}(\hat{\jmath})\big] = C_0 E(x) - D_0 \partial_x \rho - \vec{D}\cdot\partial_x \vec{m}, \\ \vec{\jmath}_m &= \mathfrak{Re}\big[\mathrm{Tr}(-\vec{\sigma}\hat{\jmath})\big] = \vec{C}E(x) - \vec{D}\partial_x\rho - D_0\partial_x\vec{m}. \end{aligned}$$

The equation on $\hat{n}$ writes

$$\partial_t \hat{n} + \partial_x \hat{\jmath} + \left[\frac{i}{2}\vec{\Omega}\cdot\vec{\sigma}, \hat{n}\right] = \frac{\frac{\mathrm{Tr}(\hat{n})}{2} I_2 - \hat{n}}{\tau_{sf}}, \tag{6.2.1}$$

where $\left[\frac{i}{2}\vec{\Omega}\cdot\vec{\sigma}, \hat{n}\right] = -\left(\vec{\Omega}\times\vec{m}\right)\cdot\vec{\sigma}$. This term describes the rotation effect of $\vec{m}$ around the effective field $\vec{\Omega}$ (precession phenomenon).

Now, we have to precise the interaction with the local magnetization $\vec{M}(t,x)$. It appears by two ways: through the diffusion constant and through the effective field. Following [9], we introduce a spin polarization parameter β' and a parameter J quantifying the interaction between the spin accumulation and the local magnetization and we write

$$\vec{D} = \beta' D_0 \vec{M}, \quad \vec{\Omega} = \frac{J}{\hbar}\vec{M},$$

where D_0 is the diffusive constant of the metal and $\hbar$ is the reduced Plank constant.

Using all these relations, we get the equations on the charge density ρ and the spin density vector:

$$\begin{cases} \partial_t \rho + \partial_x j_e = 0, & \text{with } \; j_e = C_0 E - D_0\partial_x\rho - \beta' D_0\, \vec{M}\cdot\partial_x\vec{m}, \\ \partial_t \vec{m} + \partial_x \vec{j_m} + \dfrac{J}{\hbar}\,(\vec{m}\times\vec{M}) = -\dfrac{\vec{m}}{\tau_{sf}}, & \text{with } \; \vec{j_m} = \vec{C}E - \beta' D_0 \vec{M}\partial_x\rho - D_0\partial_x\vec{m}, \end{cases} \tag{6.2.2}$$

where
- $\hbar = \frac{h}{2\pi}$ with h the Plank constant : $h = 6,62.10^{-34} J.s$,
- J quantifies the interaction between $\vec{m}$ and $\vec{M}$: J=0.1-0.4 eV,
- τ_{sf} is the relaxation time of spin switching evaluated in the order of $10^{-12}s$,
- D_0 is the diffusive constant of the metal in the order of $10^{-3} m^2.s^{-1}$,
- β' is a parameter of spin polarization.

Modeling simplification. As it is done in [9], [5], we first neglect the term containing the derivative of the charge density in the magnetic current. Then, as it is noticed in [5], the third term in $\vec{j_m}$ dominates over the first in magnetic multilayers, so we chose to neglect it in our study. So, from now on, we study the model (6.2.2) in this simplified framework. Moreover, with these assumptions, the equation on the charge density ρ is not coupled anymore with the other quantities, so we omit this first equation in the sequel, and the equation on $\vec{m}$ now writes

$$\partial_t \vec{m} - D_0\partial_x^2\vec{m} + \frac{J}{\hbar}\,(\vec{m}\times\vec{M}) = -\frac{\vec{m}}{\tau_{sf}}. \tag{6.2.3}$$

Remark 6.2.1. The simplified model we thus obtain has the nice property that it is easy to check that the positivity condition on $\hat{n}$ is satisfied, whereas it does not seem easy to do it for the full model (6.2.2). Indeed, the density matrix $\widehat{n}$ has eigenvalues $\rho \pm |\vec{m}|$. These two quantities represent the distribution functions of spin up and spin down. They have to be non-negative. More precisely, if we take initial data and boundary data that are hermitian non-negative matrices, then $\hat{n}(t,x)$ has to be a non-negative matrix for all (t,x).

With the simplified model, it is easy to prove that the condition is true for any time. Indeed, if $(\rho, \vec{m})$ satisfies the system (6.2.2), then multiplying scalarly the second equation of (6.2.2) by $\vec{m}/\|\vec{m}\|$, and combining with the equation on ρ, we obtain

$$\partial_t(\rho - |\vec{m}|) - D_0\partial_x^2(\rho - |\vec{m}|) \geq \frac{|\vec{m}|}{\tau_{sf}} \geq 0.$$

The maximum theorem then ensures that $\rho \pm |\vec{m}| \geq 0$ for all (t,x) if this condition is satisfied for initial and boundary data.

The equation on the local magnetization. The local magnetization $\vec{M}(t,x)$ satisfies the following Landau-Lifshitz equation (LL)

$$\partial_t\vec{M} = -\gamma\vec{M} \times (\vec{H}_e + J\vec{m}) + \alpha\vec{M} \times \partial_t\vec{M}, \tag{6.2.4}$$

where parameters $\gamma > 0$ and $\alpha > 0$ are respectively the gyromagnetic coefficient and the Gilbert damping parameter.

The coupling with the spin current appears via an additional term in the effective field: $J\vec{m}$. The usual effective field appearing in the LL equation is $\vec{H}_e$. It includes contributions from the external, anisotropy and demagnetizing field, and an exchange term:

$$\vec{H}_e = \vec{H}_{ext} + \nabla_{\vec{M}}\psi(\vec{M}) + \vec{H}_{demagn} + \nu\partial_x^2\vec{M}. \tag{6.2.5}$$

In our study, we make the following assumptions. First, we assume that there is no external magnetic field applied. Second, we take an anisotropy energy $\psi(\vec{M})$ of the form: $\psi(\vec{M}) = \frac{c}{2}(\vec{M}\cdot\vec{u})^2$, where c is a positive constant, and $\vec{u}$ is the anisotropy direction, a unit vector chosen orthogonal to the x-direction (i.e. in the plane of the layer). Third, as we work with thin layers (even our "thick" layer is thin from that point of view), the main effect of the demagnetizing field is of keeping the magnetization in the plane of the layer. As we have already chosen an anisotropy direction that is parallel to the layer, we can neglect this demagnetizing field. Hence, in the sequel, we work with an effective magnetic field (6.2.5) containing only the contribution from the anisotropy field and an exchange term:

$$\vec{H}_e = c(\vec{M}\cdot\vec{u})\vec{u} + \nu\partial_x^2\vec{M}. \tag{6.2.6}$$

Boundary and interface conditions

To complete the description of the model, we have to talk about the boundary and interface conditions (at $x = -L$, $x = 0$ and $x = l$) both for the spin density and the magnetization.

For the Landau-Lifshitz equation, we choose, as usual, homogeneous Neumann conditions on the boundaries of each layer (both for F^- and F^+). Consequently, we have

$$\begin{cases} \partial_x \vec{M}(t,-L) = 0, \quad \partial_x \vec{M}(t,0^-) = 0, \\ \\ \partial_x \vec{M}(t,0^+) = 0, \quad \partial_x \vec{M}(t,l) = 0, \end{cases} \qquad \forall t \geq 0. \tag{6.2.7}$$

Then, for the spin density, the conditions we impose are the following:

- at $x = -L$, we put a (non homogeneous) Dirichlet condition. This value corresponds to the injected current:
$$\vec{m}(t,-L) = \vec{m_{_L}}(t), \qquad \forall t \geq 0, \tag{6.2.8}$$
where $\vec{m_{_L}}$ is a given function.

- at the interface $x = 0$, we preserve the continuity of the spin density $\vec{m}$
$$\vec{m}(t,0^-) = \vec{m}(t,0^+), \qquad \forall t \geq 0, \tag{6.2.9}$$
and the continuity of the current $\vec{j}_m = -D_0 \partial_x \vec{m}$
$$\partial_x \vec{m}(t,0^-) = \partial_x \vec{m}(t,0^+), \qquad \forall t \geq 0. \tag{6.2.10}$$

- at $x = l$, we want the system to have a free evolution as if a non ferromagnetic layer is at the end of the device ("sandbox"). A first alternative is to take a homogeneous Neumann condition
$$\partial_x \vec{m}(t,l) = 0, \qquad \forall t \geq 0. \tag{6.2.11}$$
A second alternative is to establish a more relevant Fourier-Robin condition by solving the stationary problem on $\vec{m}$ with a infinite layer thickness and without magnetic field, that is:
$$-\partial_x^2 \vec{m} + \vec{m} = 0, \qquad x \in (0, +\infty).$$
Keeping only L^2 solutions, we get the following boundary condition at $x = l$:
$$\partial_x \vec{m}(t,l) = -\vec{m}(t,l).$$
But, since the numerical results (for the scaled system, this condition becomes $\partial_x \vec{m}(t,l) = -\varepsilon \vec{m}(t,l)$, see next paragraph) with these two conditions are very similar, we chose to use the homogeneous Neumann condition.

6.2.2 The scaled model

In order to write a dimensionless system, we introduce the small parameter $\varepsilon = \frac{l}{L}$ as the ratio between the thicknesses of the layers F^+ and F^- (then ε^2 is of order 10^{-3} for typical physical devices). We scale the space variable as $\frac{x}{L}$ in the thick material F^- and as $\frac{x}{l} = \frac{1}{\varepsilon}\frac{x}{L}$ in the thin material F^+.

For time scales, the characteristic time scale for the magnetization corresponds to $t_0 = \gamma^{-1}H^{-1}$ (with $H = |\vec{H}_e + J\vec{m}|$). This term is of order of the nanosecond. We scale the time variable as $\frac{t}{t_0}$.

Moreover, rather than keeping track of the fact that the injected current must be very intense, of order $1/\varepsilon$, through a Dirichlet data of that order at $x = -L$, we scale the spin density by a factor J/H. Hence, we will keep track of the fact that the injected current must be very intense through the factor $\frac{1}{\varepsilon}$ in front of $\vec{m}$ in the LL equation.

With that scaling, we denote $\vec{m}^- : \mathbb{R}^+ \times (-1,0) \to \mathbb{R}^3$ and $\vec{M}^- : \mathbb{R}^+ \times (-1,0) \to \mathbb{R}^3$ respectively the spin density vector and the local magnetization in the thick ferromagnetic material F^-, and $\vec{m}^+ : \mathbb{R}^+ \times (0,1) \to \mathbb{R}^3$ and $\vec{M}^+ : \mathbb{R}^+ \times (0,1) \to \mathbb{R}^3$ respectively the spin density vector and the local magnetization in the thin ferromagnetic material F^+.

We still denote t and x the new time and space variables. Writing all the constants in terms of ε, we reduce to the following dimensionless equations, written for $t \geq 0$,

$$\begin{cases} \varepsilon^2 \partial_t \vec{m}^- - \partial_x^2 \vec{m}^- + \dfrac{\vec{m}^- \times \vec{M}^-}{\varepsilon^2} + \vec{m}^- = 0, \quad x \in (-1,0), \\ \partial_t \vec{M}^- = -\vec{M}^- \times \left(c(\vec{M}^- \cdot \vec{u}^-)\vec{u}^- + \dfrac{\vec{m}^-}{\varepsilon} + \nu \partial_x^2 \vec{M}^- \right) + \alpha \vec{M}^- \times \partial_t \vec{M}^-. \end{cases} \tag{6.2.12}$$

$$\begin{cases} \varepsilon^2 \partial_t \vec{m}^+ - \dfrac{1}{\varepsilon^2}\partial_x^2 \vec{m}^+ + \dfrac{\vec{m}^+ \times \vec{M}^+}{\varepsilon^2} + \vec{m}^+ = 0, \quad x \in (0,1), \\ \partial_t \vec{M}^+ = -\vec{M}^+ \times \left(c(\vec{M}^+ \cdot \vec{u}^+)\vec{u}^+ + \dfrac{\vec{m}^+}{\varepsilon} + \dfrac{\nu}{\varepsilon^2} \partial_x^2 \vec{M}^+ \right) + \alpha \vec{M}^+ \times \partial_t \vec{M}^+. \end{cases} \tag{6.2.13}$$

$$\begin{cases} \vec{m}^-(t,-1) = \vec{m_L}(t), \\ \vec{m}^-(t,0^-) = \vec{m}^+(t,0^+), \\ \varepsilon \partial_x \vec{m}^-(t,0^-) = \partial_x \vec{m}^+(t,0^+), \\ \partial_x \vec{m}^+(t,1) = 0. \end{cases} \tag{6.2.14}$$

$$\begin{cases} \partial_x \vec{M}^-(t,-1) = \partial_x \vec{M}^-(t,0) = 0, \\ \partial_x \vec{M}^+(t,0) = \partial_x \vec{M}^+(t,1) = 0. \end{cases} \tag{6.2.15}$$

Moreover, it is easy to see that the Landau-Lifshitz equation keeps the norm of $\vec{M}(t,x)$ constant through time evolution. We assume that

$$|\vec{M}^-(0,x)| = 1 \text{ for all } x \in [-1,0], \text{ and } |\vec{M}^+(0,x)| = 1 \text{ for all } x \in [0,1], \tag{6.2.16}$$

so that this property stays true for all t, x.

Without going further in the analysis, one can notice immediately that ε orders are different in the two ferromagnetic materials. One can guess that, in the thick ferromagnetic material F^-, $\vec{m}^- \times \vec{M}^- = 0$ when $\varepsilon \to 0$. So, the spin density is polarized in the direction of the magnetization, and we recover, for the magnetization, a non-coupled Landau-Lifshitz equation. On the contrary, in the thin ferromagnetic layer, the two quantities stay coupled in the limit $\varepsilon \to 0$, and a more precise study is needed in order to guess the asymptotic behavior.

6.2.3 A first description of the various scales

Looking at the system (6.2.12)-(6.2.13)-(6.2.14)-(6.2.15), we can easily see that there are various scales (both time and space scales). As we will see in the next section, the understanding of these different scales is necessary in order to construct an appropriate numerical scheme for the previous system. In this paragraph, we make a first description of these different scales. A more precise study will be performed in Section 5 in order to construct an approximate model for the full system (6.2.12)-(6.2.13)-(6.2.14)-(6.2.15) as $\varepsilon \to 0$.

Time scales. There are two time scales for the spin density evolution: one for the behavior of $\vec{m}$ in the direction parallel to the magnetization $\vec{M}$, the other for the behavior of the part of $\vec{m}$ that is orthogonal to $\vec{M}$. In order to explain this in a simple framework, let us take the diffusive equation on the spin density with a given magnetic field $\vec{M}$, in the thick layer F^-. Assume moreover that $\vec{M}^-$ is constant (independent of t and x, this will be the case if we consider the layer at equilibrium from the beginning, $\vec{M}^-(t,x) = u^-$ for all t, x). The solution $\vec{m}^-$ of the equation

$$\varepsilon^2 \partial_t \vec{m}^- - \partial_x^2 \vec{m}^- + \frac{\vec{m}^- \times \vec{M}^-}{\varepsilon^2} + \vec{m}^- = 0$$

can thus be decomposed as $\vec{m}^-(t,x) = \mathcal{L}\left(\frac{t}{\varepsilon^4}\right)\vec{v}(t,x)$, where $\mathcal{L}(\tau)$ is the group associated with the equation

$$\partial_\tau \vec{m}^- + \vec{m}^- \times \vec{M}^- = 0,$$

and $\vec{v}$ is a solution of

$$\varepsilon^2 \partial_t \vec{v} - \partial_x^2 \vec{v} + \vec{v} = 0.$$

Since $\vec{M}^-$ does not depend on τ, the group $\mathcal{L}(\tau)$ can be explicitly computed (calculating separately the parallel and transverse components), so that

$$\vec{m}^-(t,x) = \left(\vec{v}(t,x)\cdot\vec{M}^-\right)\vec{M}^- + \sin\left(\frac{t}{\varepsilon^4}\right)\vec{M}^- \times \vec{v}(t,x) + \cos\left(\frac{t}{\varepsilon^4}\right)\vec{M}^- \times \left(\vec{v}(t,x) \times \vec{M}^-\right). \quad (6.2.17)$$

In this expression, one can see that very fast oscillations at scale t/ε^4 appear for the part of the spin density that is orthogonal to $\vec{M}^-$.

But, we remind here that the first thick layer should act as a polarizer, that is to say that $\vec{m}^-$ should be collinear to $\vec{M}^-$. This property will be satisfied by the local mean in time with

respect to the fast time variable. Indeed, the oscillating part has zero mean: when $\vec{v}$ does not depend on τ,

$$\frac{1}{2\pi}\int_0^{2\pi} \mathcal{L}(\tau)\vec{v}\, d\tau = (\vec{v}\cdot\vec{M}^-)\,\vec{M}^-. \tag{6.2.18}$$

Since these very fast oscillations at scale t/ε^4 are not significant for the phenomenon we want to study here, in the sequel, in particular for numerical simulations, we will use techniques that allow us to avoid them. The two usual techniques to that purpose are filtering and averaging. As we will explain more precisely when constructing the numerical scheme, we will actually use both.

Space scales. In order to understand the various scales with respect to the x-variable in the thick layer, let us consider again a simple setting. We consider the stationary equation on the spin density, with a given constant magnetization $\vec{M}^-$:

$$-\partial_x^2\vec{m}^- + \frac{\vec{m}^-\times\vec{M}^-}{\varepsilon^2} + \vec{m}^- = 0.$$

Now, we can write the equations on the components of $\vec{m}^-$ that are parallel or transverse to $\vec{M}^-$. For the transverse part, we write $\vec{m}^\perp = m_1\vec{w}_1 + m_2\vec{w}_2$ with $(\vec{w}_1,\vec{w}_2)$ an orthonormal basis of $(\vec{M}^-)^\perp$, and let $Z^- = m_1 + im_2$. Then, we get

$$\begin{cases} -\partial_x^2(\vec{m}^-\cdot\vec{M}^-) + (\vec{m}^-\cdot\vec{M}^-) = 0, \\ -\partial_x^2 Z^- + \left(-\dfrac{i}{\varepsilon^2}+1\right)Z^- = 0. \end{cases} \tag{6.2.19}$$

When solving the last equation, the roots $\pm\sqrt{-\frac{i}{\varepsilon^2}+1}$ appear (where $\mathfrak{Re}(z) > 0$). Since, $\sqrt{-\frac{i}{\varepsilon^2}+1} \simeq \frac{\sqrt{-i}}{\varepsilon}$ when $\varepsilon\to 0$, we get

$$Z^-(x) \simeq Z^-(0)e^{-\sqrt{-i}\frac{x}{\varepsilon}}.$$

Hence, we can see that the orthogonal part of $\vec{m}^-$ depends on the variable x/ε. This term corresponds to a boundary layer near the interface $x=0$ in the thick material, which we will describe precisely in Section 3. Thus, it will be important to take into account the two space scales in the thick layer: x and x/ε.

6.3 Numerical scheme

In this part, we describe the numerical scheme we have constructed for the system (6.2.12)-(6.2.13)-(6.2.14)-(6.2.15). In order to construct an appropriate scheme, also valid for small values of ε, it is important to take into account the various scales, in particular the very fast time oscillations and the existence of a boundary layer close to the interface in the thick material.

The two main ideas are the following. First, for the space discretization, due to this boundary layer, it is preferable to use a non-uniform space mesh, refined near the interface in the thick

material. Then, as we have described in the previous section, the behavior of the spin density is quite different in the directions parallel or transverse to the magnetization. Hence, we will use a finite element method for the equation on $\vec{m}$, using basis functions adapted to this phenomenon.

Second, it is important to treat the very fast time oscillations at scale t/ε^4, or more precisely to avoid them (since these oscillations are not relevant here). To that purpose, we "filter" these oscillations by using an implicit scheme for the time discretization of the equation on the spin density, using a time step much bigger than ε^4. But, we also have to treat in a particular way the singular term $\frac{\vec{M}\times\vec{m}}{\varepsilon}$, containing very fast oscillations, when discretizing the Landau-Lifshitz equation. On each time step, we will replace this a priori singular term by its mean with respect to the fast time variable, so that this term will not be singular any more.

Notation Let N be the spatial mesh element number and $(x_k)_{1\leq k\leq N+1}$ the coordinates of mesh points, with $x_1 = -1$ and $x_{N+1} = 1$.

We denote Δt the time step, and for all $n \in \mathbb{N}$, $t^n = n\Delta t$.

We denote $\vec{m}^n$, and $\vec{M}^n$ the discrete spin density and magnetization vectors obtained from $\big(\vec{m}(t^n, x_k)\big)_{1\leq k\leq N+1}$ and $\big(\vec{M}(t^n, x_k)\big)_{1\leq k\leq N+1}$.

Let $(\vec{e}_1, \vec{e}_2, \vec{e}_3)$ be the canonical basis in $\mathbb{R}^3$.

Let us now explain how we compute $(\vec{m}^{n+1}, \vec{M}^{n+1})$ from $(\vec{m}^n, \vec{M}^n)$. We first compute $\vec{m}^{n+1}$ by solving the spin density equation with $\vec{M}^n$. Then, we compute $\vec{M}^{n+1}$ by solving the LL equation with $\vec{m}^{n+1}$ (more precisely with an average spin density on $[t^n, t^{n+1}]$, see below).

6.3.1 Discretization of the diffusive equation on the spin density

Let $n \in \mathbb{N}$ be fixed, and assume that $(\vec{m}^n, \vec{M}^n)$ is known. To determine $\vec{m}^{n+1}$, we use an implicit Euler scheme for the time discretization and a finite element method on the non-uniform space mesh $(x_k)_{1\leq k\leq N+1}$ for the space discretization. We first describe the basis functions, and then give the appropriate variational formulation.

Basis functions

For each time t^n, each $1 \leq k \leq N+1$, we construct a triplet of basis functions $\vec{\theta}_k(t^n) = (\vec{\theta}^1_k, \vec{\theta}^2_k, \vec{\theta}^3_k)(t^n)$ supported in $[x_{k-1}; x_{k+1}]$ ($[x_1, x_2]$ for $k = 1$ and $[x_N, x_{N+1}]$ for $k = N+1$). These basis functions are defined as being solutions of the following stationary problems (with suitable modifications for the cases $k = 1$ and $k = N+1$): for $1 \leq j \leq 3$,

$$\begin{cases} -\partial_x^2\vec{\theta}_k^j + \dfrac{\vec{\theta}_k^j \times \vec{M}_k^n}{\varepsilon^2} + \vec{\theta}_k^j = 0, & \text{if } x \in]-1,0[, \\ -\partial_x^2\vec{\theta}_k^j + \vec{\theta}_k^j \times \vec{M}_k^n + \varepsilon^2\vec{\theta}_k^j = 0, & \text{if } x \in]0,1[, \\ \vec{\theta}_k^j(x_k) = \vec{e}_j, \\ \vec{\theta}_k^j(x_{k\pm1}) = \vec{0}. \end{cases}$$

that is to say that $\vec{\theta}_k^j(t^n)$ is the solution of two Dirichlet problems, the first one on $[x_{k-1}, x_k]$, the second one on $[x_k, x_{k+1}]$. The equation satisfied by $\vec{\theta}_k^j(t^n)$ on (x_{k-1}, x_k) (respectively (x_k, x_{k+1})) is the first equation above if $[x_{k-1}, x_k] \subset [-1, 0]$ (respectively $[x_k, x_{k+1}] \subset [-1, 0]$) and the second one above if $[x_{k-1}, x_k] \subset [0, 1]$ (respectively $[x_k, x_{k+1}] \subset [0, 1]$). These functions are thus piecewise exponential type functions (on $[x_{k-1}, x_k]$ and $[x_k, x_{k+1}]$). They can be written as

$$\vec{\theta}_k^j(t^n)(x) = {}^T\!P(\vec{M}_k^n)\mathcal{R}_k(x)P(\vec{M}_k^n)\vec{e}_j,$$

where $\mathcal{R}_k$ is a matrix that does not depend on t^n, so that it is computed only once (and not at each step of the numerical calculation), and $P(\vec{M}_k^n)$ is the matrix of one orthonormal basis adapted to $\vec{M}_k^n$ with respect to the canonical basis.

To obtain this formula, we separate the parallel and the transverse components compared to $\vec{M}_k^n$ (same procedure as in section 2.4). To illustrate the procedure and to give a more precise formula, let us solve the problem on $[x_{k-1}, x_k]$, if $[x_{k-1}, x_k] \subset [0, 1]$. The adaptation is straightforward for the other cases. Let us denote by $\eta_+^\varepsilon = \sqrt{\varepsilon^2 - i} = \frac{1}{\sqrt{2}}\left(\sqrt{\varepsilon^2 + \sqrt{1+\varepsilon^4}} - i\sqrt{-\varepsilon^2 + \sqrt{1+\varepsilon^4}}\right)$ the square root with positive real part and $r_k(x)e^{i\phi_k(x)} = \dfrac{\sinh\left(\eta_+^\varepsilon(x - x_{k-1})\right)}{\sinh\left(\eta_+^\varepsilon(x_k - x_{k-1})\right)}$. Then the corresponding matrix $\mathcal{R}_k$ is

$$\mathcal{R}_k(x) = \begin{pmatrix} \dfrac{\sinh\left(\varepsilon(x-x_{k+1})\right)}{\sinh\left(\varepsilon(x_k-x_{k+1})\right)} & 0 & 0 \\ 0 & r_k(x)\cos\phi_k(x) & -r_k(x)\sin\phi_k(x) \\ 0 & r_k(x)\sin\phi_k(x) & r_k(x)\cos\phi_k(x) \end{pmatrix}.$$

Once the construction of these appropriate functions is done, the implementation of the finite element method is as usual. We first give the variational formulation we used, and then the related matrix system that is actually solved numerically.

Variational formulation

In order to implement the finite element method, we have to write a variational formulation of the equation on the spin density. Since the spin density satisfies a non homogeneous Dirichlet condition at $x = -1$, we first come down to an homogeneous condition by defining the new unknown: for all (t, x),

$$\vec{\omega}(t,x) = \begin{cases} \vec{m}^-(t,x) - \vec{m}^-(t,-1)\cdot\vec{\theta}_1(t,x), & \text{for } x \in (-1,0), \\ \vec{m}^+(t,x), & \text{for } x \in (0,1), \end{cases} \tag{6.3.1}$$

where $\vec{\theta}_1$ is the first triplet of basis functions defined in the previous paragraph.

We also let

$$V = \{\vec{v} \in \mathbb{H}^1(\mathbb{R}^+ \times [-1,1], \mathbb{R}^3), \vec{v}(\cdot,-1) = 0\}.$$

In order to obtain the variational problem satisfied by $\vec{\omega}$, we combine the equation on $\vec{m}^-$ with the equation on $\vec{m}^+$ multiplied by ε, together with the boundary and interface conditions on $\vec{m}^-$ and $\vec{m}^+$. We thus get that $\vec{\omega}$ is defined as the solution in V of the problem : for all $\vec{\theta} \in V$, for all $t > 0$,

$$\begin{aligned}
&\varepsilon^3 \int_{-1}^{0} \partial_t \vec{\omega} \cdot \vec{\theta}\, dx + \varepsilon^2 \int_0^1 \partial_t \vec{\omega} \cdot \vec{\theta}\, dx + \varepsilon \int_{-1}^{0} \partial_x \vec{\omega} \cdot \partial_x \vec{\theta}\, dx + \int_0^1 \partial_x \vec{\omega} \cdot \partial_x \vec{\theta}\, dx \\
&+\frac{1}{\varepsilon} \int_{-1}^{0} \left(\vec{\omega} \times \vec{M}^-\right) \cdot \vec{\theta}\, dx + \int_0^1 \left(\vec{\omega} \times \vec{M}^+\right) \cdot \vec{\theta}\, dx + \varepsilon \int_{-1}^{0} \vec{\omega} \cdot \vec{\theta}\, dx + \varepsilon^2 \int_0^1 \vec{\omega} \cdot \vec{\theta}\, dx \\
= \;& -\varepsilon^3 \int_{-1}^{0} \partial_t \left(\vec{m}^-(t,-1) \cdot \vec{\theta}_1\right) \cdot \vec{\theta}\, dx - \varepsilon \int_{-1}^{0} \partial_x \left(\vec{m}^-(t,-1) \cdot \vec{\theta}_1\right) \cdot \partial_x \vec{\theta}\, dx \\
&-\frac{1}{\varepsilon} \int_{-1}^{0} \left(\left(\vec{m}^-(t,-1) \cdot \vec{\theta}_1\right) \times \vec{M}^-\right) \cdot \vec{\theta}\, dx - \varepsilon \int_{-1}^{0} \left(\vec{m}^-(t,-1) \cdot \vec{\theta}_1\right) \cdot \vec{\theta}\, dx,
\end{aligned}$$

which we rewrite in the following concise form

$$\langle \partial_t \vec{\omega}(t), (\varepsilon^3 \mathbf{1}_{(-1,0)} + \varepsilon^2 \mathbf{1}_{(0,1)}) \vec{\theta}(t) \rangle_{L^2_x(-1,1)} + a^\varepsilon\big(\vec{\omega}(t), \vec{\theta}(t)\big) = \mathcal{L}^\varepsilon\big(\vec{\theta}(t)\big). \tag{6.3.2}$$

Matrix system

Now, we write the discretized variational problem related to the previous variational formulation (6.3.2) and the basis $(\vec{\theta}_i^n)_{1 \le i \le N+1}$. This discretized problem is obtained in the following way. For the temporal discretization, we use an implicit Euler scheme, so that we write for $n \in \mathbb{N}$,

$$\left\langle \frac{\vec{\omega}(t^{n+1}) - \vec{\omega}(t^n)}{\Delta t}, (\varepsilon^3 \mathbf{1}_{(-1,0)} + \varepsilon^2 \mathbf{1}_{(0,1)}) \vec{\theta}(t^n) \right\rangle_{L^2_x(-1,1)} + a^\varepsilon\big(\vec{\omega}(t^{n+1}), \vec{\theta}(t^n)\big) = \mathcal{L}^\varepsilon\big(\vec{\theta}(t^n)\big). \tag{6.3.3}$$

Let $n \in \mathbb{N}$ be fixed. We decompose $\vec{\omega}(t^n)$ on the basis functions derived above:

$$\vec{\omega}(t^n, x) = \sum_{k=1}^{N+1} \vec{\omega}_k^n \cdot \vec{\theta}_k(t^n)(x), \tag{6.3.4}$$

where $\vec{\omega}_k^n \in \mathbb{R}^3$ for all $k = 1 \dots N+1$.

Next, we construct the vector $\widetilde{\omega}^n$ as being the column vector made up from the vectors $\vec{\omega}_k^n$ for $2 \le k \le N+1$ (the subscript $k = 1$ does not appear since nodes with Dirichlet conditions are not inserted in matrices). The contributions of the two first terms of the variational formulation (containing the time derivatives) are inserted in a matrix B^ε. The matrix C^ε contains the terms corresponding to a^ε. Finally, the $\mathcal{L}^\varepsilon$ terms (which allows to treat the non homogeneous Dirichlet condition) are in a vector D^ε. Finally, we write an implicit Euler scheme for the time discretization. Thus, the problem consists to solve the following matrix system

$$\left(C^\varepsilon + \frac{\varepsilon^2}{\Delta t} B^\varepsilon\right) \widetilde{\omega}_{n+1} = \left(D^\varepsilon + \frac{\varepsilon^2}{\Delta t} B^\varepsilon\, \widetilde{\omega}_n\right). \tag{6.3.5}$$

Finally, the spin density vector $\vec{m}^{n+1}$ is obtained straightforwardly from $\vec{\omega}_{n+1}$ with 6.3.1.

We would like to indicate that the coefficients of the matrices C^ε and B^ε are of the type $\int \theta_k^j(t^n)\theta_{k'}^{j'}(t^n)dx$ (or with derivatives). These integrals can be calculated analytically using the explicit formulas we obtained for the basis functions. We use these exact values in our numerical scheme.

This method of finite element with exponential basis functions allows to model quite accurately the problem with an acceptable space step. For example, taking $\varepsilon = 1.10^{-2}$, we need a space step of 5.10^{-4} with the finite differences method to take in account correctly the limit layer of thickness ε. With the finite element method, we just need to use a refined mesh in the asymptotic region. The number of point is divided by 10 and the time computation divided by 5 to obtain the same accuracy.

6.3.2 Discretization of the Landau-Lifshitz equation

For the Landau-Lifshitz equation, we use the scheme proposed by Wang, Garcia-Cervera, E [8]. We do not rewrite it here in full details. Let us just say that it is an implicit Gauss-Seidel projection scheme. It is a fractional step method adapted to the LL equation $\partial_t M = -M \times H + \alpha \partial_t M \times M$, that can be rewritten (at least for smooth solutions)

$$(1+\alpha^2)\partial_t M = -M \times H - \alpha M \times \Big(M \times H\Big).$$

The first step consists of an implicit Gauss-Seidel method. The second step corresponds to performing the heat flow, the third and last step is just the projection on $\mathbb{S}^2$ (in order to keep the norm of $\vec{M}$ constant).

The only specific difficulty in our case compared to the general scheme in [8] is that the effective field in our coupled LL equation contains a priori singular terms: $\frac{\vec{M}^- \times \vec{m}^-}{\varepsilon}$ in the thick layer, $\frac{\vec{M}^+ \times \vec{m}^+}{\varepsilon}$ and $\frac{1}{\varepsilon^2}\partial_x^2 M^+$ in the thin layer. The two terms in the thin layer do not need to be treated in a specific way. Indeed, even if they seem singular, they are actually of order $O(1)$ when $\varepsilon \to 0$ (as shown in the asymptotic study in Section 6.5). In the thick layer, the term $\frac{\vec{M}^- \times \vec{m}^-}{\varepsilon}$ has to be treated in a particular way. As we have already explained before, the spin density $\vec{m}^-$ has a nonzero transverse part, so this last term is of order $O(1/\varepsilon)$. But, this transverse part contains only very fast oscillations at scale t/ε^4, that are not significant here, so we will perform the local mean in time with respect to the fast variable, and recover a spin density that is parallel to the magnetization up to very small terms. Let us be more precise, describing how we treat the temporal fast oscillations.

Let us recall that the first step has consisted in solving the diffusive equation with $\vec{M}^n$ and obtaining $\vec{m}^{n+1}$. Then, we solve the LL equation with $\vec{m}^{n+1}$ in order to compute $\vec{M}^{n+1}$. Rather than using $\vec{m}^{n+1}$ we replace it by its mean with respect to time on the interval $[t^n, t^{n+1}]$. We

use the formula (6.2.17) to write

$$\vec{m}(t) = \Big(\vec{m}^{n+1}\cdot\vec{M}^n\Big)\vec{M}^n + \sin\Big(\frac{t-t^n}{\varepsilon^4}\Big)\vec{M}^n\times\vec{m}^{n+1} + \cos\Big(\frac{t-t^n}{\varepsilon^4}\Big)\vec{M}^n\times\big(\vec{m}^{n+1}\times\vec{M}^n\big). \quad (6.3.6)$$

We then calculate an average spin density $\vec{m}^*$ and use it in the LL equation instead of $\vec{m}^{n+1}$ to calculate $\vec{M}^{n+1}$:

$$\vec{m}^* = \frac{1}{\Delta t}\int_{t^n}^{t^{n+1}} m(t)dt. \quad (6.3.7)$$

Because of the form (6.3.6), this average $\vec{m}^*$ can be calculated explicitly by the following expression

$$\vec{m}^* = \Big(\vec{m}^{n+1}\cdot\vec{M}^n\Big)\vec{M}^n + \frac{\varepsilon^4}{\Delta t}\Big(\big(1-\cos(\Delta t/\varepsilon^4)\big)\vec{M}^n\times\vec{m}^{n+1} + \sin(\Delta t/\varepsilon^4)\vec{M}^n\times\big(\vec{m}^{n+1}\times\vec{M}^n\big)\Big). \quad (6.3.8)$$

6.4 Numerical simulations of the magnetization switching

In this part, we present our numerical simulations obtained with the scheme we have just described. In particular, we show the magnetization switching in the thin layer, and we study the impact of the intensity of the injected current on this switching phenomenon. As we will see, our numerical simulations are in accordance with physical experiments.

As initial conditions, we assume that the two ferromagnetic materials are at equilibrium before injecting the spin current, that is to say that we assume that for all x (respectively in $(-1,0)$ and $(0,1)$),

$$\vec{M}^-(t=0,x) = u^- = \begin{pmatrix} 0 \\ -\sin\theta \\ \cos\theta \end{pmatrix} \quad \text{and} \quad \vec{M}^+(t=0,x) = u^+ = \begin{pmatrix} 0 \\ 0 \\ 1 \end{pmatrix}, \quad (6.4.1)$$

where $\theta = 30^\circ$ is the angle between the two anisotropy directions u^- and u^+. As we begin the injection at $t = 0^+$, we assume that $\vec{m}(t=0) = 0$.

The following numerical simulations are done with a parameter $\varepsilon = 10^{-2}$. The time step is $\Delta t = 10^{-2}$, and the space step is 10^{-2} away from the interface, and $5\cdot 10^{-4}$ near the interface in the thick layer.

6.4.1 Observation of the magnetization switching

To start with numerical results, we present the evolution of the magnetization in a case where we observe a switching (we inject an intense enough current here, we will discuss that point in the next paragraph). In Figs.6.2 and 6.3, one can see the evolution of the magnetization components with respect to time, both in the thick and in the thin layers (the left part between

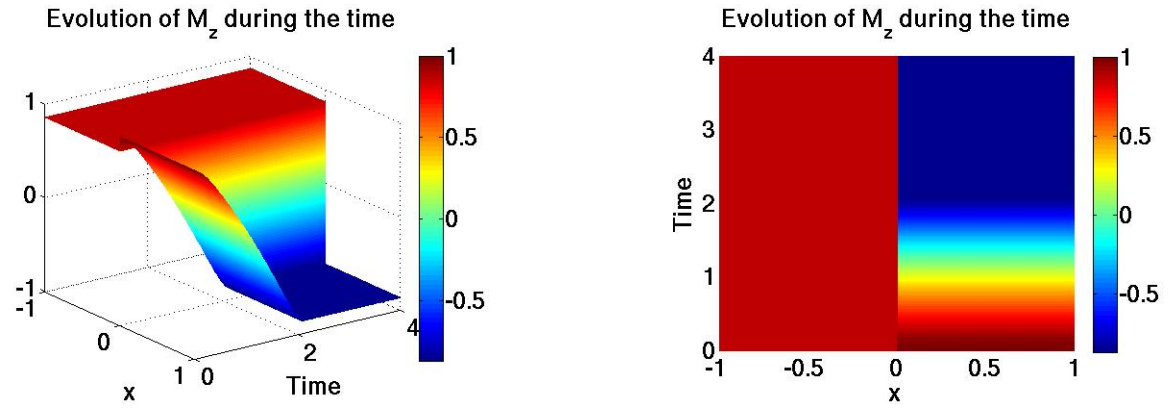

Figure 6.2: Evolution of the M_z component during the time (3D view and projection).

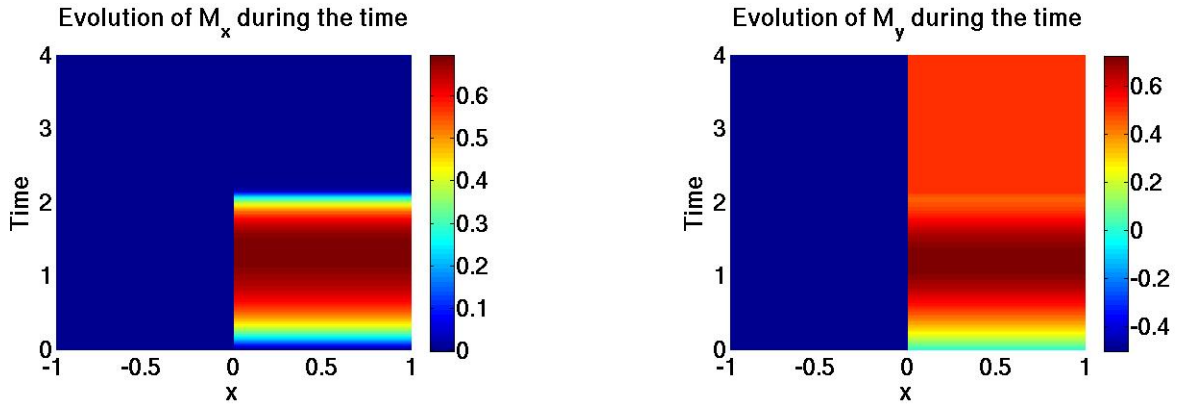

Figure 6.3: Evolution of the M_x and M_y components.

-1 and 0 describes F^- and the right part between 0 and 1 describes F^+).

On one hand, as expected, we observe that the magnetization in the thick ferromagnet F^- remains at equilibrium. On the other hand, we see that the magnetization moves in F^+ under the spin current influence, and that around time 2, it is almost completely switched. It is obvious that the end point reached by $\vec{M}^+$ is not the equilibrium point $-\vec{u}^+$, that would correspond to $M_z^+ = -1$. We identified this point as being $-\vec{u}^-$: that is to say that the magnetization in the thin material is almost reversed, but the end point point is not in the anisotropy direction of the F^+ ferromagnet but in the anisotropy direction of the thick ferromagnet F^-. This point is confirmed by Fig.6.4.

Finally, the reader can notice on Figs.6.2 and 6.3 that the magnetization $\vec{M}^+$ is constant with respect to the space variable through the thin layer. We will recover this result in our asymptotic study.

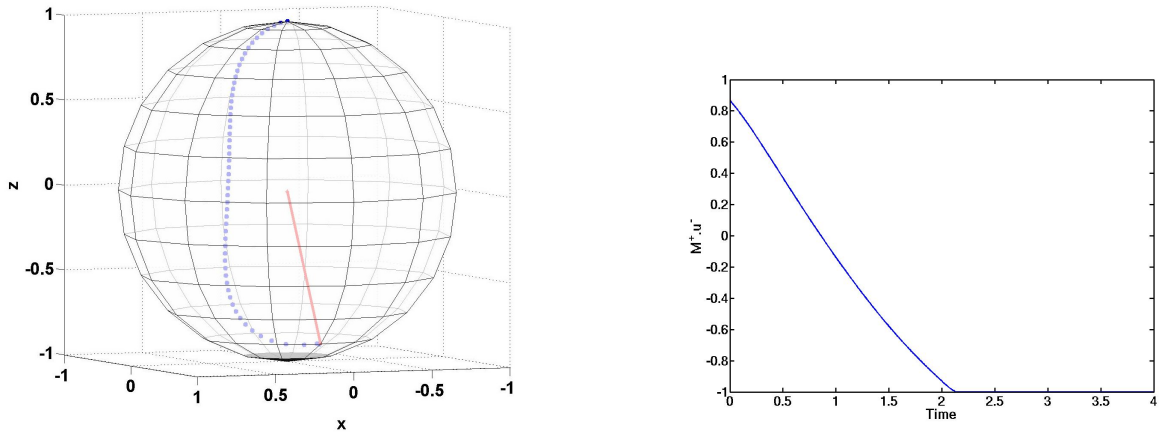

Figure 6.4: Evolution of the magnetization $\vec{M}^+$ during the time around the unit sphere (the starting point is the north pole, and the arrow points $-\vec{u}^-$) (left), evolution of $\vec{M}^+.\vec{u}^-$ during the time (right).

6.4.2 Study of the torque $\vec{m} \times \vec{M}$

It is also interesting to study the torque $\vec{m} \times \vec{M}$, since it is responsible of the magnetization switching. We remind the switching is due to interactions between the transverse component of the spin density and the magnetization in the thin material. The torque is presented in Fig.6.5. One can notice that it is indeed important in F^+ when the switching starts, but $\|\vec{m} \times \vec{M}\|$ is never greater than $O(\varepsilon)$.

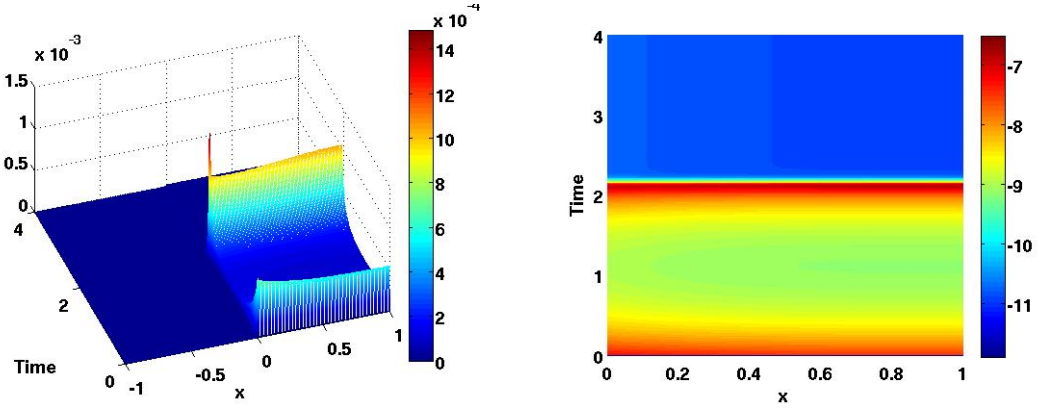

Figure 6.5: Evolution of the torque $\|\vec{m} \times \vec{M}\|^2$ during the time: 3D view (left), and with a logarithmic scale in the thin material (right).

6.4.3 Impact of the injected current

Current intensity influence

In physical experiments, it is known that there is a threshold for the intensity of the injected current above which it is possible to observe the magnetization reversal. In Fig.6.6, we plotted the results we obtain with our model about the impact of the injected current. We recover the existence of such a threshold (here between $\|\vec{m}_{_L}\| = 0.203$ and $\|\vec{m}_{_L}\| = 0.204$). Morerover, one can notice that the more intense the injected current is, the more rapid the induced reversal of the magnetization is. But, in any case of reversal, the magnetization reaches the same point $-\vec{u}^-$.

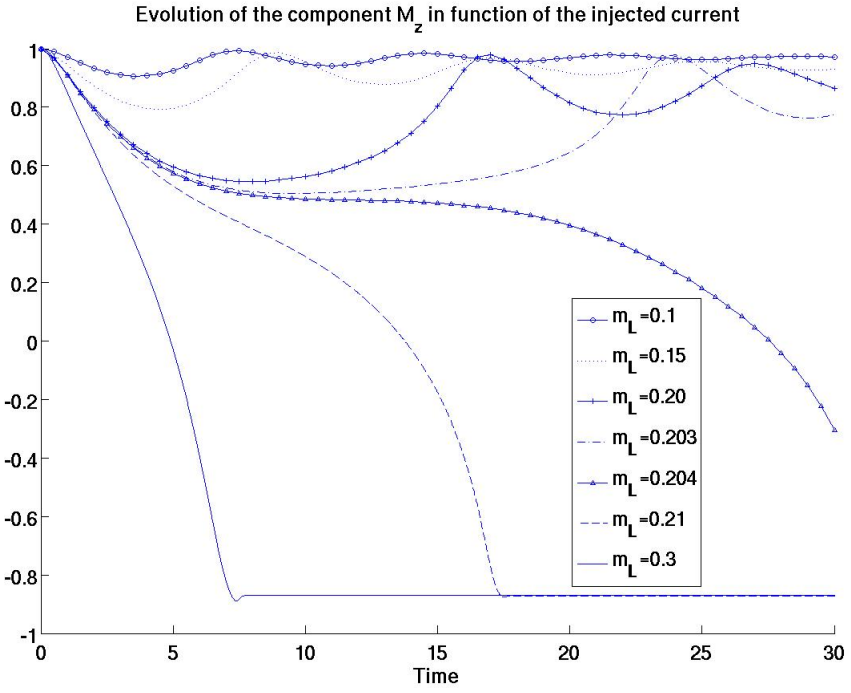

Figure 6.6: Evolution of the component M_z^+ for different values of the injected current intensity $\|\vec{m}_{_L}\|$.

Current sign influence

The second experiment is to take a current whose intensity allows a switching and to change its sign during the time. We obtain Fig.6.7. It represents the evolution of the component M_z^+ during the time.

In this case, we start with a negative sign (such that $\vec{m}_{_L} \cdot \vec{u}^- < 0$). This sign is necessary if we want to observe a magnetization switching in F^+. At time $t = 4$, the magnetization has converged to $-\vec{u}^-$ and we decide to invert the current sign. Then, the switching is reversed and

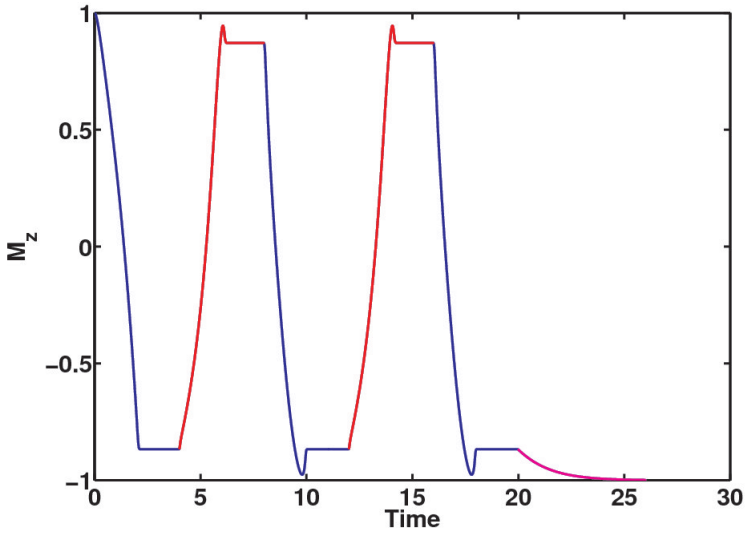

Figure 6.7: A succession of switching during the time.

the magnetization goes up to $\vec{u}^-$. At time 8, we change the sign again coming back to the initial current. The magnetization is still switching and returns to $-\vec{u}^-$. At the times 12 and 16, we make the same manipulations. The magnetization follows exactly the same way around the unit sphere as previously. Finally, at time 20, we stop the current taking $\vec{m}_{_L} = \vec{0}$. The magnetization converges slowly to the inferior pole of the sphere $-\vec{u}^+$. We recall here that $\pm u^+$ are known to be stable equilibrium states for the non coupled Landau-Lifshitz equation

$$\partial_t \vec{M}^+ = -\vec{M}^+ \times \left(c(\vec{M}^+ \cdot \vec{u}^+)\vec{u}^+ + \nu \partial_x^2 \vec{M}^+ \right) + \alpha \vec{M}^+ \times \partial_t \vec{M}^+.$$

This succession of switchings allows to see the role of the current sign. It shows that the magnetization switching is reversible. We can choose to guide the magnetization up to the superior part or down to the inferior part of the sphere.

6.5 Derivation of asymptotic models and numerical comparison

In this section, we are interested in the derivation of an approximate model for the full system (6.2.12)-(6.2.13)-(6.2.14)-(6.2.15) when ε goes to 0. Our derivation here is purely formal, and the validation is done numerically, by presenting numerical comparisons between our asymptotic model and the full system. The mathematical study of existence and convergence will be addressed in a following paper by E. Fouassier and D. Sanchez.

6.5.1 A first asymptotic model

In order to find such a model, we use a multiscale approach. We introduce the various scales appearing in the phenomena that we described in the previous section. We recall that there

were two time scales, t and t/ε^4, and two space scales in the thick material, x and x/ε.

We have already mentioned that the oscillations at the fast time scale t/ε^4 are not significant here, so we will omit that scale in the asymptotic study. Indeed, these oscillations have zero mean, so if we do not take into account this scale in our study, we recover the behavior of the local mean in time of $\vec{m}$ with respect of this fast time scale, which is what we are interested in here.

Because of the boundary layer near the interface in the thick material, we decompose the solutions in this material as

$$\begin{aligned} m^{\varepsilon -}(t,x) &= \overline{m^{\varepsilon}}^{-}(t,x) + \widetilde{m^{\varepsilon}}^{-}\left(t, \frac{-x}{\varepsilon}\right), \\ M^{\varepsilon -}(t,x) &= \overline{M^{\varepsilon}}^{-}(t,x) + \widetilde{M^{\varepsilon}}^{-}\left(t, \frac{-x}{\varepsilon}\right). \end{aligned}$$

Then, the first idea is to make the following ansatz WKB for $U = \overline{m^{\varepsilon}}^{-}$, $\overline{M^{\varepsilon}}^{-}$, $m^{\varepsilon +}$ or $M^{\varepsilon +}$, and $\widetilde{U} = \widetilde{m^{\varepsilon}}^{-}$ or $\widetilde{M^{\varepsilon}}^{-}$: we expand U and $\widetilde{U}$ as a sum of powers of ε with profiles that are independent of ε, in the form:

$$\begin{aligned} U(t,x) &= U_0(t,x) + \varepsilon U_1(t,x) + \varepsilon^2 U_2(t,x) + \dots \\ \widetilde{U}(t,z) &= \widetilde{U}_0(t,z) + \varepsilon \widetilde{U}_1(t,z) + \varepsilon^2 \widetilde{U}_2(t,z) + \dots \end{aligned} \tag{6.5.1}$$

In these ansatz, we assume that the profiles $\widetilde{U}_j(t,z)$ together with all their derivatives go to 0 when $z \to +\infty$: they describe a boundary layer at the right end of the thick ferromagnetic layer (near the interface $x = 0$). To simplify the notations we let $m_j^- = \overline{m}_j^- + \widetilde{m}_j^-$ and $M_j^- = \overline{M}_j^- + \widetilde{M}_j^-$ for all j.

Our aim is then to obtain the equations fulfilled by the first orders profiles. To do this, we plug the asymptotic expansion into the equations (6.2.12)-(6.2.13)-(6.2.14)-(6.2.15), and identify powers of ε. Each equation can then be rewritten in the following form

$$\sum_{j \geq -2} \varepsilon^j P^j(\overline{m}_k^{\pm}, \widetilde{m}_k^{\pm}, \overline{M}_k^{\pm}, \widetilde{M}_k^{\pm}) = 0,$$

where P^j's are operators acting on some profiles $\overline{m}_k^{\pm}, \widetilde{m}_k^{\pm}, \overline{M}_k^{\pm}, \widetilde{M}_k^{\pm}$ (with several indices k). From this, as usual, we now identify

$$P^j(\overline{m}_k^{\pm}, \widetilde{m}_k^{\pm}, \overline{M}_k^{\pm}, \widetilde{M}_k^{\pm}) = 0 \quad \text{for all } j \geq -2.$$

In order to separate the boundary layer profiles $\widetilde{U}_j$ from the other part $\overline{U}_j$, we take the limit $z \to +\infty$ in the previous equations. Thus, we first obtain equations on $\overline{U}_j$ profiles, and we then make the difference between the first equations and the last ones to obtain equations on the boundary layer part.

Finally, we plug the ansatz into the boundary and interface conditions and into the condition $|\vec{M}^{\pm}|^2 = 1$, and we again identify powers of ε. For instance, we get $|M_0|^2 + 2\varepsilon M_0 \cdot M_1 + \dots = 1$, from which we deduce $|M_0|^2 = 1$, $M_0 \cdot M_1 = 0$ and so on.

To calculate the first profiles, and obtain an asymptotic model, we need the equations satisfied at orders ε^{-2}, ε^{-1}, and ε^{0}.

Equations in the thick ferromagnet

At order ε^{-2} in the two equations in the thick material, we first obtain the following equations. First, $\overline{m_0^-} \times \overline{M_0^-} = 0$, so there exists a profile a_0 such that

$$\overline{m_0^-}(t,x) = a_0(t,x)\overline{M_0^-}(t,x). \tag{6.5.2}$$

Second, we get

$$M_0^- \times \partial_z^2 \widetilde{M_0^-} = 0. \tag{6.5.3}$$

Morerover, since $|M_0^-|^2 = 1$, we have $M_0^- \cdot \partial_z \widetilde{M_0^-} = 0$. Using this property and (6.5.3), we write $\partial_z^2 \widetilde{M_0^-} = \big(\partial_z^2 \widetilde{M_0^-} \cdot M_0^-\big) M_0^-$. We then multiply by $\partial_z \widetilde{M_0^-}$ and we obtain $\partial_z^2 \widetilde{M_0^-} \cdot \partial_z \widetilde{M_0^-} = 0$. Now, we integrate twice and we use that $\widetilde{M_0^-}$, $\partial_z \widetilde{M_0^-} \to 0$ as $z \to \infty$, to conclude that $\widetilde{M_0^-} = 0$.
Third, we obtain the equation fulfilled by the boundary layer profile $\widetilde{m_0^-}$

$$-\partial_z^2 \widetilde{m_0^-} + \widetilde{m_0^-} \times \overline{M_0^-} = 0. \tag{6.5.4}$$

Since, $\overline{M_0^-}$ does not depend on z, we can explicitly solve this equation (as it has been done before). The property that we will use in the sequel on $\widetilde{m_0^-}$, is that this equation allows us to write a Dirichlet to Neumann relation on $\widetilde{m_0^-}$

$$\partial_z \widetilde{m_0^-}(t,0^-) = D\widetilde{m_0^-}(t,0^-), \text{ where } D \text{ is a positive matrix.} \tag{6.5.5}$$

At order ε^{-1}, we then obtain

$$\overline{m_0^-} \times \overline{M_1^-} + \overline{m_1^-} \times \overline{M_0^-} = 0, \tag{6.5.6}$$

and

$$M_0^- \times \partial_z^2 \widetilde{M_1^-} = 0. \tag{6.5.7}$$

As above, we combine (6.5.7) with $M_0^- \cdot M_1^- = 0$ and it gives $\widetilde{M_1^-} = 0$.
We also have

$$-\partial_z^2 \widetilde{m_1^-} + \widetilde{m_1^-} \times \overline{M_0^-} + \widetilde{m_0^-} \times \overline{M_1^-} = 0. \tag{6.5.8}$$

At order ε^{0}, we get

$$-\partial_x^2 \overline{m_0^-} + \overline{m_0^-} \times \overline{M_2^-} + \overline{m_1^-} \times \overline{M_1^-} + \overline{m_2^-} \times \overline{M_0^-} + \overline{m_0^-} = 0, \tag{6.5.9}$$

which gives, taking the scalar product with $\overline{M_0^-}$, and using (6.5.6)

$$-\partial_x^2 a_0 + (1 + |\partial_x \overline{M_0^-}|^2) a_0 = 0. \tag{6.5.10}$$

Here again, we used that the norm of the magnetization $\overline{M_0^-}$ is preserved: $|\overline{M_0^-}|^2 = 1$ so that $\overline{M_0^-} \cdot \partial_x \overline{M_0^-} = 0$ and $\overline{M_0^-} \cdot \partial_x^2 \overline{M_0^-} = -|\partial_x \overline{M_0^-}|^2$.

We then write the equation on $\overline{M_0^-}$. Using (6.5.6), we get the non coupled LL equation satisfied by $\overline{M_0^-}$

$$\partial_t \overline{M_0^-} = -\overline{M_0^-} \times \big(c\overline{M_0^-} \cdot u^- u^- + \nu \partial_x^2 \overline{M_0^-}\big) + \alpha \overline{M_0^-} \times \partial_t \overline{M_0^-}. \tag{6.5.11}$$

Equations in the thin ferromagnet

At order ε^{-2}, we first obtain the following equations

$$-\partial_x^2 m_0^+ + m_0^+ \times M_0^+ = 0, \tag{6.5.12}$$

and

$$M_0^+ \times \partial_x^2 M_0^+ = 0. \tag{6.5.13}$$

Combined with $|M_0^+|^2 = 1$ and the Neumann conditions (6.5.22), equation (6.5.13) gives that $M_0^+(t,x)$ is independent of the space variable x.

At order ε^{-1}, we then obtain

$$-\partial_x^2 m_1^+ + m_1^+ \times M_0^+ + m_0^+ \times M_1^+ = 0, \tag{6.5.14}$$

$$-M_0^+ \times (\nu \partial_x^2 M_1^+ + m_0^+) = 0. \tag{6.5.15}$$

At order ε^0, we get

$$\partial_t M_0^+ = -M_0^+ \times \big(c(M_0^+ \cdot u^+)u^+ + \nu \partial_x^2 M_2^+\big) - (M_0^+ \times m_1^+ + M_1^+ \times m_0^+) + \alpha M_0^+ \times \partial_t M_0^+.$$

Since M_0^+ is independent of x, an integration over $x \in [0,1]$ of the previous equation gives

$$\begin{aligned} \partial_t M_0^+ \quad = \quad & -M_0^+ \times \big(c(M_0^+ \cdot u^+)u^+\big) + \alpha M_0^+ \times \partial_t M_0^+ \\ & -M_0^+ \times \big(\nu \partial_x M_2^+(t,1) - \nu \partial_x M_2^+(t,0)\big) + \big(\partial_x m_1^+(t,1) - \partial_x m^+ 1(t,0)\big). \end{aligned}$$

Boundary and interface conditions

We will use (or we have already used) the following conditions with indices $i = 0$ and $i = 1$:

$$\overline{m}_0^- = m^{\varepsilon -}(-1) \text{ independent of} \varepsilon, \quad \overline{m}_1^-(-1) = 0, \tag{6.5.16}$$

$$\partial_x m_i^+(1) = 0, \tag{6.5.17}$$

$$\overline{m}_i^-(t, x = 0^-) + \widetilde{m}_i^-(t, x = 0^-, z = 0) = m_i^+(t, x = 0^+), \tag{6.5.18}$$

$$-\partial_z \widetilde{m}_i^-(t, 0^-, z = 0^+) + \partial_x \overline{m}_{i-1}^-(t, 0^-) = \partial_x m_i^+(t, 0^+), \tag{6.5.19}$$

$$\partial_x \overline{M}_i^-(-1) = 0, \tag{6.5.20}$$

$$-\partial_z \widetilde{M}_i^-(t, 0^-, 0^+) + \partial_x \overline{M}_{i-1}^-(t, 0^-) = 0, \tag{6.5.21}$$

$$\partial_x M_i^+(t, 0^-) = \partial_x M_i^+(t, 1) = 0. \tag{6.5.22}$$

Determination of the spin density

We first use the equation on m_0^+ and the Dirichlet to Neumann equation (6.5.5) to write the following energy estimate

$$\int_0^1 |\partial_x m_0^+(t,x)|^2 dx + D\widetilde{m}_0^-(t, 0^-) \cdot \widetilde{m}_0^-(t, 0^-) = 0.$$

Since D is a positive matrix, we deduce the two following properties

- $\widetilde{m}_0^-(t,0^-)=0$, so that $\widetilde{m}_0^-(t,z)=0$ for all t,z (see equation 6.5.4),
- $\partial_x m_0^+=0$, so that m_0^+ is independent of x. Using the transmission condition at $x=0$ (6.5.18), and we write $m_0^+(t)=m_0^-(t,0^-)=a_0(t,0^-)\overline{M}_0^-(t,0^-)$. We plug this into the equation on m_0^+, and we get $a_0(t,0^-)\overline{M}_0^-(t,0^-)\times M_0^+(t)=0$. Hence,

$$\textbf{if } \overline{M}_0^-(t,0^-)\times M_0^+(t)\neq 0, \text{then } a_0(t,0^-)=0. \tag{6.5.23}$$

From this result, we can deduce all the spin density profiles at order ε^0, while the condition $\overline{M}_0^-(t,0^-)\times M_0^+(t)\neq 0$ is satisfied:

- there is no boundary layer at order ε^0 : $\widetilde{m}_0^-(t,z)=0$,
- $\overline{m}_0^-$ is polarized along $\overline{M}_0^-$: $\overline{m}_0^-=a_0\overline{M}_0^-$ where a_0 is entirely determined by the equation

$$\begin{cases} -\partial_x^2 a_0+(1+|\partial_x\overline{M}_0^-|^2)a_0=0, \quad t>0,\ x\in[-1,0], \\ a_0(t,-1) \text{ given}, \\ a_0(t,0)=0. \end{cases} \tag{6.5.24}$$

- the spin density in F^+ satisfies $m_0^+=0$.

Determination of M_0^+

To obtain the equation fulfilled by $M_0^+(t)$ we also need to compute the profile m_1^+ (at least its values at the boundaries). As previously, it can be done using the equations fulfilled by the three profiles $\overline{m}_1^-$, $\widetilde{m}_1^-$ and m_1^+ and the transmission and boundary conditions that link them.

After these calculations, we get the equation satisfied by the magnetization M_0^+. In order to write it, we need the following notations. We let $A+iB=e^{-i\pi/4}\tanh e^{-i\pi/4}$ and

$$p=\frac{A^2+B^2}{A^2+B^2+\sqrt{2}A}\approx 0.6810, \qquad q=\frac{-\sqrt{2}B}{A^2+B^2+\sqrt{2}A}\approx 0.9843.$$

Let also $\gamma(t,x)=\overline{M}_0^-(t,0^-)\cdot M_0^+(t,x)$. The vector field M_0^+ then fulfills

$$\partial_t M_0^+=-M_0^+\times\left(CM_0^+\cdot u^+u^+ +\frac{\partial_x a_0(t,0^-)}{1-\gamma^2}\left(-(p\gamma+q)\overline{M}_0^- +\overline{M}_0^-\times M_0^+\right)\right) \quad +\alpha M_0^+\times\partial_t M_0^+.$$

Since $|M_0^+(t)|^2=1$ for all t, as it is usual when dealing with LL equations, this last equation can be rewritten as

$$\begin{aligned} &(1+\alpha^2)\partial_t M_0^+ \\ &=-M_0^+\times\left[CM_0^+\cdot u^+u^+-\partial_x a_0(t,0)\frac{p\gamma(t)+q-\alpha}{1-\gamma^2(t)}\overline{M}_0^-(t,0)\right] \\ &\quad -M_0^+\times\left[M_0^+\times\left(\alpha CM_0^+\cdot u^+u^+-\partial_x a_0(t,0)\frac{\alpha p\gamma(t)+\alpha q+1}{1-\gamma^2(t)}\overline{M}_0^-(t,0)\right)\right], \end{aligned} \tag{6.5.25}$$

where a_0 satisfies (6.5.24).

Let us explain how to see on this limit equation that the magnetization M_0^+ will be switched. First, let us mention that when there is no spin-current ($a_0(t,-1)=0$ which implies $a_0(t,x)=0$ for all (t,x)), the magnetization M_0^+ satisfies a non coupled Landau- Lifshitz equation, and it classically converges to the nearest stable equilibrium state ($\pm u^+$). On the contrary, when $a_0(t,-1)=f(t)\neq 0$, we can study the behavior and the switching of M_0^+ thanks to the quantity $\gamma(t)=\overline{M}_0^-(t,0)\cdot M_0^+(t)$, that is a solution of

$$\begin{aligned}
&(1+\alpha^2)\partial_t\gamma(t)\\
&=-M_0^+\times\left(CM_0^+\cdot u^+u^+ +\alpha M_0^+\times\left(CM_0^+\cdot u^+u^+\right)\right)\cdot\overline{M}_0^-(t,0)+M_0^+\cdot\partial_t\overline{M}_0^-(t,0)\\
&\quad +M_0^+\times\left(M_0^+\times\left(\partial_x a_0(t,0)\frac{\alpha p\gamma(t)+\alpha q+1}{1-\gamma^2(t)}\overline{M}_0^-(t,0)\right)\right)\cdot\overline{M}_0^-(t,0)\\
&=F(\overline{M}_0^-,M_0^+)-\partial_x a_0(t,0)(\alpha p\gamma+\alpha q+1),
\end{aligned}$$

where $F(\overline{M}_0^-,M_0^+)$ is bounded. In this equation, $\partial_x a_0(t,0)$ writes $-f(t)u(t)$ where $u(t)$ is bounded, greater than a strictly positive constant and only depends on $\overline{M}_0^-$. Thus, for $a_0(t,0)=f(t)$ large enough, $\gamma(t)$ converges in finite time to ±1, which means that M_0^+ converges to $\pm\overline{M}_0^-$. Here again, we see that our limit model is valid only up to convergence, when M_0^+ and $\overline{M}_0^-$ are not collinear. Indeed, this limit model has a singularity when $\gamma(t)$ converges to ±1.

6.5.2 Comparison between the full system and the first asymptotic expansion

In this part, we compare the asymptotic expansion obtained in Section 6.5.1 (when M^+ and M^- are never collinear) with the general system. All the following calculations are done with $\varepsilon=1.10^{-2}$. The errors are calculated in the $\mathbb{L}^2$ norm with respect to x at each instant.

Discretization of the limit system

We will not give many details on the discretization of the limit system, since we use a simple finite difference method. Let us just say that for the LL equation satisfied by M_0^+, we use the scheme proposed by Joly and Vacus [4]. This is a Crank-Nicholson scheme that has the nice property to keep the norm of the magnetization constant during time evolution, as the LL equation does. It is written as follows, $\vec{M}$ is approximated by $\frac{\vec{M}^{n+1}+\vec{M}^n}{2}$:

$$\frac{\vec{M}^{n+1}-\vec{M}^n}{\Delta t}=-\frac{\vec{M}^n+\vec{M}^{n+1}}{2}\times H_e(\vec{M}^{n+1})+\alpha\frac{\vec{M}^n+\vec{M}^{n+1}}{2}\times\frac{\vec{M}^{n+1}-\vec{M}^n}{\Delta t},\tag{6.5.26}$$

where H_e is the total effective field.

Numerical comparison

As we expected, our limit model is a good approximation up to order $O(\varepsilon)$ only up to the magnetization switching in the thin material. The three following figures show the L_x^2 error between

the solutions of the full system and the solutions of the limit model. When the magnetization is switched in the thin material, the errors between the magnetization of the full system $M^{\varepsilon,+}$ and M_0^+ and between $m^{\varepsilon,-}$ and m_0^- grow up to the order 0.1 whereas the small parameter ε equals 10^{-2}.

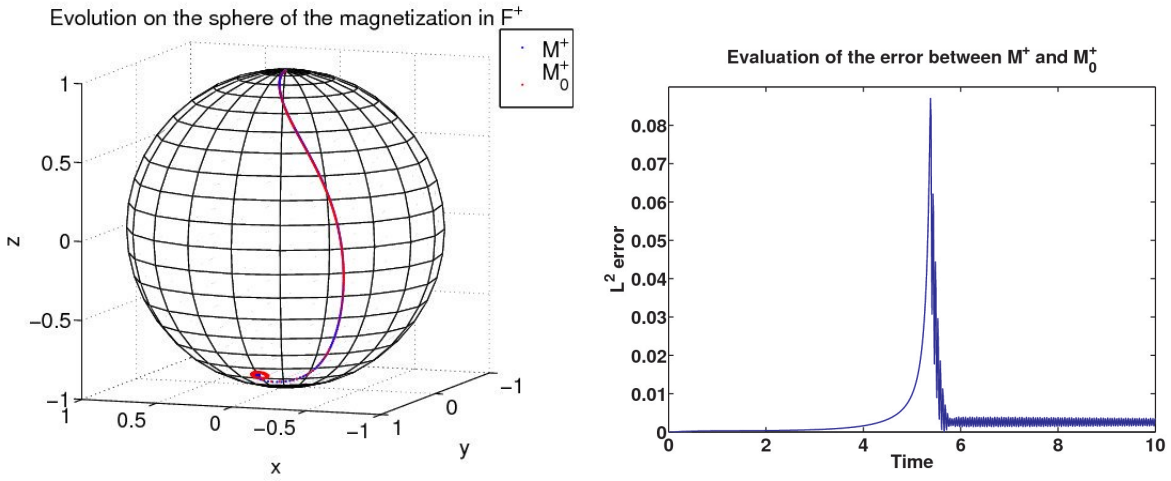

Figure 6.8: Comparison of $\vec{M}^+$ and $\vec{M}_0^+$.

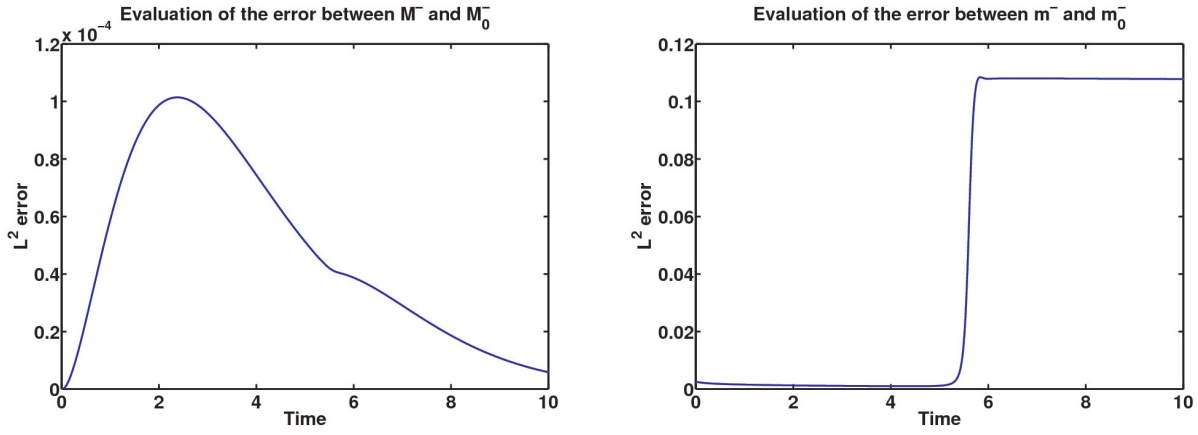

Figure 6.9: Comparison of $\vec{M}^-$ and $\vec{\overline{M}_0^-}$ (left), comparison of $\vec{m}^-$ and $\vec{\overline{m}_0^-}$ (right).

The problems observed on the magnetization M^+ are linked to the variations of the spin density $\overline{m}_0^-$ (the asymptotic expansion gave $m_0^+ = 0$) and we find when M_0^+ goes to $\overline{M}_0^-$ that the already big $\mathbb{L}^2$-error on the spin density increases even more and never decreases again (Fig.6.9). This error comes from the behavior of m^-: in the full system, the norm of m^- increases brutally when the magnetization M^+ and M^-become collinear (Fig.6.10) whereas in the asymptotic model the norm of the spin density $\overline{m}_0^-$ does not vary.

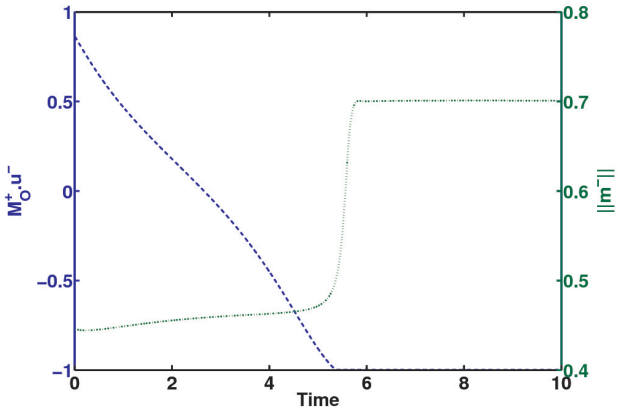

Figure 6.10: $\vec{M}^+.\vec{u}^-$ (blue) and $\|\vec{m}^-\|$ (green).

6.5.3 A modified asymptotic expansion

The previous asymptotic model is not satisfying from two points of view. First, it is valid only up to convergence. Second, due to the behavior of the solution of the limit ordinary differential equation satisfied by the magnetization M_0^+, the limit model is not reversible, in the sense that if we change the sign of the injected current the magnetization will not come back to the upper position.

In order to obtain a limit model with a bigger domain of validity, we use a slightly different approach, that we could call a Chapman-Enskog approach. The idea is of keeping a dependence on the parameter ε for the profiles in our expansion to better track the change of behavior when M_0^+ and $\overline{M}_0^-$ are almost collinear.

Our approach could be described by two (equivalent) ways. We look for an approximate model that is a good approximation of the full model up to order $O(\varepsilon)$, when $\varepsilon \to 0$. The idea is of putting together the profiles with indices 0 and 1 obtained previously. One possible approach to do this is to write the equations satisfied by $m_0 + \varepsilon m_1$, and so on ..., and to truncate them at order $O(\varepsilon)$. Or, equivalently, we can repeat the previous procedure with an Ansatz containing only even powers of ε, and keep the orders ε^{2k} and ε^{2k-1} together to obtain the equations fulfilled by the profiles (now depending on ε). In the sequel, we present our results using the second approach.

So, we look for a formal limit model approximating the equations up to first order. As before, since we expect the formation of a boundary layer in the thick ferromagnet near $x = 0^-$, we make the following ansatz:

$$m^{\varepsilon-}(t,x) = \overline{m}^{\varepsilon-}(t,x) + \widetilde{m}^{\varepsilon-}\left(t, \frac{-x}{\varepsilon}\right), \quad M^{\varepsilon-}(t,x) = \overline{M}^{\varepsilon-}(t,x) + \widetilde{M}^{\varepsilon-}\left(t, \frac{-x}{\varepsilon}\right).$$

With these notations, the boundary conditions write

$$\begin{aligned}
&\overline{m}^{\varepsilon-}(t,-1) = m^{\varepsilon-}(t,-1) \text{ (given, independent of } \varepsilon),\\
&\partial_x m^{\varepsilon+}(t,1) = 0,\\
&\\
&\partial_x \overline{M}^{\varepsilon-}(t,-1) = 0, \partial_x \overline{M}^{\varepsilon-}(t,0) + \frac{1}{\varepsilon}\partial_z \widetilde{M}^{\varepsilon-}(t,0) = 0,\\
&\partial_x M^{\varepsilon+}(t,0) = \partial_x M^{\varepsilon+}(t,1) = 0,
\end{aligned}$$

and the transmission conditions now write

$$\begin{aligned}
&\overline{m}^{\varepsilon-}(t,0) + \widetilde{m}^{\varepsilon-}(t,0) = m^{\varepsilon+}(t,0),\\
&-\frac{1}{\varepsilon}\partial_z \widetilde{m}^{\varepsilon-}(t,0) + \partial_x \overline{m}^{\varepsilon-}(t,0) = \frac{1}{\varepsilon}\partial_x m^{\varepsilon+}(t,0).
\end{aligned}$$

Equations in the thick ferromagnet

By taking the limit as z goes to $+\infty$ in the equation in the thick ferromagnet we obtain

$$\varepsilon^2 \partial_t \overline{m}^{\varepsilon-} - \partial_x^2 \overline{m}^{\varepsilon-} + \frac{\overline{m}^{\varepsilon-} \times \overline{M}^{\varepsilon-}}{\varepsilon^2} + \overline{m}^{\varepsilon-} = 0, \tag{6.5.27}$$

$$\partial_t \overline{M}^{\varepsilon-} = -\overline{M}^{\varepsilon-} \times \left(C(\overline{M}^{\varepsilon-} \cdot u^-)u^- + \frac{\overline{m}^{\varepsilon-}}{\varepsilon} + \nu \partial_x^2 \overline{M}^{\varepsilon-} \right) + \alpha \overline{M}^{\varepsilon-} \times \partial_t \overline{M}^{\varepsilon-}. \tag{6.5.28}$$

To obtain an approximate solution exact up to order 1 in ε we perform an asymptotic expansion of the equation in ε^2 by keeping the orders ε^{2k} and ε^{2k-1} together for $k \geq -1$. Let us denote by $\overline{m}_0^{\varepsilon-}$, $\overline{M}_0^{\varepsilon-}$, ..., the first profiles we are looking for. In this way we do not have to perform further approximations on the Landau-Lifshitz equation: $\overline{M}_0^{\varepsilon-}$ satisfies (6.5.28).

Then, thanks to this policy the equation on $\overline{m}^{\varepsilon-}$ gives

$$\overline{m}_0^{\varepsilon-} \times \overline{M}_0^{\varepsilon-} = 0 \quad \text{and} \quad -\partial_x^2 \overline{m}_0^{\varepsilon-} + \overline{m}_0^{\varepsilon-} = 0.$$

In the same way, we now obtain equations on $\widetilde{M}_0^{\varepsilon-}$ and $\widetilde{m}_0^{\varepsilon-}$: keeping the terms of order -2 and -3 in ε we have

$$\begin{aligned}
&{M^{\varepsilon}}_0^- \times \partial_z^2 {M^{\varepsilon}}_0^- = (\overline{M}_0^{\varepsilon-} + \widetilde{M}_0^{\varepsilon-}) \times \partial_z^2 \widetilde{M}_0^{\varepsilon-} = 0,\\
&-\partial_z^2 \widetilde{m}_0^{\varepsilon-} + \widetilde{m}_0^{\varepsilon-} \times (\overline{M}_0^{\varepsilon-} + \widetilde{M}_0^{\varepsilon-}) = 0.
\end{aligned}$$

Since $M^{\varepsilon-}$ is a solution to the Landau-Lifshitz equation, $|M^{\varepsilon-}| = 1$ which implies that $\partial_z^2 {M^{\varepsilon}}_0^- = \partial_z^2 \widetilde{M}_0^{\varepsilon-} = 0$ and then $\widetilde{M}_0^{\varepsilon-} = 0$.

This implies that $\overline{M}_0^{\varepsilon-}$ fulfills the classical Landau-Lifshitz equation in $[-1,0]$ with Neumann boundary conditions in $\{-1,0\}$:

$$\begin{cases}
\partial_t \overline{M}_0^{\varepsilon-} = -\overline{M}_0^{\varepsilon-} \times \left(C(\overline{M}_0^{\varepsilon-} \cdot u^-)u^- + \nu \partial_x^2 \overline{M}_0^{\varepsilon-} \right) + \alpha \overline{M}_0^{\varepsilon-} \times \partial_t \overline{M}_0^{\varepsilon-},\\
\overline{M}_0^{\varepsilon-}(0,x) \text{ given},\\
\partial_x \overline{M}_0^{\varepsilon-}(t,-1) = \partial_x \overline{M}_0^{\varepsilon-}(t,0) = 0.
\end{cases}$$

We also have the existence of a function $a^- : \mathbb{R}_t^+ \times [-1,0] \to \mathbb{R}$ such that

$$\overline{m}_0^{\varepsilon -}(t,x) = a^-(t,x)\overline{M}_0^{\varepsilon -}(t,x).$$

By taking the scalar product with $\overline{M}_0^{\varepsilon -}$ of the equation on $\overline{m}_0^{\varepsilon -}$ we obtain the following equation on a^-

$$\begin{aligned} &-\partial_x^2 a^- + (1 + |\partial_x \overline{M}_0^{\varepsilon -}|^2)a^- = 0, \quad x \in [-1,0], \\ &a^-(-1) = m^{\varepsilon -}(t,-1) \cdot \overline{M}_0^{\varepsilon -}(t,-1) \text{ given.} \end{aligned}$$

The equation on $\widetilde{m}_0^{\varepsilon -}$ becomes

$$-\partial_z^2 \widetilde{m}_0^{\varepsilon -} + \widetilde{m}_0^{\varepsilon -} \times \overline{M}_0^{\varepsilon -} = 0.$$

Solving this equation, we get

$$\widetilde{m}_0^{\varepsilon -}(t,z) = \beta_1(z)\overline{M}_0^{\varepsilon -}(t,x) \times \left(\widetilde{m}_0^{\varepsilon -}(t,0) \times \overline{M}_0^{\varepsilon -}(t,x)\right) - \beta_2(z)\widetilde{m}_0^{\varepsilon -}(t,0) \times \overline{M}_0^{\varepsilon -}(t,x),$$

where $(\beta_1 + i\beta_2)(z) = e^{-\sqrt{-i}z}$ with $\sqrt{-i} = e^{-i\pi/4}$.

Equations in the thin ferromagnet

We study in the same way the equations in the thin ferromagnet by performing the same asymptotic expansion. We get at orders ε^{-3} and ε^{-2}:

$$\begin{aligned} &M^{\varepsilon +}_0 \times \partial_x^2 M^{\varepsilon +}_0 = 0, \\ &-\partial_x^2 m^{\varepsilon +}_0 + m^{\varepsilon +}_0 \times M^{\varepsilon +}_0 = 0. \end{aligned}$$

As before, this implies that $M^{\varepsilon +}_0$ is independent from x and we have an explicit formula for $m^{\varepsilon +}_0$:

$$m^{\varepsilon +}_0(x) = (m^{\varepsilon +}_0(0) \cdot M^{\varepsilon +}_0)M^{\varepsilon +}_0 + \beta_1'(x)m^{\varepsilon +}_0(0) \times M^{\varepsilon +}_0 + \beta_2'(x)M^{\varepsilon +}_0 \times \left(m^{\varepsilon +}_0(0) \times M^{\varepsilon +}_0\right),$$

where $(\beta_1' + i\beta_2')(x) = i\dfrac{\cosh(\sqrt{-i}(x-1))}{\cosh(\sqrt{-i})}$.

At orders ε^{-1} and ε^0 we obtain

$$\partial_t M^{\varepsilon +}_0 = -M^{\varepsilon +}_0 \times \left(C(M^{\varepsilon +}_0 \cdot u^+)u^+ + \frac{m^{\varepsilon +}_0}{\varepsilon}\right) + \alpha M^{\varepsilon +}_0 \times \partial_t M^{\varepsilon +}_0.$$

Since $M^{\varepsilon +}_0$ does not depend on $x \in [0,1]$, we perform an integration over $x \in (0,1)$:

$$\partial_t M^{\varepsilon +}_0 = -M^{\varepsilon +}_0 \times \left(C(M^{\varepsilon +}_0 \cdot u^+)u^+ + \frac{1}{\varepsilon}\int_0^1 m^{\varepsilon +}_0(x)\,dx\right) + \alpha M^{\varepsilon +}_0 \times \partial_t M^{\varepsilon +}_0.$$

Determination of $m_0^{\varepsilon+}(x=0)$

We now use the transmission conditions at $x=0$. Here is the only difference with the first asymptotic model we obtained. They can be written now as

$$\begin{aligned}&\widetilde{m}_0^{\varepsilon-}(t,0)+a^-(t,0)\overline{M}_0^{\varepsilon-}(t,0)=m_0^{\varepsilon+}(t,0)\\&-\frac{1}{\varepsilon}\partial_z\widetilde{m}_0^{\varepsilon-}(t,0)+\partial_x a^-(t,0)\overline{M}_0^{\varepsilon-}(t,0)=\frac{1}{\varepsilon}\partial_x m_0^{\varepsilon+}(t,0).\end{aligned}$$

Thanks to the previous results we obtained on $\widetilde{m}_0^{\varepsilon-}$ and $m_0^{\varepsilon+}$, we get

$$\begin{aligned}m_0^{\varepsilon+}(t,0)=\;&\frac{\frac{\sqrt{2}}{2}a^-(t,0)-\varepsilon\partial_x a^-(t,0)}{a^2+b^2+a\sqrt{2}+1-b\gamma(t,0)\sqrt{2}+a\frac{\sqrt{2}}{2}(1-\gamma(t,0)^2)}\times\\&\Big[\big(-b+\gamma(t,0)(a^2\sqrt{2}+b^2\sqrt{2}+a)\big)\,M_0^{\varepsilon+}(t,0)\\&+\Big(-b\gamma(t,0)+a+\sqrt{2}\Big)\,\overline{M}_0^{\varepsilon-}(t,0)+(a\gamma(t,0)+b)\,\overline{M}_0^{\varepsilon-}(t,0)\times M_0^{\varepsilon+}(t,0)\Big],\end{aligned}$$

with $a+ib=\sqrt{-i}\tanh\sqrt{-i}$ and $\gamma(t,x)=M_0^{\varepsilon+}(t,x)\cdot\overline{M}^{\varepsilon-}(t,0)$.

Determination of $M_0^{\varepsilon+}$ and Dirichlet to Neumann condition on a^-

We finally obtain an ordinary differential equation that rules the behavior of $M_0^{\varepsilon+}$:

$$\begin{aligned}\partial_t M_0^{\varepsilon+}=\;&-M_0^{\varepsilon+}\times\Big[C(M_0^{\varepsilon+}\cdot u^+)u^+ + D\Big((a^2+b^2)\gamma-b\sqrt{2}\Big)\,\overline{M}_0^{\varepsilon-}(t,0)\\&-D(a^2+b^2+a\sqrt{2})\overline{M}_0^{\varepsilon-}(t,0)\times M^{\varepsilon+}\Big]+\alpha M_0^{\varepsilon+}\times\partial_t M_0^{\varepsilon+},\end{aligned}$$

with

$$D=\frac{1}{\varepsilon}\frac{\frac{\sqrt{2}}{2}a^-(t,0)-\varepsilon\partial_x a^-(t,0)}{a^2+b^2+a\sqrt{2}+1-b\gamma\sqrt{2}+a\frac{\sqrt{2}}{2}(1-\gamma^2)}.$$

We now only need to determine a condition on $a^-(t,0)$ and $\partial_x a^-(t,0)$ to solve the problem. We compute the scalar product of the transmission condition with $\overline{M}_0^{\varepsilon-}(t,0)$ and we obtain $a^-(t,0)=m_0^{\varepsilon+}(t,0)\cdot\overline{M}_0^{\varepsilon-}(t,0)$ which gives the following Dirichlet-to-Neumann condition:

$$\partial_x a^-(t,0)=-\frac{a^-(t,0)}{\varepsilon}\frac{\big(a^2+b^2+a\sqrt{2}\big)\big(1-\gamma(t)^2\big)}{\big((a^2+b^2)\sqrt{2}+a\big)\gamma(t)^2-2b\gamma(t)+a+\sqrt{2}}.$$

As one can easily see, this model is a generalization of the model we obtained thanks to the first asymptotic expansion. If we perform the extra assumption that $M_0^{\varepsilon+}$ and $M_0^{\varepsilon-}$ are never collinear we come down to the previous asymptotic model.

6.5.4 Comparison between the full system and the modified asymptotic model

Numerical comparison

In this part, we compare the modified asymptotic expansion obtained in Section 6.5.3 with the general system. We use the same parameters as in the previous simulations ($\varepsilon = 1.10^{-2}$). With this new asymptotic model we obtain a better qualitative behavior of the magnetization $M_0^{\varepsilon+}$ in the thin ferromagnet F^+ (no more spinning around the expected limit) and the $\mathbb{L}^2$-error always remains (even in the worst case, when $M_0^{\varepsilon-}$ and $M_0^{\varepsilon+}$ line up) of order at most ε^2 (Fig.6.11). Moreover, Fig.6.12 shows that this better behavior of the model also appears on the spin density $m_0^{\varepsilon-}$ with a better $\mathbb{L}^2$ error and a better qualitative behavior of $m_0^{\varepsilon-}$.

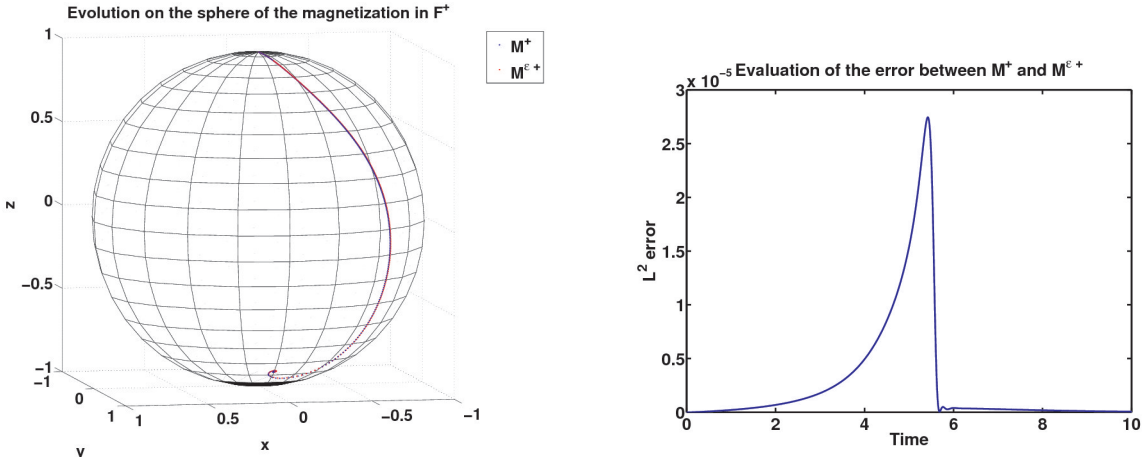

Figure 6.11: Comparison of $\vec{M}^+$ and $\vec{M}_0^{\varepsilon+}$.

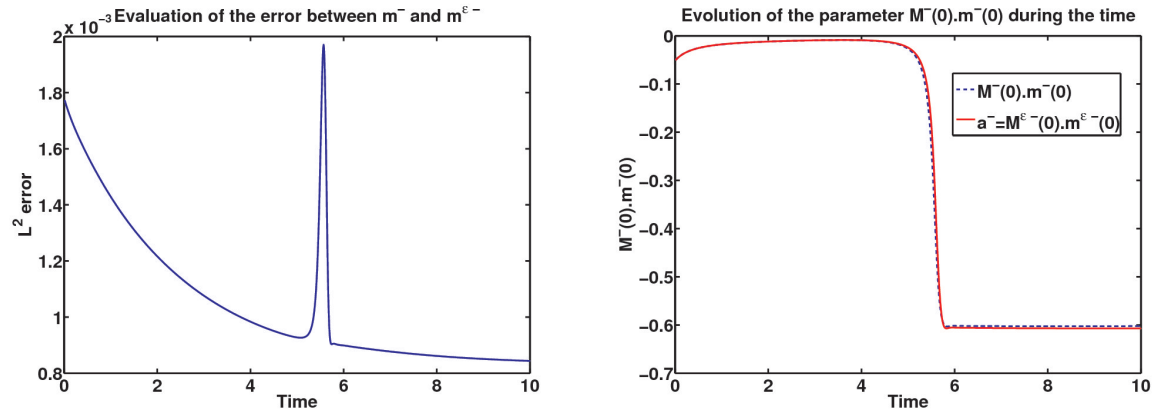

Figure 6.12: Comparisons of $\vec{m}^-$ and $\overline{m}^{\varepsilon-}$.

Computational time

To compute the general problem, we have to solve a large linear system at each time iteration and we have to take a refined space step in regions with an asymptotic behavior (specially when ε is small). Consequently, the computation time is important. With the asymptotic expansion, we only solve the first order. It saves a considerable amount of time. For example, on the same machine, the simulation of the general problem with $\varepsilon = 1.10^{-2}$ takes 1 hour 23 minutes whereas the first order of the asymptotic expansion takes 19 seconds. Therefore, the asymptotic expansion is a very interesting tool to treat cases when ε is really small.

6.6 Conclusion

In this chapter, we studied the model of magnetization reversal proposed by [9], in a one dimensional framework. We emphasized the different time and space scales that exist in the model and we constructed a numerical scheme that is appropriate to treat these scales. This scheme allowed us to recover the results observed in the experiments lead by the physicists on the magnetic switching thanks to a spin current.

The second part of our work consisted in the derivation of an asymptotic model as $\varepsilon \to 0$. We ended up with a limit model that is very easy to handle numerically and is good approximation of the original model (up to $O(\varepsilon^2)$). It could be a good alternative to the original model when dealing with very small values of ε.

As we mentioned in the introduction, spin transfer appears to be a turning point in spintronics and is the subject of an extensive research for applications. The spin transfer torque seems to be involved in several different phenomena: the magnetization switching, that we studied here, magnetization excitations (or magnetic oscillators), or domain wall motion. The very fast oscillations we pointed out in this chapter could appear to be a key point in the magnetic oscillators applications, and the study of that phenomenon, both theoretically and numerically, will be our next target.

Bibliography

[1] N. Ben Abdallah, E. Fouassier, C. Jourdana, and D. Sanchez. On a model of magnetization switching driven by a spin current: modelization and numerical simulations. Preprint IMATI-CNR 17PV11/13/0.

[2] L. Berger. Emission of spin waves by a magnetic multilayer traversed by a current. *Phys. Rev. B*, 54(13):9353–9358, 1996.

[3] C. J. García-Cervera and X.-P. Wang. Spin-polarized currents in ferromagnetic multilayers. *J. Comput. Phys.*, 224(2):699–711, 2007.

[4] P. Joly and O. Vacus. Mathematical and numerical studies of nonlinear ferromagnetic materials. *M2AN Math. Model. Numer. Anal.*, 33(3):593–626, 1999.

[5] A. Shpiro, P. M. Levy, and S. Zhang. Self-consistent treatment of nonequilibrium spin torques in magnetic multilayers. *Phys. Rev. B*, 67(10):104430, 2003.

[6] J.C. Slonczewski. Current-driven excitation of magnetic multilayers. *Journal of Magnetism and Magnetic Materials*, 159:L1–L7, 1996.

[7] M. D. Stiles and A. Zangwill. Anatomy of spin-transfer torque. *Phys. Rev. B*, 66(1):014407, 2002.

[8] X.-P. Wang, C. J. García-Cervera, and W. E. A Gauss-Seidel projection method for micromagnetics simulations. *J. Comput. Phys.*, 171(1):357–372, 2001.

[9] S. Zhang, P. M. Levy, and A. Fert. Mechanisms of spin-polarized current-driven magnetization switching. *Phys. Rev. Lett.*, 88(23):236601, 2002.

Conclusion and Perspectives

In this PhD thesis, we have proposed mathematical modeling and numerical simulation of innovative electronic devices. First, we have studied an ultra-scaled confined nanostructure, in which the electron transport is unidimensional, and the cross-section comprises so few atoms that an atomistic description is necessary. We have performed an asymptotic process using an envelope function decomposition in order to establish a new effective mass model. We have also presented numerical simulations for a one-wall simplified carbon nanotube, in order to test the capability of this model to describe the electron transport in this strongly confined structure. Next, we have considered the case of non-ballistic transport where the evolution of charged particles is mainly driven by collisions with phonons. In this case, we have derived and analyzed an effective mass diffusive model. Finally, we have considered a hybrid classical-quantum approach where the drift-diffusion model is spatially coupled with the quantum effective mass model. In the last part, we have modeled and simulated the magnetization switching of a ferromagnetic material driven by a spin-current, without applying any external magnetic field. In particular, we have presented the model used for this spintronic problem, we have constructed an appropriate numerical scheme that allows to recover numerically various results of physical experiments and we have performed a formal asymptotic study.

Along this PhD thesis, we have given great importance to the study of the various time and space scales involved in the studied phenomena. It is essential that the conceived models and the implemented schemes take into account in an optimal way the multiscales. For example, we have used an envelope function decomposition to completely separate the oscillating part of the wave function from its slowly varying one in the study of the effective mass model. Moreover, in the spintronic problem, we have chosen exponential basis functions to consider that the behaviour of the spin density is quite different in the directions parallel or transverse to the magnetization. Consequently, we have obtained some accurate and computationally efficient numerical simulations. All the presented results are in accordance, at least qualitatively, with the physical expectations. Moreover, an effort has been done in the parallelization of the code to develop high performance computations. For all these reasons, this PhD work provides an interesting progress in the modeling of innovative electronic devices. In the future, it could be used in complementarity of physical experiments, and it could become an interesting tool to improve the electronic behaviour of future devices and eventually to design new performant architectures.

Let us now expose some perspectives to this work. First of all, concerning the ultra-scaled confined nanostructures, an interesting point would be to test numerically our effective mass models for more relevant physical devices. In this thesis, we consider only a simplified one wall carbon nanotube as toy problem. We focused on the derivation and the implementation of the coupling between the one dimensional transport equations and the three dimensional Poisson equation. The obtained numerical simulations allow us to say that our models are able to capture correctly the qualitative behavior of the physical quantities. In order to obtain results for more realistic devices, the Bloch problem should be improved, incorporating relevant physical parameters. In particular, it is essential to improve the geometry of the cross-section, the position of the atoms in the unit cell (in order to model a real crystal lattice), the thickness of the oxide layer, the choice of the pseudo-potential... All this will allow on the one hand to compare our numerical simulations with the physical experiments, and on the other hand to understand how some of the involved parameters affect the simulations. For example, it should be interesting to investigate numerically which is the optimal number of energy bands to be taken into account, whether or not this number depends on the lattice spacing ϵ. To reach this goal, it would be precious to establish collaboration with physicists or electrical engineers.

From a modeling and/or a mathematical point of view, there are also attractive extensions. First, a rigorous derivation of the model proposed in Chapter 2 is necessary. Moreover, as Naoufel had in mind already at the beginning of this project, the study of a mildly curved structure is an exciting open problem since nanowires are never fully straight. Some works exist in the study of the transport in curved quantum waveguides. The idea would be to try to apply them to ultra-scaled confined nanostructures and, expecting to obtain variable effective masses depending on the curvature of the wire. Also, the derivation of a quantum drift-diffusion model for ultra-scaled confined nanostructures seems interesting to be investigated. It should allow to incorporate quantum effects in the macroscopic nanowire problem and could be compared with the hybrid quantum-classical strategy, or even be inserted into the domain decomposition approach in place of the drift-diffusion equation in the collisional region. Next, in this PhD thesis, the treatment of the multiple eigenvalues has been discussed only for the quantum model. In ultra-scaled devices, the degeneracy of energy bands is crucial. Consequently, it would be interesting to take it into account in the drift-diffusion equation. The formal derivation of a collisionless Vlasov system from a system of coupled Schrödinger equations (as obtained in Proposition 2.4.2) seems a reasonable work. However, the choice of the collision operator to be added heuristically to the collisionless system seems to be a deep problem.

To finish, concerning the study of ferromagnetic multilayer materials, we can say that the spin transfer is a challenging problem of spintronics. In this PhD thesis, we study the magnetization switching driven by a spin current. But it seems that the spin transfer is involved in other phenomena : magnetization excitations (or magnetic oscillators), domain wall motion... So, a natural extension would be to use the knowledges that we acquired during this work to study numerically other spintronic applications. In particular, the very fast oscillations that appeared in our work could turn out to be a key point in magnetic oscillators.

Mathematical modeling and numerical simulation of innovative electronic nanostructures

Summary : In this PhD thesis, we are interested in the modeling and the simulation of innovative electronic nanodevices. First, we formally derive an effective mass model describing the quantum motion of electrons in ultra-scaled confined nanostructures. Numerical simulations aim at testing the relevance of the obtained model for a simplified (but already significant) device. The second part is devoted to non-ballistic transport in these confined nanostructures. We rigorously analyse a drift-diffusion model and afterwards we describe and implement a classical-quantum spatial coupling approach. In the last part, we model and simulate a spintronic nanodevice. More precisely, we study the magnetization switching of a ferromagnetic material driven by a spin-current.

Keywords : ultra-scaled confined nanostructures, effective mass approximation, classical/quantum transport, Schrödinger-Poisson system, drift-diffusion equation, spintronics, spin transfer, Landau-Lifshitz equation, multiscale analysis, asymptotic expansions, numerical simulation.

Mathematical modeling and numerical simulation of innovative electronic nanostructures

Author : Clément JOURDANA,

Supervisors : Paola PIETRA (Pavia),
Pierre DEGOND standing in for Naoufel BEN ABDALLAH (Toulouse),

Defense date : November 25^{th}, 2011.

Résumé : Dans cette thèse, nous nous intéressons à la modélisation et la simulation de dispositifs nanoélectroniques innovants. Premièrement, nous dérivons formellement un modèle avec masse effective pour décrire le transport quantique des électrons dans des nanostructures très fortement confinées. Des simulations numériques illustrent l'intérêt du modèle obtenu pour un dispositif simplifié mais déjà significatif. La deuxième partie est consacré à l'étude du transport non ballistique dans ces mêmes structures confinées. Nous analysons rigoureusement un modèle de drift-diffusion et puis nous décrivons et implémentons une approche de couplage spatial classique-quantique. Enfin, nous modélisons et simulons un nanodispositif de spintronique. Plus précisement, nous étudions le renversement d'aimantation dans un matériau ferromagnétique multi-couches sous l'effet d'un courant de spin.

Mots clés : nanostructures à fort confinement, approximation de la masse effective, transport classique/quantique, système Schrödinger-Poisson, équation de dérive-diffusion, spintronique, transfert de spin, équation de Landau-Lifshitz, analyse multi-échelles, développements asymptotiques, simulations numériques.

Riassunto : Questa tesi è dedicata alla modellazione e alla simulazione di dispositivi nanoelettronici innovativi. Nella prima parte, deriviamo formalmente un modello a masse efficace per descrivere il trasporto quantistico degli elettroni in nanostrutture fortemente confinate. Simulazioni numeriche illustrano l'interesse del modello ottenuto per un dispositivo semplificato ma già significativo. La seconda parte è dedicata al trasporto non balistico sempre in nanostrutture confinate. Si analizza rigorosamente un modelo di drift-diffusion e, in seguito, si presenta e si implementa un algoritmo di accoppiamento spaziale classico-quantistico. Infine, modelliamo e simuliamo un nanodispositivo di spintronica. Più precisamente, studiamo l'inversione di magnetizzazione in un materiale ferromagnetico multi-strato sotto l'effetto di una corrente di spin.

Parole chiave : nanostrutture fortemente confinate, approssimazione della massa efficace, trasporto classico/quantistico, sistema di Schrödinger-Poisson, equazione di drift-diffusion, spintronica, transferimento di spin, equazione di Landau-Lifshitz, analisi multiscala, sviluppi asintotici, simulazione numerica.

Research laboratory address

Institut de Mathématiques de Toulouse
Université Paul Sabatier
118 route de Narbonne
31062 Toulouse Cedex 9, France

Dipartimento di Matematica "F. Casorati"
Università degli Studi di Pavia
via Ferrata, 1
27100 Pavia, Italy